


This item was submitted to Loughborough University as a PhD thesis by the author and is made available in the Institutional Repository (<https://dspace.lboro.ac.uk/>) under the following Creative Commons Licence conditions.




CC creative commons
COMMONS DEED


Attribution-NonCommercial-NoDerivs 2.5


You are free:

- to copy, distribute, display, and perform the work

Under the following conditions:

 **Attribution.** You must attribute the work in the manner specified by the author or licensor.


 **Noncommercial.** You may not use this work for commercial purposes.

 **No Derivative Works.** You may not alter, transform, or build upon this work.

- For any reuse or distribution, you must make clear to others the license terms of this work.
- Any of these conditions can be waived if you get permission from the copyright holder.

Your fair use and other rights are in no way affected by the above.

This is a human-readable summary of the [Legal Code \(the full license\)](#).

[Disclaimer](#) 

For the full text of this licence, please go to:
<http://creativecommons.org/licenses/by-nc-nd/2.5/>

**Simulation Study on PEM Fuel Cell Gas Diffusion
Layers Using X-Ray Tomography Based Lattice
Boltzmann Method**

By

Yu Liu

Submitted in partial fulfilment of the requirements for the award of

Doctor of Philosophy of Loughborough University

November 2011

©Copyright by Yu Liu, 2011

Acknowledgement

The research work presented in this thesis is supported by the UK Technology Strategy Board (TSB Project no: TP/6/S/K3032H). The project is on Prediction and Management of Fluid Transport in PEM Fuel Cells and involves team partners of Liverpool University, Birmingham University, Loughborough University, Technical Fibre Products Ltd., Intelligent Energy Ltd., Johnson Matthey Fuel Cells Ltd., AVL List GmbH and Saati Group Inc. As one of the team members from Loughborough University, I have completed the work on LB model tuning, combining the LB model with the x-ray imaging technique and carrying out the simulation of fluid flow transport through the GDL; however, this research would not be successful without the support from all the partners.

I would like to acknowledge the kind support from all the team partners for making my research successful by providing technical support, sharing knowledge and experience and providing physical support throughout the whole project. Every minute you spent and effort you devote to my research will always be highly appreciated, in particular:

Dr. Xiaoxian Zhang, Liverpool University, for providing the LB source code and sharing your experience on LB simulation.

Dr. Hossein Ostadi and Professor Kyle Jiang, Birmingham University, for providing the 3D reconstructed GDL x-ray tomography images.

Dr. Pratap Rama, Loughborough University during the project then Intelligent Energy Ltd., for sharing your expertise on PEM fuel cell.

Michael Jeschke and Rosemary Fisher, Technical Fibre Products Ltd., for supplying carbon paper samples and the test data

Mark Jones and Dr. Paul Adcock, Intelligent Energy Ltd., for providing technical advices.

Graham Hards, Dr. Ian Harkness and Dr. Jonathan Sharman, Johnson Matthey Fuel Cells Ltd., for supplying technical advices and the test data.

Paolo Fracas, Saati Group Inc., for providing carbon cloth samples.

Last but not least, my supervisor, Professor Rui Chen, for your continuous guidance, encouragement and constructive reviews. Your tireless effort put in to ensure my successful completion of the research will always be cherished.

For those whose assistance went to see me through, and are not mentioned herein, I would like to thank you too and recognize your value to me.

ABSTRACT

The Polymer Electrolyte Membrane (PEM) fuel cell has a great potential in leading the future energy generation due to its advantages of zero emissions, higher power density and efficiency. For a PEM fuel cell, the Membrane-Electrode Assembly (MEA) is the key component which consists of a membrane, two catalyst layers and two gas diffusion layers (GDL). The success of optimum PEM fuel cell power output relies on the mass transport to the electrode especially on the cathode side. The carbon based GDL is one of the most important components in the fuel cell since it has one of the basic roles of providing path ways for reactant gases transport to the catalyst layer as well as excess water removal. A detailed understanding and visualization of the GDL from micro-scale level is limited by traditional numerical tool such as CFD and experimental methods due to the complex geometry of the porous GDL structural. In order to take the actual geometry information of the porous GDL into consideration, the x-ray tomography technique is employed which is able to reconstructed the actual structure of the carbon paper or carbon cloth GDLs to three-dimensional digital binary image which can be read directly by the LB model to carry out the simulation.

This research work contributes to develop the combined methodology of x-ray tomography based the three-dimensional single phase Lattice Boltzmann (LB) simulation. This newly developed methodology demonstrates its capacity of simulating the flow characteristics and transport phenomena in the porous media by dealing with collision of the particles at pore-scale. The results reveal the heterogeneous nature of the GDL structures which influence the transportation of the reactants in terms of physical parameters of the GDLs such as porosity, permeability and tortuosity. The compression effects on the carbon cloth GDLs have been investigated. The results show that the c applied compression pressure on the GDLs will have negative effects on average pore size, porosity as well as through-plane permeability. A compression pressure range is suggested by the results which gives optimum in-plane permeability to through-plane permeability. The compression effects on one-dimensional water and

oxygen partial pressures in the main flow direction have been studied at low, medium and high current densities. It's been observed that the water and oxygen pressure drop across the GDL increase with increasing the compression pressure.

Key Words: PEM fuel cell, GDL, LB simulation, SPSC, SPMC, x-ray tomography, carbon paper, carbon cloth, porosity, permeability, degree of anisotropy, tortuosity, flow transport.

List of Figures

Figure 1.1 Fuel cell system components and flow chart.....	22
Figure 1.2 Polymer Electrolyte Membrane (PEM) fuel cell.....	25
Figure 1.3 Fuel cell polarization curve.....	30
Figure 2.1 scanning electron microscope (SEM) images of (a) carbon paper, and (b) carbon cloth.....	46
Figure 2.2 Three-dimensional view of schematic of pore-network model for a carbon paper GDL in the work of Sinha and Wang.....	53
Figure 3.1 D3Q19 LB cube.....	63
Figure 3.2 The nineteen velocities in (a) the x-y plane; (b) z-x plane; (c) z-y plane in the D3Q19 LB scheme.....	64
Figure 3.3 Treatment of gas-solid boundary by the bounce-back method in the x-y plane of a LB cube; the shadowed area is solid and the white is void space; the line ABC is the boundary.....	67
Figure 4.1 The micro/nano tomography system.....	72
Figure 4.2 X-ray tomography images of a carbon cloth sample. (a) typical two-dimensional shadow image; (b) reconstructed greyscale cross-section image by CTAn software with microtomography.....	73
Figure 4.3 Variation of fiber diameter and porosity of 5% threshold band (13 grey levels). (a) average fiber diameter; (b) porosity.....	75
Figure 4.4 The effect of 5% change in threshold on fiber continuity. The highlighted parts are example of this discontinuity. (a) low threshold; (b) high threshold.....	75
Figure 4.5 2D and 3D images of a GDL carbon paper sample; (a) 2D shadow X-ray tomographic image; (b) 2D reconstructed grey scale image using CTAn software; (c) binary image of the cross section shown in (b). (d) an isometric view of the reconstructed image of carbon paper GDL with 680nm resolution using CTAn.....	76

Figure 5.1 Flowchart of X-ray tomography imaging and LB simulation.....	84
Figure 5.2 The overall 14 regions of 3D shadow image of the carbon paper GDL for the LB simulation, provided by the x-ray microtomography.....	85
Figure 5.3 The simulated absolute permeability of 14 regions, the mean simulated absolute permeability, and the measure values for the same sample.....	86
Figure 5.4 The binary 3D images of region 1(a), region 8(b), and region 14(c) from Figure 5.3.....	88
Figure 5.5 Rotated 3D binary images of (a), (b) and (c) to show the fibril structure and void space of region 1, region 8 and region 14, respectively.....	89
Figure 5.6 Simulated absolute permeability of two in-plane direction: x direction (a) and z direction (b).....	90
Figure 6.1 X-ray microtomography structure of the carbon paper GDL. The simulation region is shown in size of $78.3 \mu m \times 78.3 \mu m \times 252.3 \mu m$, in x, y and z direction, respectively.....	98
Figure 6.2 3D stream tubes of the reconstructed 3D digital image of the carbon paper GDL shown in Figure 6.1.....	99
Figure 6.3 Simulation area of PEM fuel cell for SPMC LB model.....	99
Figure 6.4 General modeling scheme of the multicomponent fluid transport through x-ray micro-tomography reconstructed 3D digital GDL stricture.....	101
Figure 6.5 Convergence of SPMC Lattice Boltzmann simulations.....	103
Figure 6.6 Simulated boundary condition of partial pressure at cathode GDL/channel interface B1 for the LB model by 1D fuel cell model.....	105
Figure 6.7 Simulated boundary condition of flow rate at GDL/catalyst layer interface B2 for the LB model by 1D fuel cell model.....	106

Figure 6.8 Comparison of LB model and 1D GTE fuel cell model predictions of gas partial pressure profile along the GDL flow direction at $A_D C_D$ condition; (a) water; (b) oxygen; (c) nitrogen.....	109
Figure 6.9 Comparison of LB model and 1D GTE fuel cell model predictions of gas partial pressure profile along the GDL flow direction at $A_W C_W$ condition; (a) water; (b) oxygen; (c) nitrogen.....	111
Figure 6.10 Comparison of LB model and 1D GTE fuel cell model predictions of gas partial pressure profile along the GDL flow direction at $A_W C_D$ condition; (a) water; (b) oxygen; (c) nitrogen.....	113
Figure 6.11 Comparison of LB model and 1D GTE fuel cell model predictions of gas partial pressure profile along the GDL flow direction at $A_D C_W$ condition; (a) water; (b) oxygen; (c) nitrogen.....	115
Figure 6.12 3D visualization of water pressure distribution in the carbon paper GDL volume in size of $78.3\mu\text{m} \times 78.3\mu\text{m} \times 252.3\mu\text{m}$ simulated by SPMC LB model, (a) $A_D C_D$; (b) $A_W C_W$; (c) $A_W C_D$ (d) $A_D C_W$	117
Figure 7.1 Overall 3D image of the carbon cloth GDL of numbered with 21 divided regions.....	121
Figure 7.2 Calculated absolute permeability of total 21 regions of the carbon cloth GDL by LB mode of (a) through-plane y direction; (b) in-plane x direction; (c) in-plane z direction.....	124
Figure 7.3 3D image structure of (a) region 12; (b) region 8 and (c) region 7.....	125
Figure 7.4 Permeability against porosity.....	126
Figure 7.5 Calculated degree of anisotropy in the (a) in-plane x direction; (b) in-plane z direction.....	138
Figure 7.6 Through-plane permeability prediction on porosity by LB mode, Carman-Kozeny (KC) model, and Tomadakis-Sotirchos (TS) model.....	130

Figure 8.1 Compressed carbon cloth GDL encapsulated in PDMS.....	134
Figure 8.2 Reconstructed structures (left column) and corresponding binary cross section image (right column) of the compressed carbon cloth GDL under compression pressure of (a) 0.0 MPa; (b) 0.1 MPa; (c) 0.3 MPa; (d) 1.0 MPa; (e) 3.3 MPa; (f) 10.0 MPa; (g) 20.0 MPa; (h) 100.0 MPa.....	140
Figure 8.3. Pore size distribution data of the carbon cloth GDL with compression pressure of: (a) 0.0 MPa; (b) 0.1 MPa; (c) 1.0 MPa; (d) 10.0 MPa; and (e) 20.0 MPa and (f) 100.0 MPa.....	143
Figure 8.4 Maximum pore radius and mean pore radius against compression pressure, as summarized from PSD data in Figure 8.3.....	144
Figure 8.5 Main pore radius band (10 -14 μm) population to overall pore volume in percentage against compression pressure.....	145
Figure 8.6 (a) Calculated through-plane and in-plane permeability tensors, and (b) Calculated degree of anisotropy on the compression pressure. k_{zz} for through-plane z-direction, k_{zy} and k_{zx} for in-plane x-direction and y direction, respectively.....	147
Figure 8.7. Porosity variation on compression pressure for compressed samples of 0.1 MPa to 20.0 MPa.....	148
Figure 8.8. Non-dimensional through-plane permeability against the corresponding porosity.....	149
Figure 8.9. non-dimensional through-plane permeability as a function of carbon cloth GDL compression pressure.....	150
Figure 8.10. Through-plane tortuosity as a function of porosity for all uncompressed and compressed carbon cloth GDL samples.....	151
Figure 8.11. Compression effect on partial pressure of water at 0.2 A/cm ² current density.....	153
Figure 8.12. Compression effect on partial pressure of water at 0.6 A/cm ² current density.....	154

Figure 8.13. Compression effect on partial pressure of water at 1.2 A/cm ² current density.....	155
Figure 8.14 Simulated water flow rate at GDL/catalyst layer interface for the GDL with 1.0 MPa compression pressure at 0.2 A/cm ² , 0.6 A/cm ² and 1.2 A/cm ² current density condition.....	155
Figure 8.15 Compression effect on partial pressure of oxygen at 0.2 A/cm ² current density.....	157
Figure 8.16. Compression effect on partial pressure of oxygen at 0.6 A/cm ² current density.....	157
Figure 8.17. Compression effect on partial pressure of oxygen at 1.2 A/cm ² current density.....	158
Figure 8.18 The pressure drop of water vapour across the GDL against the compression pressure of 0.0~20.0 MPa at current density of 0.2 A/cm ² , 0.6 A/cm ² and 1.2 A/cm ²	159
Figure 8.19 The pressure drop of oxygen across the GDL against the compression pressure of 0.0~20.0 MPa at current density of 0.2 A/cm ² , 0.6 A/cm ² and 1.2 A/cm ²	159

List of Tables

Table 4.1 General classification of computed tomography.....	70
Table 5.1 Image sizes for each region of the 3D carbon paper image.....	85
Table 6.1 Physical Properties of PEM fuel cell component layers and thermodynamic operating conditions.....	104
Table 6.2 Simulation cases for boundary conditions and cross-validation.....	105
Table 6.3 Percentage difference on partial pressure for water, oxygen and nitrogen between LB model and GTE model.....	116
Table 7.1 Average permeability of the 21 regions for both through-plane and in-plane.....	122
Table 8.1 Image sizes of 3D reconstructed carbon cloth GDL from x-ray microtomography.....	135
Table 8.2. Thermodynamic operating conditions for calculating the boundary conditions for LB model.....	152

Nomenclature

- a = Activity
- c_i = concentration, mol/cm³
- Δc = concentration gradient
- c_s = lattice sound speed
- D_0 = free diffusion coefficient
- D_e = effective diffusion in the porous structure
- $D_{i,j}^{eff}$ = effective binary diffusivity of the pair i and j
- D_i^T = thermal diffusion coefficient, cm²/s
- E = Cell potential, V
- E^0 = Reversible cell voltage at standard pressure, V
- $E_{i,n}$ = error
- e_k = velocity of particles moving the k th direction
- F = Faraday constant, 96487 C
- f_k = particle distribution function
- f_k^{eq} = equilibrium distribution function
- $f_k^i(\mathbf{x}, t)$ = the particle distribution function in the direction of k for species i .
- ΔG_f = Gibbs free energy of formation,
- $\Delta \bar{g}_f^0$ = The change in molar Gibbs free energy of formation at standard pressure
- $\Delta \bar{h}_f$ = Enthalpy of formation
- J = Current density, A/cm²
- J_0 = Exchange current density, A/cm²
- J_L = Limiting current density, A/cm²
- K_{KC} = KC constant

- k_j = permeability pre-factor accounting for liquid saturation
- k = absolute permeability
- L = length along thickness direction
- L_x, L_y, L_z = sample length in the x, y, and z direction, respectively
- M_i = molecular weight of species i , g/mol
- N_A = Avogadro number, molecules/mol
- N = total number of pore voxels in the structure
- \dot{n}_i = molar flux rate, mol/cm²-s
- P = Partial pressure, atm
- ΔP = applied pressure gradient
- $Q^{ii}(\mathbf{x}, t)$ = self-collision function between particles of species i .
- $Q^{ij}(\mathbf{x}, t)$ = cross-collision function between particles of species i and species j
- q = average velocity in the pressure gradient direction
- q_i = flow rate by LB model in terms of particle distribution functions of all species
- $q_{x,i}$ = species flow towards x direction at node i in the 3D lattice.
- q_x, q_y, q_z = average velocity in the x, y, and z direction, respectively
- R = Universal gas constant, 8.3143 J/mol K
- $R^{internal}$ = Internal resistance, V
- r = average fiber radius, mm
- t = time
- u_f = Fuel utilization
- V_c = Average voltage of one cell in a stack, V
- T = Temperature

- u_i = bulk velocity of species i , cm/s
- \bar{V}_w = Molar volume of water
- v_i = molecular velocity, cm/s
- w_i = weighting factor for the D3Q19 LB model.
- x_i = Mole fraction of species i
- x, y, z = coordination of the origin of elements in the LB scheme

Greek Letters

- φ = Fuel cell efficiency
- η = Overpotential, V
- η_s = Surface overpotential, V
- ξ_i = Electro-osmotic drag ratio of species i
- ξ_k^i = the particle velocity of species i in direction k
- ζ = Parametric coefficient
- μ = kinetic viscosity
- μ_j = phase viscosity
- ψ = error estimator
- Θ_{perm} = order of magnitude of measured absolute permeability
- Ω = steady state estimator
- ρ_i = density of species i , g/cm³
- Φ_i = electrochemical potential, J/mol
- τ_i = dimensionless relaxation parameter for self-collision of species i .
- τ_{ij} = dimensionless relaxation parameter for cross-collision of species i and j .
- Γ_i = percentage difference of the average pressure of each gases

- ε = porosity of the material
- ε_p = percolation threshold of TS equation
- γ = degree of anisotropy based on permeability
- α = tuning parameter of TS equation
- ε_0 = percolation threshold of porosity
- σ = through-plane tortuosity of the material
- μ_G = Gas phase Viscosity, Pa s

Abbreviations

- AFC = Alkaline Fuel Cell
- DMFC = Direct Methanol Fuel Cell
- GDL = Gas diffusion layer
- HHV = Higher heating value
- LHV = Lower heating value
- MEA = Membrane electrolyte assembly
- OCV = Open circuit voltage
- ORR = Oxygen reduction reaction
- PAFC = Phosphoric Acid Fuel Cell
- PEMFC = Polymer electrolyte membrane fuel cell
- MCFC = Molten Carbonate Fuel Cell
- SOFC = Solid oxide fuel cell
- SPSC = single phase single component
- SPMC = single phase multi-component
- $A_D C_D$ = both anode and cathode are supplied with dry gases

$A_W D_W$ = both anode and cathode are supplied with humidified gases

$A_W C_D$ = only anode is supplied with humidified gases

$A_D C_W$ = only cathode is supplied with humidified gases

List of Publications

1. Rama, P., Liu, Y., and Chen, R., "*Polymer Electrolyte Fuel Cell Transport Mechanisms: Simulation Study of Hydrogen Crossover and Water Content*", SAE 2008-01-1802, 2008 SAE International Powertrains, Fuels and Lubricants Congress, Shanghai, 2008
2. Ostadi, H., Rama, P. Liu, Y. Chen, R. Zhang, X., Jiang, K., "*Micr/Nano Tomography for Analysis of Gas Diffusion Layers of Microfuel Cells*", Power MEMS 2009 Workshop, Washington DC, USA, 1-4 Dec. 2009.
3. Ostadi, H., Rama, P. Liu, Y. Chen, R. Zhang, X., Jiang, K., "*Nanotomography Based Study of Gas Diffusion Layers*", *Microelectronic Engineering*, 87 (2010) 1640–1642, doi:10.1016/j.mee.2009.10.027.
4. Ostadi, H., Rama, P. Liu, Y. Chen, R. Zhang, X., Jiang, K., "*3D Reconstruction of a Gas Diffusion Layer and a Microporous Layer*", *J. Membrane Science* 351 (2010) 69–74. doi:10.1016/j.memsci.2010.01.031
5. Rama, P., Liu, Y., and Chen, R., Ostadi, H., Jiang, K., Zhang, X. X., Fisher, R., Jeschke, M., "*An X-Ray Tomography Based Lattice-Boltzmann Simulation Study on Gas Diffusion Layers of Polymer Electrolyte Fuel Cell*", *Transactions of the American Society of Mechanical Engineers (ASME), J. Fuel Cell Science and Technology*, Vol. 7, (2010), doi:10.1115/1.3211096.
6. Rama, P., Liu, Y., and Chen, R., Ostadi, H., Jiang, K., Zhang, X. X., Gao, Y., Fisher, R., Jeschke, M., "*Multi-Scale Modelling of Single-Phase Multi-Component Transport in the Cathode Gas Diffusion Layer of a Polymer Electrolyte Fuel Cell*", *Energy & Fuels*, (2010), 24, 3130–3143, DOI:10.1021/ef100190c.
7. Ostadi, H., Rama, P. Liu, Y. Chen, R. Zhang, X., Jiang, K., "*Threshold Fine-Tuning and 3D Characterisation of Porous Media using X-ray Nanotomography*", *Current Nanoscience*, Vol.6-2, pp.226-231, (2010).
8. Ostadi, H., Rama, P. Liu, Y. Chen, R. Zhang, X., Jiang, K., "*Influence of Threshold Variation on Determining the Properties of a Polymer Electrolyte Fuel Cell Gas Diffusion Layer in X-ray Nano-tomography*", *J. Chemical Engineering Science*, 65(2010)2213–2217, doi:10.1016/j.ces.2009.12.019.
9. Ostadi, H., Rama, P. Liu, Y. Chen, R. Zhang, X., Jiang, K., "*Multi-Scale Simulation of Single-Phase Multi-Component Transport in the Cathode Gas Diffusion Layer of a Polymer Electrolyte Fuel Celltalized*", *ECS Transactions*, 28 (27) 103-111 (2010), DOI:10.1149/1.3496618 © The Electrochemical Society
10. Rama, P., Liu, Y., Chen, R., Ostadi, H., Jiang, K., "*Determination of the Anisotropic Permeability of a Carbon Cloth Gas Diffusion Layer through X-ray Computer*

Micro-Tomography and Single-Phase Lattice Boltzmann Simulation", Intl. J. for Numerical Method in Fluids, (2010), DOI: 10.1002/flid.2378.

11. Rama, P., Liu, Y., and Chen, R., Ostadi, H., Jiang, K., Zhang, X. X., Gao, Y., Brivio, D., Grassini, P., "A Numerical Study of Structural Change and Anisotropic Permeability in Compressed Carbon Cloth Polymer Electrolyte Fuel Cell Gas Diffusion Layers", Fuel Cells, DOI: 10.1002/fuce201000037, (2010).
12. Rama, P., Liu, Y., and Chen, R., Ostadi, H., Jiang, K., Zhang, X. X., Gao, Y., Fisher, R., Jeschke, "Simulation of Liquid Water Breakthrough in a Nano-Tomography Reconstruction of a Carbon Paper Gas Diffusion Layer", American Institute of Chemical Engineers (AIChE Journal), (2010). DOI 10.1002/aic.12581

CONTENTS

CHAPTER 1. Introduction	17
1.1. Introduction of Fuel Cell	17
1.1.1. Introduction	17
1.1.2. Fuel Cell Types	19
1.1.3. Fuel Cell System	22
1.2. Polymer Electrolyte Membrane Fuel Cell	24
1.2.1. Introduction	24
1.2.2. Electrochemical Reactions and Thermodynamics	26
1.2.3. Irreversible Voltage	30
1.2.4. Literature Reviews on PEM Fuel Cells	33
1.3. Objective of the Research	36
CHAPTER 2. Literature Reviews on Gas Diffusion Layers	37
2.1. Gas Diffusion Layers in PEM Fuel Cells	37
2.1.1. Characteristics of Gas Diffusion Layers	37
2.1.2. Materials and Structures of the Gas Diffusion Layers	44
2.1.3. Mass Transport in the Gas Diffusion Layers	47
2.2. Gas Diffusion Layers Models	49
2.2.1. Macroscopic and Microscopic Models	49
2.2.2. CFD Models	52
2.2.3. Lattice Boltzmann Models	53
2.3. Imaging and Reconstruction of the Gas Diffusion Layer	54
2.4. Aim and Methodology of the Research	55
2.5. Outline of the Thesis	56
CHAPTER 3. The Lattice Boltzmann Method	58
3.1. Introduction	58
3.2. Theory and Key Numerical Equations	59
3.2.1. Lattice Boltzmann Automata	59
3.2.2. Kinetic Theory of Gases	60
3.2.3. The Lattice Boltzmann Equations	61
3.3. Lattice Boltzmann Models	64
3.3.1. Bhatnagar-Gross-Krook Model	64

3.3.2. Boundary Treatment.....	66
3.4. Conclusions	67
CHAPTER 4. X-Ray Tomography Imaging Technique.....	68
4.1. Introduction.....	68
4.2. Equipment and Methodologies.....	69
4.2.1. Two-Dimensional Image Acquisition	71
4.2.2. Image Processing and Threshold Tuning	72
4.2.3. Three-Dimensional Digital Reconstruction	74
4.3. Conclusions	75
CHAPTER 5. X-Ray Tomography Based Lattice Boltzmann Simulations.....	77
5.1. Introduction.....	77
5.2. Methodology	78
5.2.1. Single Phase Single Component LB Model	78
5.2.2. X-ray Microtomography	79
5.3. Simulation	79
5.3.1. Permeability Calculation	80
5.3.2. Simulation scheme	82
5.4. Results and Validation	83
5.4.1. The through-plane absolute permeability	85
5.4.2. The In-plane Absolute Permeability	88
5.5. Conclusions	89
CHAPTER 6. Simulation Studies on Carbon Paper Gas Diffusion Layer.....	91
6.1. Introduction.....	91
6.2. Methodology	91
6.2.1. Single Phase Multicomponent LB model	92
6.2.2. 1D General Transport Equation Based Fuel Cell Model.....	95
6.2.3. X-ray Tomography imaging	96
6.3. The Simulations	98
6.3.1. Interfacial Conditions.....	98
6.3.2. Simulation Scheme	100
6.4. Results and Validation	102
6.4.1. Boundary Conditions	102
6.4.2. Prediction on 1D Partial Pressure Profile of Multi-species.....	105

6.4.3. Three-dimensional Visualizations.....	115
6.5. Conclusions	116
CHAPTER 7. Simulation Studies on Carbon Cloth Gas Diffusion Layer	118
7.1. Introduction.....	118
7.2. Methodology	119
7.3. Simulated Permeability	120
7.3.1. Results and Validation.....	120
7.3.2. Permeability and Porosity Relationship.....	124
7.4. Degree of Anisotropy	125
7.5. Prediction of Permeability	127
7.6. Conclusions	129
CHAPTER 8. Numerical Studies on Compressed Carbon Cloth Gas Diffusion Layer.....	131
8.1. Introduction.....	131
8.2. Methodology	133
8.2.1. Sample preparation	133
8.2.2. Three-dimensional reconstruction	134
8.2.3. Key Equations	134
8.3. Simulation Results	136
8.3.1. Compressions Effects on Structure and Pore Size Distribution.....	136
8.3.2. Compression Effects on Anisotropic Permeability	144
8.3.3. Compression Effects on Porosity	147
8.3.4. Compression Effects on Tortuosity	149
8.3.5. Compression Effect on 1D Partial Pressure.....	151
8.4. Conclusions	160
CHAPTER 9. Conclusions.....	162
9.1. Conclusions	162
9.2. Recommendation for Future Work	167

REFERENCES

CHAPTER 1. **Introduction**

1.1. Introduction of Fuel Cell

1.1.1. Introduction

The environment issue has been concerned more and more with the rapid development in technology on energy generation. The fossil fuels which still serve as the majority energy nowadays have resulted in global warming and put species on earth in danger regarding health. Global warming is becoming more serious year by year due to the usage of fossil fuels, and the side effects of burning fossil fuels give rise to increasing pollutant emissions. Also, the booming population means there will be higher demands on energy resource in the future, and this implies that the environment and pollutions situations will become worse. Therefore, the need for environment friendly clean energy has been voiced as the main trends in energy consumptions. Fuel cells have been widely accepted as one of the most promising technologies to achieve this global goal.

The principle of fuel cells was first discovered in 1838 by German scientist Christian Friedrich Schonbein. Soon after this discovery, in 1839 Sir William Grove developed the first fuel cell in England. He demonstrated his experience by using electricity to decouple water into hydrogen and oxygen. The first commercial use of fuel cells was launched by General Electric Company. In 1958, Leonard Niedrach, a GE chemist invented the fuel cell using the membrane deposited with platinum which served as catalyst for the electrochemical reaction, and this fuel cell is named “ Grubb-Niedrach fuel cell’ after the inventors. GE followed up developing this technology with NASA and McDonnell Aircraft for further use during Project Gemini. Until 1969, Dr. Bacon successfully produced a

practical fuel cell device which was capable of producing 5 kW of power for supplying a welding machine. Since the 1970s, fuel cell technology gained more attention. A number of companies and research organizations began serious researches into fuel cells on areas of identifying the optimum fuel source, material development and component design in order to mature the technology for commercial applications. During the 1980s, fuel cell technology started to be applied and tested on vehicles. Early in the 1990s Daimler-Benz worked in collaboration with Ballard on producing Polymer Electrolyte Membrane (PEM) fuel cell powered cars. In 1991, the first hydrogen fuel cell vehicle was developed by Roger Billings¹. Two years later fuel cell vehicles developed by the Canadian company Ballard firstly appeared in the market. In 1996, Toyota manufactured a hydrogen-fuelled fuel cell/battery hybrid passenger car. In 2000, AeroVironment selected PEM technology to provide night time power for its solar-powered *Helios* long-duration aircraft². The goal was to make an unpiloted aircraft that could fly continuously for up to six months by using photovoltaic panels during the day to run electric motors and electrolyze water. At night, the fuel cell ran the motors by converting the hydrogen and oxygen back into water. Several test flights were made with and without a fuel cell from 2001 to 2003. In more recent years, a number of manufacturers including major auto makers and various federal agencies have supported ongoing research into the development of fuel cell technology for use in fuel cell vehicles (FCV) and other applications, since air quality regulations grow steadily stricter. Energy Partners and the U. S. Department of Energy's Office of Advanced Automotive Technologies provided two 20 kW fuel cell stacks to Virginia Tech and Texas Tech universities to evaluate performance in hybrid electric cars. Major automakers like Ford and Volkswagen are also testing PEM vehicles. In 2005, the NASA Glenn Research Centre initiated the development of a fuel-cell-powered utility vehicle as a way to reduce pollution in industrial settings, fossil-fuel consumption and operating cost for transportation systems. The utility vehicle provides an inexpensive approach to advance the state of the art for electric vehicle technology in a practical application. Honda delivered FCX, an advanced hydrogen-powered fuel cell vehicle, to the world's first individual customer. The 2005 FCX model was powered by Honda's originally developed fuel cell stack (Honda FC Stack) with the breakthrough capability to start and operate at sub-freezing temperatures as low as -4°C, along with increased performance, range and fuel efficiency compared with earlier models.

Fuel cells have been widely recognized as the candidate for future power system and are now expected to replace traditional power sources in coming years from micro fuel cells

to be used in cell phones to high-powered fuel cells for stock car racing, and even military communications equipment. Since fuel cell can provide power from a few watts up to megawatts³, this makes fuel cell a unique energy converter. In recent few decades, massive work has been carried out by researchers and industries from which harvest valuable achievements on fuel cell research, development and manufacturing.

1.1.2. Fuel Cell Types

A fuel cell is an electrochemical energy converter that converts chemical energy of fuel directly into electricity. The earliest fuel cell basically consists of an electrolyte and two catalyst coated electrodes after its development for decades, nowadays there are mainly six types of fuel cells depending on the fuel source, electrolyte materials and operation principles:

Alkaline Fuel Cell (AFC)

The Alkaline Fuel Cells (AFC) were one of the first developed fuel cells which demonstrate efficiency of 60%~70%. Due to their high performance, since 1960s the AFCs have been used by the U.S. in space program for providing electrical energy and water for the on-board systems. An AFC employs a water-based aqueous solution of potassium hydroxide (KOH) as the electrolyte. Depending on the concentration of the electrolyte, it can operate at temperature range between 60°C and 250°C. The catalyst requirement for the AFC is easy managed, as it can be any inexpensive metal materials. However, one disadvantage of the AFC is its sensitivity to carbon dioxide (CO₂) which may exist in fuel or in air. The reason is that even a small amount of CO₂ will react with the electrolyte and poison it. This can result in serious degradation of the fuel cell performance. Therefore the fuel requirement for AFC is restricted to pure hydrogen and oxygen to ensure the fuel cells' operation and lifetime. Due to this reason, on one side it adds more cost on AFC manufacturing; on the other side it limits the AFC application to automobile applications.

Phosphoric Acid Fuel Cell (PAFC)

The Phosphoric Acid Fuel Cell (PAFC) is the first commercialized fuel cell which is used for stationary power generation. The PAFC uses hydrogen and oxygen as fuel, high concentration or near pure liquid phosphoric acid as its electrolyte and porous carbon electrodes coated with platinum as catalyst. One important characteristic of the PAFC is

that the electrolyte of phosphoric acid is temperature sensitive. Since pure phosphoric acid solidifies at temperature of 42°C, it requires that the operation of PAFC must be above this temperature. For the optimum performance, the operation temperature of a PAFC is usually between 180°C and 220°C⁴. A PAFC produces higher efficiency of 70%~85% when it is used in co-generation electricity applications, but gives only 30%~40% of efficiency for its solo application in generating electricity. Another advantage of this type of fuel cell is that CO₂ does not affect the electrolyte. So it can be operated with the reformed fossil fuel without sacrificing the performance of the fuel cell. Due to the usage of platinum catalyst, the cost of the PAFC is expensive.

Molten Carbonate Fuel Cell (MCFC)

The Molten Carbonate Fuel Cell (MCFC) is a high-temperature fuel cell which uses a molten mixture of carbonate salts as electrolyte. The molten mixture used usually is lithium carbonate and potassium carbonate, or lithium carbonate and sodium carbonate, which is immobilized in a porous, chemically inert ceramic lithium aluminum oxide matrix. In order to melt the carbonate salts to enable high ion mobility through the electrolyte, the MCFC operates at very high temperature of 650°C and above. At this temperature the fuels can be converted to hydrogen within the fuel cell internally. This advantage provides the fuel flexibility and also it means that an external fuel processor will be needed for obtaining hydrogen from those fuels. The electrical efficiency of a typical MCFC is near 50%, but when it is combined with other heat and power application such as turbine, the efficiency can reach to 65% or above. When the waste heat is reused, the overall fuel efficiency can approach close to 85%. One of the main disadvantages of the MCFC is that at very high operating temperature, the carbonate electrolyte can cause electrode corrosion problem and further decreasing the cell life. Therefore for scientists, corrosion-resistant materials for the component and better fuel cell design are one of the important issues for improving the MCFC durability.

Solid Oxide Fuel Cell (SOFC)

The Solid Oxide Fuel Cell (SOFC) is another type fuel cell which operates at high temperature of 600°C ~1000°C. It usually uses a solid ceramic as the electrolyte. The materials needed for the electrode are specially required to be able to withstand the high-temperature environment and exhibit conductivity and catalytic activity. For the anode electrode, the common material is nickel-YSZ (yttria-stabilized zirconia) cermet.

For the cathode side, the electrode material can be chosen among strontium-doped lanthanum manganite (LSM), Lanthanum-strontium ferrite (LSF), Lanthanum-strontium cobaltite (LSC) and Lanthanum strontium cobaltite ferrite (LSCF). Due to the high operating temperature, the SOFC has the advantage of using various types of fuels. It also offers operating efficiency around 50%~60%, and when combined with heat and power application, the overall fuel cell efficiency can reach 80%~90%. However, the high operating temperature also brings challenges for the SOFC. One of the main issues is the durability requirements on materials. Others include sealing issues, relative expensive components and fabrication. An intermediate temperature SOFC operating below 800 °C could relieve most problems associated with high temperature operation.

Proton Exchange Membrane Fuel Cell (PEMFC)

The Polymer Electrolyte Membrane (PEM) Fuel Cell or Proton Exchange Membrane Fuel Cell (PEMFC) is a type of fuel cell which uses hydrogen and oxygen as fuel and a solid polymer as electrolyte. It operates at relative low temperature around 80°C which allows it to start quickly. Also the usage of solid electrolyte simplifies the sealing issue compared with using liquid electrolyte. Other advantages are low sensitivity to orientation and high power-to-weight ratio. Therefore PEM fuel cells are practically suitable for use in passenger cars and buses and portable applications. Despite those advantages that the PEM fuel cells offer, disadvantages still exist. For example, the usage of platinum as catalyst brings in the problem of carbon monoxide poisoning to the catalyst as well as the cost issue; another difficulty limiting the PEM fuel cell application on vehicles is to store enough hydrogen on-board. Due to its advantages of low emission and high efficiency, the PEM fuel cells have gained wide attentions by the researches and industries.

Direct Methanol Fuel Cell (DMFC)

The Direct Methanol Fuel Cell (DMFC) was developed in early 1990s and is relative young compared to other type of fuel cells. Similarly to PEMFC, it also uses polymer as electrolyte. But different from the PEMF which uses hydrogen as fuel operating at temperature in range of 50°C ~120°C, the DMFC is powered by pure methanol which is oxidized in presence of water at the anode. Because methanol has higher energy density than hydrogen, the DMFC does not have the fuel storage problem compared to other fuel cells. Therefore the DMFC is an ideal candidate for small applications. One of the main

concerning of the DMFC is that methanol is toxic. Therefore ethanol has been considered as the fuel supply to be developed which is called the Direct Ethanol Fuel Cell (DEFC), though the performance of the DEFC is currently much lower than the DMFC.

1.1.3. Fuel Cell System

The purpose of fuel cell system is to deliver required amount of power to the specific applications. Since a single fuel cell can provide only about 0.6-0.7 V at operational current level, multiple fuel cells are required to meet the power needs. Besides fuel cells, other components are also needed in order to ensure the fuel cells running, such as fuel supply systems, cooling systems, and power regulation system. The design of fuel cell systems is complicated and varies significantly depending upon fuel cell types and applications. But in general, most fuel cell systems consist of four basic subsystems: (1) the fuel cell stack; (2) fuel delivery/processor; (3) power electronic subsystem and (4) thermal management subsystem. Figure 1.1 illustrates the fuel cell system components and the flow chart.

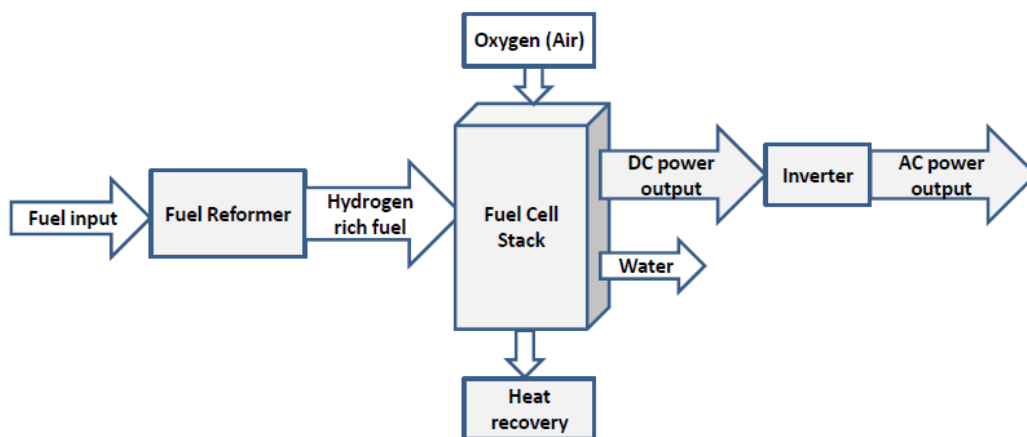


Figure 1.1 Fuel cell system components and flow chart

Fuel Cell Stack

In order to improve the power density output, rather than using a single fuel cell unit, a series of fuel cells are interconnected to generate much larger voltage. Such multiple-fuel cells is called fuel cell stack which is the most important part of a fuel cell

system. A typical fuel cell stack may consist of hundreds of single fuel cells. Even though factors such as fuel cell type, size and operating temperature may affect the amount of power output, overall the fuel cell stack can produce considerable energy for various applications.

Fuel Delivery/Processor

Providing fuel to fuel cell system is an important issue. Nowadays, most of the practical fuel cells use hydrogen or compounds containing hydrogen as fuel. This leads to two main choices for fueling fuel cell system which are either using hydrogen directly or using a hydrogen carrier. For the former, the concern is hydrogen storage since hydrogen is not an easily available fuel. There are three most adopted ways to store hydrogen: as a compressed gas, as a liquid or in a metal hydride. If a hydrogen carrier is used, it permits higher energy storage density. A hydrogen carrier is a chemical species that is used to convey hydrogen to a fuel cell. Typical hydrogen carriers are methane, methanol, sodium borohydride, formic acid and gasoline. Instead of directly using in fuel cell, most hydrogen carriers need to be processed to produce hydrogen gas. Only a few hydrogen carriers can be used directly by fuel cells, such as methane for SOFCs and MCFCs and methanol for DMFCs.

Power Electronic Subsystem

The power electronic subsystem performs main functions of power inversion and power regulation. A fuel cell generates electricity in the form of fluctuate Direct Current (DC) which is not stable, hence the current firstly will be converted to a stable and specified DC voltage output. Besides, it also needs to be converted into Alternating Current (AC) before it can be supplied to various applications. Therefore an AC/DC converter will transform the DC power into specified AC power according to applications.

Thermal Management Subsystem

During operation, the fuel cell stacks will generate amount of heat, and if the rate of heat generation is too quick, it may overheat the cell stacks. If there is not sufficient cooling for the stacks, the heat will accumulate and have negative effects on fuel cell performance. So the requirements of cooling system largely depend on fuel cell types and their size. Cooling can be achieved through methods such as forced convection or active liquid cooling. On the other hand, for those fuel cells that operate at high

temperature such as solid oxide fuel cell systems and molten carbonate fuel cell systems, the generated heat is often used beneficially such as to provide heat for the electrochemical reactions for their own cells or to be converted to electricity via a gas turbine.

1.2. Polymer Electrolyte Membrane Fuel Cell

1.2.1. Introduction

As introduced briefly before, the PEM fuel cell stands for Polymer Electrolyte Membrane fuel cell, or Proton Exchange Membrane fuel cell, using hydrogen as its fuel choice and the polymer membrane as its electrolyte. In order to maintain the conductivity, the polymer membrane must be hydrated with liquid water. The operating temperature of PEM fuel cell is usually around 80°C. Figure 1.2 illustrates the basic PEM fuel cell structure.

Typical PEM fuel cells have five main compartments: anode and cathode gas channels, anode and cathode porous diffusers and polymer electrolyte membrane.

Anode gas channel —— reactant gases, hydrogen and water vapour, are supplied to the fuel cell through the anode gas channel.

Anode porous electrode —— the porous electrode/ gas diffuser provides the reactant gases the path to diffuse through the electrode to the catalyst layer, which is sandwiched between the electrode and membrane. Electrons will be conducted from the catalyst layer to the electrode.

Anode catalyst layer —— the place where the chemical reaction takes place. During the reaction, hydrogen transported from the electrode will be oxidized and releases protons (hydrogen ions) and electrons.

Proton exchange membrane —— hydrogen ions will diffuse through the membrane to the cathode catalyst layer to join the chemical reaction. Water within the membrane will not only diffuse from cathode to anode, but also be electro-osmotically dragged from anode to cathode, as can be seen in Figure 1.2. The anode electrode, membrane and cathode electrode together are usually called the membrane electrode assembly (MEA).

Cathode catalyst layer — the place where the oxygen reduction reaction takes place. Oxygen, proton ions diffusing from anode to cathode catalyst layer and the electrons coming from external circuit together react to form water.

Cathode porous electrode — through this porous electrode/gas diffuser, reactant gases coming from the gas channel will reach the cathode catalyst layer to take part in the chemical reaction.

Cathode gas channel — from which the reactant gases, oxygen, nitrogen and water vapour, are supplied to the fuel cell.

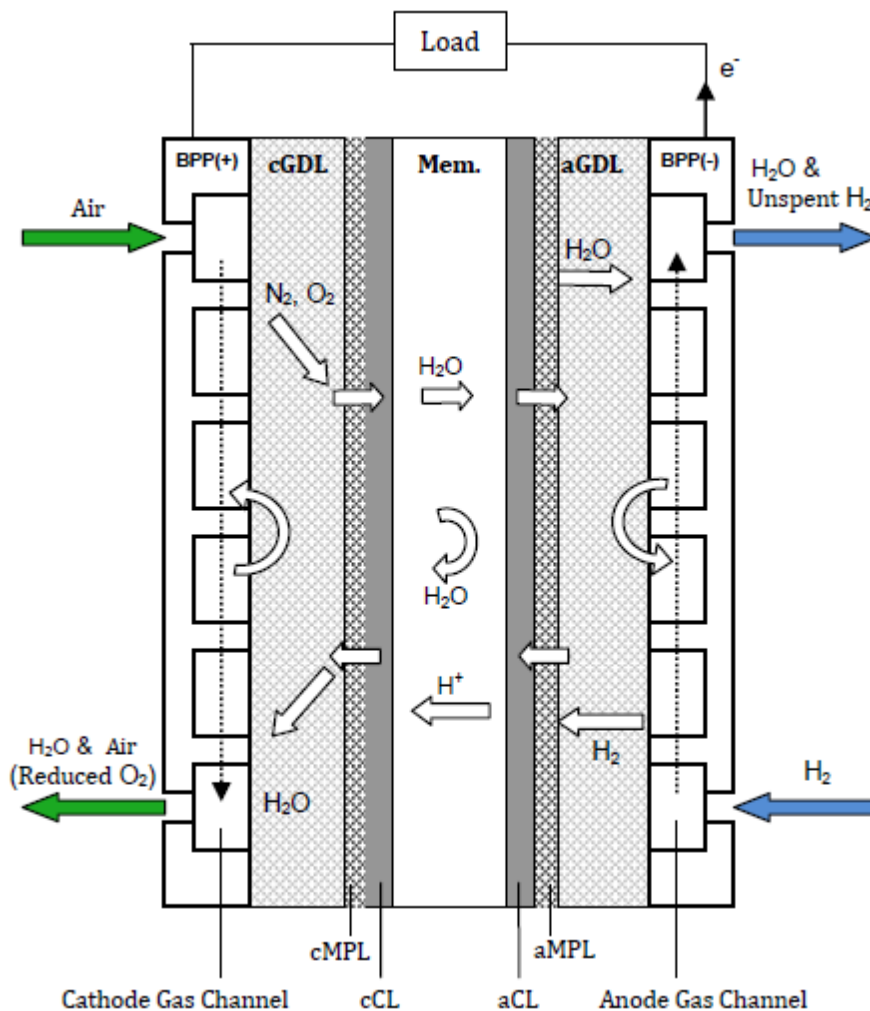


Figure 1.2 Polymer Electrolyte Membrane (PEM) fuel cell

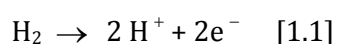
So it is known that the core component in a PEM fuel cell is the membrane electrolyte assembly (MEA). The electrolyte membrane which is in between the anode and cathode gas diffuser, is typically made of perfluorocarbon-sulfonic acid ionomer. Hydrated membrane presents good conductivity for protons and prevents electrons from getting through. The electrolyte is an ion conducting polymer, in which hydrogen ions can move freely. The catalysed electrodes are bonded to both sides of the membrane, and provide pathway for gases and water to move through. The basic structure of a PEM fuel cell is shown in Figure 1.1. The chemical reaction takes place at the catalyst layers. During the chemical reaction, hydrogen splits into electrons and hydrogen ions at anode side catalyst layer. By the oxygen reduction reaction at the cathode side, liquid water is generated as product. Since the voltage of a single cell is about 1V, more cells are needed for higher voltage requirement to meet practical applications. And this can be achieved by stacking up series single fuel cells. Depending on application, the output voltage may be between 6V and 200V or even more.

PEM fuel cells have many advantages that make them distinguished from other energy conversion resources, such as: (1) High power density. Since the fuel cell efficiency is much higher than the efficiency of internal combustion engines, PEM fuel cells now are attractive for vehicle applications. (2) Low or zero emissions. Due to the usage of hydrogen as fuel, PEM fuel cell is operating with zero emissions. The only exhaust is the unused air and product water. However, as hydrogen fuel is not readily available, if a hydrogen generator is used, for example, some emissions will be generated including carbon dioxide. Overall, these emissions are lower than other conventional energy conversion technologies⁵. (3) Good start and off capability.

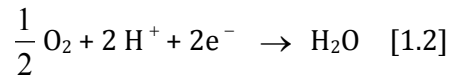
1.2.2. Electrochemical Reactions and Thermodynamics

Basic Chemical Reactions

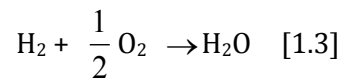
In a PEM fuel cell, hydrogen humidified with water vapour is supplied to the fuel cell from the anode gas channel. The flow of gases diffuses through porous gas diffuser by diffusion and convection, and reaches anode catalyst layer. Hydrogen fuel mixture reacts at the catalyst–membrane–gas interface via the electrochemical reaction:



Two electrons generated by one molecule of hydrogen in this reaction flow through external circuit to the cathode catalyst layer while the hydrogen protons transport through the membrane to the cathode catalyst layer. The oxygen diffuses through the porous electrode reaching the cathode catalyst layer. The oxygen reduction reaction therefore take place at cathode catalyst layer and water is generated as the product.



The overall reaction happen within the fuel cell is:



Open Circuit Voltage

In a PEM fuel cell, the chemical energy of hydrogen and oxygen convert to the electrical energy. In order to define this chemical energy, Gibbs free energy is introduced. It can be defined as ‘the energy available to do external work, neglecting any work done by changes in pressure and/or volume’. In the fuel cells, it is the change in the Gibbs free energy of formation ΔG_f that gives the energy release⁵. This change is the difference between the Gibbs free energy of the products $\Delta G_{f,P}$ and the Gibbs free energy of the reactants $\Delta G_{f,R}$.

$$\Delta G_f = \Delta G_{f,P} - \Delta G_{f,R} \quad [1.4]$$

For the PEM fuel cell using hydrogen as fuel, this gives the change in molar Gibbs free energy of formation $\Delta \bar{g}_f$:

$$\Delta \bar{g}_f = (\bar{g}_f)_{\text{H}_2\text{O}} - (\bar{g}_f)_{\text{H}_2} - \frac{1}{2}(\bar{g}_f)_{\text{O}_2} \quad [1.5]$$

If there are no losses in fuel cell, then all the Gibbs free energy is converted into the electrical energy. The voltage under this condition therefore is considered as the ‘open circuit voltage’ (OCV).

The electrical work done = $-2FE$

$$\text{so: } \Delta \bar{g}_f = -2FE$$

where E is the cell potential, and F is the Faraday constant, 96487 C/mol.

Therefore, the OCV is defined as:

$$E = -\frac{\Delta \bar{g}_f}{2F} \quad [1.6]$$

Efficiency

The heat produced by the chemical reaction is called the 'enthalpy of formation', $\Delta \bar{h}_f$, which is negative when energy is released. There are two different values for $\Delta \bar{h}_f$. Higher calorific value (HHV) stands for the liquid water product and lower calorific value (LHV) stands for the vapour phase water product. Generally, LHV is used in calculation since it gives higher efficiency. For a 100% efficiency fuel cell system, the voltage will be gained as:

$$\begin{aligned} E &= -\frac{\Delta \bar{h}_f}{2F} \\ &= 1.48 \quad (\text{using HHV}) \\ \text{or } &= 1.25 \quad (\text{using LHV}) \quad [1.7] \end{aligned}$$

Since the hydrogen fuel fed to a fuel cell will not be completely used, a fuel utilisation coefficient u_f is introduced:

$$u_f = \frac{\text{mass of fuel reacted in cell}}{\text{mass of fuel input to cell}}$$

The fuel cell efficiency φ therefore is given by:

$$\varphi = \mu_f \frac{V_c}{1.48} \times 100\%$$

or

$$\varphi = \mu_f \frac{V_c}{1.25} \times 100\% \quad [1.8]$$

where V_c is the average voltage in one cell.

Nernst equation

Since the reactant gases in the fuel cell are considered as 'ideal gases', the partial pressure of the reactant gases can be associated with 'activity' which is defined as:

$$\text{activity } a = \frac{P}{P_0}$$

where the P_0 is the standard pressure, P is the partial pressure of the reactant gas. The activity of the reactants and products modify the Gibbs free energy change of a reaction. From thermodynamic point of view in the case of the fuel cell reaction [1.3], it can be expressed as:

$$\Delta \bar{g}_f = \Delta \bar{g}_f^0 - RT \ln\left(\frac{a_{H_2} \cdot a_{O_2}^{\frac{1}{2}}}{a_{H_2O}}\right) \quad [1.9]$$

where the $\Delta \bar{g}_f^0$ is the change in molar Gibbs free energy of formation at standard pressure. For the vapour phase of water, the activity is $a_{H_2O} = \frac{P_{H_2O}}{P_{H_2O}^0}$. In the case of liquid water product, it is reasonable to assume that $a_{H_2O} = 1$

Substituting Equation [1.9] into Equation [1.6] gives:

$$\begin{aligned} E &= -\frac{\Delta \bar{g}_f^0}{2F} + \frac{RT}{2F} \ln\left(\frac{a_{H_2} \cdot a_{O_2}^{\frac{1}{2}}}{a_{H_2O}}\right) \\ &= E^0 + \frac{RT}{2F} \ln\left(\frac{a_{H_2} \cdot a_{O_2}^{\frac{1}{2}}}{a_{H_2O}}\right) \quad [1.9] \end{aligned}$$

Equation [1.9] is called *Nernst equation* which reflects the voltage in terms of product and reactant activity. Since the activity of liquid water equates to one, Equation [1.9] for liquid water then can be simplified to the form shown in Equation [1.10] which was reported in the work of Amphlett *et al*³⁰:

$$E = E^0 + 4.3085 \times 10^{-5} [p_{H_2} p_{O_2}^{1/2}] \quad [1.10]$$

where $E^0 = 1.229 - 0.85 \times 10^{-3} (T - 298.15)$

1.2.3. Irreversible Voltage

In a fuel cell, the voltage will deviate from its equilibrium voltage and decrease with increasing current density. Primarily, there are four factors contributing to this voltage drop:

- Activation polarization
- Ohmic polarization
- Mass transfer and concentration polarization
- Fuel crossover and internal current

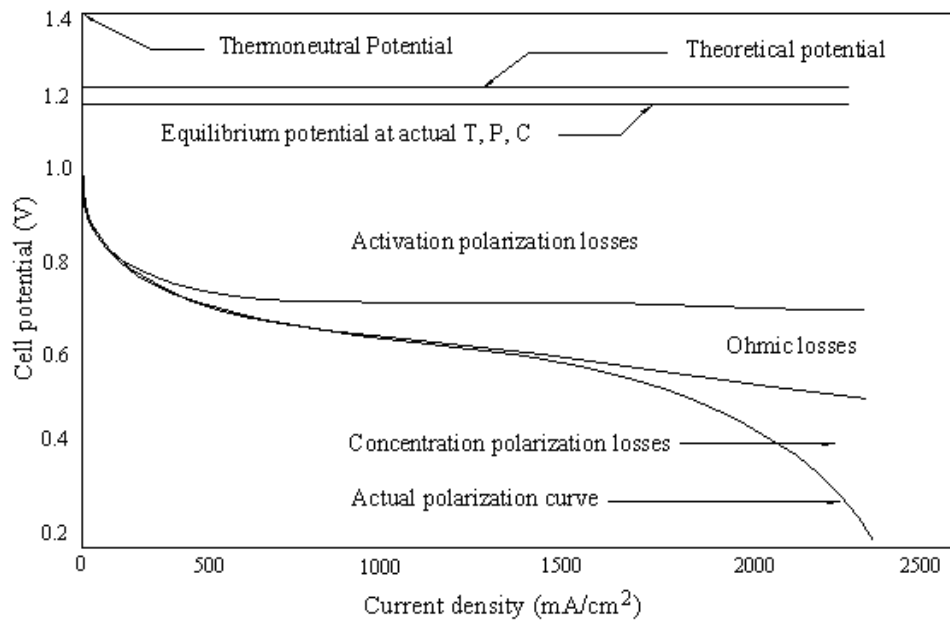


Figure 1.3 Fuel cell polarization curve⁶

Activation polarization

The activation polarization is due to the electrochemical reaction taking place. A portion of voltage will drop due to driving the electrons to or from the electrode during the chemical reaction. This voltage is highly non-linear and is necessary for starting up the chemical reaction. It can be given related to current density by Tafel equation:

$$\eta_{act} = \frac{RT}{2F} \ln\left(\frac{J}{J_0}\right) \quad [1.11]$$

where J is the current density, R and T are Universal gas constant and temperature, respectively. J_0 is the exchange current density at which the overvoltage begins to move from zero.

From the work of Amphlett *et al*⁷, parametric coefficients have been applied to define the total activation polarization.

$$\eta_{act} = \zeta_1 + \zeta_2 T + \zeta_3 T \ln(c_{O_2}) + \zeta_4 \ln(J) \quad [1.12]$$

And these parametric coefficients have been experimentally determined from the Ballard Mark IV fuel cell:

$$\eta_{act} = -0.9514 + 0.00312T + 7.4 \times 10^{-5} T \ln(c_{O_2}) - 0.000187[\ln(J)] \quad [1.13]$$

The activation overpotential is the largest loss at any current density, as can be seen from Figure 1.3. At low and medium temperature fuel cell, the activation polarization is the most significant irreversibility and causes voltage drop (mainly at cathode for hydrogen fuel cell). In fuel cells using fuels other than hydrogen such as methanol, the activations at both anode and cathode electrodes are important.

Ohmic polarization

This voltage drop exists because of the resistant from electrode materials, inter connections from which electrons flow through and the resistant from the membrane when ions flow through it. The voltage drop is linear proportional to the current density. The Ohmic polarization is important in all types of fuel cell, especially in solid oxide fuel cell (SOFC). The total ohmic polarization is expressed by:

$$\eta_{ohmic}^{total} = \eta_{ohmic}^{electronic} + \eta_{ohmic}^{protons} = -JR^{internal} \quad [1.14]$$

where i is the current density in mAcm^{-2} , and $R^{internal}$ is the total internal resistance of the fuel cell.

An empirical relationship of cell temperature and current density on the active area of the resistance of the fuel cell was developed by Amphlett *et al*³⁰

$$R^{internal} = 0.01605 - 3.5 \times 10^{-5} T + 8.0 \times 10^{-5} J \quad [1.15]$$

Combining equation [1.14] and [1.15] gives:

$$\eta_{ohmic}^{total} = -JR^{internal} = -J(0.01605 - 3.5 \times 10^{-5} T + 8.0 \times 10^{-5} J) \quad [1.16]$$

Mass transport or concentration polarization

During the reaction, the concentration of reactant gases on the surface of electrodes will change as the fuel is consumed. This concentration loss results in the loss of reactant gases transferring to the surface of electrodes. So this concentration polarization is also called mass transport loss and is defined by:

$$\eta_{mass\ transport} = \frac{RT}{2F} \ln\left(1 - \frac{J}{J_L}\right) \quad [1.17]$$

where J_L is the limiting current density. This limiting current density relates to the maximum rate of consumption at the catalyst surface and the diffusion rate of the reactant. When the fuel consumption is faster than it can be delivered to the surface, the surface concentration reaches zero. The current density when this happens is called the limiting current density.

If internal current density due to fuel crossover is included, equation [1.17] becomes:

$$\eta_{mass\ transport} = \frac{RT}{2F} \ln\left(1 - \frac{J + J_n}{J_L}\right) \dots [1.18]$$

An empirical expression describing the polarization losses was suggested by Kim *et al*⁸:

$$\eta_{mass\ transport} = c \cdot \exp\left(\frac{J}{d}\right) \quad [1.19]$$

where: c and d are all empirical coefficients, with values of $c=3 \times 10^{-5}$ V and $d=0.125 \text{ Acm}^{-2}$.

The mass transport or concentration polarization is particularly important where hydrogen fuel is supplied from some kind of reformer, for it will be difficult in increasing hydrogen supply rate to satisfy the reaction demand. In PEM fuel cell, the removal of water can also cause the problem of mass transport or concentration loss.

Fuel crossover and internal current

This voltage drop is due to the loss of unused hydrogen fuel moving from anode through the membrane to the cathode and reacts directly with oxygen, which is called fuel crossover. The hydrogen crossover will not only reduce the cathode potential and lower the efficiency, but will also produce peroxide at cathode side which will attack the catalyst later and cause membrane degradation. The internal current caused by fuel crossover can be included into equation [1.16] as discussed above.

Combining the Irreversibilities

The operating voltage of a fuel cell can be obtained by combining all these polarization losses (Eqn [1.11], Eqn [1.16], Eqn [1.18]). This gives the overall equation:

$$E = E^0 + 4.3085 \times 10^{-5} [p_{H_2} (p_{O_2})^{\frac{1}{2}}] - \eta_{act} - \eta_{Ohmic} - \eta_{mass\ transport} \quad [1.20]$$

1.2.4. Literature Reviews on PEM Fuel Cells

PEM fuel cell technology has been developed and improved dramatically during the past few decades especially on numerical modeling and simulation^{9,10} in order to have a better understanding on the phenomena occurring in the PEM fuel cells. In the earlier works, simple zero dimensional models were introduced^{11,12,13,14}. Even though these models are simple compared to today's models, they can still fit the experimental data. However, these models are difficult in predicting the PEM fuel cell performance in depth.

In the past several decades, research works on fuel cell are moving towards developing more complex, accurate and complete models. Many models have incorporated complex effects such as two phase flow and flow field design^{15,16}, multi-dimensional, transient, and microscopic effects¹⁷. These models provide engineers and manufacturers with information on cell performance given geometric parameters, material properties and operating conditions such as temperature, pressure and humidity. Most modeling contributions focus on modeling of water profile in fuel cell especially in the membrane region, cathode losses and integrated modeling of the combined losses in the fuel cells¹⁸. Furthermore other modeling approaches such as computational fluid dynamics has made efforts in areas of flow in the gas channel, convection in the gas diffuser and the study of interdigitated flow field¹⁹. The earlier pioneer works of Bernardi and Verbrugge^{20,21} and Springer *et al*²² have made great contributions to PEM fuel cell modelling. Bernardi and Verbrugge built their model to estimate the water transport and cell polarization as well as catalyst utilization. In the work of Springer *et al*, they also introduced a one-dimensional model from fundamental theory to analyse the water transport through the cell. Although these works are based on fundamental theory, they have enlightened future researchers since many model developed later are based on their contributions.

For the PEM fuel cell, the MEA is considered as a very important part in the PEM fuel cells. The electrolyte is a proton-conducting membrane which allows the transport of water and protons. It is known that the membrane needs to be kept hydrated in order to conducting ions. So an important element responsible for PEMFC performance is the water content dependency of the proton conductivity of the membrane. The water in the membrane is driven by diffusion, osmotic-drag and hydraulic permeation. Numerical modeling of water transportation through the membrane region was reported at various levels by many groups. In earlier work of Verbrugg *et al*^{23,24} they reported extensive modeling study on transport properties of ion exchange membrane based on dilute solution theory. Zawodzinski *et al*²⁵ described the water transport and uptake characteristics and conductivity of Nafion 117 membranes under conditions relevant to PEMFCs. Fuller and Newman²⁶ developed a two-dimensional PEM fuel cell model to investigate the water management through the membrane electrolyte region and suggested a proper hydration of membrane for maintaining the effective conductivity. Similar work was reported by Nguyen and White²⁷. They developed a two-dimensional model which accounted for the influence of humidification design on water transport by osmotic-drag and diffusion in the membrane as well as cell their influences on cell

performance. Djilali *et al*²⁸ demonstrated the two-dimensional effects on water management in membrane and electrodes through investigation of cell voltage, concentration polarization and humidification. Gurau *et al*²⁹ numerically studied the whole PEM fuel cell sandwich including the channels and revealed liquid water velocity distribution in membrane region and oxygen and water distribution in channels. Amphlett *et al*^{30,31} developed a PEM fuel cell model using combined mechanistic and empirical technique. The mass transport properties were treated using Stefan-Maxwell equations by the mechanistic model while the empirical analysis accounted for the parametric coefficient used in the model. The obtained results agreed well with the experimental data. The fluid transport through porous electrode was examined by Mennola *et al*³². In their work a two-dimensional isothermal PEM fuel cell model was developed by which the mass transport on the cathode of a free convection cell was examined using measured current distribution data to prescribe boundary conditions for oxygen and water fluxes. Springer *et al*³³ modeled the detailed losses in the cathode of the PEM fuel cell. They concluded that based on the measurements of the overall cell polarization and of cathode polarization, the anode losses in a well humidified PEM fuel cell with pure hydrogen supplement are negligible. Vafai and Khakpo³⁴ firstly reported a comprehensive analytical PEM fuel cell model for studying the transport phenomena within PEM fuel cells. Their work included both transverse and axial convection transport as well as transverse diffusive transport process in gas supply channels and porous GDLs which were treated as macroscopically homogeneous porous media. Other works on water transportation were reported by Mazumder *et al*³⁵, Nam *et al*³⁶, Natarajan *et al*³⁷, Kulikovskiy³⁸ and Weber and Newman^{39,40,41}.

The research works of PEM fuel cell are exhaustive. Besides above listed literatures, many other modeling works have been carried out dealing with aspects such as gas channel study^{42,43,44,45,46,47} and the catalyst layer modeling^{48,49,50,51,52,53,54}. Among those works main modeling effort usually focus on water profile in the cell especially in MEA region, cathode losses, thermal management or overall polarization in the cell. The modeling approaches are various from one-dimensional to three-dimensional models and from single phase to multi phase modeling. By these efforts the PEM fuel cell research has gained extensive progress and moving towards new level. However, in almost all the literatures, the studies of the porous GDL in PEM fuel cell were limited by using stochastic techniques to generate the reconstructed three-dimensional GDL. The actual microstructures of the GDLs have to be neglected due to the restrictive length scale involved. Therefore the requirement of actual microstructure reconstruction of the

GDLs is necessary in order to gain a better understanding of the interior structural characteristics of GDLs and flow transport phenomena from pore-level.

1.3. Objective of the Research

The GDLs are carbon based materials of either carbon paper or carbon cloth. Due to the complex geometries of the carbon based GDLs, the requirement of detailed understanding of the microstructural of GDLs from pore-scale is necessary. The object of this project therefore is to investigate the microstructures of the porous carbon based GDLs and the fluid flow transport phenomena within the GDLs. It is known that the mass transfer effects are more significant in the cathode than anode; also the anode can be modelled as a simplified cathode model. For these reasons the simulation interest mainly focuses on the cathode GDL model throughout the whole study.

CHAPTER 2. Literature Reviews on Gas Diffusion Layers

2.1. Gas Diffusion Layers in PEM Fuel Cells

In a PEM fuel cell, the GDL plays important roles including: (1) to enable the reactants transport through to the catalyst layers; (2) to drive away excess water from the catalyst layers to the channels and (3) to conduct electrons from the catalyst layers to the bipolar plates. These functions therefore require better understanding of the GDLs from structure, material and transport phenomena points of views since it is essential that the GDLs are designed and manufactured to meet their requirements for fuel cell conditions^{55,56}.

2.1.1. Characteristics of Gas Diffusion Layers

The performance of the PEM fuel cells can be strongly influenced by the GDL properties such as hydrophobicity and hydrophilicity, porosity and pore connectivity, permeability and electrical conductivity. These critical properties have to be characterized to ensure that they can be balanced properly so that the fuel cells can operate without problems such flooding.

Hydrophobicity and Hydrophilicity

Hydrophobicity of a GDL manages the water in the fuel cell. It equips the electrode with water removal ability. Polytetrafluoroethylene (PTFE) is known as the most common hydrophobic agent to improve the hydrophobicity of a GDL^{57,58}. The effect of PTFE on PEM fuel cell performance has been examined widely. When the PTFE content increases,

the porosity of the GDL will conversely decrease which will result in increasing of oxygen transport resistance⁵⁹. However, if the PTFE content is too low, the water removal ability of GDLs will be weakened⁶⁰. In the literature the optimum PTFE content for near saturation condition was reported to be between 15 and 20 wt %⁶¹.

Wang and Lim⁶² studied the effect of hydrophobic fluorinated ethylene propylene (FEP) content on power performance of the PEM fuel cell and suggested that an optimum FEP loading of 10% is enough to exhibit good hydrophobicity for effective water removal while also remains the GDL surface suitable for the reactant and product transportation. Lin and Nguyen⁶³ found that gas transport and liquid water transport can be improved by adding PTFE to the GDL to increase the wet-proof level when a cell operates under flooding condition. However, they also pointed out that too much PTFE loading can reduce the hydrophilic pathways and it will prevent liquid water from diffusing out of the catalyst layer and through the GDL hence make the electrodes in the risk of flooding. Gostick *et al*⁶⁴ presented a work to measure the capillary pressure curves to determine the pore size distribution and the void fractions of only hydrophilic pores of various commercially available GDLs. Their measurements enabled the determination of the flooding situations in the GDLs. Liu *et al*⁶⁵ examined the effect of hydrophobic agent content on GDL thickness, contact angle, air permeability and surface and through-plane resistivity. The results revealed the relationship between the hydrophobic agent content of the carbon fiber cloth and fuel cell performance. Prasanna *et al*⁶⁶ concluded that at low quantity of hydrophobic content of the porous gas diffusion media the reactant permeability is affected by poor water removal but higher hydrophobic loading the gas diffusion loss increases. A model for investigating the influence of hydrophobicity and porosity of the gas diffusion media on water impregnation and gas diffusion through the GDL was presented to explain the influence of the diffusion layer morphology on cell performance by Jordan *et al*⁶⁷. Park *et al*⁶⁸ studied the effect of PTFE concentration in the MPL on the PEM fuel cell performance. The mercury porosimetry and water permeation experiments show that PTFE increases the resistance to water flow through the gas diffusion while increases volume fraction of hydrophobic pores. The electrochemical polarization analysis reveals that the optimum PTFE content improves the oxygen transport in the catalyst layers and in the GDL by controlling the liquid water saturation in the MEA. Nakajima *et al*⁶⁹ reported the effects of hydrophobic treatment and MPL addition to a GDL in a PEMFC. From water balance analysis at the electrode, the GDL and flow channel in the cathode they concluded that the hydrophobic treatment

with MPL addition is effective to improve the start-up performance by suppressing the water accumulation at the electrode.

Porosity

The porosity measures the void space in a material. The GDL is typically a dual-layer carbon based porous materials. It includes a macroporous substrate for providing mechanical strength, electron transfer and mass transport for the gas reactants and water. The other layer is a thin microporous layer (MPL) which is in contact with the catalyst layer. It performs to improve the electrical conductivity as well as the water management. The MPL at cathode side at this point performs the effective function of removing the product water to clear the pore volume so that the reactant can transport through to reach the catalyst side⁷⁰. Bulk porosity of a GDL is defined as the ratio of the total pore volume over the summation of the total pore volume plus its solid volume. The porosity can affect the effective diffusion coefficient of a porous medium by relationship⁷¹:

$$D_{i,j}^{eff} = \frac{\varepsilon_g}{\tau_g} D_{i,j} \quad [2.1]$$

Where $D_{i,j}^{eff}$ is the effective diffusion coefficient, ε_g and τ_g is the porosity and tortuosity of the volume in gas phase, respectively; and $D_{i,j}$ is the binary diffusion coefficient.

The determination of bulk porosity of a GDL can be carried out by two methods which are mercury porosimetry and the immersion method⁷². The Mercury porosimetry uses a mercury pore size analyzer to evaluate the total pore volume by measuring the amount of mercury penetrated into the pores of a porous media as a function of the applied pressure. The pressure level needed to enable penetration of mercury into a certain size of pores is related to the pore diameter. The immersion method determines the bulk porosity by calculating the weights of the sample before and after immersing in a wetting liquid. Williams *et al*⁷³ used the mercury porosimetry method to obtain the pore size distribution. Pore size distributions of all GDLs and bare macroporous substrates were collected using a Quantachrome Pore- Master 33 which can analyze any porous media with a pore size range between 3nm-300 mm.

The porosity and tortuosity of the GDL enables the transport of reactant transport to the catalyst layer and the removal of excess water for water balance. Yan *et al*⁷⁴ presented a two dimensional model to study the effects of the flow distributor and the diffusion layer morphologies on the transport of reactant. Their work revealed the effects of the cross-section of the flow and the porosity of the GDL on the performance of PEM fuel cell as well as the morphology of the GDL. A one-dimensional model was used by Zhan *et al*⁷⁵ to analyze the liquid water saturation distribution for the GDL including structures of uniform porosity, a sudden change porosity and a gradient change in porosity. The effects of carbon powders in MPL on the performance of PEM fuel cell was studied by Wang *et al*⁷⁶. By examining the GDL properties of surface morphology, gas permeability, hydrophilic/hydrophobic porosity and electron conductivity, the cell performance with peak power density was obtained by the MPL with 10 wt % Black Pearls 2000 in composite carbon black. Gostick *et al*⁷⁷ developed a pore network model of the GDL in a PEM fuel cell. The model treated the GDL as an idealized regular cubit network of pore bodies and pore throats following respective size distribution. The results showed that even though a dry GDL does not limit the performance of a PEM fuel cell, it may become a main source of concentration polarization when the GDL is gradually saturated with water. Roshandel *et al*⁷⁸ investigated the effects of porosity variation distribution by both compression of the electrodes and the water generated at cathode GDL on PEM fuel cell performance. Their result showed that the compression pressure can result in 32% decrease in porosity and the decreasing of GDL average porosity reach 23% at 0.85 A/cm². Experimental investigation of MPL with graded porosity was carried out by Tang *et al*⁷⁹. By comparing the cell performance of graded MPL and traditional homogeneous MPL, the results concluded that the fuel cells with graded MPL have better performance than those using conventional homogeneous MPLs at high current densities. Chen *et al*⁸⁰ developed a two phase flow model using multiphase mixture theory to study the transport characteristics in the cathode GDL of a PEM fuel cell with a gradient in porosity. The results agreed well with experimental data and confirmed that the GDL with gradient porosity can improve the two phase transport performance. The porosity distribution variation and liquid saturation on the GDL through differently structured GDL of PEM fuel cells have been studied by Zhan *et al*⁸¹. The results demonstrated that increasing porosity and contact angle of the uniform porosity GDL can improve the gas diffusion, and the same result can also found in gradient change porosity GDL when increasing the porosity gradient. For GDL with MPL, increasing porosity of MPL can result in stronger gas diffusion. The effect of MPL on the overall net water transport in a

standard 100 cm² active area PEM fuel cell has been experimentally investigated by Atiyeh *et al*⁸². Cells with a MPL on either electrode or on both electrodes exhibited better overall performance and durability compared to cells without a MPL. These results confirm the function of MPL in improving the cell performance. In the work of Han *et al*⁸³, a carbon-filled gas diffusion layer (CFGDL) has been examined and compared with conventional carbon paper-based single layer and dual layer GDLs. Although the analysis reports lower porosity of 67% and smaller average pore diameter of 4.7 μm of the CFGDL, it gives the highest limiting current density which means the improvement in mass transport. Kannan *et al*⁸⁴ developed a functionally graded GDL with four layered MPL containing various compositions of nano-chain and nano-fibrous carbons on the macroporous carbon paper substrate. The results showed that the GDL with pores as small as 75 nm in the MPL towards catalyst layer can keep the product water maintaining hydration of the electrolyte, hence guarantee the proton conductivity at operating condition of 85 °C and 50% RH.

Permeability

The permeability is one of the critical parameters influencing the reactant transport and water management in PEM fuel cells. The reactants transportation through the GDL reaching the catalyst layers and product water removal out of the GDL to the channels depend on the permeability. Lower permeability will increase the resistant of reactant transport and generate higher pressure gradient. This will raise difficulties for reactants to move through the GDL to the catalyst layers. For PEM fuel cell that is equipped with inter-digitated flow fields, the convection driven gas flow transport through the GDL by in-plane and through-plane velocity components. It has been suggested that for both isotropic and orthotropic permeability the in-plane permeability is of greater importance over the through-plane permeability for the convective transport using computational fluid dynamic method⁸⁵. It also has been found that convection effects become dominant beyond a threshold permeability value of around 1x10⁻¹³ m². The gas permeability measurements in three perpendicular directions of several common GDL materials were carried out by Gostick *et al*⁸⁶. The Carman-Kozeny model was used to express the data to predict the permeability as a function of porosity. The results agree well with literature⁸⁷ and report that in perpendicular in-plane direction, the permeability exhibit significant anisotropy. Besides, the highest anisotropy is found at the materials with the most highly aligned fibers and permeability accordingly could vary as much as a factor of 2. They also concluded the influence of the compression

effect on the GDL. Typically by compressing the GDL sample to half of its original thickness, the permeability will decrease by one order of magnitude. In the work of Feser *et al*⁸⁸, they carried out experiments to measure the permeability of woven samples, non-woven samples and carbon fiber based GDLs at various levels of compression using air as the impregnating fluid. The results showed that for woven, non-woven and carbon fiber paper samples, the first two types give significantly higher in-plane permeability compared the last type. A three-dimensional steady state of a PEMFC model was developed by Lum and McGuirk⁸⁹ using CFD code. The validated model was used to study the degree of permeability. The results concluded that a thinner electrode layer and a smaller shoulder to channel width are advantageous for reactant gases transport to the catalyst layer. Decreasing permeability of the electrode enhances species transport in the spanwise direction, but it is only useful if the shoulder area is large. In-plane permeability and through-plane permeability, viscous and inertial permeability coefficients of macroporous substrates and MPLs were presented in the work of Gurau *et al*⁹⁰. The GDL containing the MPL with higher PTFE content was found to have a higher permeability coefficient than those with lower PTFE content. They also mentioned that in-plane permeability and through-plane viscous permeability coefficients depend on the carbon type. In the work of He *et al*⁹¹, a fractal model for predicting the permeability and liquid water relative permeability of the GDL in PEM fuel cells has been presented. The results indicated that the permeability increases with decreasing of the tortuosity dimension or increasing of the area dimension. And the water relative permeability in the hydrophobicity case is higher than in the hydrophilicity case. Various anisotropic permeability influences on water and thermal management in PEM fuel cells have been reported⁹². It was found that higher permeability in either in-plane direction or through-plane direction all can improve the water and thermal management. In contrary, lower permeability negatively influence the water and thermal management. From the results the authors suggested that modeling with isotropic permeability conditions may overpredict the cell performance and cause inaccurate prediction on the water and thermal management in the PEMFCs. Hussaini and Wang⁹³ reported their experimental measurement of absolute permeability and air-water relative permeability for four typical GDLs: Toray carbon paper (TGP-H-060, -090, -120) and E-Tek carbon cloth. Carbon paper materials were found to be with higher absolute in-plane permeability than its through-plane permeability in values by about 18%; but the carbon cloth material has opposite results. The through-plane permeability is found to be 75% higher than its in-plane permeability

value. Very recently, Tamayol and Bahrami⁹⁴ have presented a new analytical approach to evaluate the in-plane GDL permeability in PEM fuel cells. The permeability of the mixture was model as a blend of the permeabilities of its components. The results have shown a compact relationship of gas in-plane permeability as a function of the porosity and fibers diameter.

Electron conductivity

The lateral electronic resistance of the GDL is affected by the electronic conductivity, GDL thickness and the gas channel width. It performs an important function of determining the current distribution and fuel cell performance⁹⁵. Experimental measurement of current density distribution under constant current and constant voltage modes were carried out by Natarajan and Nguye⁹⁶ on MEA fabricated with segmented and unsegmented electrodes. From the results they recommended segmenting the electrode along with the current collector. The current density distribution at the GDL and catalyst interface was examined⁹⁷ and reported that it can be influenced by either electron transport or mass transport in the GDL. Zhang *et al*⁹⁸ reported two effective methods for estimating the contact resistance between the bipolar plate (BPP) and the GDL based on contact resistance-pressure constitutive relation. A novel and simple technique for the measurement of local current distributions in PEMF fuel cells with serpentine flow fields using a measurement gasket was developed by Sun *et al*⁹⁹. The results indicated the importance of gas humidification on fuel cell current distribution. The report explained that low, medium and high humidification level cause the local current increasing monotonically along the channel, increasing first then decreasing along the channel, and decreasing monotonically along the channel, respectively. Zhou *et al*¹⁰⁰ presented a micro-scale contact model to predict the contact resistance between the BPP and the GDL in PEMFCs. They numerically determined the contact spots between the BPP and the GDL given a separation of the two surfaces, and calculated the contact status for every single contact spot using the Hertz theory. By summarizing the results from each contact spot they obtained the total resistance and the pressure. Based on the original model from the work of Zhou *et al*¹⁰⁰, Wu *et al*¹⁰¹ introduced a new model which included the material anisotropy of the GDL carbon fibers and their bending features. The results showed that the contact resistance tends to decrease due to fiber bending, but increases if the anisotropic factor is included in the model. The authors suggested that the contact resistance can be reduced by controlling the surface roughness of the BPP, the fiber configuration of the GDL and

selecting low contact resistance conducting materials. Freunberger *et al*¹⁰² measured the current density distribution with a resolution smaller than the channel/rib scale of the flow field in PEMFC. The results revealed that the electrical and ionic resistances may affect the current distribution at low current regimes; besides, mass transport limitations locally obstructs the current generation at high loads. Wang and Liu¹⁰³ directly measured the current density under the channel and the shoulder in PEM fuel cell separately. The results demonstrated that except in the high current density region, the current density generated under the channel was lower than that under the shoulder. Barber *et al*¹⁰⁴ demonstrated that the real contact area in fuel cell components strongly influences the contact resistance. By evaluating the effects of bipolar plate surface roughness, coating thickness of the gold plating on the current collector and the clamping force on real contact area, they found that among smoother materials, thicker gold coating and higher clamping force give a higher real percentage contact area. A complicated two-dimensional two phase model was employed by Bapat and Thynell¹⁰⁵ to analyze the effects of anisotropic electrical resistivity on current density and temperature distribution in a PEMFC. They revealed that the current density in the region adjacent to the gas channel was negatively affected by a higher in-plane electrical resistivity of the GDL which generates slightly higher current densities in the region adjacent to the current collector. A mechanical–electrical FEM model was developed based on the coupled mechanical–electrical nature of the contact resistance by Lai *et al*¹⁰⁶. They reported that the contact resistance decrease quickly with the increasing of the clamping pressure especially when the clamping pressure is in a small value range. Moreover, they also observed that the optimal round corner value of 0.6 mm can balance the effects of contact length and contact pressure. The in-plane current profile was examined by Li *et al*¹⁰⁷ who concluded that the interplay between the ohmic control and mass transport control resulted in the current distribution variation; besides, they found the dependency of the ohmic and mass transport management on the two-phase water transport along the in-plane direction. They also reported the significant effects of the channel/land width and GDL compression on the in-plane current density profile.

2.1.2. Materials and Structures of the Gas Diffusion Layers

In a typical PEMFC, the porous gas diffusion media is placed in contact with the flow field and inlet gas in flow channels. It serves as the pathway for the reactant gases to transport to the catalyst layer. It also supports the fuel cell to handle compression load to avoid the cell components being excessively stressed. Due to the good electrical

conductivity and high porosity, carbon-based materials are usually chosen to produce gas diffusion layers. There are two common GDL materials which are carbon paper (non-woven) and carbon cloth (woven). The carbon cloth materials are manufactured using a textile process that weaves carbon fibers filaments into a thin material. Carbon cloths have features of mechanical resiliency, low density and high permeability¹⁰⁸. They are typically 350~500 μm thick but can be compressed up to 30%~50% when fitted into a fuel cell system. The compression load applied can influence the electrical and gas permeation properties. The carbon paper materials are produced by bonding a random arrangement of carbon fiber in to a thin, stiff and light weighted sheet. Since carbon paper is a non-woven material, a carbonized resin is used as a binder material to maintain the mechanical integrity. The carbon paper GDLs employed in the PEM fuel cell applications are usually in thickness of 150~250 μm . Compared to the carbon, the carbon paper tends to be stiff and brittle. The compression loads they can afford are 10%~20% less than that applied to carbon cloth. The scanning electron microscope (SEM) images of a carbon paper and a carbon cloth are illustrated below.

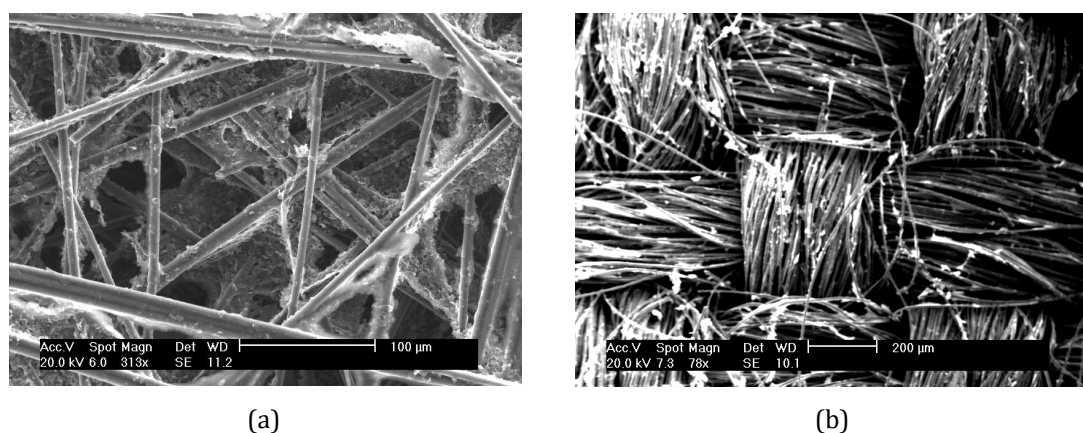


Figure 2.1 scanning electron microscope (SEM) images of (a) carbon paper, and (b) carbon cloth.

There have been various studies on carbon paper and carbon cloth on their performance on PEM fuel cell performance. Due to the difference in structures, carbon paper and carbon cloth can influence the cell performance at various aspects. A numerical study on the relationship between carbon cloth and carbon paper GDL structures and PEM fuel cell performances were carried out by Wang *et al*¹⁰⁹. The comparison of water, oxygen and current distributions with the two material concluded that carbon cloth is suitable

as the GDL material for high humidity operation conditions since carbon paper tends to block mass transport due to its highly tortuous structure. Besides, smooth surface of carbon paper causes serious water coverage on the surface hence increased mass transport loss. On the other hand, with low humidity level, these features of carbon paper help MEA store water in it therefore improving the membrane hydration. Radhakrishnan and Haridoss¹¹⁰ studied the impact of the difference in structure and properties of carbon cloth and carbon paper on the design of the PEMFC flow field. By comparison, they found that carbon cloth shows about 43%~125% more intrusion into the channel than that with carbon paper for the conditions tested. Also the compression studies demonstrated that at lower compression load the cloth lacks compression rigidity and suffers strain more than that of carbon paper. SGL 10BB based on carbon paper and ELAT-LT-1400W based on carbon cloth were characterized by Park and Popov¹¹¹. The results showed that SGL 10BB based on carbon paper exhibits dual pore size distribution and higher water flow resistance compared to ELAT-LT-1400W based on carbon cloth; also using SFL 10BB in the membrane electrode assembly improved the fuel cell performance. Lin *et al*¹¹² used carbon papers of various thickness (130~330 μm) to exam the thickness influence on cell performance under different humidity conditions. The carbon paper employed was treated with a dispersion agent Novec-7300 in isopropyl alcohol of highly consistent carbon slurry containing Pureblack carbon and vapor grown carbon fiber (3:1 ratio) with 25 wt.% Teflon. The results were that for the carbon paper with 330 μm thickness the power density was about 1400 and 700 mWcm^{-2} with H_2/O_2 and H_2/air at 60% RH, respectively. Zamel *et al*¹¹³ studied the through-plane and in-plane effective thermal conductivity in a dry carbon paper GDL without Teflon treatment. The results reported the dependency of the effective thermal conductivity on the fiber distribution. The influence of porosity on effective thermal conductivity showed that decreasing of porosity will improve the effective thermal conductivity. A correlation of a dry carbon paper GDL without binder was developed for the porosity range between 0.4 and 0.85 inclusive. In the work of Liu *et al*¹¹⁴, the carbon cloth GDLs with different structures in PEM fuel cell were used to reveal the relationship between cell performance and the structure of the carbon cloths as well as the effect of carbon cloths thickness.

During PEM fuel cell assembly, the GDLs are clamped into the system and the compression load is applied to ensure the close contact between components. This applied compression pressure will change the structures of the GDLs and causing the change of GDL parameters such as porosity and permeability hence influencing the cell

performance. In the work of Sun *et al*¹¹⁵, they assumed the cathode GDL under shoulder area was 15% thinner than that under the channel area in order to take the compression effect into consideration. From the results they summarized that moderate GDL compression does not dramatically influence the cathode performance at single phase flow conditions. The GDL compression effect increases the resistance to oxygen diffusion to the region under shoulder area causing a lower local oxygen concentration. But on the other hand, compression increases the local conductivity for easier transportation of electrons to the region under the shoulder, resulting in increasing in local overpotential. They also noticed that the predicted total current density does not change significantly with the GDL compression, but the current density distribution changes noticeably. The effect of the GDL deformation on the flow crossover caused by the compression in a fuel cell assembly process was studied by Shi and Wang¹¹⁶ using a three-dimensional structural mechanics model. The oxygen crossover was reduced by compression effects since the permeability and porosity of the GDL are lower. The flow crossover between adjacent channels decreases regardless of the increasing in pressure drop due to the applied compression. Higher pressure drop along the flow direction at the cross section was observed with compression because of the increasing in flow resistance by GDL deformation.

2.1.3. Mass Transport in the Gas Diffusion Layers

Due to the complex porous structures of the GDLs, the transportation of reactant gases and product water are complex. If there is large amount of water accumulating in the pores of the GDL, it will be difficult for reactant to reach to the catalyst layer hence lower the cell performance, and this also may cause flooding problem. Therefore it is important to gain the structural characteristics in order to better understand the reactant and water behaviors. The effects of the GDL material properties and structures have been widely studied in order to investigate their relationships with the cell performance.

Jang *et al*¹¹⁷ developed a two-dimensional isothermal numerical model to investigate the performance of the PEM fuel cell. Parameters of the GDL porosity and thickness were included for analyzing their effects on cell performance. The results showed that with increasing of the GDL porosity the mass transfer of reactants increase, therefore the cell performance is improved regardless of the liquid water effect. If the GDL thickness is reduced at lower operating voltage, the cell performance increases due to the higher concentration gradients building up from the decrease in the GDL thickness.

In the study of on flow pattern and pressure field in general single serpentine flow field geometries, Feser *et al*¹¹⁸ found that the thickness of the GDL has little effects on the relative influence of convection, but it highly depends on in-plane permeability of the GDL and channel length. Jeng *et al*¹¹⁹ also examined the effects of thickness and porosity of the GDL on cell performance using a two dimensional PEM fuel cell model. They reported that cell performance decreasing with increasing the GDL thickness if the GDL porosity is lower. They pointed out that there is an optimal GDL thickness which influences the maximum PEM fuel cell performance at higher GDL porosity. And the existence of such an optimal GDL thickness indicated that a GDL with directional preference in mass transfer can be employed to improve the PEMFC performance. In the work of Pharoah *et al*¹²⁰, they emphasized the anisotropic nature of the porous electrodes on simulating the cathode of the PEMFC using a two dimensional model. They stated that although both isotropic and anisotropic models generate virtually identical polarization curves, the current density distributions are completely different. Therefore they suggested that appropriately characterizing of the anisotropic properties of the porous electrode and physics processes are important in PEMFC modeling. Influence of permeability and thickness of the GDL on the cross flow and pressure drop of the reactant streams were carried out by Park and Li¹²¹ using a three-dimensional numerical PEMFC model. The results showed that there is a large amount of cross flow through the GDL. The effect of permeability and thickness of GDL on the pressure drop becomes more obvious if two parameters are increased, and this significant reduction occurs in the permeability range of $10^{-12} \sim 10^{-8} m^2$. Markicevic *et al*¹²² investigated the change of relative permeability and capillary pressure as a function of liquid water saturation. Also two parameters named network size and network heterogeneity were introduced to analyzing their influence on relative permeability as well as capillary pressure. The results revealed that the relative permeability is constant for low saturation, but follows a power law of saturation for high saturations, with an exponent of about 2.4 which is independent of network size or heterogeneity. Besides, increasing in network size and decreasing in heterogeneity tend to reduce the relative permeability. The relative permeabilities are obtained smaller than unity even for saturations as large as 0.8. Berning and Djilali¹²³ using the CFD method developed a three-dimensional multiphase PEMFC model. They reported that the predicted saturation level strongly depends on the permeability of the GDL. The results showed that liquid water saturation in excess of 20% at anode side can be observed for large values of the GDL permeability, and the saturation levels decrease with permeability due to the liquid water formed by

condensation at GDL/channel interface. However, at the cathode side, they found that liquid water saturation increases with decreasing permeability because the produced water can become trapped inside the GDL.

2.2. Gas Diffusion Layers Models

2.2.1. Macroscopic and Microscopic Models

One of the main roles of the GDL is to serve as the pathways for reactant and product water due to their porous structures. There are many modeling works on the GDL using different methodologies. Among these, they can generally be categorized into two types: the macroscopic models and microscopic models.

Macroscopic Models

The macroscopic models are most commonly used for fuel cell modeling. In the macroscopic modeling approach, the detailed geometry information of the modeling domains are usually neglected and assuming the electrode to be isotropic. The transport properties within the domain are averaged over the electrode volume³⁹. For the gas transports through the electrode, most research groups have worked in similar ways. Since there will be a mole fraction gradient across the electrodes, the Stefan-Maxwell equation [2.2] is normally employed for gas-phase transportation by assuming that the reactant gases with water vapour acts as ideal gases.

$$\nabla x_i = RT \sum_j \frac{x_i \dot{n}_j - x_j \dot{n}_i}{PD_{i,j}^{eff}} \quad [2.2]$$

Where: x_i is the mole fraction of species i ; $D_{i,j}^{eff}$ represents the effective binary diffusivity of the pair i and j ; P is the pressure; \dot{n}_i is the flow rate; R is the universal gas constant and T is temperature.

In the early work of Springer *et al*²², the Stefan-Maxwell equation [2.2] was applied to define mole fraction gradient assuming that only concentration gradients across the electrodes not total pressure gradients. Water and oxygen mole fraction at cathode and

water mole fraction at anode were then calculated. The pressure-diffusivity terms for was estimated by Equation [2.3]:

$$PD_{ij} = a \left(\frac{T}{T_{c,ij}} \right)^b (M_{ij})^{-\frac{1}{2}} (P_{c,ij})^{\frac{2}{3}} (T_{c,ij})^{\frac{5}{6}} \varepsilon^{\frac{3}{2}} \quad [2.3]$$

where D_{ij} is the binary diffusivities, T_c and P_c are critical temperature and critical pressure, respectively. M_{ij} is the mass of species i and j . $\varepsilon^{3/2}$ is the Bruggeman correction factor for porosity. a and b are constant. $a = 0.0002745$, $b = 1.832$ for H_2 , O_2 and N_2 , and $a = 0.000364$ and $b = 2.334$ for water vapor.

As for the liquid phase, the existing theoretical models using the macroscopic approach are usually based on two-phase Darcy's law in Equation [2.4] to investigate liquid water transport in PEFC.

$$\dot{n}_{w,L} = -\frac{k_G}{\bar{V}_w \mu_G} \nabla P_L \quad [2.4]$$

Where $\dot{n}_{w,L}$ is liquid water flux; \bar{V}_w is the molar volume of water; k_G and μ_G are the gas phase effective permeability and viscosity, respectively and ∇P_L is liquid pressure.

Since the macroscopic models treat the GDL as a macro-homogeneous porous layer, the effects of structural morphology of the GDL reach their limits. Therefore for liquid water treatment, these models have to require material-specific capillary pressure–liquid saturation and relative permeability–liquid saturation relationships.

Microscopic Models

Compared with the macroscopic models which are continuum and volume-averaged, the microscopic models simulate the transport phenomena on pore level. The microscopic models therefore require the detailed information on the microstructures of the porous media. The pore network model is a simple approach which neglects the dynamic process, reduces the expression of the full pore morphology to adjust to a statistical description of the pore size distribution and the pore connectivity and permits

the prediction of hydraulic properties¹²⁴. Works using pore network models to account for the micro-characteristics of the structures have been reported in literatures. The pore network model was employed in the work of Sinha and Wang¹²⁵ to account for liquid water management and flooding in a carbon paper GDL. They developed the pore-network model describing governing physics of liquid water transport in a GDL at the pore-level. In their pore network modeling, the GDL is presented at microscopic scale as a lattice of wide pore connected by narrower bound called throats. The schematic view of the pore network model for a carbon paper GDL in three-dimensional view is shown in Figure 2.2 They concluded that at extremely low capillary numbers that encountered in the fuel cell, it is the fractal capillary fingering that controls the liquid water transport in the homogeneously hydrophobic GDL. Liquid water transport through the GDL in the form of connected clusters, researches several dead ends because of the presence of narrow regions, and eventually percolates through the path of least resistance. Chapuis *et al*¹²⁶ also carried out pore-network simulations on two phase flow combined with visualizations on transparent micromodels. They constructed the system by using randomly distributed equal-sized cylinders to form a similar structure of a cross-section through an anisotropic arrangement of equal diameter fibers. The results showed that the process of liquid water invasion in a hydrophobic medium can be simulated using the classical invasion percolation algorithm on condition that the contact angle is far below 90 degree. More recently, Lee *et al*¹²⁷ predicted the water transport in a hydrophobic GDL of PEMFC using a pore network model which included the microscale behavior of liquid water in pore and through throats. The results showed that the water saturation distribution in GDLs has a concave shape along the flow direction, indicating the invasion percolation process an important transport mechanism. Gostick *et al*⁷⁷ have investigated the pore scale distribution of water and gas under drainage conditions using an invasion percolation algorithm by the developed pore network model of GDL in a PEM fuel cell.

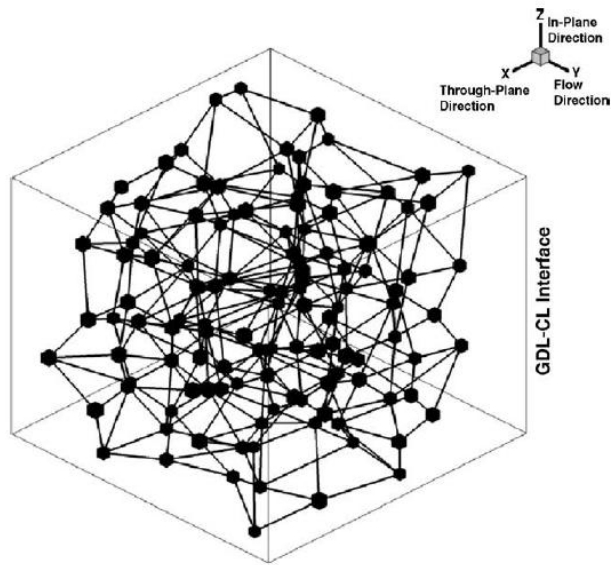


Figure 2.2 Three-dimensional view of schematic of pore-network model for a carbon paper GDL in the work of Sinha and Wang¹²³.

2.2.2. CFD Models

The computation fluid dynamics (CFD) is a traditional tool for simulation of fluid flow and has been widely used in PEM fuel cell modeling for evaluating the PEMFC performance. The CFD method can be used to simulate the transport of multiphase and multicomponent through porous or non-porous layers of the fuel cell. Usually conservation of mass, momentum and energy are used to carry the calculation on mass and heat transfer and liquid water transport through the cell based on finite element frame work analysis. CFD model can be applied to simulate bulk transport through the GDL by assuming the volume-averaged properties of porous layer such as porosity and tortuosity. Basically, the CFD method demands the usage of fixed geometry meshes for the volume region. Therefore for a porous geometry with compressibility such as the GDL, the CFD method is found to have limited ability in dealing with such situation. Shimpalee *et al*¹²⁸ studied the effects of the micro/macro porous media on cell performance using computational fluid dynamics method. They used conservation of mass, the Navier-stokes equations, the species transport equations, the energy equation and the water phase change mode and also assumed homogeneous two phase flow. The simulation results showed that the cell performance is slightly better without the MPL than with the MPL. But for the local distributions, the existence of the MPL gives more uniform local distribution. Martinez *et al*¹²⁹ established a three-dimensional single phase non-isothermal PEM fuel cell analysis used a commercial CFD program to study

the performance of cell under different operating conditions by solving the conservation equations for species, energy, charge, mass and momentum. In the work of Dawes *et al*¹³⁰, the effects of water flooding on cell performance parameters was studied using the CFD method. In order to characterize the effects of water flooding on gas diffusion, the effective diffusivity models that account for the tortuosity and relative water saturation of the porous electrode were obtained from percolation theory and coupled with the CFD model. The governing equations of the overall three-dimensional PEMFC are a representative of the coupled CFD and percolation theory based effective diffusivity. Review of CFD models for PEMFCs with emphasis on mass and heat transfer modeling was reported by Siegel¹³¹. Um *et al*¹³² employed a finite-volume based CFD technique to simulate the multidimensional behaviors of the PEMF. The developed model predicted the detailed reactant and product distribution inside the cell, and explored the hydrogen dilute effects in anode feed. Sivertsen and Djilali¹³³ took advantages of parallel processing architecture of the Fluent CFD code to simulate the fluid transport within the channels and the porous electrodes and the heat transfer by a three-dimensional single phase PEM fuel cell model. Works of Djilali¹³⁴, Berning *et al*¹³⁵, Seigel *et al*¹³⁶, Dutta *et al*^{137,138} and Dawes *et al*¹³⁹ also presented the CFD applications on PEMFC modelling focusing on transport phenomena and liquid water management.

2.2.3. Lattice Boltzmann Models

In recent years, the Lattice Boltzmann Method (LBM) has been recognized as an effective tool in simulating the fluid flow. In the conventional Navier-stokes equations, the calculations are based on the discrete macroscopic continuum equations. In comparison, the LBM solves the microscopic Boltzmann equation where the fluid flow is expressed by the distribution function of fluid particles based on the kinetic theory. Due to its kinetic nature, it is easy for the LB method to simulate the fluid flow in porous media especially with complex geometries. LBM is capable to incorporate the essential physics of microscopic or mesoscopic process into simplified kinetic models, and to ensures the macroscopic average properties to follow the desired macroscopic equations.

A simulation study of multi-phase flow through inhomogeneous GDLs of carbon cloth and carbon paper of PEM fuel cell using LBM was presented by Li and Park¹⁴⁰. Two different LB models for simulations were used and the results showed that the permeability of porous media can be influenced by the fiber construction, and the calculated permeability of the porous medium agreed well with those in the literatures. In the recent work of Ju¹⁴¹ a three dimensional, two phase numerical PEMFC model was

developed to investigate the in-plane and through-plane GDL thermal conductivities as well as two phase transport characteristics. Munekata *et al*¹⁴² studied the effects on the diffusivity and permeability in the GDL of the PEMFC at operating conditions using the LBM with D3Q19 scheme. The GDL structure was constructed using the randomly laminated fibers. Since the generated water during cell operation will filled into to the GDL, the water configuration for the simulation is modelled by the water droplets. The results revealed that the heterogeneous water network and the high porosity improve the diffusivity and the permeability, while the hydrophobic surface decreases the permeability. Another application of LB method was reported by Wang and Afsharpoya¹⁴³. The effects of multi-time scales and interface between the porous GDL and the clear channel were carried out using the LBM. They considered that the flow in a two-dimensional channel filled with porous media of given porosity and permeability. Also they assumed that the macroscopic variables average over a representative elementary volume and they are governed by the momentum equation incorporating a Brinkman-extended Darcy's law. Their work demonstrated that the LB method can be used to study the flow through a porous medium with an interface on condition that the existence of multiple macroscopic time scales is taken into consideration. Other research works of Hao and Cheng¹⁴⁴, Niu *et al*¹⁴⁵, and Hao and Cheng¹⁴⁶ showed that the LBM has been recognized as a powerful tool for simulating multi-species and/or multi-phase fluid flow in simple or complex geometry of porous mediums and these works have provided valuable information in the LB applications. In the research work presented in this thesis, the LBM was employed as a numerical tool for applying to simulations on porous GDL s of PEM fuel cells.

2.3. Imaging and Reconstruction of the Gas Diffusion Layer

The GDL is usually a carbon based material. Its porous structure provided pathways for reactant gases and product water. The fluid flow transport through the GDL has been studied at various levels. However due to the complex geometry, the detailed understanding of the structural characteristics of the GDL at pore-scale is less reported. Recently, more advanced imaging technique has been employed to capture important information regarding reactants and water transport in the fuel cells, including Scanning Electron Microscopy (SEM), Nuclear Magnetic Resonance (NMR) Microscopy, neutron imaging, micro/nano tomography, and fluorescence microscopy¹⁴⁷. Lim and Wang¹⁴⁸ employed the SEM to exam the surface morphology of a carbon paper impregnated with

FEP in their study on effects of hydrophobic polymer content within a carbon paper of the cathode GDL on power performance of a PEMFC. By comparing the carbon paper GDLs of untreated and treated with 20 wt.% FEP using the SEM images, they found that significant number of pores near the surface were blocked by thin FEP films; only large pores were kept open in the wet-proofed carbon paper. They concluded that the FEP hydrophobic polymer is localized more in the surface region than in the bulk interior region of the carbon paper. In the work of Kramer *et al*¹⁴⁹, the neutron imaging technique was applied to operating PEM fuel cell to investigate two phase flow phenomena in the cathode GDL. They observed the liquid water formation at the cathode GDL, and revealed the strong sensitivity between liquid in the GDL and electrochemical performance under high load conditions. They suggested that an improved understanding of the transport processes inside the porous GDL is at least of the same importance to increase PEMFC tolerance towards flooding as further optimization of the flow field geometries. The available x-ray microtomography technique has been used widely for three-dimensional visualization as well as providing structural and composition information. For example, in the work of Lee *et al*¹⁵⁰, they evaluated the water distribution in a PEMFC by visualizing quantitatively the water in between of the separator and the GDL and gas channel using x-ray tomography imaging technique. The results showed the feasibility of using x-ray imaging technique in visualizing the water distribution in the cell components. A novel fluorescence microscopy technique was employed by Litster *et al*¹⁵¹ for visualizing the dynamic behaviour and distribution of liquid water through the GDLs in PEM fuel cells. The results suggested that the water does not transport via a converging capillary tree; however, the transportation is dominated by fingering and channelling. This proposed new water transport scheme is as the basis for developing improved models for water transport in hydrophobic GDL s with the assistant of fluorescence microscopy technique.

2.4. Aim and Methodology of the Research

The GDL of a PEMFC plays an important role of providing path ways for reactant gases to reach the catalyst layers; removing excess product water away from the catalyst layer to the gas channels and enabling electron transport to the bipolar plate. All these functions require GDLs to maintain good properties such as porosity, permeability and electrical conductivity. GDLs are typically carbon based materials of either in the form of carbon paper or carbon cloth. The two materials have different characteristics but all

give the complexity of the micro-structure as GDLs. The detailed understanding of the carbon based GDLs are needed from micro-scale point of view. This therefore requires microscopic level of modelling as well as an proper imaging technique in analysing the transport phenomena within GDLs.

Extensive research works have been carried out for investigating the GDLs using various methodologies in literatures such as macroscopic models, pore-network models, CFD models and LB method. Among those, the LB method has distinguished itself from others due to its ability of constructing simplified kinetic models which incorporate the essential physics of micro/mesoscopic process to desired macroscopic averaged properties. Its kinetic nature enables it to be an efficient numerical method compared to the traditional CFD method. Due to the complex geometry of the GDLs, it is difficult to obtain a detailed understanding of the structures and the characteristics from pore level. Also in order to ensure the modelled the GDL structural information is as close to reality as possible, an advanced imaging technique such as x-ray micro/nano tomography technique is necessary to capture the structural and geometry information of the porous GDLs.

The aim of this research is to investigate the porous carbon based GDLs structural characteristics and the fluid flow transportation within the GDL. The methodology employed in this research is using the LBM to carry out the flow simulation within the three-dimensional digital images of the actual structures GDLs which are reconstructed by the x-ray tomography imaging technique. This combined technique has the ability of revealing the structural and transport properties of the GDL by simulating the partial collisions within the actual microstructural of the GDL from pore-scale.

2.5. Outline of the Thesis

This thesis reports the research work and the obtained results are in the following structure: Chapter 1 introduces the basic knowledge of fuel cells and fundamentals of PEM fuel cell. Literature reviews on GDLs and advanced imaging technique is presented in Chapter 2. Chapter 3 and Chapter 4 explain methodologies of the LBM and the x-ray tomography technique, respectively. The study of the combined technique of LB method and x-ray tomography on a carbon paper GDL is presented in Chapter 5 in which the validated results show the capability of the combined technique of producing trustable

results. Chapter 6 carries out the simulation study of carbon paper GDL on multicomponent transport through the GDL. Carbon cloth GDL is studied in Chapter 7 focusing on characteristics of woven carbon cloth structures and properties such as permeability and porosity. In Chapter 8, the compression effects on actual structures and transport properties of carbon cloth GDLs are studied. The 1D pressure of water and oxygen across the GDL thickness at low, medium and high current densities are investigated to study the flow transport within GDL with compression

CHAPTER 3. The Lattice Boltzmann Method

3.1. Introduction

The LBM is a numerical model which has been developed rapidly over the past twenty years and become a promising alternative numerical tool in computational fluid dynamics (CFD). It is based on kinetic theory and has been largely used to simulate fluid flow in porous media, multiphase flow, particulate and suspension flows¹⁵². The basic idea of the LBM is to present the desired macroscopic equations by accumulating the mechanics of microscopic or mesoscopic individual particles in the system, however without being affected by the details of microscopic system. The LB method was developed from the Lattice Gas Cellular Automata (LGCA) which is a discrete kinetic based using discrete lattice and discrete time. Due to its advantage of constructing simple model for complex system, it has been widely employed and developed to simulate fluid flow problems in the 1980s, such as flows in porous media, immiscible flows, and granular flows and for some physical situations such as reaction diffusion process and traffic process. However, because the LGCA uses the Boolean particle number which easily gives the statistical noise, the development of LGCA moves to using the real number which is known as the distribution function. Besides, in order to simplify the kinetic equations and avoid dealing with individual particle in molecular dynamics, the LBM is therefore prompt to construct simpler kinetic based method for better understanding macroscopic phenomena from investigating the microscopic or mesoscopic world.

The main features of the LBM that differs itself from other numerical solutions are impressive. For examples, the incompressible Navier-Stokes equations can be acquired

in the nearly incompressible limit at macroscopic level. Also, the combined process of streaming and collision realizes the recovery of the nonlinear macroscopic advection. Therefore compared to the traditional CFD method which employs complex Partial Differential Equations (PDE) such as the Navier-Stokes Equations, the LBM has gained more attention in various applications especially in fuel cell research. In the research work presented in this thesis, the LB method is used to simulate the fluid flow through the porous gas diffusion layer. The carbon fiber based material of the GDLs determines that the structure of GDL is porous and heterogeneous with complex boundaries. Due to the importance of the GDL in the PEM fuel cell as a path way for reactant and water to travel through, the detailed understanding of the internal structure of the porous GDL is necessary.

3.2. Theory and Key Numerical Equations

3.2.1. Lattice Boltzmann Automata

The Lattice Boltzmann (LB) method was initially developed from the Lattice Gas Cellular Automata (LGCA) or Lattice Gas Automata (LGA). Both LB method and LGA are originated from the Cellular Automata (CA)¹⁵³. The CA was introduced by Von Neumann in the late 1940s. It is an algorithmic entity that occupies position on a lattice point and interacts with its identical neighbours. It examines its own state and the states of some number of its neighbors at any particular time step and then resets its own state for the next time step according to simple rules of Boolean¹⁵⁴. It is an idealization of a physical system in which space and time are discrete and the physical quantities (or state of the automaton) take only a finite set of values^{155,156,157}. One of the important features of the CA is that they can present a complex system from simply interacting components in the system. This potential of the CA had attracted many researchers to search for greater understanding and the CA has been applied to many areas to solve scientific problems^{158,159,160,161,162,163}. Further step of research recognizes that the CA can represent an actual model of a given physical system rather than only restrict to certain dynamical processes¹⁶⁴.

Generally speaking, a LGA consists of a regular lattice with fictitious particles situated on the nodes. The Boolean variables $n_i(x,t)$ ($i = 1, \dots, k$) is used to describe the particle

occupation, where k is the number of direction of the particle velocities at each node. The equation of the LGA is defined as:

$$n_i(x + e_i, t + 1) = n_i(x, t) + \Omega_i(n(x, t)) \quad (i = 0, \dots, k) \quad [3.1]$$

Where $n_i(x, t)$ ($i = 1, \dots, k$) is the Boolean variables, e_i is the particle velocity and $\Omega_i(n(x, t))$ is the collision operator. The Lattice Gas Automata (LGA) was introduced as a forward step from the Cellular Automata by Frisch, Hasslacher and Pomeau¹⁶⁵ in 1986. They presented a Lattice Gas model to simulate the two-dimensional Navier-Stokes equations. This model is also called the 'FHP' model named after these authors. Their work shows that for a system such as the flow of a fluid, for example, even if the individual microscopic behaviour is different, their macroscopic behaviour is similar. The basic idea of LGA is to construct simple artificial lattice where particles habitat on the nodes of the lattice with conservation of mass and momentum by interactions. With this simplicity, it brought a greater convenience on computing. However due to the defects of statistic noise and difficulties in complex three-dimensional handling, the Lattice Boltzmann Method was developed from LGA by using the lattices, streaming and a further approach of distribution function to deal with the after-collision situation where particles bounced to the neighbouring nodes.

3.2.2. Kinetic Theory of Gases

The kinetic theory of gases describes the random motion and interactions of gases from microscopic points of view to give the macroscopic phenomena of gases. In kinetic theory, it is assumed that the particles are large individuals possessing physical properties but are relatively small compared to the distance between two particles. Particles randomly distribute in the space in a velocity and they carry on elastic collision with each other as well as with the container. Therefore the kinetic theory explains that it is the collision of the gases that results in the macroscopic properties of gases, rather than external forces such as pressure.

In the early work of Broadwell¹⁶⁶, he studied the shock structures by employing the simplified kinetic equation with a single-particle speed to simulate fluid flows. The model presented can actually be considered as a simple one-dimensional Lattice Boltzmann equation. The LBM was originated from the LBA which is a discrete particle kinetics using a discrete lattice and discrete time. This demonstrates that the LBM can

also be viewed as a special finite difference scheme for the kinetic equation of the discrete-velocity distribution function¹⁵¹. The reason for using these simplified kinetic-type methods for macroscopic fluid flow is that the collective behavior of many microscopic particles in the system contributes to the macroscopic dynamics of a fluid; however the macroscopic dynamics is not sensitive to the details of the microscopic physics of the particles^{167,168}.

3.2.3. The Lattice Boltzmann Equations

Due to the limitation of the Boolean variables, in the work of McNamara and Zanetti¹⁶⁹ in 1988, they suggested to translate the LGA into a related Boltzmann model. The Boolean site populations of the LGA then became real numbers between 0 and 1 representing their average value, and their time evolution of the mean values of the one-particle distribution functions are controlled by the Boltzmann equation deriving from the Lattice gas model. This approach is called the Lattice Boltzmann Method (LBM) which is numerically more efficient than the Boolean dynamics and more efficient on computational time. One year later Higuera *et al*^{170,171} followed up their work and further simplified and enhanced the LBM by assuming that the distribution is close to local equilibrium state. The LB method has shown advantages over the traditional CFD method which is implemented by solving the Partial Differential Equations (PDEs), since the LB method simulates the flow with collision models. Because the LB method describes the physics of fluids in a way both mesoscopic and dynamic, the kinetic nature of the LB method equips the LB method with the capability of modelling problems in which both macroscopic hydrodynamics and microscopic statistics are important.

Intrinsically the LB method has two processes involved in a lattice at each time step which are called collision process and streaming process. When a particle meets others, they collide and change moving direction subject to certain collision rules which are required to maintain the conservation of mass, momentum and energy throughout the collision processes. In the streaming process, each fictitious particle is moving to their neighbouring nodes depending on its velocity. At each time step the state of a particle at certain node is therefore determined by both itself and its neighbouring particles before the time step. In the LB method, the density distribution function is used to eliminate the statistical noise which is a major disadvantage in LGA. Accordingly, the discrete collision rule used in LGA is replaced by the collision operator.

The LB models can be operated on different lattices with different dimensions. Usually the way of expressing the lattices scheme is called the DnQm scheme in which 'Dn' stands for 'n dimensions' and term 'Qm' stands for 'm velocities directions'. For example, the D3Q19 LB scheme shown in Figure 3.1 is a three-dimensional LB model in a cubic lattice in which particles can move towards total nineteen velocity directions $e_0 \sim e_{18}$. In the lattice cube, the fundamental measurement of the length is the lattice unit δx and δt is the time step.

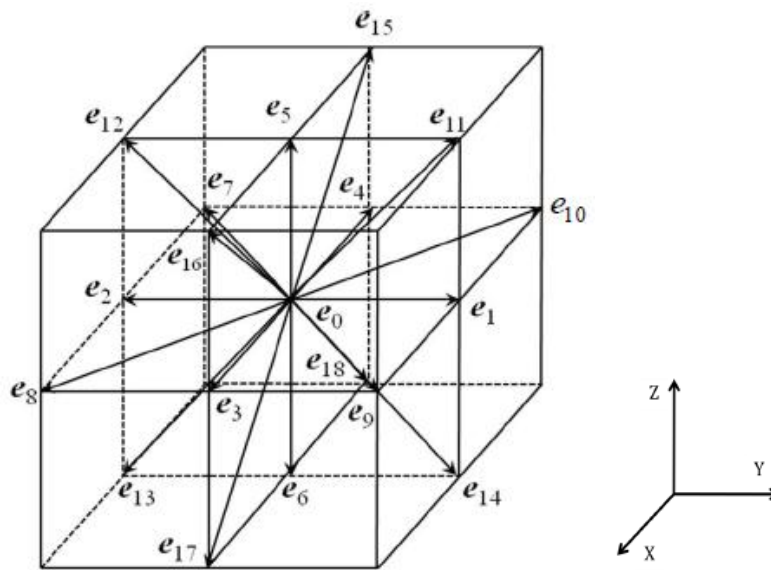


Figure 3.1 D3Q19 LB cube

The flow domain are divided into equal sized lattices and in each lattice there are nineteen velocities for the particles to move from the origin stagnant point, as can be seen from Figure 3.1, namely stagnation at the origin $(0,0,0)/\delta t$, velocities in the x direction $(\pm \delta x, 0, 0)/\delta t$, y direction $(0, \pm \delta x, 0)/\delta t$, z direction $(0, 0, \pm \delta x)/\delta t$, in the x - y plane $(\pm \delta x, \pm \delta x, 0)/\delta t$, y - z plane $(0, \pm \delta x, \pm \delta x)/\delta t$ and x - z plane $(\pm \delta x, 0, \pm \delta x)/\delta t$.

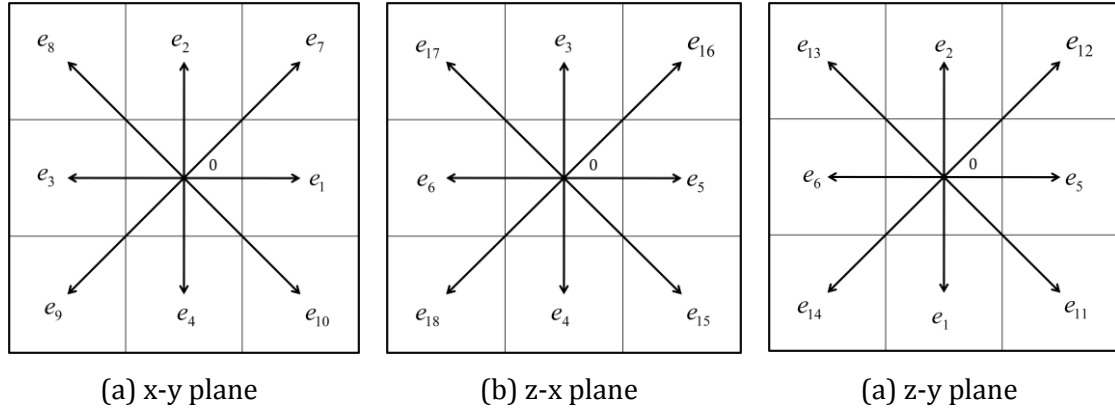


Figure 3.2 The nineteen velocities in (a) the x-y plane; (b) z-x plane; (c) z-y plane in the D3Q19 LB scheme.

The basic Lattice Boltzmann Equation (LBE) can be obtained from a discrete kinetic equation for the particle distribution function:

$$f_k(x + \xi_k \delta t, t + \delta t) = f_k(x, t) + Q_k(x, t) \quad [3.2]$$

where δt is the time step, $f_k(x, t)$ is the particle velocity distribution function representing probability of finding a particle at location x and at time t , moving towards k th direction in velocity ξ_k . $Q_k(x, t)$ represents the change rate of $f_k(x, t)$ due to collision, in another name, collision operator. The density and the momentum are expressed as particle velocity distribution function f_k :

$$\rho = \sum_k f_k(x, t) \quad \rho \xi_k = \sum_k f_k(x, t) \xi_k \quad [3.3]$$

And the collision operator $Q_k(x, t)$ is required to meet the conservation of total mass and total momentum at each lattice:

$$\sum_k Q_k(x, t) = 0 \quad \sum_k Q_k(x, t) \xi_k = 0 \quad [3.4]$$

3.3. Lattice Boltzmann Models

3.3.1. Bhatnagar-Gross-Krook Model

The LB equation [3.2] is directly obtained from the LGA by taking ensemble average of equation [3.1]. However, due to the difficulty in generalizing in the three-dimensions and computing which are brought by the collision operator, the lattice Boltzmann equation needs to be further simplified. It is Bhatnagar, Gross and Krook who discovered that the main effect of the collision term is to bring the velocity distribution function closer to the equilibrium distribution. In order to reduce the complexity, the single relaxation term of Bhatnagar-Gross-Krook (BGK) is introduced to approximate the collision operator and have been independently suggested by many authors^{172,173}.

$$Q_k(x, t) = -\frac{1}{\tau} [f_k(x, t) - f_k^{eq}(x, t)] \quad [3.5]$$

where τ is the dimensionless relaxation time parameter; $f_k^{eq}(x, t)$ is the equilibrium distribution function which is the value of $f_k(x, t)$ under equilibrium state. The BGK operator $Q_k(x, t)$ is a single-time relaxation scheme in which all lattice speeds relax on the same time scale¹⁷⁴. Therefore by combining the equation [3.2] and equation [3.5], the complete lattice Boltzmann equation can be expressed as follows:

$$f_k(x + \xi_k \delta t, t + \delta t) = f_k(x, t) + \frac{1}{\tau} [f_k^{eq}(x, t) - f_k(x, t)] \quad [3.6]$$

Equation [3.6] describes the redistribution processes when a particle collides with one another, and with the solid wall in the lattice space. The original statue of a particle at position x , time t in speed of ξ_k after the collision will be updated to $(x + \xi_k \delta t)$ at time $(t + \delta t)$ with new gained velocity which depends on the lattices and its classification. So the right hand side of equation [3.6] is to calculate the collision step:

$$f_k^{\wedge}(x, t) = f_k(x, t) + \frac{1}{\tau} [f_k^{eq}(x, t) - f_k(x, t)] \quad [3.7]$$

After the collision step, the streaming step occurs during which the particles are

redistributed which means that term $f_k^{\wedge}(x, t)$ after the collision will be moved to the location $(x + \xi_k \delta t)$ at time $(t + \delta t)$, and become:

$$f_k(x + \xi_k \delta t, t + \delta t) = f_k^{\wedge}(x, t) \quad [3.8]$$

The gas densities and velocities after the streaming step will be updated through:

$$\rho(x, t + \delta t) = \sum_k f(x, t + \delta t), \quad [3.9]$$

and

$$\rho u = \sum_k f_k(x, t + \delta t) \xi_k. \quad [3.10]$$

Depending on the dimension of the lattice scheme, variety of velocity sets for different lattice schemes give the corresponding weight factor values and equilibrium distribution function that are frequently used in the literatures. Furthermore, the equilibrium distribution function depends only on the gas density and gas velocity of local information. For the D3Q19 scheme employed in the current study, the weight factors are given by: $w_k = \frac{1}{3}$ for $k=0$, $w_k = \frac{1}{18}$ for $k=1-6$ and $w_k = \frac{1}{36}$, for, $k=7-18$.

The equilibrium distribution function $f_k^{eq}(x, t)$ is adopted from the work of He Luo¹⁷⁵ which is originally developed from the general form of the equilibrium equation introduced by Chen *et al*¹⁷⁶:

$$f_k^{eq}(x, t) = w_k \rho \left\{ 1 + \frac{\xi_k \cdot u}{c_s^2} + \frac{1}{2} \left(\frac{\xi_k \cdot u}{c_s^2} \right)^2 - \frac{u \cdot u}{2c_s^2} \right\} \quad [3.11]$$

Where c_s is the lattice sound speed and is given by $c_s = 1/\sqrt{3}$. ρ and u are gas density and gas velocity, respectively, and can be calculated by:

$$\rho = \sum_k f_k = \sum_k f_k^{eq} \quad [3.12]$$

$$\rho u = \sum_k f_k \xi_k = \sum_k f_k^{eq} \xi_k . \quad [3.13]$$

3.3.2. Boundary Treatment

In the study of carbon based porous GDL, the fluid flow in the porous GDL structure is constrained in the void space. The interface between the solid structure and the void space is assumed to be a non-slip boundary which was used by Wolfram¹⁷⁷ and Lavallee *et al*¹⁷⁸. This non-slip boundary is solved by the Bounce-Back scheme which is one of the simplest methods. By this bounce back method, it means that any particle that hits a solid wall is bounced back to the origin direction where it came from. The boundary treatment is needed in the streaming the collision results after the collision steps. Many literatures have applied the non-slip boundary conditions into their works^{179,180,181,182}. Due to the simplicity of this bounce back boundary treatment, it is ideal for simulating fluid flows in complex geometries such as porous gas diffusion layer.

Figure 3.3 illustrates the x-y plane view of an LB element for this boundary treatment. The solid area, void space and void-solid interface are represented in grey color, white color and ABC line, respectively.

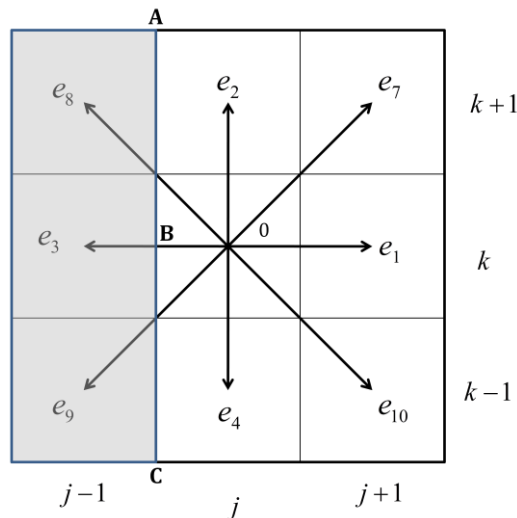


Figure 3.3 Treatment of gas-solid boundary for the bounce-back method in the x-y plane of a LB cube; the shadowed area is solid and the white is void space; the line ABC is the boundary.

As can be seen from Figure 3.3 that after collision at time t from the origin o , particles $f_3^*(o,t)$, $f_8^*(o,t)$, and $f_9^*(o,t)$ are moving toward the solid wall. Since these particles located at the centre of the cube, they hit the solid wall through half way of its one-time-step journey at time $(t + \frac{\delta t}{2})$, and then bounced back to the origin point at time $(t + \delta t)$ after the collision with the wall. Since the moving directions of particles are change after the bounce-back, these particles will move in the opposite direction at the end of the one-time step process, as shown below:

$$f_1(o, t + \delta t) = f_3(o, t)^* \quad [3.14]$$

$$f_7(o, t + \delta t) = f_9(o, t)^* \quad [3.15]$$

$$f_{10}(o, t + \delta t) = f_8(o, t)^* \quad [3.16]$$

Where the superscript * indicates the particles moving towards the solid filled element after the collision before hitting this interface. Similarly, particles moving towards the solid parts in the x-z, and y-z plane can be calculated in the same way.

3.4. Conclusions

<1>. Originally developed from the LGCA, the LB method is an advantageous method on simulating the fluid flow in complex porous geometry by tracking the collision within element. It shows great advantage of simplicity on simulation by avoiding solving the Navier-Stokes equation, compared to traditional method such as CFD method.

<2>. The LB method has the capability of constructing micro/mesoscopic behavior of particles to investigate the macroscopic phenomena and also it independently focus on micro-world without being restricted by the macroscopic phenomena of the system.

<3>The adoption of the single relaxation term of BGK in the current work of using LB method helps the velocity distribution function get close to the equilibrium status. The non-slip boundary condition is solved by the bounce-back method due to its simplicity. In this study, the D3Q19 lattice scheme is used which states that for particles on the three-dimensional cube there are 19 velocity directions available for moving.

CHAPTER 4. X-Ray Tomography Imaging Technique

4.1. Introduction

The X-Ray tomography is a non-invasive technique which is able to reveal the interior features of opaque solid objects and their three-dimensional geometries and properties. Initially developed and applied in medicine field for the imaging of bones, x-ray tomography is now widely extended and adapted to various materials researches including rock, ceramic, metal and microstructures such as carbon based GDL s. The first commercial computed tomography scanner was introduced by Hounsfield in 1972. Since then this new technology has been rapidly explored and developed by academic and industrial researches aiming to improve and apply this technique. Nowadays, the x-ray tomography technology has been improved greatly, which enables us to visualize details as small as a few microns in size.

The x-ray tomography scanners can be categorized into four groups according to their resolution and the size of the objects that they are capable to scan¹⁸³, as shown in Table 4.1. The majority of medical systems employ the conventional computed tomography. The industrial employed tomography systems can cover all the ranges of scanners from conventional to ultra-higher resolution tomography. The micro-tomography x-ray is popular and has been applied in many areas from geosciences to material research due to its high resolution capability^{184, 185, 186}. The successful application of x-ray tomography in academic research and industry is in that the x-ray tomography has advantages such as: (1) it provides entirely non-destructive three-dimensional imaging; (2) there is no sample pre-preparation required and (3) the micro/nano-level details can be extracted

by three-dimensional reconstruction. Though there are still limitations of x-ray tomography existing such as: (1) higher resolution requires small objects; (2) finite resolution may bring some blurring of material boundaries; (3) considerable computer resources for visualization and analysis can be required for large data volumes (gigabytes+).

Type	Scale of Observation	Scale of Resolution
Conventional	m	mm
High-resolution	dm	100 μ m
Ultra-high-resolution	cm	10 μ m
Microtomography	mm	μ m

Table 4.1 General classification of computed tomography¹⁸².

Due to the advantages that the x-ray tomography imaging technique can offer, the x-ray tomography is employed for producing reconstructed three-dimensional binary images of carbon cloth and carbon paper GDLs. The generated 3D images provide not only the accurate microstructures of the carbon based GDL materials in digital binary images, which can be used for LB modelling; they also give the visualization of the structures from micro-scale level.

4.2. Equipment and Methodologies

Typically, an x-ray tomography system consists of an x-ray source, series of detectors and a target to be imaged.

X-ray Sources:

The x-ray tubes are used as the x-ray sources which are characterized by three main factors: (1) focal spot size; (2) x-ray energy spectrum and (3) x-ray intensity. The focal spot size provides the number of source-detector paths which will intersect a given point in the target to be scanned. The energy spectrum determines the penetrative ability of the x-rays when they scan through the object materials as well as the relative

attenuation resulting from the different density of the materials. Though higher energy x-rays have strong penetration ability, they have to sacrifice the sensitivity to changes in material composition and density. The x-ray intensity influences the signal to noise ratio. Higher intensity improves the image clarity, but requires a larger focal spot size.

X-ray Detectors:

The majority of the x-ray use scintillators as x-ray detectors since the scintillators materials are able to count the flashes of light which is generated by the x-rays. Nowadays it's common that the x-ray system employs the charge coupled device (CCD)-based detector arrays. The important parameters of the detectors are the size, materials and their efficiency in catching the energy spectrum generated by the x-ray source. The size of a detector is in charge of the amount of a target that is averaged into a single intensity reading. Usually the scintillation materials are cesium iodide, gadolinium oxysulfide and sodium metatungstate. The efficiency of scintillation detectors depends on the x-ray energy since higher energy x-ray can gives more penetration than lower energy x-ray ones.

Figure 4.1 shows the schematic view of an x-ray tomography system employed in this work. The x-ray tomography system includes an x-ray source, a rotating sample holder and an x-ray detector. The x-rays are converted to flashes of light by a scintillator screen. A Hamamatsu x-ray camera is used as the x-ray detector for this system which includes a scintillator and a charge coupled device (CCD) chip. The CCD chip size is smaller than that of the scintillator and can be damaged by x-rays under long exposure condition. In order to reduce damage, a tapered fiber-optic bundle is used and glued to the scintillator screen at one end and the CCD chip at the other end. The bundle translates the position from the scintillator down to the CCD chip at 1:1 precisely. The camera has a CCD chip with 1024x1024 pixels and a 12 bit depth. The resolutions for generating microtomography images and Nanotomography images are different depending on the scanning system. The microtomography scanner system provides a resolution of 1~10 μm , while the nanotomography scanner can give a resolution less than 100 nm¹⁸⁷,¹⁸⁸. The maximum resolution of a system is calculated from the object diameter of the camera and the number of the pixel cross it.

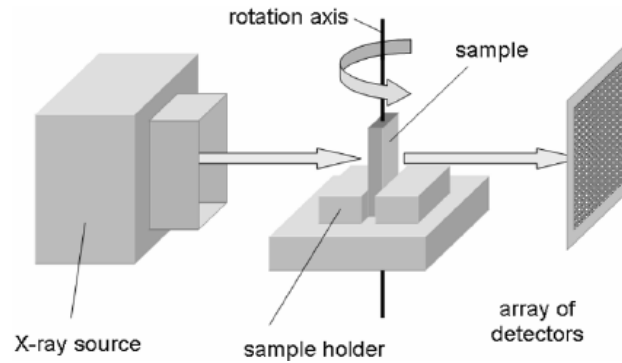


Figure 4.1 The micro/nano tomography system

To reconstruct three-dimensional binary images, there are mainly three steps involved: (1) two-dimensional image acquisition; (2) image processing and thresholding and (3) three-dimensional digital reconstruction.

4.2.1. Two-Dimensional Image Acquisition

For the x-ray tomography technique, there is no need to prepare the sample before the imaging process. It only needs to make sure that the target is inside the field of view without moving during the whole scanning process. During the process a sample is held in front of the x-ray source. By rotating step by step through 180° relative to the x-ray source, a series of 2D shadow image are recorded using an x-ray detector array. At this step, the 2D gray scale shadow images obtained can be used to generate a virtual 3D image of the GDL. Microtomography images are acquired using a Skyscan 1072 system with an X-ray source of 50 kV at $100 \mu\text{A}$ and a rotation step of 0.9 deg. The 200 two-dimensional shadow images can be acquired in 45 min with a resolution of $1.76 \mu\text{m}$. Nanotomography images are acquired using a Skyscan 2011 system with X-ray source of 25 kV at $200 \mu\text{A}$ and a rotation step of 0.5 deg. The 371 two-dimensional shadow images can be acquired in 40 min with a resolution of 680 nm pixels.

The next step is to find the cross section image of the 2D gray scale shadow images obtained by the x-ray detector. A cross section image is defined as an image view as cutting through the scanning plane and this is implemented by CTAn software¹⁸⁹. The typical 2D shadow image of a $100 \times 300 \times 100 \mu\text{m}^3$ carbon cloth GDL scanned by the

x-ray nano-tomography with resolution of 680 nm and the cross-section image are shown in Figure 4.2(a) and (b), respectively.

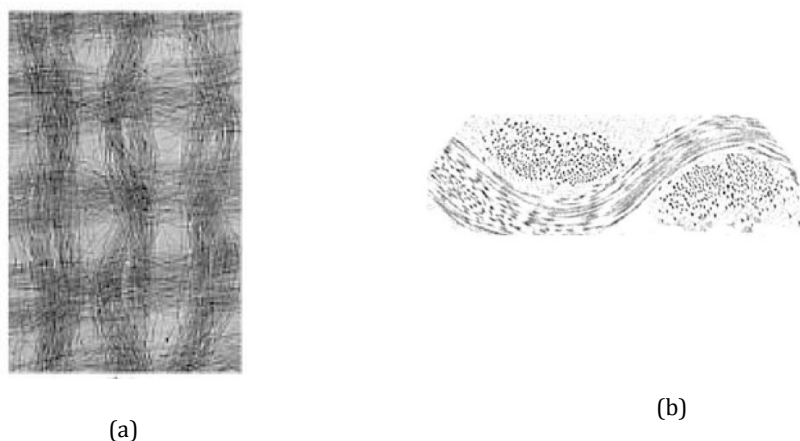


Figure 4.2 Typical x-ray tomography images of a 100 x 300 x 100 μm^3 carbon cloth GDL sample. (a) a typical two-dimensional shadow image scanned by x-ray nano-tomography with 680nm resolution; (b) the reconstructed greyscale cross-section image by CTAn software with microtomography¹⁹¹.

4.2.2. Image Processing and Threshold Tuning

In order to investigate the structure and pore-scale characteristics of the GDL, it requires an accurate representative three-dimensional model for the simulation and analysis. The reconstructed three-dimensional images of GDL samples have to be ready for the LB simulation analysis. Therefore the threshold tuning process on the grey scale cross section images are carried out to produce three-dimensional binary images for the simulation.

Currently, the appropriate threshold tuning is often determined by visual inspection or by a scanner-supplied algorithm^{190,191}. A heuristic technique was developed by Ostadi *et al*¹⁹². They determined the threshold level by comparing the surface of the three-dimensional image generated by the x-ray tomography with a reference scanning electron microscopy (SEM) image of the same surface in terms of average fiber diameter and connectivity. For the study of carbon fiber based GDL materials, a method for fine-tuning the threshold of nanotomography images was employed from the same author¹⁹³. Using this method, the porosity and average fiber diameter of a GDL material obtained from a series of thresholded X-ray nanotomography images were compared to

the reference values of porosity and average fiber diameter acquired from density experiment and SEM images respectively. SEM is a type of electron microscope that images a sample by scanning it with higher energy electrons to generate a variety of signals at the surface of solid samples. SEM can generate a two-dimensional image from a selected area of the surface of the sample. The generated SEM images can reveal information about the sample including external texture, chemical composition and orientation of materials making up the sample.

The thresholding is applied on the 2D grey scale image which is composed of up to 256 grey shades. The thresholding processes describes the grey scaled 2D image sample by assuming that lighter regions corresponds to void space and darker regions corresponds to solid space; which means digital number 0 and 1 are designated to represent void space and solid space, respectively. Firstly a 2D SEM image of one surface of the imaged sample is taken, as shown in Figure 4.5(a). The SEM can provide high-contrast and high resolution grey scale image of the surface of the imaged sample; hence it allows the features of the carbon fibrils of the GDL to be investigated. The appropriate threshold level is then determined by using SEM images as a reference for determining the average diameter of the sample fibers using CTAn software. It is assumed that the average fiber diameter determined from the reference image is representative of that for the entire 3D structures. Among the thresholded images, the threshold level applied is accepted when the average fiber diameter and porosity of the 3D image is within $\pm 1\%$ of measured fiber diameter. The porosity in the reference image and the fiber continuity is also checked.

The fiber diameter and the porosity obtained from the tomography can be affected by the threshold variation. The measurements were carried out to identify the relationship between the threshold variation and the pore size by Ostadi *et al*¹⁹². They reported that by increasing the threshold level to 5% (13 grey levels), the average fiber diameter fluctuates about 10% for the carbon paper and decreases 5% for carbon cloth; while the porosity of both carbon paper and carbon cloth increase linearly about 5% over the threshold for 5% threshold variation, as shown in Figure 4.3. The effect of threshold variation on continuity of the fibers is also considered. Figure 4.4(a) and (b) shows an example of the effect of 5% variation on threshold on the fiber continuity of the carbon cloth GDL. It is clearer to see from the highlighted circle in (a) and (b), that higher level thresholded image shows better fiber continuity than the low thresholded one.

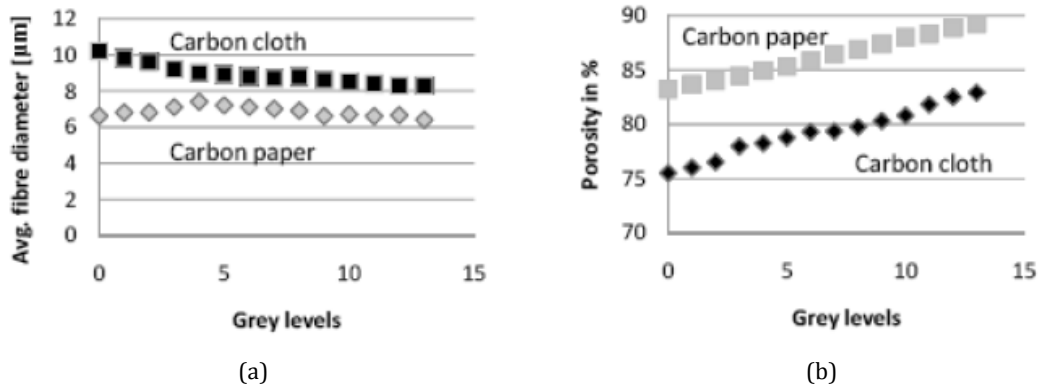


Figure 4.3 Variation of fiber diameter and porosity of 5% threshold band (13 grey levels). (a) average fiber diameter; (b) porosity



Figure 4.4 The effect of 5% change in threshold on fiber continuity. The highlighted parts are example of this discontinuity. (a) low threshold; (b) high threshold¹⁹⁴.

4.2.3. Three-Dimensional Digital Reconstruction

The reconstruction of the 3D binary image is a standard process using CTAn software and there are several algorithms that can be used such as Marching Cube 33, Double-Time Cubes or Adaptive Rendering¹⁹⁵. The detailed imaging process is discussed in greater detail elsewhere¹⁹⁰.

Figure 4.5(a) ~ (d) illustrates the images of 3D and 2D images of a $100 \times 300 \times 100 \mu\text{m}^3$ carbon paper GDL sample nano-tomography. Figure 4.5(a) shows the shadow tomography image of carbon paper scanned with 680 nm resolution scanned by the x-ray. (b) and (c) give the reconstructed 2D cross section image slice using CTAN software and its binary image, respectively. It can be seen that the grey scale shadow image in (a) has shown clear void space (white/lighter) and solid space (darker/black)

in (b) and (c) after the threshold tuning process. (d) shows the reconstructed binary image using optimal threshold value. The reconstructed 3D images are saved as three dimensional arrays of binary digitals in which 0 and 1 represent void space and solid space, respectively. The reconstructed binary image of the GDL sample then can be readily supplied to the LB model for simulation.

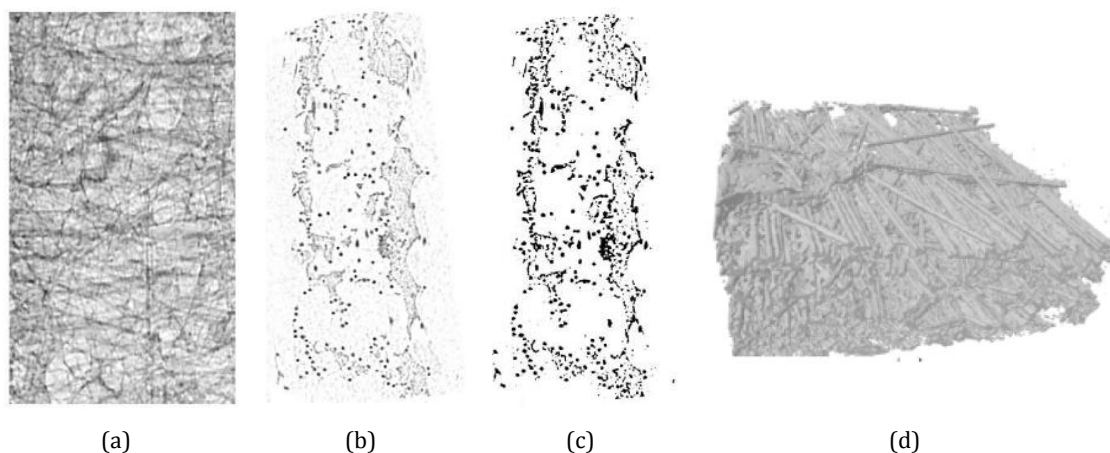


Figure 4.5 2D and 3D images of a $100 \times 300 \times 100 \mu\text{m}^3$ GDL carbon paper sample; (a) 2D shadow X-ray tomographic image with 680 nm resolution scanned by the x-ray nano-tomography (b) 2D reconstructed grey scale image using CTAn software; (c) binary image of the cross section shown in (b). (d) an isometric view of the reconstructed image of carbon paper GDL with 680 nm resolution using CTAn.

4.3. Conclusions

<1>. The x-ray micro/nano tomography technique has been employed as an effective tool for seeing inside structures of complex porous GDL by reconstructing actual 3-dimensional structure of the samples.

<2>. The processes of generating a reconstructed 3D digital image involves firstly the 2D shadow image taking, and then the important threshold estimation is carried out by using the SEM images as references to tune the grey level of the shadow images. The fine tuned images are then used to generate the three-dimensional digital images in which number 1 represents the solid space and number 0 represents the void space. This

threshold process ensures that the 3D digital images generated are as close to reality as possible.

<3>. The 3D digital binary images are reconstructed by the x-ray tomography from the real geometry of the GDL samples. Therefore they contain actual microstructural information of the GDL structure and are ready to be supplied directly to the LB model for simulation.

CHAPTER 5. X-Ray Tomography Based Lattice Boltzmann Simulations

5.1. Introduction

The carbon based porous GDL provides pathway for transporting reactants to the catalyst layer, mechanical supports between the channel and electrolyte and allow excess water being expelled out of the channel. It is usually in the form of carbon paper or carbon cloth, which consists of carbon fibrils and regular woven bundles of carbon fiber, respectively. For either the carbon paper or carbon cloth, the individual carbon strands is about 7-12 μm in diameter, while in carbon cloth the woven bundle diameter can be in the region of 400 μm ¹⁹⁶. The maximum pore diameter can be as large as 250 μm in carbon cloth while in carbon paper the maximum pore diameter is around 40 μm . For both carbon paper and carbon cloth, parameters such porosity, permeability and pore connectivity largely rely on fibril content, woven bundle diameter and the fibers arrangement. Due to the complex carbon fiber structure of the porous GDLs, the anisotropic characteristics of the material determines that the fluid flow that transports through those materials will be multi-direction. In order to investigate micro-scale fluid flow behavior through the porous GDL, therefore it needs a greater understanding on the actual interior structural side of the material.

The LB method has shown great potential on simulating fluid flow on complex geometry. Hao and Cheng¹⁴⁵ studied the anisotropic permeability of carbon paper GDLs using LB model. Similarly, in the work of Niu *et al*¹⁴⁴ they developed a LB model to investigate the liquid-gas transport through the PEM GDL, absolute permeability and relative permeability. There are other works in literatures on simulating fluid flow problems in

porous medias^{197,198,199,200,201,202}. However, it is necessary to note that the current models are limited by using the software generated artificial 2D or 3D geometries of the GDL structures which are not close to real ones in terms of internal microstructure. In order to model the PEM fuel cell GDL with more realistic situation, it is ideal to generated accurate 2D or 3D structural models based on real carbon fiber GDL samples.

In this chapter the 3D digital binary image of a carbon paper GDL is reconstructed using x-ray computational tomography technique which has been introduced previously. The reconstructed binary image is then supplied to the single phase single component LB model to simulate the flow transport through the interested GDL structure. The calculated result of permeability using this combined technique is validated against experimental data. The results prove the capacity of the combined technique of x-ray tomography based LMB for predicting the flow characteristics in GDL microstructures.

5.2. Methodology

5.2.1. Single Phase Single Component LB Model

The LB model for simulating a single gas is called the Single Phase Single Component (SPSC) LB model. An existing LB model for soil structures is employed and modified to a single phase single component model to simulate the flows through the porous media^{203,204}. The SPSC LB model used in this study is to simulate air transport through the carbon paper GDL. The SPSC LB Model with single relaxation time of D3Q19 scheme has been described in Figure 3.1 in Chapter 3. By using this scheme, the sample space is divided into regular lattice, and the particles in each lattice (voxel) are assumed to move in nineteen directions from the original position. The bounce-back method is used here to treat the solid and void boundary of the porous structure. It means that particles that collide with wall will simply bounced back to their original positions at the beginning of the time step. A pressure difference as the inlet and outlet boundary of the simulation domain is imposed to through-plane direction to drive the gas flow. The key equations of this LB model were previously described in by Equation [3.2] ~ Equation [3.11].

5.2.2. X-ray Microtomography

The x-ray microtomography is employed to generate the 3D reconstruction image of the carbon paper GDL. For microtomography images, a Skyscan 1072 system with an X-ray source of 50 *kV* at 100 μA and a rotation step of 0.9 degree is used and 200 shadow images with a resolution of 1.76 μm can be obtained in 45 mins. The maximum resolution of a system is defined by the object diameter of the camera as well as the number of pixel across it. In the Skyscan 1072 microtomography system, the resolution is calculated as the object diameter (1.8 *mm*) divided by 1024 pixels giving 1.76 μm .

5.3. Simulation

The 3D images that reconstructed by the x-ray microtomography are saved as three dimensional arrays of binary digitals. The binary digital image is presented by 0 and 1 which indicates void space and solid parts, respectively. It is necessary to know that in order to ensure that the 3D digital images generated are spatially and computationally fit the LB model, it requires that the coordinate selection during the images generation are consistent with that for LB model; and the lattice size of the LB model needs to match with the resolution of 3D images. The reason is that it will easily allow each voxel of the 3D binary digital image to be fed as the lattices of the LB model. Moreover, the image size, the complexity of the image structure and the computational resource availability also need to be considered before the simulation.

A carbon paper GDL sample is used for the experimental measurement of the permeability which has a nominal thickness of 217 μm , a density of 397 Kg/m^3 under a compression pressure of 50 *kPa*. The sample used for x-ray microtomography is taken from the same batch. However, due to the limitation of the x-ray detector area as well as the computational resource, it is difficult to image and simulate the whole area of the GDL. Therefore a relatively representative large 3D area (total areal representation < 1.0%) of the carbon paper sample were imaged and divided into 14 series of digital regions. Then each region is supplied to the SPSC LB model to calculate the absolute air permeability for each supplied region by simulating the gas velocity. The pressure difference applied to each region for driving the flow is 20 *Pa* according to the literature suggestion that the pressure drop across a GDL in an operating fuel cell needs to be less than 100 *Pa*²⁰⁵. Because the absolute permeability shows linear dependency of gas flow

rate on the pressure gradient applied, the selected pressure difference has to ensure this linearity as the gas flow rate is concerned. In order to minimize the effects of local heterogeneities in the porous carbon paper structure which would cause overprediction or underprediction of simulated permeability, the average mean value of simulated absolute permeability of all 14 regions is calculated to compare with the measured value.

The measured value of air absolute permeability was implemented by using a Frazier air tester. The volumetric flow rate and the pressure drop along through plane direction were measured when system reached steady state. By applying the measured values of average flow rate and the pressure drop to Equation [5.1], the absolute air permeability of the carbon paper GDL was obtained. All the measurement was carried out at standard room temperature, and the GDL sample for the testing does not contain an MPL.

5.3.1. Permeability Calculation

The GDL is an important component in the PEM fuel cell since it provides pathways for reactant gases transport through. Permeability represents the abilities of conducting gases of a porous carbon based GDL. The absolute permeability k of a GDL can be calculated based on the Darcy's law:

$$k = \frac{\rho \mu q}{(\Delta P / L)} \quad [5.1]$$

where q is the average gas velocity through the GDL in the direction along the imposed pressure gradient when the flow reaches its steady state. ρ is the gas density which can be calculated from equation [3.3]. ΔP is the pressure gradient applied along the through-plane direction across the GDL image. The kinetic viscosity μ is related to the dimensionless relaxation time τ by²⁰⁶:

$$\mu = \frac{\delta x^2 (\tau - 0.5)}{3 \delta t} \quad [5.2]$$

where δx is the lattice unit and δt is the time step.

In fact, when a pressure gradient is applied to the through-plane direction, the gas can also flow in the in-plane direction. Therefore, there will be six components of the permeability tensor (k_{mn} , $m, n = x, y, z$ and $k_{mn} = k_{nm}$), and these can be calculated by applying the pressure difference in the different directions of the image.

For example, if the pressure difference is applied in the x direction parallel to the flow direction, the three components of the permeability tensor can be calculated as:

$$k_{xx} = \frac{\rho\mu q_x}{(\Delta P / L_x)}; \quad k_{xy} = \frac{\rho\mu q_y}{(\Delta P / L_x)}; \quad k_{xz} = \frac{\rho\mu q_z}{(\Delta P / L_x)} \quad [5.3]$$

Accordingly, by applying the pressure difference to the other two directions, the other components of the permeability tensor are to be calculated.

When the pressure gradient was applied in the y direction,

$$k_{yx} = \frac{\rho\mu q_x}{(\Delta P / L_y)}; \quad k_{yy} = \frac{\rho\mu q_y}{(\Delta P / L_y)}; \quad k_{yz} = \frac{\rho\mu q_z}{(\Delta P / L_y)} \quad [5.4]$$

And when applying the pressure gradient in the z direction:

$$k_{zx} = \frac{\rho\mu q_x}{(\Delta P / L_z)}; \quad k_{zy} = \frac{\rho\mu q_y}{(\Delta P / L_z)}; \quad k_{zz} = \frac{\rho\mu q_z}{(\Delta P / L_z)} \quad [5.5]$$

where q_x , q_y , and q_z are the average velocities, and L_x , L_y , and L_z are the lengths of the simulation domain in the x, y, z direction, respectively. The permeability tensor k_{mn} ($m=x,y,z; n=x,y,z$) for each component can be explained as the permeability of the porous medium in the m direction when the pressure difference is imposed in the n direction.

The average velocities is defined as

$$q_x = \frac{\sum_i u_x(x_i)}{L_x L_y L_z}; \quad q_y = \frac{\sum_i u_y(x_i)}{L_x L_y L_z}; \quad q_z = \frac{\sum_i u_z(x_i)}{L_x L_y L_z} \quad [5.6]$$

Where the subscript i represents the elements; $\sum_i u_x(x_i)$, $\sum_i u_y(x_i)$, $\sum_i u_z(x_i)$ are the summation of three simulated velocities components for each element for the simulated image. All the variables in Equation [5.3] - [5.6] are measured in a spatial unit δx and a temporal unit δt .

The parameter Ω is used to adjudge the steady state condition once its value fall within the range $\Omega < 10^{-5}$:

$$\Omega = \frac{\sum_i |u_j(x_i, t + 100) - u_j(x_i, t)|}{\sum_i |u_j(x_i, t)|}; \quad (j = x, y, z) \quad [5.7]$$

5.3.2. Simulation scheme

Figure 5.1 shows the flow chart of simulation process of LB modeling with x-ray tomography imaging as well as the experimental test. The LB model was programmed using C++ language. The simulation was implemented on a quad-core 2.33 GHz computational resource with 3.25 Gbytes of RAM. A single-phase simulation for one region can take up to 240 mins.

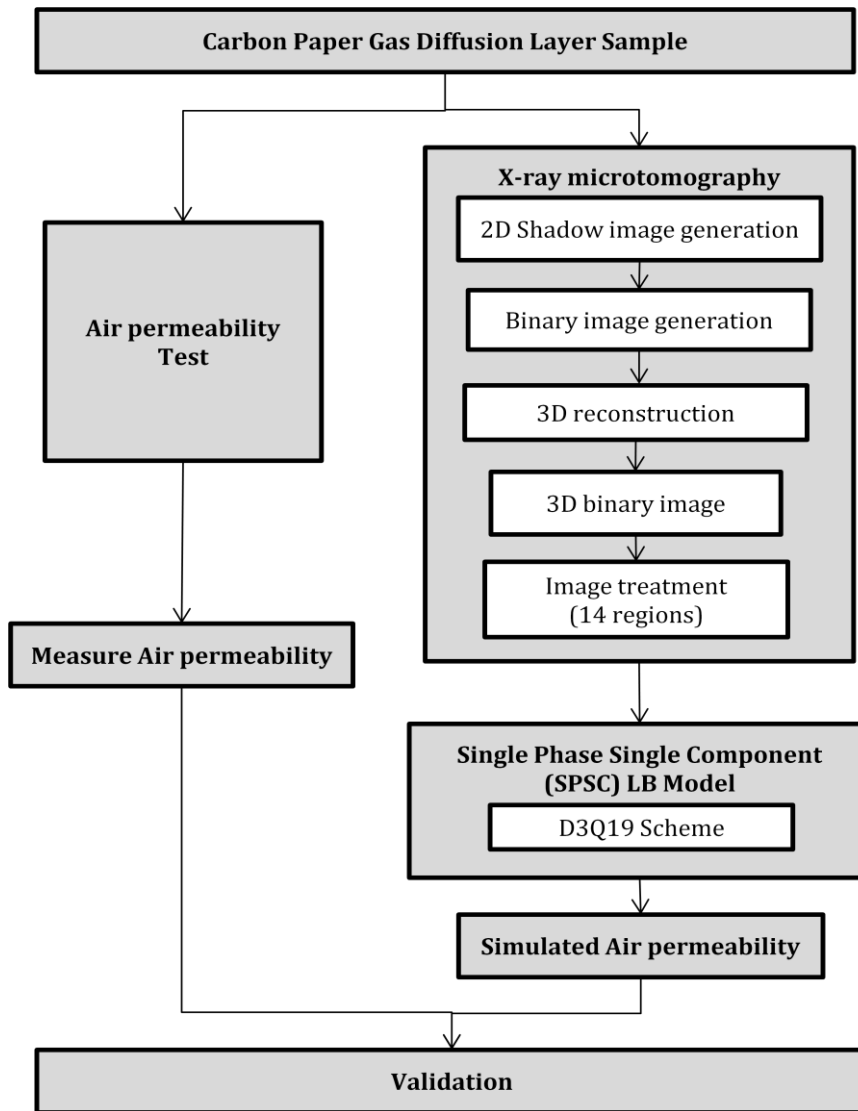


Figure 5.1 Flowchart of X-ray tomography imaging and LB simulation

5.4. Results and Validation

The whole size of the simulated carbon paper sample is $1246 \times 1716 \times 271 \mu\text{m}^3$ with a resolution of $1.76 \mu\text{m}$. The through-plane y direction which is perpendicular to the x - z plane is the main simulation direction along which the pressure gradient is applied. The 3D shadow image of the overall sample is shown in Figure 5.2. The sizes of the 14 regions of this sample are shown in Table 5.1 which gives both the voxel size as well as the physical size.

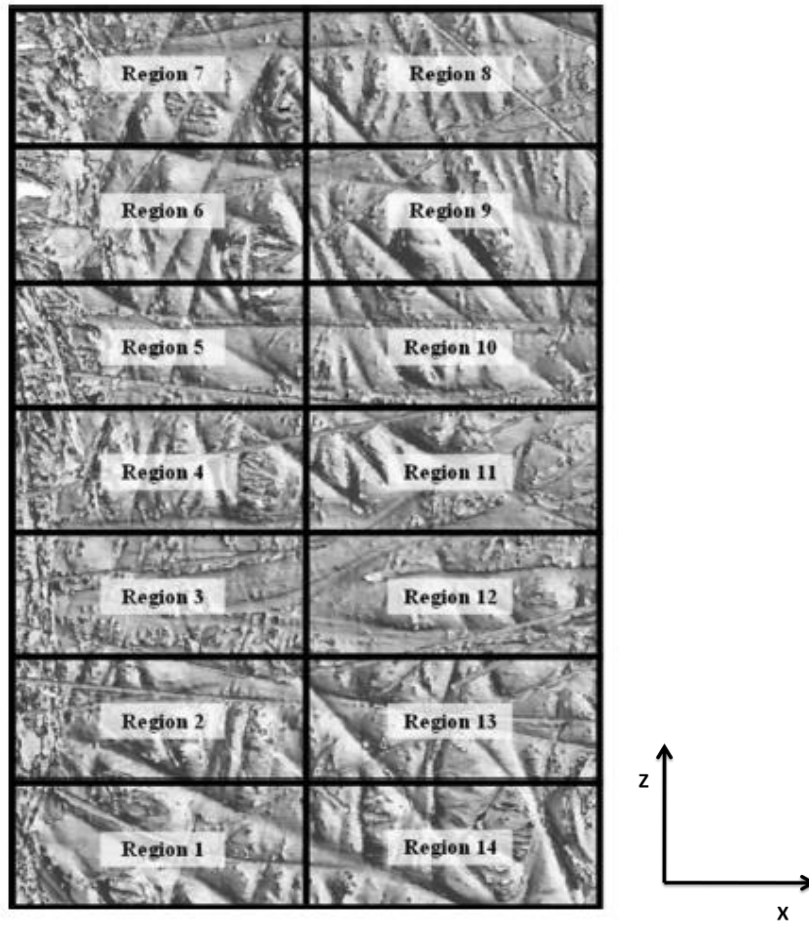


Figure 5.2 The overall 14 3D shadow images of a $1246 \times 1716 \times 271 \mu\text{m}^3$ carbon paper GDL with $1.76 \mu\text{m}$ resolution for the LB simulation, provided by the x-ray microtomography.

	Region 1-6			Region 7 and 8			Region 9- 14		
	X	Y	Z	X	Y	Z	X	Y	Z
Image size in voxel	354	154	150	354	154	75	354	154	150
Resolution, μm	1.76	1.76	1.76	1.76	1.76	1.76	1.76	1.76	1.76
Image size, μm	623	271	264	623	271	132	623	271	264

Table 5.1 Image sizes for each region of the 3D carbon paper image

5.4.1. The through-plane absolute permeability

The through-plane absolute permeabilities of 14 individual regions were simulated by the LB model and the mean absolute permeability was calculated. The results are shown in Figure 5.3. The measured value of absolute permeability is also presented in the same figure for comparison.

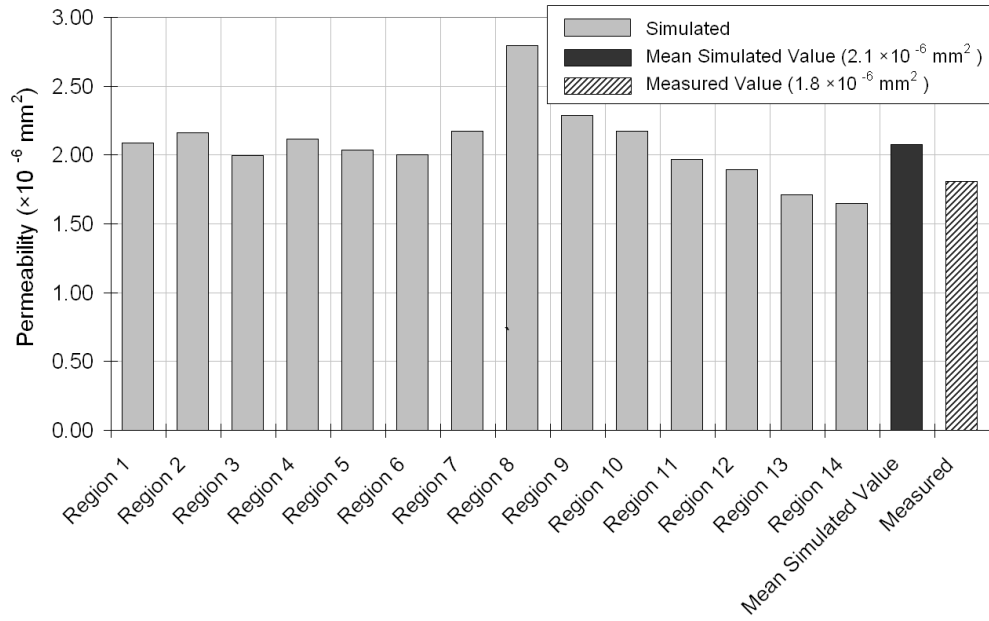


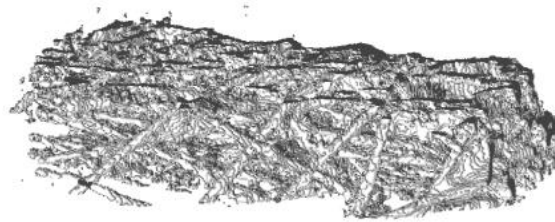
Figure 5.3 The simulated absolute permeability of 14 regions, the mean simulated absolute permeability, and the measure values for the same sample

The simulated mean value of the absolute permeability of all 14 regions is $2.1 \times 10^{-6} \text{ mm}^2$ and the measure permeability is $1.8 \times 10^{-6} \text{ mm}^2$ both of which are in the same order of magnitude. In order to exam the accuracy of simulation results, a parameter ψ is introduced here to calculate the error. ψ is defined as the ratio of the difference between measured and calculated value of absolute permeability over the order of magnitude of the measured value Θ_{perm} , as shown in Equation [5.9]. The error shows that the simulated value is only 3% greater than the measure one.

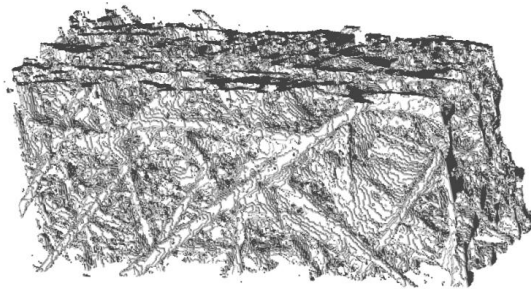
$$\psi = \frac{|k_{meas} - k_{calc}|}{\Theta_{perm}} \times 100\% \quad [5.9]$$

Comparing values of the simulated absolute permeability of fourteen regions with the mean value of $2.1 \times 10^{-6} \text{ mm}^2$ gives the standard deviation of $2.7 \times 10^{-7} \text{ mm}^2$. This means that there is $\pm 13\%$ difference around the mean simulated value which indicates the heterogeneous characteristic of the porous media.

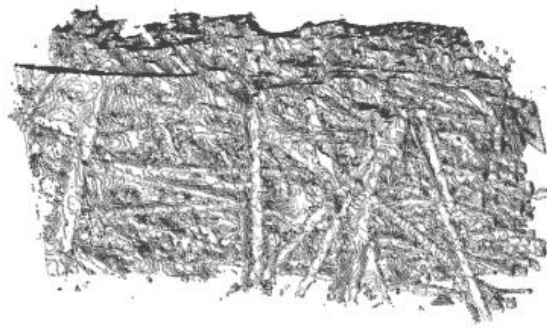
Figure 5.4 and Figure 5.5 give three-dimensional views of three representative regions out of the fourteen which are region 1, region 8 and region 14. Figure 5.4 are the 3D images as can be seen in Figure 5.2 and the Figure 5.5 shows the rotated 3D images of the three individual images. The reason for choosing these three regions is that Region 8 and region 14 are the ones with highest permeability value of $2.8 \times 10^{-6} \text{ mm}^2$ and lowest value of $1.7 \times 10^{-6} \text{ mm}^2$, respectively. Region 1 has the permeability value of $2.1 \times 10^{-6} \text{ mm}^2$ which is most close to the mean simulated value.



(a) region 8



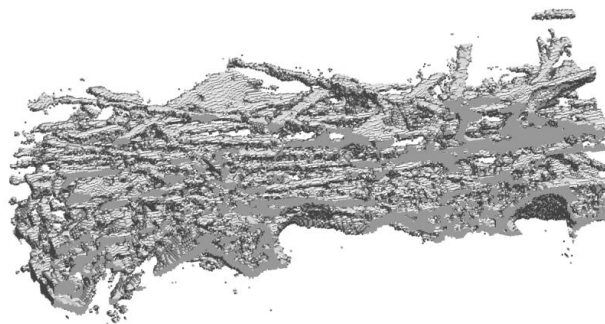
(b) region 14



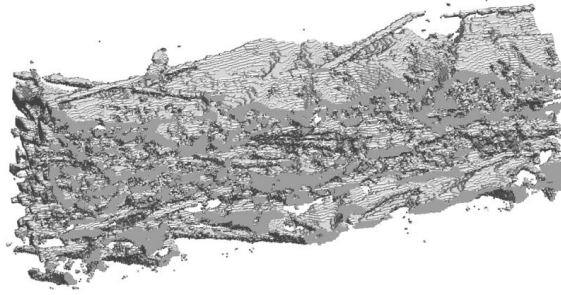
(c) region 1

Figure 5.4 The binary 3D images of: (a) region 8 with size of $354 \times 154 \times 75 \mu\text{m}^3$, (b) region 14 with size of $354 \times 154 \times 150 \mu\text{m}^3$ and (c) region 1 with size of $354 \times 154 \times 150 \mu\text{m}^3$, as seen from Figure 5.3

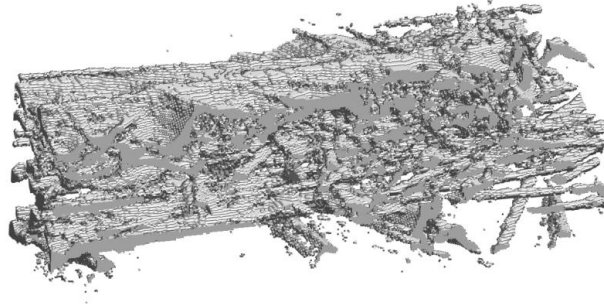
Figure 5.5 shows rotated 3D view of region 8, region 14 and region 1 in (a), (b) and (c), respectively. It gives clearer view of the fiber layout. Region 8 has more void space as can be seen from (a) which gives more space for gas to travel through. Region 14 in (b) has also relatively large void space; however, the fibrils organization is more compact compared to that of region 8. This layout limits the permeation of air through the structure which causes a lower permeability value. In comparison with region 8 and region 14, region 1 in (c) has a structure with moderately organized fibril and relative large void space. It has the permeability most close to the average value.



(a) region 8



(b) region 14

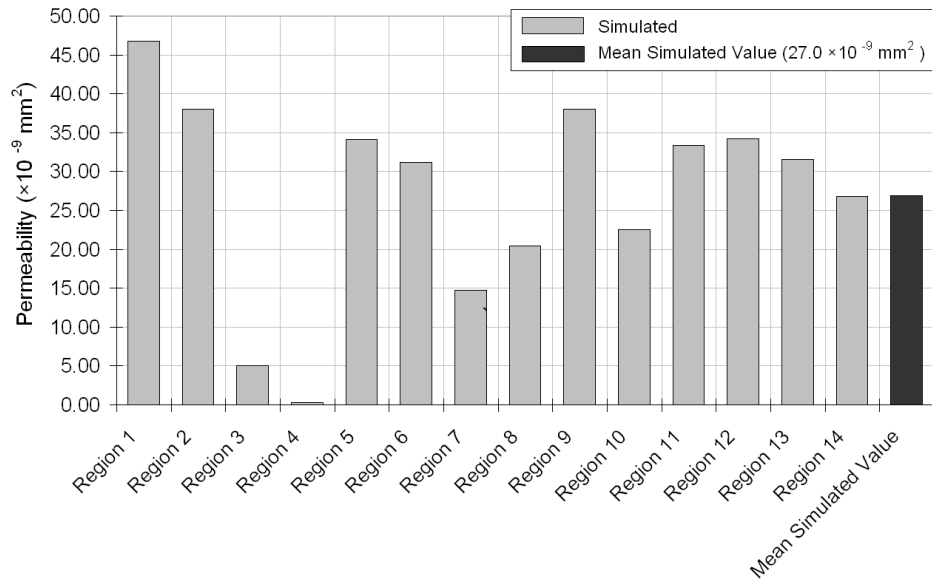


(c) region 1

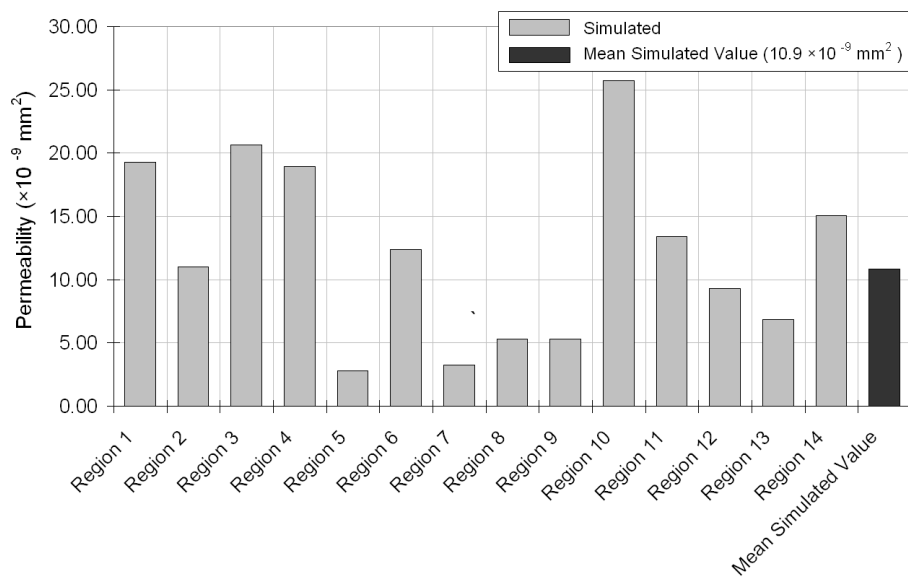
Figure 5.5 Rotated 3D binary images of: (a) region 8 with size of $354 \times 154 \times 75 \mu m^3$, (b) region 14 with size of $354 \times 154 \times 150 \mu m^3$ and (c) region 1 with size of $354 \times 154 \times 150 \mu m^3$

5.4.2. The In-plane Absolute Permeability

The simulated absolute in-plane permeability of x direction and of z direction for all the fourteen regions are presented in Figure 5.6(a) and (b), respectively. The calculated mean simulated absolute permeability in x direction is $27.0 \times 10^{-9} mm^2$ and that in z direction is $10.9 \times 10^{-9} mm^2$. It's been known from Figure 5.4 that the mean simulated absolute permeability of through-plane y direction is $2.1 \times 10^{-6} mm^2$. Then by comparing the in-plane absolute permeability with that of the through-plane, it is noticed that the mean values in both in-plane directions are two orders of magnitude smaller than that of through-plane direction. This shows that even though the pressure gradient is imposed to the through-plane direction, there will still be gas pass through from the in-plane direction but with much slower rate compared to that of the gas flow through the through-plane direction.



(a)



(b)

Figure 5.6 Simulated absolute permeability of two in-plane direction: (a) x direction and (b) z direction

5.5. Conclusions

A three-dimensional single phase LB model previously developed for soil structure has been modified by Zhang *et al*²⁰³ to simulate air flow transportation within a carbon

paper GDL. The actual GDL structure was reconstructed to three-dimensional binary images by the x-ray tomography technique and can be directly supplied to the LB model to carry out the simulation. The absolute air permeability of through-plane direction and two in-plane directions have been simulated by the LB model. The agreement of the calculated permeability with the experimental values proves the feasibility of the combined methodology. The results of this study are concluded below:

<1>. The x-ray microtomography technique has been employed to generate the 2D shadow images of carbon paper GDL sample, which is then processed and converted into 3D digital binary images by applying a threshold tuning treatment. The sample size of $1246 \times 1716 \times 271 \mu\text{m}^3$ is selected to enclose the heterogeneous properties of the carbon paper structure as much as possible. The sample is further divided into fourteen regions since the large size of the image is difficult to handle due to the computer resource. The 3D digital binary images of the carbon GDL sample of all 14 regions are reconstructed by the x-ray tomography and are supplied to the LB model for simulation.

<2>. The simulated absolute permeability in the main through-plane y direction is compared with the measured value of the same carbon paper GDL under the standard temperature. The mean simulated absolute permeability value of total fourteen regions is $2.1 \times 10^{-6} \text{ mm}^2$. This value has the same order of magnitude with the measured value of $1.8 \times 10^{-6} \text{ mm}^2$. The structural inspection shows that the structure with large void space usually has higher permeability than that with less void space. However, if the structure is very compact even though there is large void space existing, the permeability of the structure can be lowered.

<3>. The gas flow in the in-plane direction occurs even though the pressure gradient is imposed in the through-plane direction. The absolute permeability of in-plane x-direction and in-plane z-direction are $27.0 \times 10^{-9} \text{ mm}^2$ and $10.9 \times 10^{-9} \text{ mm}^2$, respectively. By comparing with the through-plane permeability, the two in-plane values are two orders of magnitude smaller.

<4>. An indicator of error ψ is introduced to examine the accuracy of the simulation results in the order of magnitude of the measured permeability. Only 3% difference is found which shows the feasibility of using the combined method of x-ray tomography based LB model.

CHAPTER 6. Simulation Studies on Carbon Paper Gas Diffusion Layer

6.1. Introduction

The single phase LB model combined with x-ray microtomography technique has been presented in the previous chapter for single species simulation on air absolute permeability. The overall results show the capability of the combined technique for pore-scale modeling for porous media. The study in previous chapter restrains the LB model on single component simulation. It is known that there are two or three main species to supply to the PEM fuel cell anode or cathode. In this chapter, three species of oxygen, water and nitrogen transportation through a carbon paper GDL is studied. The LB simulates the gases one-dimensional partial pressure along the flow direction under four fuel cell operating conditions.

6.2. Methodology

The previously presented three-dimensional single phase single component (SPSC) Lattice Boltzmann model was modified to single phase multicomponent (SPMC) model to simulate multi-component flow through cathode side of carbon paper GDL. The 2D shadow image of the carbon paper structure is captured by x-ray microtomography and reconstructed into three-dimensional digital binary image and is supplied to the multicomponent LB model. A previously developed 1D numerical General Transport Equation (GTE) based PEM fuel cell model is employed to calculate the boundary conditions at the two sides of the GDL for the LB model²⁰⁷. Structural property of the

GDL such as permeability, porosity and tortuosity are calculated by the single phase single component LB model which was introduced in previous chapter. For the simulation study in this chapter, four different sets of boundary conditions at the GDL/channel interface are provided by the 1D GTE fuel cell model in terms of flow rates and partial pressure for oxygen, nitrogen and water, respectively. The simulated results will be compared with results from the 1D fuel cell model for validation.

6.2.1. Single Phase Multicomponent LB model

The LBM for SPSC modeling was used to simulate a single gas transport within the GDL. In order to apply the LBM in fuel cell context, multicomponent of LB model is necessary. In the literature, there are few studies of multicomponent transport using LBM. Arcidiacono *et al*²⁰⁸ proposed a simulation study on multicomponent mixture by LBM which gives an extension application on planar opposite jets and planar micro-couette flow. In the work of Joshi *et al*²⁰⁹, multicomponent transport in a solid oxide fuel cell (SOFC) anode using a two-dimensional LBM was presented to investigate the porous geometry influence on porosity, fuel delivery as well as water removal. In the work of Chiu *et al*²¹⁰, they extended the previous work²⁰⁸ of three components to five species to study the mass transfer through the porous anode of SOFC. These literatures provided simulation study of multicomponent transport; however, with their focuses on SOFC. In the study presented in this chapter, the LB model for binary mixture proposed by Luo *and Girimaya*²¹¹ is adopted and modified to simulate three components flow. The theory and key equations of the LBM has been introduced in Chapter 4. D3Q19 scheme for the LB method is illustrated in Figure 3.1.

In the three component system, the particles movement include both self-collision and cross-collision which is different from single component system where only self-collision is involved. The LB Equation [3.2] can be modified for multicomponent as²¹²:

$$f_k^i(x + \xi_k^i \delta t, t + \delta t) = f_k^i(x, t) + Q_k^{ii}(x, t) + \sum_{j \neq i} Q_k^{ij}(x, t) \quad [6.1]$$

where $f_k^i(x, t)$ represents the particles velocity distribution function along the k th direction in velocity ξ_k^i . Term $Q_k^{ij}(x, t)$ represents the cross-collision which is the

collision between particles of specie i and of specie j . $Q_k^{ii}(x,t)$ means self-collision of species i , ($i, j=1,2,3$).

For species i at location x and at time t , the density ρ_i is calculated by

$$\rho_i(x,t) = \sum_k f_k^i(x,t), \quad [6.2]$$

And the velocity u_i by

$$\rho_i u_i(x,t) = \sum_k f_k^i(x,t) \xi_k^i \quad [6.3]$$

Hence, the total mass density and the average bulk velocity of the system can be obtained:

$$\rho(x,t) = \sum_i \rho_i(x,t) \quad [6.4]$$

$$\rho(x,t)u(x,t) = \sum_i \rho_i(x,t)u_i(x,t) \quad [6.5]$$

The single relaxation time approximation is used to describe the self-collision term followed by the work of Luo *et al*²¹⁰:

$$Q_k^{ii}(x,t) = \frac{1}{\tau_i} [f_k^{i[0]}(x,t) - f_k^i(x,t)] \quad [6.6]$$

Where τ_i is the dimensionless relaxation time parameter which is related to the viscosity of species i . $f_k^{i[0]}(x,t)$ is the equilibrium distribution function.

The corss-collision between species i and species j is calculated by:

$$Q_k^{ij}(x,t) = \frac{1}{\tau_{ij}} \frac{\rho_i}{\rho} \frac{f_k^{i[eq]}}{\delta t \cdot c_i^2} (\xi_k^i - u)(u_i - u_j) \quad [6.7]$$

Where τ_{ij} is the dimensionless relaxation parameter for cross-collision of species i and j , ($i, j=1,2,3$). c_i is the lattice sound speed of species i . The term $f_k^{i[eq]}(x,t)$ in Equation [6.7] is the equilibrium distribution function. The values of $f_k^{i[0]}(x,t)$ and $f_k^{i[eq]}(x,t)$ is defined by:

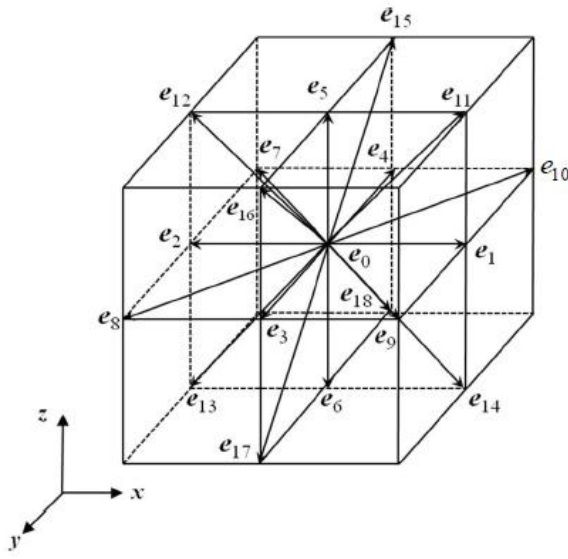
$$f_k^{i[0]}(x,t) = \left[1 - \frac{(\xi_k^i - u)(u_i - u)}{c_i^2} \right] f_k^{i[eq]}(x,t) \quad [6.8]$$

$$f_k^{i[eq]}(x,t) = w_k \rho_i \left[1 + \frac{\xi_k^i \cdot u}{c_i^2} + \frac{(\xi_k^i \cdot u)^2}{2c_i^4} + \frac{u \cdot u}{2c_i^2} \right] \quad [6.9]$$

where w_k is the weight factor. $w_k = \frac{1}{3}$ for $k=0$; $w_k = \frac{1}{18}$ for $k=1\sim6$ and $w_k = \frac{1}{36}$ for $k=7\sim18$.

Since different species have different weights, their corresponding velocities are different. If M_1, M_3 , and M_2 are designated as the molecular weights of species 1, species 3, and species 2, and they are assumed to have the lightest, heaviest and the medium weights, respectively. Term ξ_k^1 represents the velocity of species 1 along k th direction.

In the D3Q19 lattice scheme, it means that there are the nineteen velocities directions ($e_0 \sim e_{19}$):



$$\xi_0^1 = (0, 0, 0)$$

$$\xi_k^1 = (\pm\delta x / \delta t, 0, 0), k=1,2$$

$$\xi_k^1 = (0, \pm\delta x / \delta t, 0), k=3,4$$

$$\xi_k^1 = (0, 0, \pm\delta x / \delta t), k=5,6$$

$$\xi_k^1 = (\pm\delta x / \delta t, \pm\delta x / \delta t, 0), k=7\sim 10$$

$$\xi_k^1 = (\pm\delta x / \delta t, 0, \pm\delta x / \delta t), k=11\sim 14$$

$$\xi_k^1 = (\pm\delta x / \delta t, 0, \pm\delta x / \delta t), k=15\sim 18$$

where δx is the side length of the cubic voxels of the 3D image and δt is the time step.

The individual velocities of the particles of species 2, and of species 3 can be obtained by

$$\xi_k^2 = \sqrt{\frac{M_1}{M_2}} \xi_k^1 \quad \text{and} \quad \xi_k^3 = \sqrt{\frac{M_1}{M_3}} \xi_k^1, \text{ respectively}$$

The partial pressure is calculated by:

$$p_i = \rho_i \frac{\delta x^2}{3\delta t^2} \sqrt{\frac{M_1}{M_i}} \quad [6.10]$$

6.2.2. 1D General Transport Equation Based Fuel Cell Model

The one dimensional mathematical PEM fuel cell model is employed which was previously developed and validated based on General Transport Equation (GTE)²⁰⁶. The main GTE was derived from fundamental molecular theory and focus on the species transportation driven by: (a) concentration gradients; (b) pressure gradients; (c) temperature gradients and (d) an electric field, as described below in Equation [6.11]:

$$\begin{aligned}
c_i \left[\nabla \Phi_i + \bar{s}_i \nabla T - \frac{M_i}{\rho} \nabla p \right] - RT \dot{n}_{H^+} \frac{c_m}{c_T} \left(\frac{\xi_i}{D_{i,m}} - \frac{\rho_i}{\rho} \sum_{j \neq i, mem}^v \frac{\xi_j}{D_{j,m}} \right) \\
= RT \sum_j \frac{c_i c_j}{c_T D_{ij}} \left[v_j - v_i + \left(\frac{D_j^T}{\rho_j} - \frac{D_i^T}{\rho_i} \right) \nabla \ln T \right] \quad [6.11]
\end{aligned}$$

where c_i is the molar concentration, Φ_i is the electrochemical potential, \bar{s}_i is the molar entropy, \dot{n}_i is the molar flux rate, ξ_i is the electro-osmotic drag ratio, v_i is the molecular velocity and D_i^T is the thermal diffusion coefficient. For the current study, the effect of temperature gradients along the through-plane direction is negligible. Therefore in absence of term ∇T , Equation [6.11] becomes:

$$c_i \left[\nabla \mu_i - \frac{M_i}{\rho} \nabla p \right] - RT \dot{n}_{H^+} \frac{c_m}{c_T} \left(\frac{\xi_i}{D_{i,m}} - \frac{\rho_i}{\rho} \sum_{j \neq i, mem}^v \frac{\xi_j}{D_{j,m}} \right) = RT \sum_j \frac{c_i c_j}{c_T D_{ij}} [v_j - v_i] \quad [6.12]$$

Since the electro-osmotic drag does not exist in electrical neutral material of GDL, the second term on the left side of Equation [6.12] does not occur.

The pressure gradient ∇P_j of species j , through the GDL can be determined by Darcy's Law:

$$\nabla P_j = - \frac{\dot{n}_j \mu_j}{c_j k_j K} \quad [6.13]$$

where K is the absolute permeability and k_j is the relative permeability prefactor which accounts for liquid saturation, respectively. μ_j is phase viscosity.

6.2.3. X-ray Tomography imaging

The x-ray microtomography is used to generate the three-dimensional digital binary image of a carbon GDL. Before reconstructing the 3D digital image, the thresholding is carried out to tune the 2D grey scale image. The reference image taken by SEM is compared with that of the same surface image from the 3D model in terms of average

fiber diameter which are $7.5 \mu\text{m}$ and $7.9 \mu\text{m}$, respectively. The interested size for simulation of the carbon paper structure is shown in Figure 6.2. The size of the region is $78.3 \mu\text{m} \times 78.3 \mu\text{m}$ in x-y plane and $252.3 \mu\text{m}$ in through-plane z direction which corresponds to $45 \times 45 \times 145$ pixel size with resolution of $1.74 \mu\text{m}$

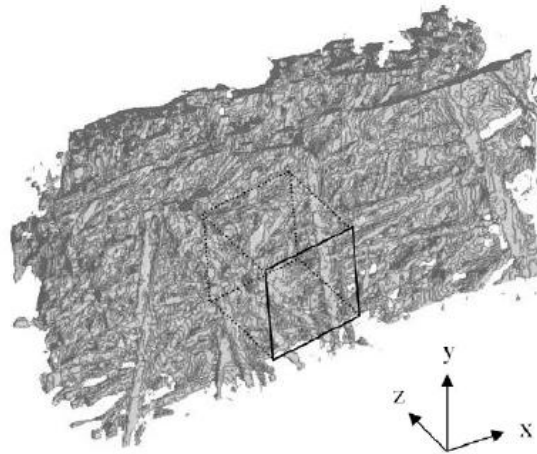


Figure 6.1 X-ray microtomography structure of the carbon paper GDL in size of $610.7 \mu\text{m} \times 252.3 \mu\text{m} \times 252.3 \mu\text{m}$. The interested simulation region is shown in size of $78.3 \mu\text{m} \times 78.3 \mu\text{m} \times 252.3 \mu\text{m}$, in x, y and z direction, respectively.

The tortuosity in the through-plane and the porosity of the reconstructed carbon paper can be calculated by the SPSC LB model and the values are 1.15 and 84%, respectively. These values can then be supplied to the 1D GTE fuel cell model. Figure 6.2 illustrates the tracks of the transporting gases through the GDL structure in size of $610.7 \times 252.3 \times 252.3 \mu\text{m}^3$ as shown in Figure 6.1. It can be seen that the flow streams do not transport in the straight lines following the main direction within the GDL. Some travel towards in-plane directions and some travel along paths that are full of twists and turns. This indicates that the porous carbon GDL structure has heterogeneity characteristic which enforces the gas flow transporting along tortuous paths rather than following the main direction.

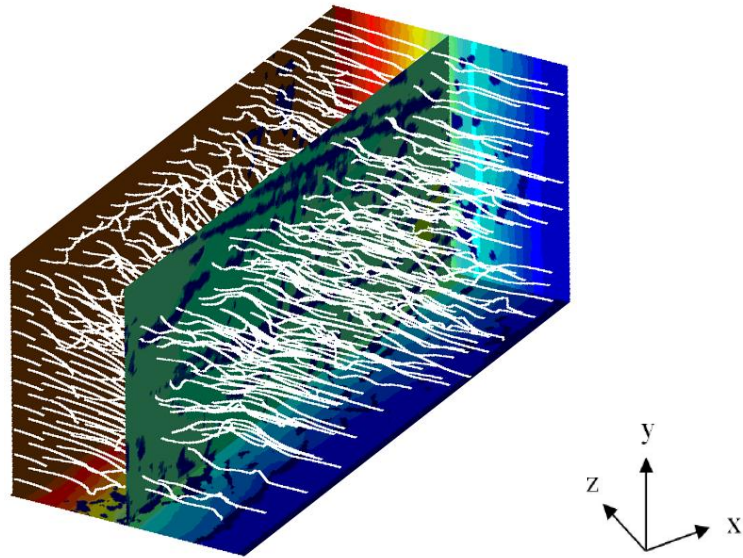


Figure 6.2 3D stream tubes of the reconstructed 3D digital image of carbon paper GDL in size of $610.7\mu\text{m} \times 252.3\mu\text{m} \times 252.3\mu\text{m}$, in x, y and z direction as shown in Figure 6.1

6.3. The Simulations

6.3.1. Interfacial Conditions

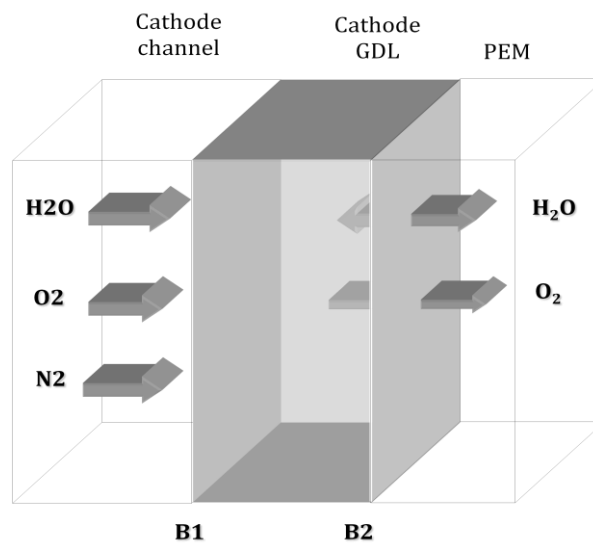


Figure 6.3 Simulation area of PEM fuel cell for SPMC LB model

Figure 6.3 shows the cathode side of the PEM fuel cell. The grey coloured area is the GDL. The GDL/channel interface B1 and GDL/catalyst layer interface B2 are the inlet and outlet boundaries for the LB model, respectively. The simulation was running on operation condition at 0.5 A/cm² current density.

GDL/Channel Interface B1

The partial pressure of each species at interface B1 is specified by the work proposed in previous chapter, and it is assumed that the partial pressures of each gas do not change with time.

GDL/Catalyst Layer Interface B2

At interface B2, the flow rates of each species are various. At GDL interface B2, the oxygen consumption rate can be obtained from the 1D GTE based numerical fuel cell model at given operating condition. As for the nitrogen, it is assumed that nitrogen is not allowed to pass through the GDL/catalyst layer interface which means that flow rate of nitrogen at B2 interface is considered zero and it is solved by the bounce-back method as discussed previously. Water vapour movement in the cathode GDL are from two sources: (a) water generated by the electrochemical reaction and (b) water that transports from anode side through the membrane. Therefore the water flow rate can be calculated by the 1D fuel cell model based on the operating current density as well as the net water flux ratio²⁰⁶.

In the SPMC LB model the flow rate of a species can be determined in terms of the particle distribution function of all three species (oxygen, water and nitrogen) in Equation [6.14]²¹⁰. This equation is accounted for the oxygen and water vapour at B2 interface where their respective flow rate are specified.

$$\mathbf{q}_i = \sum_{k=1}^{18} f_k^i \xi_k^i + \sum_{j \neq i} \frac{1}{2\rho\tau_{ij}} \left(\rho_i \sum_{k=1}^{18} f_k^j \xi_k^j - \rho_j \sum_{k=1}^{18} f_k^i \xi_k^i \right) \quad [6.14]$$

Substituting term $\sum_k^{18} f_k^i \xi_k^i$ by Equation[6.3], Equation[6.14] can be can be transformed and solve in terms of microscopic particles movement. This transformed

equation also reflects the Stefan-Maxwell equation which discusses the transport phenomena in a macroscopic level.

6.3.2. Simulation Scheme

The simulation scheme is shown in Figure 6.4.

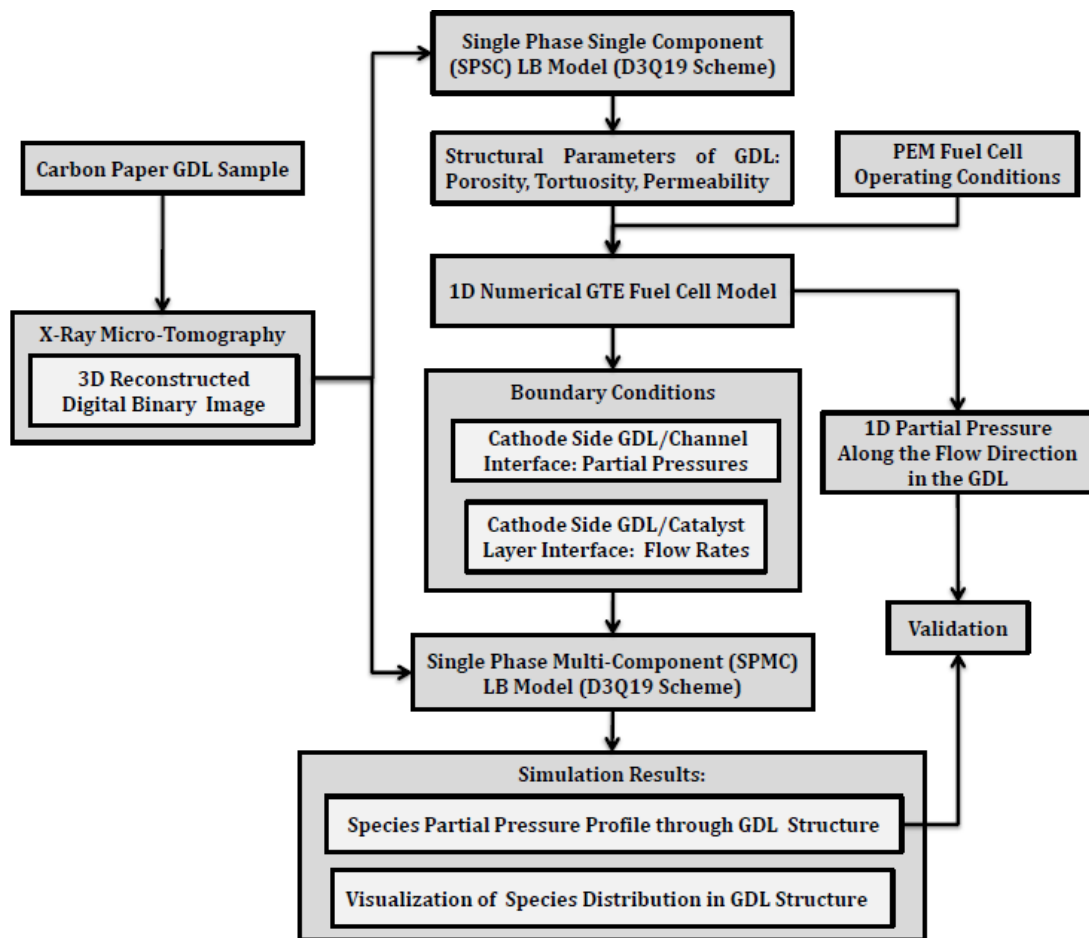


Figure 6.4 General modeling scheme of the multicomponent fluid transport through x-ray micro-tomography reconstructed 3D digital GDL structure

The multicomponent LB simulation was implemented on a quad-core computer of 2.33 GHz with 3.25 GB RAM size which is the same computational resource used in previous study. The accuracy of the simulation results of the LB model is subject to the

computational timesteps that the code is able to perform. It is known that enough timesteps are necessary for the LB simulation in order to reach the steady-state accuracy; however, this will require longer computational time to perform accordingly. Therefore a reasonable computational time range needs to be designed to ensure that the acceptable accuracy can be obtained without sacrificing too much computational time. In this simulation work, the overall computational timesteps allowance which is processed by the LB simulation is up to 350,000 timesteps. The total simulation time required for each of the four simulation conditions is around 120 hours. The convergence is estimated every 5000 timesteps and starts from the 10,000th timestep. The error $E_{i,n}$ of species i is defined by the timesteps n processed in Equation [6.15], and the error in a percentage form relative to the 5000th timestep is shown in Equation [6.16].

$$E_{i,n} = \int_0^1 P_i|_{LB,n} \cdot dx - \int_0^1 P_i|_{LB,n-5000} \cdot dx \quad [6.15]$$

$$E_{i,n} (\%) = \frac{E_{i,n}}{E_{i,10000}} \times 100\% \quad (n \leq 350,000) \quad [6.16]$$

The percentage error in terms of LB computational timesteps is illustrated in Figure 6.5 which presents the simulation of three gases in one of the four simulation conditions. The results show that the percentage error for water vapor converges quicker than that for nitrogen. After 300,000 timesteps, the percentage error of both water and oxygen fall below 5%, and both further decrease down less than 3% by 350,000 time steps. However, compared to water vapor and oxygen, the percentage error of nitrogen drops to only 12% at 300,000 timestep; and by 350,000 timesteps it reaches less than 7% which is relatively higher. The reason may be due to the partial pressure of nitrogen is higher than the partial pressures of water vapor and oxygen, more computational timesteps are required to converge to a desirable error. Overall, by 350,000 timesteps, the fluctuation of average partial pressure of each gas is within 1Pa, which is acceptable. Therefore it is safe to conclude that 350,000 computational timesteps for conducting the multicomponent LB simulation is adequate to generate accurate results; and more computational timesteps will not reduce the error further more.

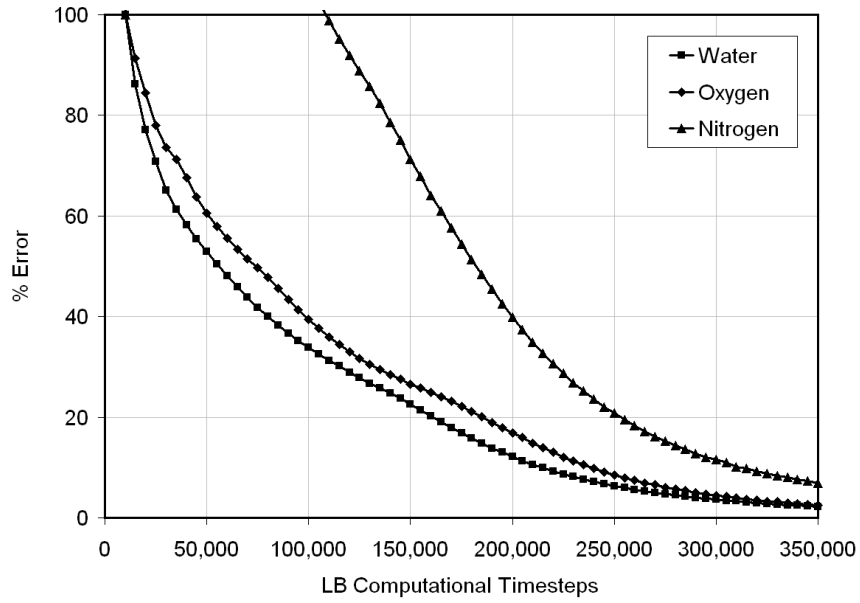


Figure 6.5 Convergence of SPMC Lattice Boltzmann simulations

6.4. Results and Validation

6.4.1. Boundary Conditions

The simulations were implemented at a fixed current density of 0.5 A/cm^2 . Table 6.1 gives the physical properties of the PEM fuel cell component layers and the operating conditions used in calculating the boundary conditions for the LB model.

Properties	Values
Physical Properties of thermodynamic	Operating Conditions
Cell temperature, °C	70.00
Cathode gas composition	21%/79% ~ O ₂ /N ₂
Cathode pressure, bar	1.00
Cathode dry gas flow rate, <i>slpm</i>	0.9
Anode gas composition	100% ~ H ₂
Anode pressure, bar	1.50
Anode dry gas flow rate, <i>slpm</i>	0.2
Physical Properties of Fuel Cell Component Layers	
Cell area, <i>cm</i> ²	5.00
PEM thickness, <i>μm</i>	25.40
PEM equivalent weight, <i>g/cm</i> ³	1100.00
PEM dry density, <i>g/cm</i> ³	2.00
GDL thickness, <i>μm</i>	252.3
GDL porosity	84 %
GDL tortuosity	1.14

Table 6.1 Physical Properties of PEM fuel cell component layers and thermodynamic operating conditions

There are four simulation cases generated by the 1D GTE fuel cell model in terms of humidification of the gases at anode and cathode inlets. They are (1) both anode and cathode are supplied with dry gases, A_DC_D; (2) both anode and cathode are humidified, A_WC_W; (3) Anode gases are humidified while keeps cathode gases dry, A_WC_D; and (4), Anode gases keeps dry and cathode gases are humidified, A_DC_W. The four cases are summarized in Table 6.2.

	RH at Anode	RH at Cathode
$A_D C_D$	0%, 70°C	0%, 70°C
$A_W C_W$	100%, 70°C	100%, 70°C
$A_W C_D$	100%, 70°C	0%, 70°C
$A_D C_W$	0%, 70°C	100%, 70°C

Table 6.2 Simulation cases for boundary conditions and cross-validation

For these four simulation cases, the boundary conditions of partial pressure and flow rate at cathode GDL/channel interface B1 and GDL/catalyst layer interface B2 are predicted by the 1D GTE fuel cell model and are shown in Figure 6.6 and Figure 6.7, respectively. As can be seen in Figure 6.6, the partial pressure of water vapor at B1 increases dramatically when cathode gases are humidified as in cases $A_W C_W$ and $A_D C_W$, compared to when the cathode is supplied with dry gases as in cases $A_D C_D$ and $A_C C_D$. This effect accordingly decreases the nitrogen partial pressure by 31.7% at $A_W C_W$ and 28.5% at $A_D C_W$, compared to $A_C C_D$ case.

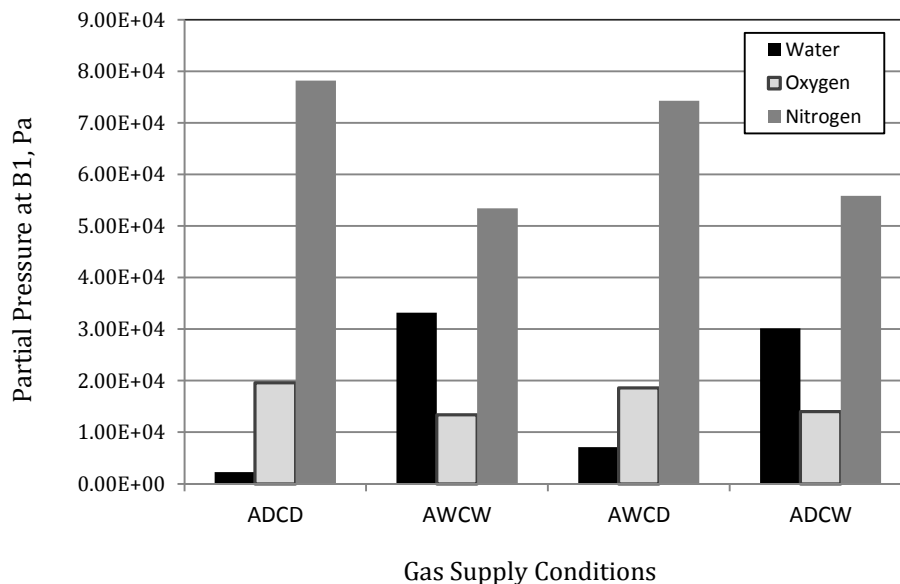


Figure 6.6 Simulated boundary condition of partial pressure at cathode GDL/channel interface B1 for the LB model by 1D fuel cell model

In Figure 6.7 it can be seen that when dry gases are supplied to the cathode as in $A_D C_D$ and $A_W C_D$ cases, the water flows in the direction from the cathode GDL/catalyst layer towards gas channel. This happens in the cases of either anode is supplied with dry gases or supplied with humidified gases. The reason is that the water at the catalyst layer/GDL interface is not enough to hydrate the cathode side membrane to let the gases to transport against the electro-osmotic drag; hence the water vapor travels back to the channel. When both gases at anode and cathode are humidified as in $A_W C_W$ case, however, the water vapor still moves out of cathode GDL towards the channel. This is again because of the strong electro-osmotic drag which dominates the transport of water, and forces the water out of GDL towards the gas channel side. If only cathode is supplied with humidified gases as in $A_D C_W$, the diffusive water flux dominates which enables water vapor transports through the cathode GDL.

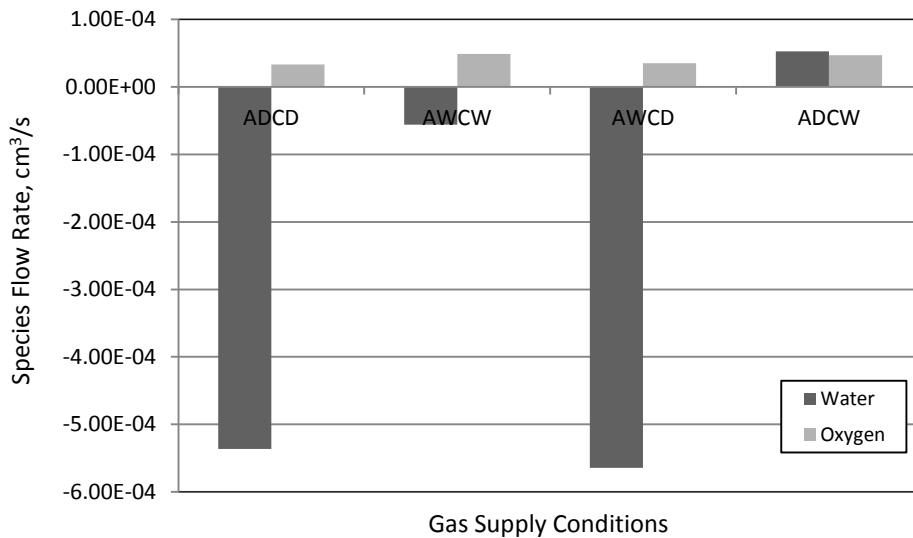


Figure 6.7 Simulated boundary condition of flow rate at GDL/catalyst layer interface B2 for the LB model by 1D fuel cell model

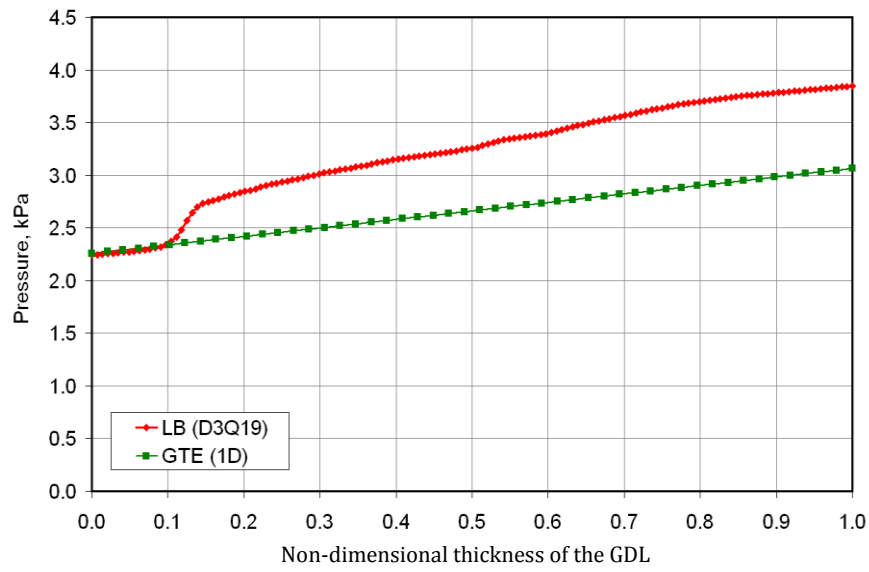
6.4.2. Prediction on 1D Partial Pressure Profile of Multi-species

Figure 6.8 ~ Figure 6.11 present the comparison of simulated one-dimensional partial pressure profiles of water vapor, oxygen and nitrogen across the thickness of the GDL by the LB model and 1D PEM fuel cell model under the above four simulation cases. The x axis represents the non-dimensional thickness of the GDL where 0.0 represents the position at channel/GDL interface B1 and 1.0 is the position at GDL/catalyst layer

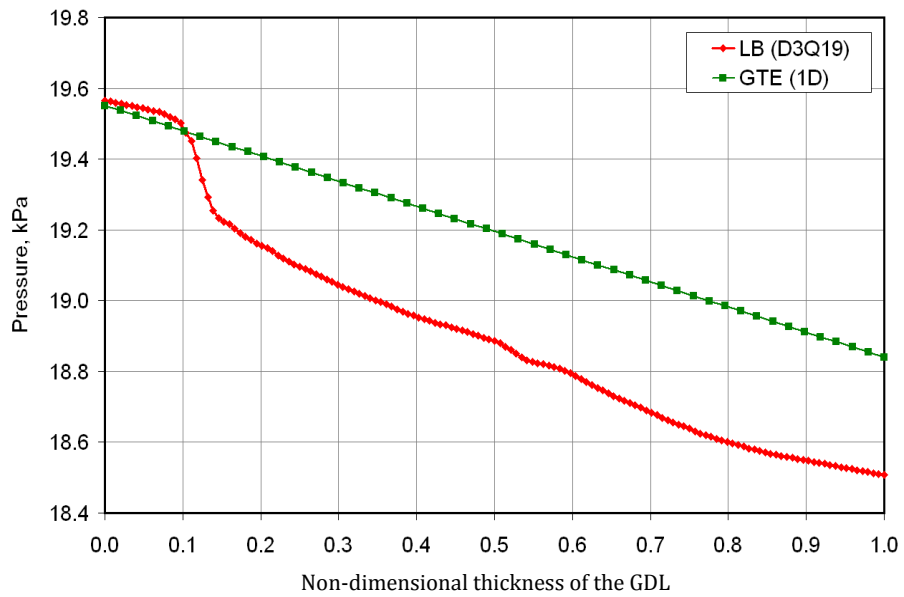
interface B2. Overall, the 1D pressure profile of all the species predicted by the LB model show good agreement with that calculated by the 1D PEM fuel cell model. The results obtained from the LB model show non-linearity compared to that of the 1D model.

For the $A_D C_D$ condition shown in Figure 6.8, the water vapor pressure has an increasing gradient from B1 channel/GDL interface towards B2 GDL/catalyst layer interface which is opposite to the water flux direction. The predicted total increasing of pressure by the LB model is 1.61 kPa and the 1D GTE fuel cell model shows a result of 0.81 kPa. Due to the oxygen reduction reaction at catalyst layer, the pressure of oxygen at B1 interface is higher than the pressure at B2 interface. The pressure drop from B1 to B2 predicted by LB model and GTE model are 1.06 kPa and 0.71 kPa, respectively. Nitrogen pressure decreases from B1 interface towards B2 in value of 1.31 kPa by LB model and by GTE model the value is 0.1 kPa.

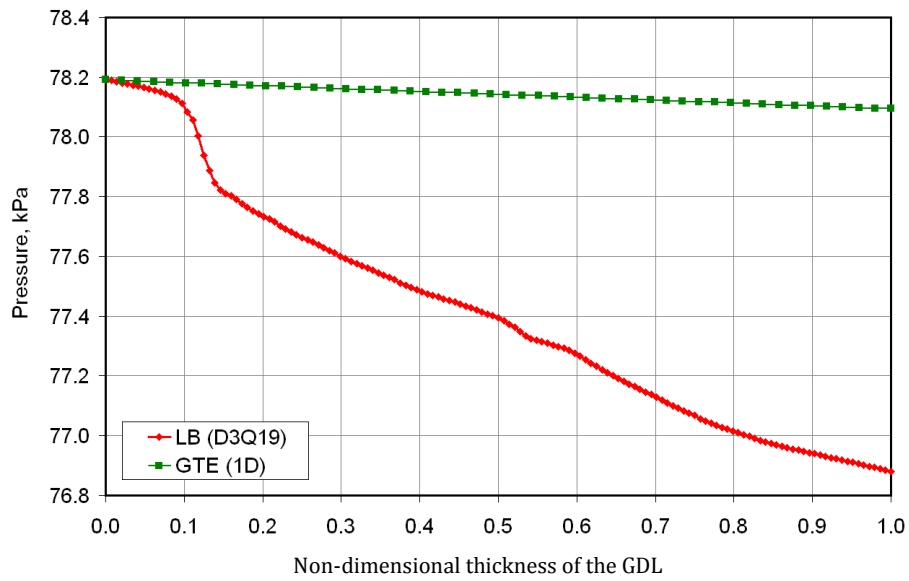
In addition, a noticeable small water pressure drop near interface B1 can be observed in Figure 6.8(a). It is known that the porous carbon paper has heterogeneous structure with randomly distributed pores, and the local structural feature varies from sample to sample. Therefore for this pressure drop, the reason might be because the selected GDL sample has special local feature close to the GDL surface near the channel side. The existence of large open pores enable the water flow transport through this preferential path hence causes the pressure drop. Similarly, the pressure appearance of oxygen and nitrogen near the channel side in other figures can be explained. Oxygen and nitrogen flow can transport easily through these large void space hence the gradient of the pressure near B1 interface is close to that of the 1D fuel cell model predicted.



(a) water



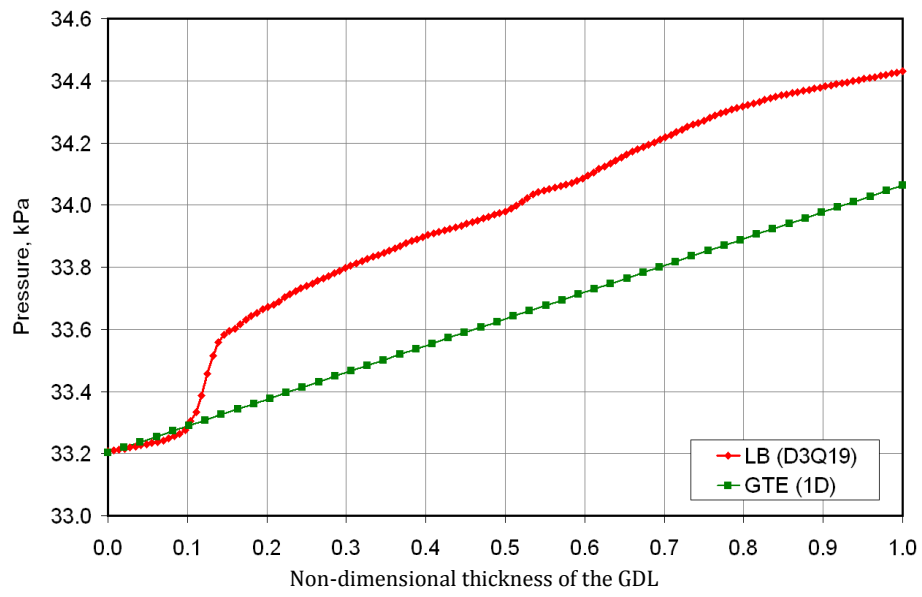
(b) Oxygen



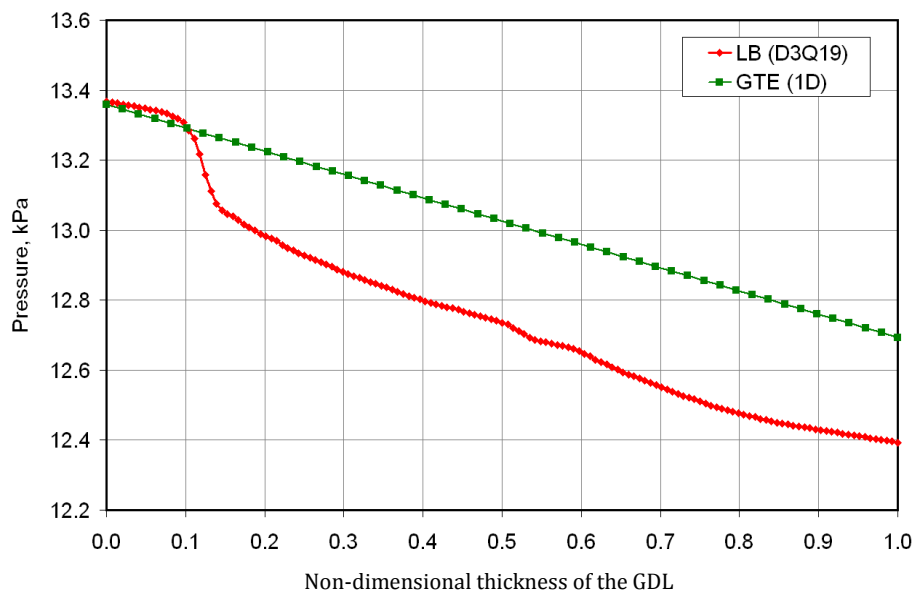
(c) Nitrogen

Figure 6.8 Comparison of LB model and 1D GTE fuel cell model predictions of gas partial pressure profile along the GDL flow direction at $A_D C_D$ condition; (a) water; (b) oxygen; (c) nitrogen

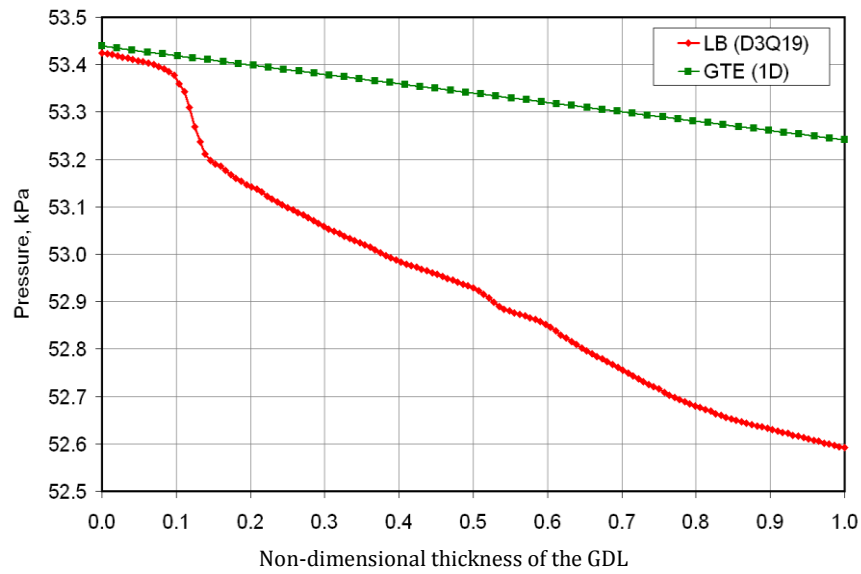
When both anode and cathode are supplied with humid gases as in $A_W C_W$ case, the water flows from GDL/catalyst layer interface B2 towards the channel which causes water pressure higher at GDL/catalyst layer interface B2, as shown Figure in 6.9(a). The pressure increasing is 1.22 kPa as predicted by LB model and by 1D GTE model the value is 0.87 kPa. Both oxygen and nitrogen pressure decreases towards B2 interface by 0.96 kPa and 0.83 kPa, respectively.



(a) water



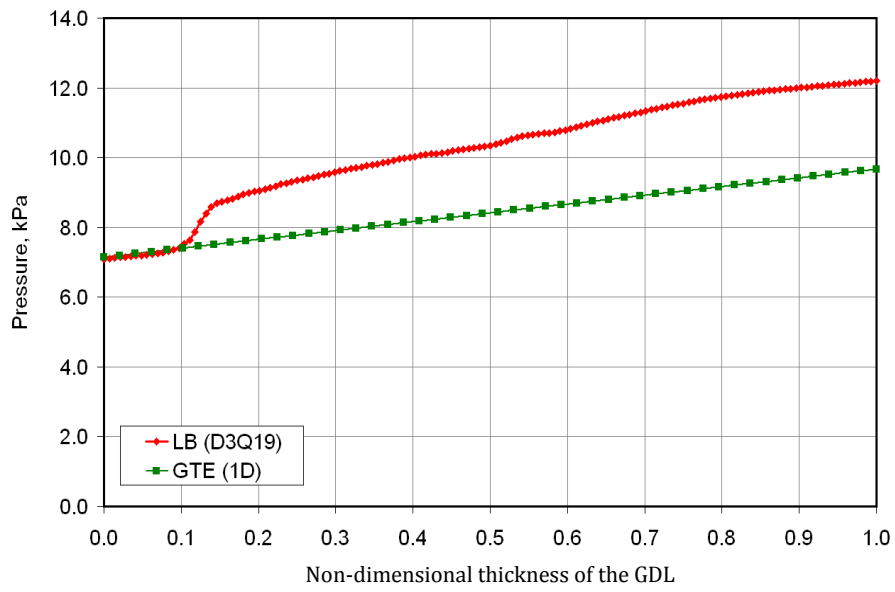
(b) Oxygen



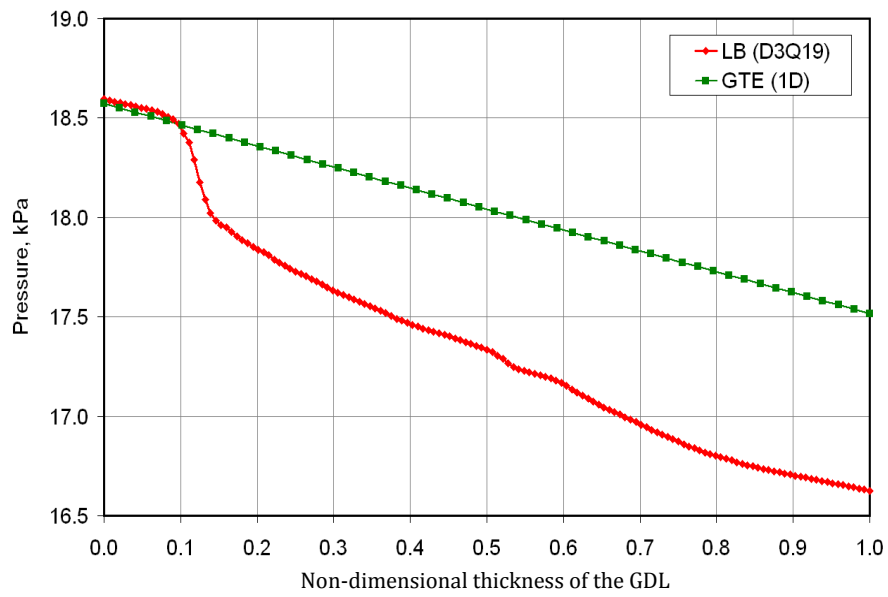
(c) Nitrogen

Figure 6.9 Comparison of LB model and 1D GTE fuel cell model predictions of gas partial pressure profile along the GDL flow direction at A_wC_w condition; (a) water; (b) oxygen; (c) nitrogen

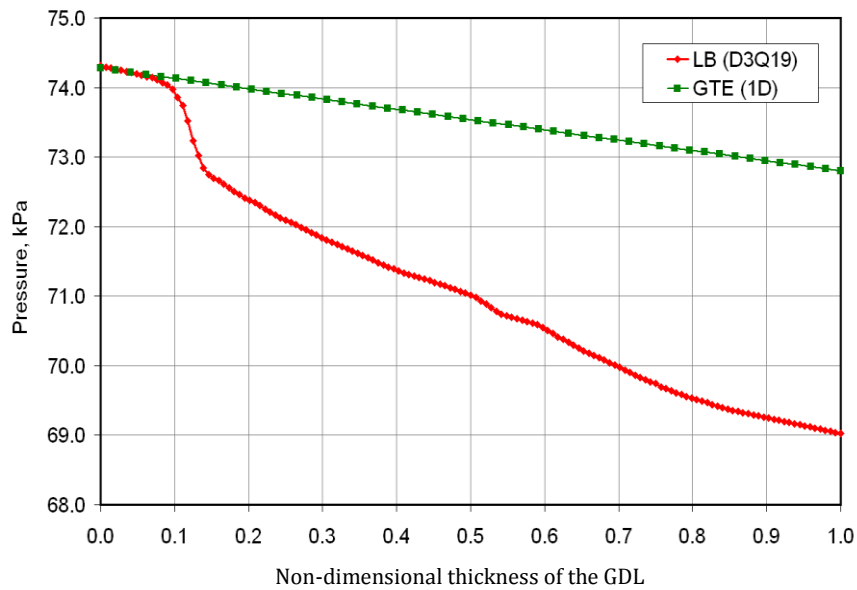
Figure 6.10 shows the results of simulation condition when anode is supplied with wet gases and cathode with dry gases as in case A_wC_d . Since the water travels from catalyst layer side of the GDL towards the channel side, this results in water pressure increasing from the channel/GDL interface B1 towards the GDL/catalyst layer interface B2. The LB method prediction of pressure rise is 5.10 kPa from B1 and B2, and GTE model suggests a result of 2.50 kPa. Due to the consumption of oxygen at cathode catalyst layer, the pressure drop across the GDL from channel side to the catalyst side predicted by LB model and GTE mode are 1.97 kPa and 1.06 kPa, respectively. Also nitrogen pressure decreases by 5.29 kPa according to the LB model and 1.48 kPa according to the 1D GTE model.



(a) water



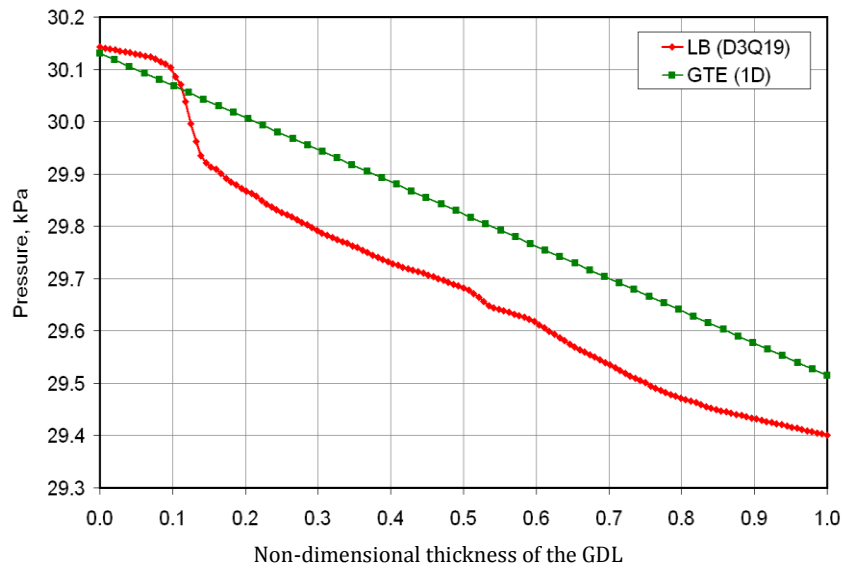
(b) Oxygen



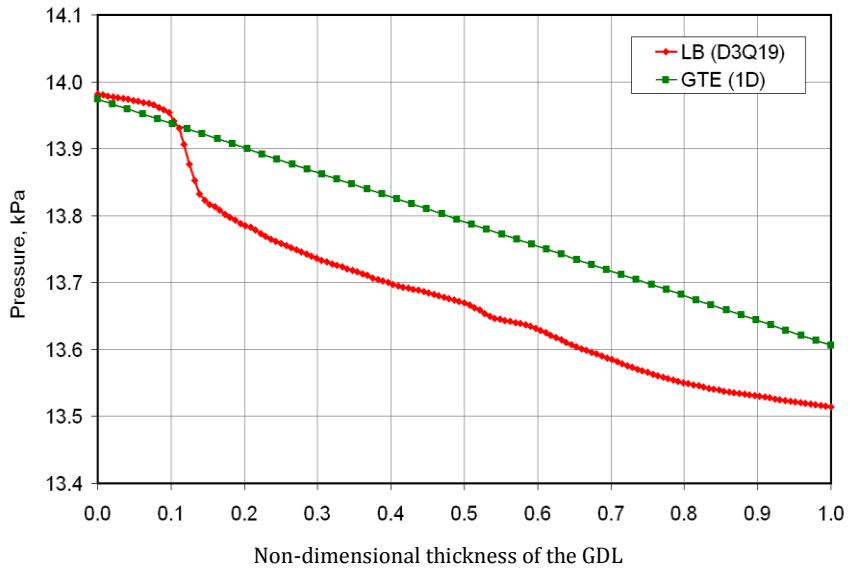
(c) Nitrogen

Figure 6.10 Comparison of LB model and 1D GTE fuel cell model predictions of gas partial pressure profile along the GDL flow direction at $A_W C_D$ condition; (a) water; (b) oxygen; (c) nitrogen

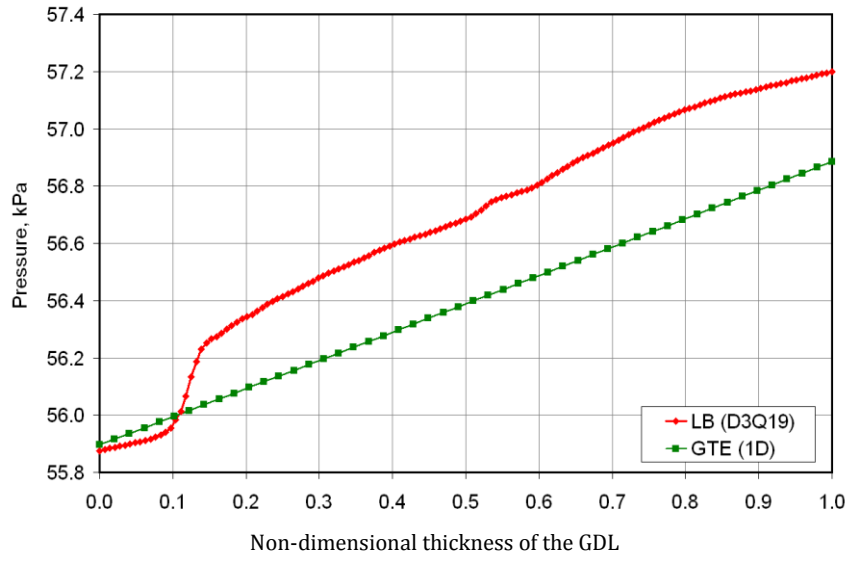
Figure 6.11 shows the results when humidified gases are supplied to cathode and anode is supplied with dry gases as in $A_D C_W$ condition. In this case, the water flows through cathode GDL towards GDL/catalyst layer interface B2; therefore the water pressure increases in the reverse direction from GDL/catalyst layer interface B2 towards channel side. The pressure rise predicted by the LB model is 0.74 kPa, which agrees well with the value calculated by GTE mode of 0.61 kPa. Since oxygen travels through the cathode GDL to the catalyst layer, the predicted pressure drop LB method and 1D GTE model are 0.47 kPa and 0.37 kPa, respectively. Nitrogen partial pressure rises towards the GDL/catalyst interface B2 is due to the decreasing of both water vapor and oxygen partial pressure towards the B2 interface. The LB model calculated rise is 1.32 kPa and by GTE model is 0.99 kPa.



(a) water



(b) Oxygen



(c) Nitrogen

Figure 6.11 Comparison of LB model and 1D GTE fuel cell model predictions of gas partial pressure profile along the GDL flow direction at $A_D C_W$ condition; (a) water; (b) oxygen; (c) nitrogen

Results presented in Figure 6.8~6.11 show that the multicomponent LB model is able to correctly predict the partial pressure of three different gases across the GDL thickness under four boundary conditions, by comparison with the same results obtained from previously validated GTE based 1D PEM fuel cell Model. Since the LB model calculates the results through collisions between particles in a real porous geometry reconstructed by the x-ray tomography, on one hand the results indicate the heterogeneous properties of the porous structure of the carbon paper GDL; and on the other hand it reveals that the actual species distribution through the GDL will be subject to the actual structural properties of the material. In summary, the percentage pressure differences of average partial pressure of each species by the LB method and the GTE model for the four simulation conditions can be calculated using Equation [6.16], and are summarized in Table 6.3. It can be seen that the maximum percentage difference between the two models is only 2.4% and the lowest one is 0.1% according to the total pressure in the GDL. This indicates the capability of the SPMC LB model of accurately predicting the partial pressure of the multispecies.

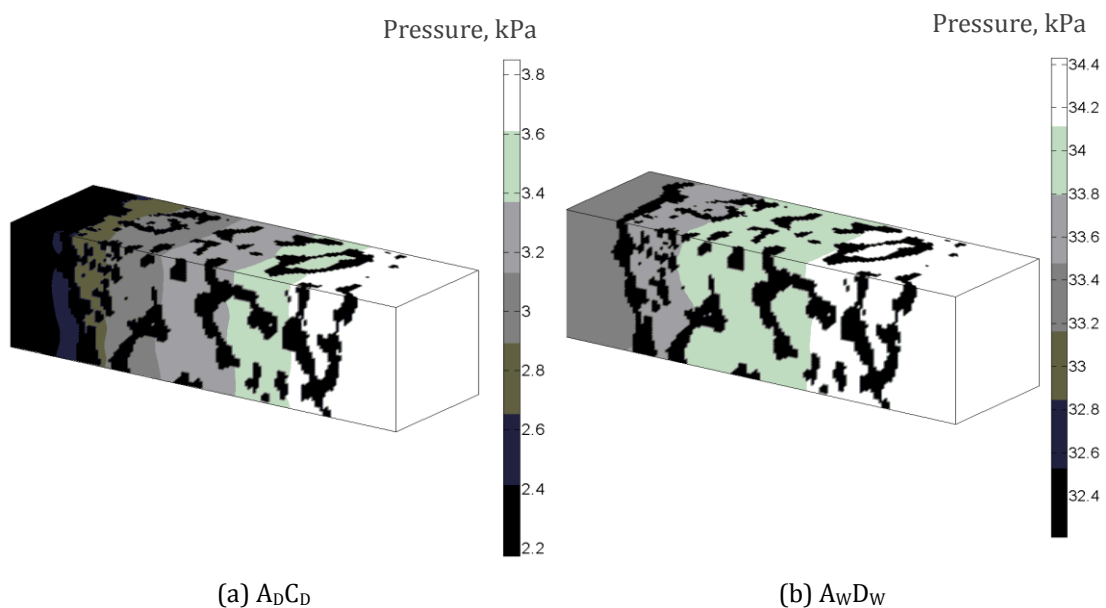
$$\Gamma_i = \left\{ \frac{\int_0^1 P_i|_{GTE} \cdot dx - \int_0^1 P_i|_{LB} \cdot dx}{P_{tot}} \right\} \times 100\% \quad [6.16]$$

	$A_D C_D$	$A_W C_W$	$A_W C_D$	$A_D C_W$
Water	-0.6%	-0.3%	-1.8%	0.1%
Oxygen	0.3%	0.3%	0.7%	0.1%
Nitrogen	0.7%	0.4%	2.4%	-0.3%

Table 6.3 Percentage difference on partial pressure for water, oxygen and nitrogen between LB model and GTE model

6.4.3. Three-dimensional Visualizations

Figure 6.12 (a)~(d) illustrate the three-dimensional visualization of predicted water vapor partial pressure distribution through the reconstructed 3D carbon paper GDL structure under four simulation conditions. The left ends of the 3D images represent the channel/GDL side and the right ends of the images represent the GDL/catalyst layer side. The color bar shows the range of pressure values where pressure value increases towards lighter color range and decreases towards darker color range. Again the results show the same trends as shown in Figure 6.11 all (a) figures. It can be seen that the water partial pressure within the GDL is not uniformly distributed along its gradient, which indicates the heterogeneous interior of the porous GDL structure.



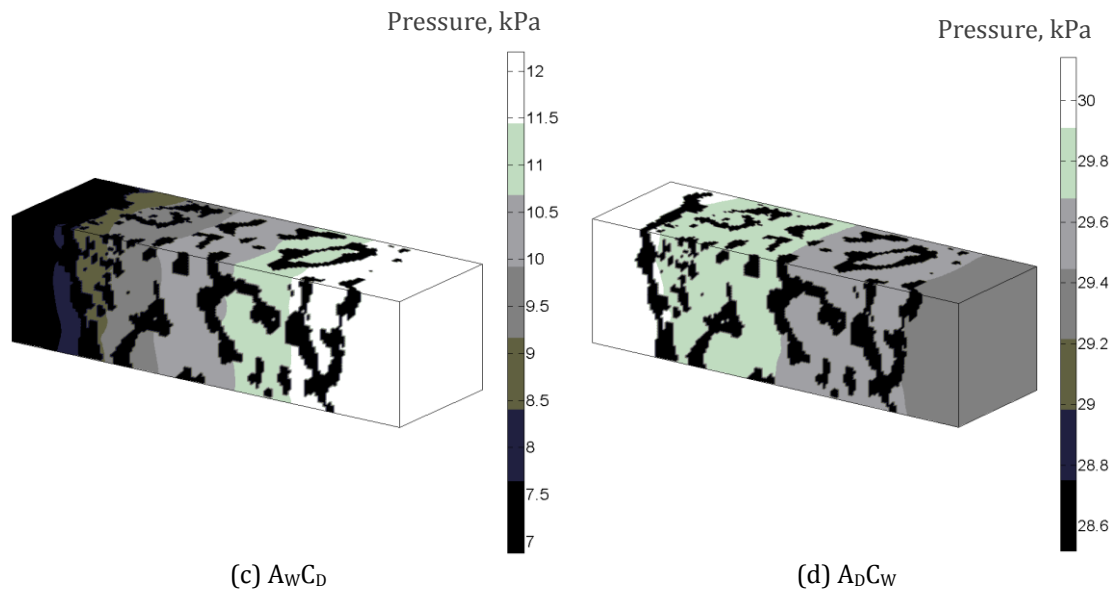


Figure 6.12 3D visualization of water pressure distribution in the carbon paper GDL volume in size of $78.3\mu\text{m} \times 78.3\mu\text{m} \times 252.3\mu\text{m}$ simulated by SPMC LB model, (a) $A_D C_D$; (b) $A_W C_W$; (c) $A_W C_D$ (d) $A_D C_W$

6.5. Conclusions

A SPMC LB simulation on multi-species partial pressure distribution through a carbon paper GDL structure is carried out at four boundary conditions. The results have been validated by the general transport equation based 1D numerical PEM fuel cell model. The conclusions are that:

<1>.The SPMC LB model has been presented to simulate the multicomponent transportation through the 3D digital image of the carbon paper GDL, which is reconstructed by the x-ray microtomography technique. The reconstructed carbon paper image for the simulation is in size of $78.3 \times 78.3 \times 252.3 \mu\text{m}^3$.

<2>. The boundary conditions at cathode GDL/channel and cathode GDL/catalyst layer are specified by a previously validated GTE based 1D PEM fuel cell model. The boundary conditions are calculated at 0.5 A/cm^2 current density with four different gas supplement conditions in terms of gas humidification level, which are (1) both anode and cathode are supplied with dry gases, $A_D C_D$; (2) both anode and cathode are supplied with humidified gases, $A_W C_W$; (3) anode gases are humidified and cathode are supplied

with dry gases, $A_W C_D$ and (4) anode and cathode are supplied with dry gases and humidified gases, respectively, $A_D C_W$.

<3>. The convergence estimation is carried out to judge the computational timestep range to ensure that the accurate results can be obtained within the reasonable timestep. The results show that by 350,000 timesteps, the percentage error of both water vapor and oxygen reduce to lower than 3% and that of nitrogen is below 7%. The fluctuation of the pressures is around 1Pa. This results indicates that 350,000 timesteps is sufficient for the LB simulation with a GDL structure volume of $78.3 \times 78.3 \times 252.3 \mu m^3$ which equivalences to about 120 hours simulation time.

<4>. The results of the partial pressure of water vapor, oxygen and nitrogen are predicted by the LB model and validated by comparing the results with that of the 1D GTE model. The results show good agreement. At $A_D C_D$, $A_W C_W$ and $A_W C_D$ conditions, the water partial pressure shows decreasing from catalyst side of GDL down to the channel side of the GDL, while at $A_D C_W$ condition the pressure gradient decreases from channel side to catalyst layer side of the GDL. The non-linearity of the pressure profiles of all the gases predicted by the LB model indicates the heterogeneity of the porous GDL structure, since the LB simulation is performed by tracking the collisions between particles and with the walls.

CHAPTER 7. Simulation Studies on Carbon Cloth Gas Diffusion Layer

7.1. Introduction

The GDL plays an important role as a bridge in between the gas channel and the catalyst layer. It is usually made of carbon fiber paper or woven carbon cloth. Many literatures^{213,214,215} have demonstrated their works on carbon paper GDLs by using LBM; however, few has been reported on carbon cloth. Park and Li²¹⁶ studied the carbon cloth GDL using LBM. By modeling the GDL as a void space and porous region, they investigated the fiber tow orientation influence on the effective permeability. In the work of Pharoal *et al*⁸⁵, the through-plane and in-plane permeabilities are calculated using the LBM. They reported that the anisotropic geometry caused by the fiber alignment has important influence on the permeability.

Previously, the studies on a carbon paper GDL are carried out by combine the single phase LB model with the x-ray tomography technique to investigate the microscopic properties of the material. In this study, the same technique continuously contributes the simulation work on a woven carbon cloth GDL. The SPSC LB model is used to simulate the permeability in through-plane direction as well as two in-plane directions. The through-plane direction is the main flow direction along which the gas is supplied. X-ray tomography technique processes the carbon cloth structure and reconstructed it into a readable 3D digital structure for the LB model. The results report the degree of anisotropy which is validated by the values obtained from the experiments.

7.2. Methodology

The single phase LB model has been proved to be able to generate reliable results by tracking particles distribution in the lattice structure. The LB model with D3Q19 scheme is presented to simulate the gas phase flow through a carbon cloth. The LB method basically deals with particle movements and the distribution function describes the particle distribution after the collisions. The key equation of LB method are as shown in Equation [3.6] ~ [3.11] in Chapter 3. In the LB mode, a pressure gradient is imposed to the two side of the structure to drive the flow along the through-plane direction, which is the main direction. The boundary condition at solid/void interface is treated as non-slip boundary where the velocity of gas is restrained to zero. The bounce-back method is used to solve this solid/void boundary by assuming that particles that collide with a solid wall will simply bounced back to where it comes. The detailed equations of LB model can be found in previous chapter.

In order to feed the LB model with an acceptable structure, the x-ray tomography is used to reconstruct a three-dimensional digital binary image of the carbon cloth structure. The standard process of generating the image involves: (a) 2D shadow image acquisition; (b) image processing by thresholding and (c) three-dimensional reconstruction. The equipment of the x-ray tomography system as well as the imaging methodology was introduced previously in Chapter 4. The average fiber diameter of the carbon cloth employed in this study is $7.8 \mu\text{m}$ by measuring from the SEM reference image and value from the same surface of the reconstructed 3D digital image is $8 \mu\text{m}$. So the error in the average fiber diameter of the image tuned by the thresholding is 2.6%.

Due to the large size of the carbon cloth sample, it is difficult to implement the simulation by LB method which is limited by the computational resource; the reconstructed image is therefore split into 21 regions. The resolution is $1.74 \mu\text{m}$ which is determined by the object diameter and the camera pixel size of the x-ray tomography system. The size of each region is $442 \times 442 \times 223 \mu\text{m}^3$ corresponding to x, y, and z direction, respectively; therefore the size of the overall 3D image is $1326 \times 442 \times 1561 \mu\text{m}^3$. The porosity of this carbon cloth is found more than 80%. The overall 3D image of the interested carbon cloth is illustrated in Figure 7.1.

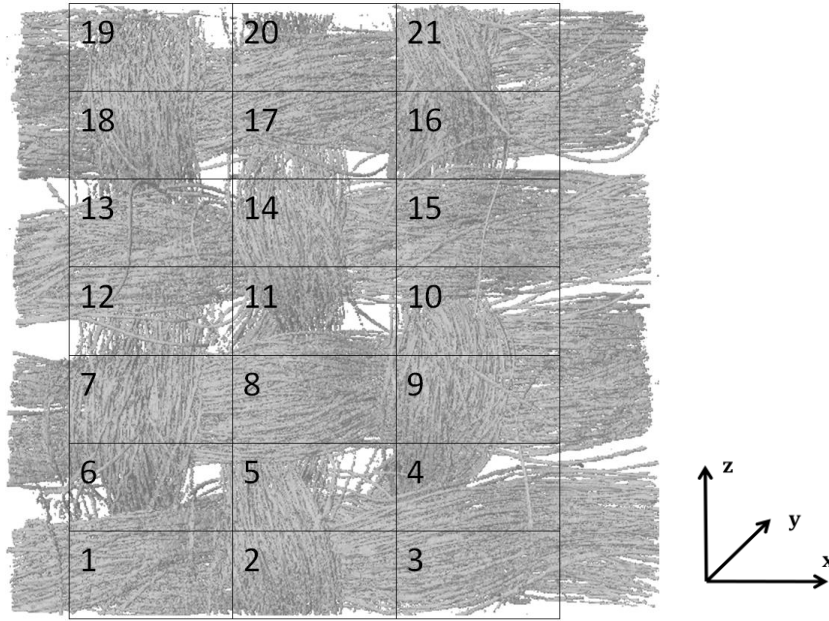


Figure 7.1 The 3D image of a 1326(x) x 442(y) x 1561(z) μm^3 carbon cloth GDL with 21 divided regions in equal size of 442(x) x 442(y) x 223(z) μm^3 .

7.3. Simulated Permeability

7.3.1. Results and Validation

Despite the gas flows in the main direction along which the pressure gradient is applied, gas can also flow in the in-plane direction. The permeability of a GDL can be calculated

from Darcy's law $k = \frac{\rho\mu q}{(\Delta P/L)}$. By applying a pressure gradient to the structure in

different direction, the three components of the permeability tensor in each direction can be calculated. For example, when the pressure is imposed in the x direction, the

three components of the permeability tensor are: $k_{xx} = \frac{\rho\mu q_x}{(\Delta P/L_x)}$, $k_{xy} = \frac{\rho\mu q_y}{(\Delta P/L_y)}$,

$k_{xz} = \frac{\rho\mu q_z}{(\Delta P/L_z)}$. The permeability tensors in the other two directions can be obtained

similarly and were introduced in section 5.3.1.

The experimental value for the permeability is carried out with a Texas Instrument FX 3300 at room temperature using a sample carbon cloth taken from the same batch which is used for the x-ray tomography imaging. The carbon cloth does not contain a

MPL. The measured through-plane volumetric flow rate is applied to the permeability calculation equation above to obtain the corresponding permeability tensor.

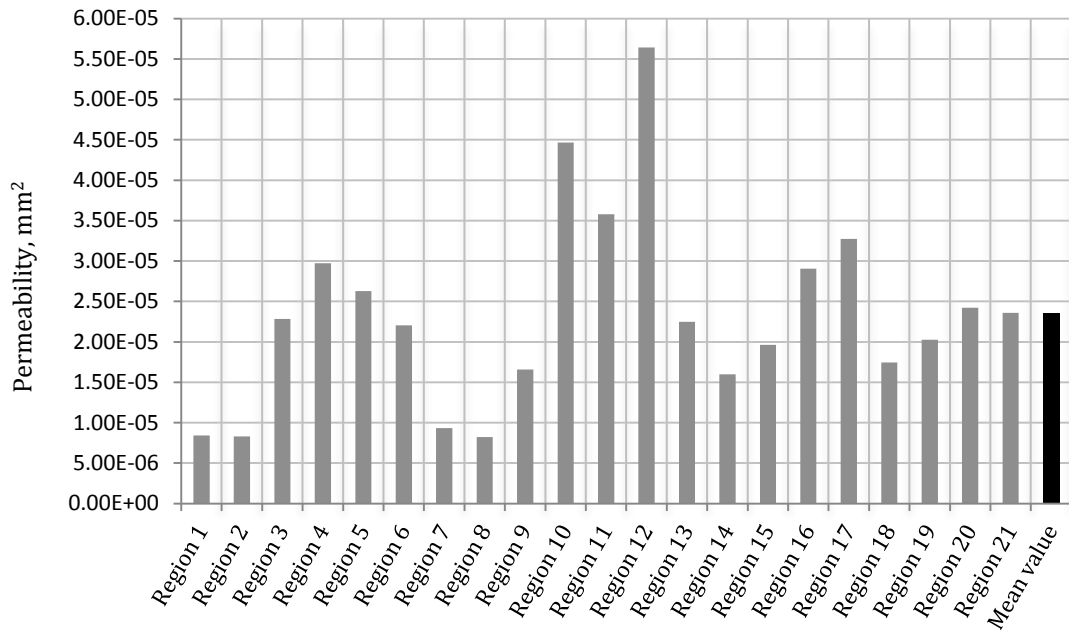
Table 7.1 shows the average calculated permeability of through-plane y direction as well as in-plane x - and z -directions of the whole carbon cloth GDL. Overall, the calculated average permeability for the through-plane direction is $2.35 \times 10^{-5} \text{ mm}^2$, while the in-plane average permeabilities of the x - direction and the z -direction are $5.3 \times 10^{-6} \text{ mm}^2$ and $6.5 \times 10^{-6} \text{ mm}^2$, respectively. Both two in-plane permeabilities are one order of magnitude smaller than that for the through-plane.

	<i>k, mm²</i>
Through-plane y direction	2.35×10^{-5}
In-plane x direction	0.53×10^{-5}
In-plane z direction	0.65×10^{-5}

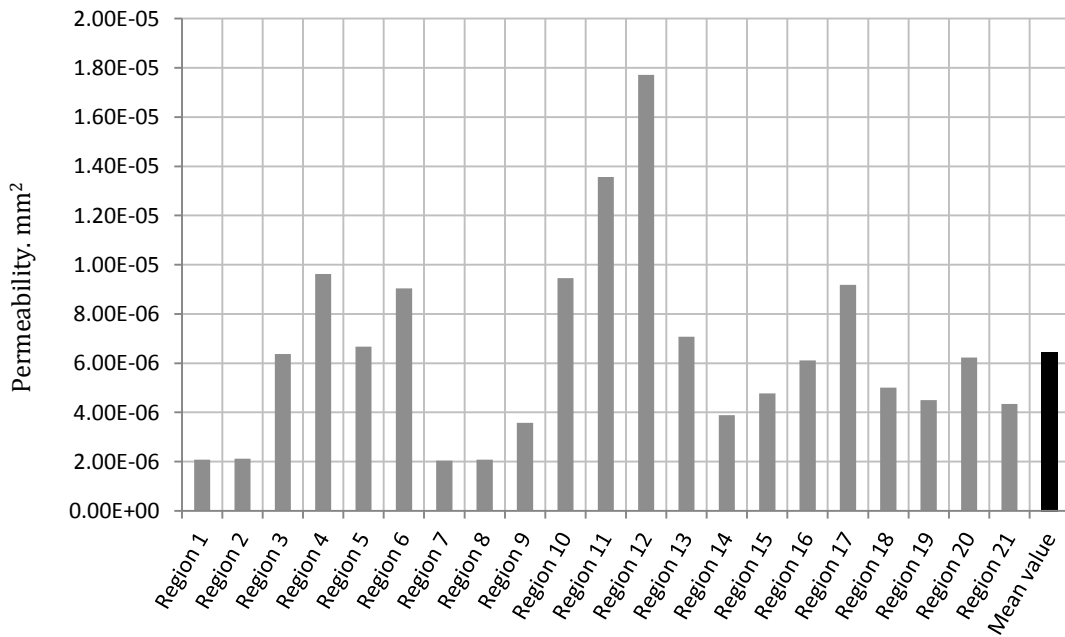
Table 7.1 Average permeability of through-plane and in-plane of the whole GDL sample.

Figure 7.2 illustrated simulated absolute permeabilities of total 21 regions of the carbon cloth GDL in main through-plane y direction and in-plane x - and z - directions. The pressure gradient is along the through-plane y direction. The calculated average through-plane permeability is $2.35 \times 10^{-5} \text{ mm}^2$ and the standard deviation of the through-plane permeability is $1.21 \times 10^{-5} \text{ mm}^2$. It can be seen that among all 21 regions, region 12 exhibits the highest through-plane permeability of $5.64 \times 10^{-5} \text{ mm}^2$. In comparison, region 8 has the lowest through-plane permeability of $0.82 \times 10^{-5} \text{ mm}^2$. For in-plane x -direction, region 12 still shows the highest in-plane permeability of $1.33 \times 10^{-5} \text{ mm}^2$. The lowest in-plane permeability in x -direction is found in region 7 with the value of $0.15 \times 10^{-5} \text{ mm}^2$. The mean value of the in-plane permeability in the x -direction is $5.3 \times 10^{-6} \text{ mm}^2$ and the standard deviation is $0.40 \times 10^{-6} \text{ mm}^2$. Region 12 and region 7 have also been found having the highest and lowest in-plane permeabilities in the z -direction, and the values are $1.77 \times 10^{-6} \text{ mm}^2$ and $0.20 \times 10^{-6} \text{ mm}^2$, respectively. The standard deviation of in-plane permeability in the z -direction is $0.32 \times 10^{-6} \text{ mm}^2$ and the mean value is $0.65 \times 10^{-6} \text{ mm}^2$. It is observed that even though these 21 individual regions are divided from the same one carbon cloth GDL, the calculated absolute

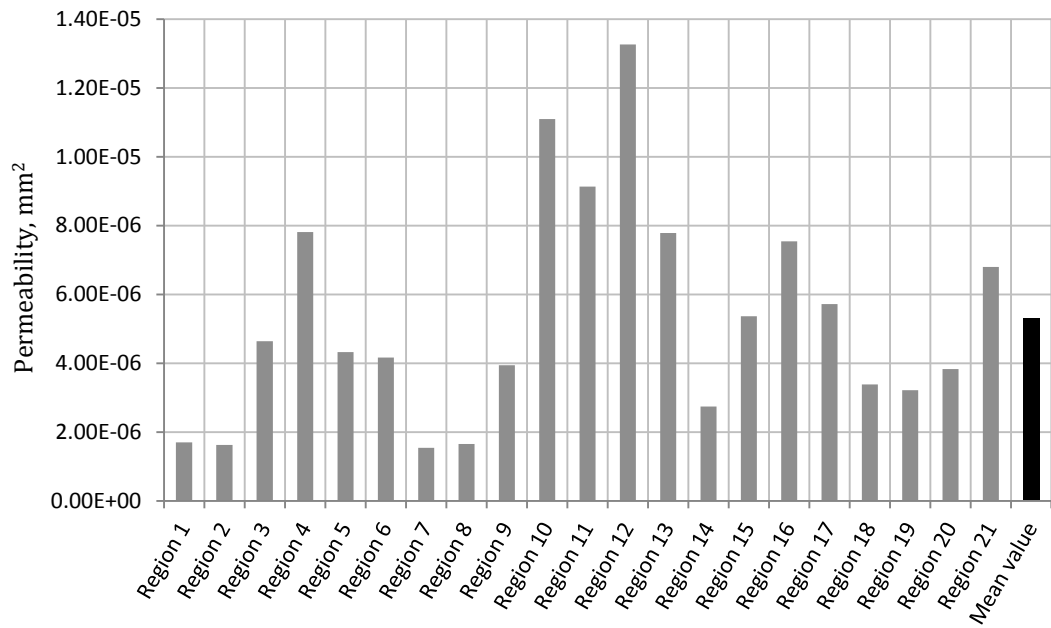
permeability in all three directions for all 21 regions shows variations which indicates the heterogeneous feature of the porous carbon cloth GDL structure.



(a) through-plane y direction



(b) in-plane x direction



(c) in-plane z direction

Figure 7.2 Calculated absolute permeability of total 21 regions of the carbon cloth GDL by LB mode of (a) through-plane y direction; (b) in-plane x direction and (c) in-plane z direction

In order to understand the variations on permeability of all 21 regions in terms of structural characteristics, the three-dimensional structures of three representative regions are inspected and shown in Figure 7.3. The three regions are shown in rotated 3D view for clearer structural inspections. Region 12 is chosen since it has the highest permeability in through-plane direction and two in-plane directions of all 21 regions. Region 8 shows the lowest through-plane permeability. Region 7 has the lowest in-plane permeability in both *x*-/*z*-directions. It can be seen that there are large void spaces existing in region 12 since region 12 located at a place where two fiber tissue cross each other, as illustrated in Figure 7.1. This structure provides large pore volume for the gas flow transport through which results in higher absolute permeability. In comparison with region 12, region 7 and region 8 are next to each other and the fibers are tightly overlap one another in regular weave form. This kind of structure results in less void space for gas transport through, hence lower absolute permeability. Other regions of the cloth with relative higher or lower permeabilities can be explain similarly, where tightly arranged fibers such as two intersection fiber bundles can result in a lower permeability while loosely assembled structures posses large void spaces hence exhibiting higher

permeability. Therefore, it can be understood that the porosity has an important influence on the permeability.

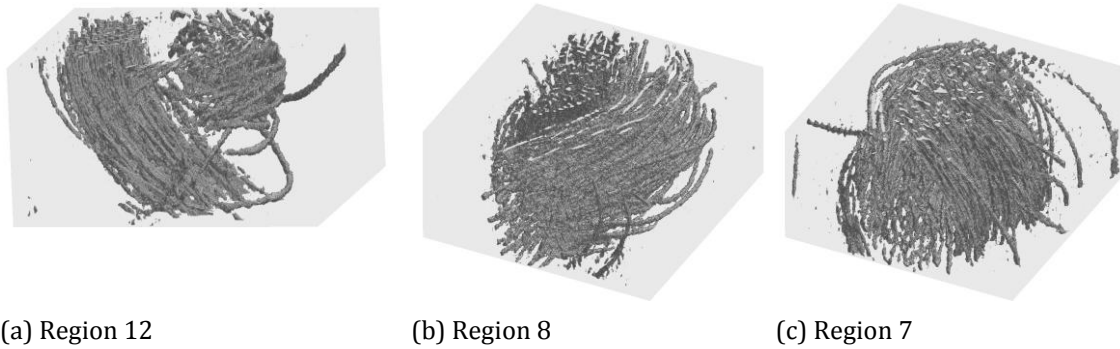


Figure 7.3 3D image structure of (a) region 12; (b) region 8; (c); region 7

7.3.2. Permeability and Porosity Relationship

Figure 7.4 shows the permeability in through-plane y-direction and in-plane x- and z-directions in relation to the porosity of the total 21 regions of the carbon cloth. The three best fit lines corresponding to these three sets of data points are shown in the same figure. It can be seen that the porosity of all 21 regions are higher than 90% with values ranging from 91% to 95.5%. For permeability in through-plane y direction, its best fit line shows a rise from the lowest value of $0.8 \times 10^{-5} \text{ mm}^2$ to $4.0 \times 10^{-5} \text{ mm}^2$ with increasing the porosity from 91% to 95.5%. The best fit lines for in-plane permeabilities of x-direction and z-direction both increase from $0.2 \times 10^{-6} \text{ mm}^2$ to around $1.0 \times 10^{-6} \text{ mm}^2$ within the porosity range. The results therefore show that for the carbon cloth employed in this study, a 5% increasing of local porosity due to the local fiber bundle structures can result in the permeability increasing around five times for both through-plane and two in-plane cases.

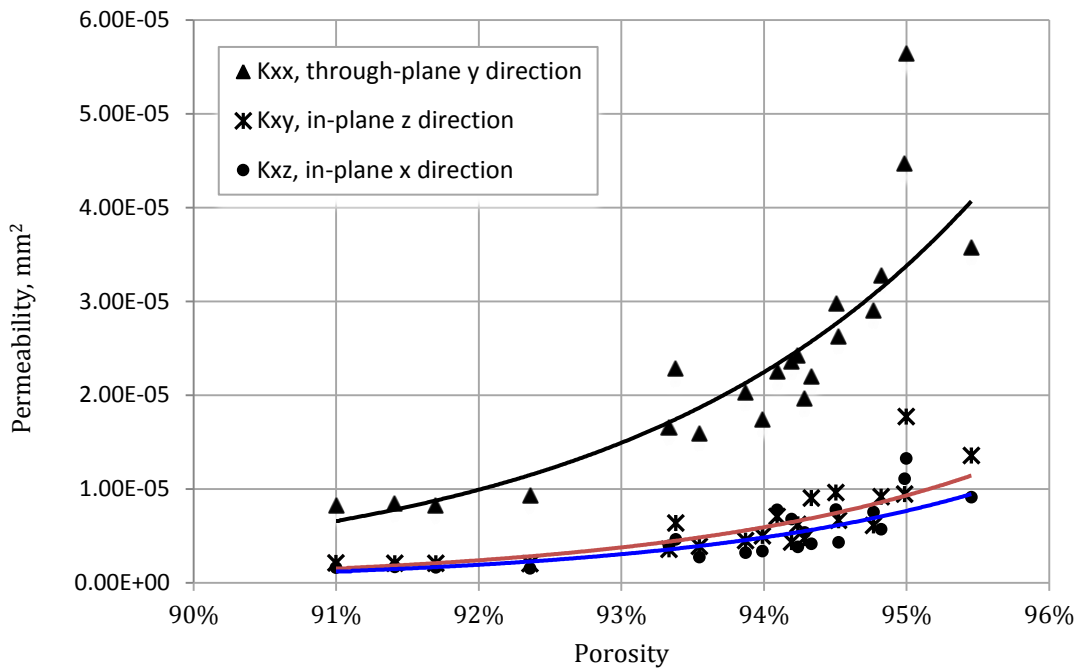


Figure 7.4 Permeability against porosity

7.4. Degree of Anisotropy

The degree of anisotropy is defined by comparing the in-plane permeability to the through-plane permeability:

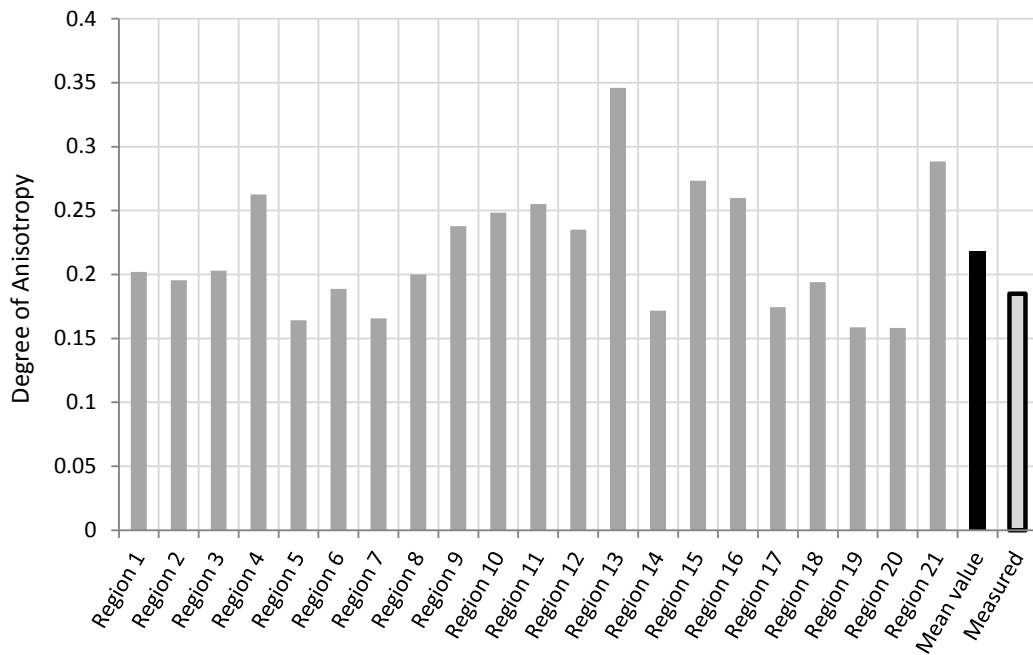
$$\gamma_{ij} = \frac{k_{ij}}{k_{ii}} \quad [7.1]$$

where i denotes the main through-plane y direction, and j denotes the in-plane x or z direction.

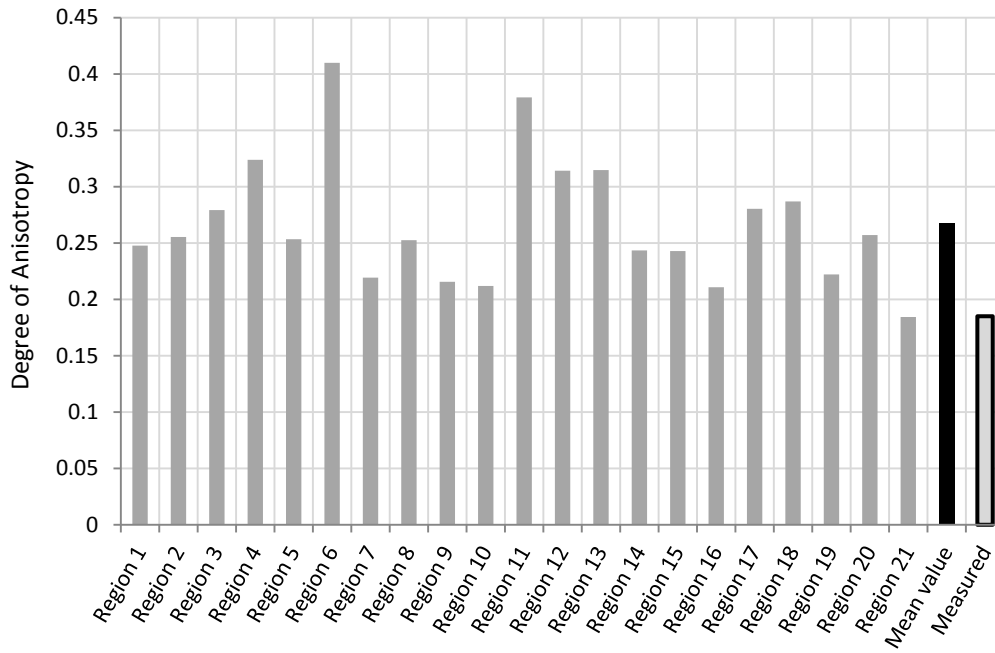
The degree of anisotropic is a factor which shows the influence on the quantity of the gases transporting through the gas diffusion layer following the main through-plane direction. Therefore it can be an important factor for in the selection of porous materials for fuel cell development and application such as for inter-digitated flow channel. The degree of anisotropy in the in-plane x - and z - directions are calculated and compared with the experimental results.

Figure 7.5 shows the calculated degree of anisotropy in the in-plane x- and z- directions for all 21 regions using the data reported in Figure 7.2. The calculated values and the average value are compared with the experimental measurements. The results show that the average degree of anisotropic of in-plane x direction to through-plane y direction is 0.22 and that of in-plane z direction to y direction is 0.27. The experimental measured degree of anisotropy value is 0.19. The results show good agreement between calculated and measure anisotropic permeability for the carbon cloth.

In order to have a deeper understanding of the obtained results, it is necessary to look at the fiber structure of the material again in Figure 7.1. For regions where have higher degree of anisotropy exceeding 0.35 such as region 6 and region 11 in Figure 7.5(b), they all locate at four bundles intersecting area with large void spaces in between. This type of structure layout will make the flow transport through preferential direction. So when the flow transports through region 6 and region 11 in the through-plane y direction, this structure layout will make one portion of the air transporting along the main flow y direction while makes the other portion of air flowing towards preferential direction into region 1 and region 8, respectively. Therefore it explains that the degree of anisotropy for region 6 and region 11 in the z-direction is higher compared to that in the x-direction.



(a) in x-direction



(b) in z-direction

Figure 7.5 Calculated degree of anisotropy in the (a) in-plane x direction; (b) in-plane z direction

7.5. Prediction of Permeability

The permeability k of a porous media usually can be expressed related to its porosity. The semi-empirical formula of Carman-Kozeny (KC) has been reported by literature⁸² and shows the ability of predicting the through-plane permeability of a porous material. The KC equation is defined by:

$$\frac{k}{r^2} = \frac{\varepsilon^3}{4K_{KC}(1-\varepsilon)^2} \quad [7.2]$$

where r is the average fiber radius, ε is the material porosity. K_{KC} is the KC constant and it is a tuning parameter which relies on the type of material and the fiber layout. Besides the Carman-Kozeny equation, the Tomadakis-Sotirchos (TS) equation developed by Tomadakis and Sotirchos²¹⁷ has comprehensively demonstrated the relationship between the absolute permeability and the porosity⁸⁶. The TS model can be expressed by:

$$\frac{k}{r^2} = \frac{\varepsilon}{8 \ln^2 \varepsilon} \frac{(\varepsilon - \varepsilon_p)^{\alpha+2}}{(1 - \varepsilon_p)^\alpha [(\alpha + 1)\varepsilon - \varepsilon_p]^2} \quad [7.3]$$

where ε_p is the percolation threshold and α is a constant. The two parameters depend on fiber arrangement as well as the flow direction. By using the through-plane permeability results obtained in Figure 7.4 and the average fiber radius, the simulated data from LB model can be fitted by the KC model and TS model by tuning their corresponding parametric coefficients. Therefore both the KC constant in KC model and ε_p and α in TS model need to be tuned in order to minimize the average error relative to the absolute permeability of the 21 regions as low as possible,

By using the porosity data of each of all 21 regions presented previously, the prediction on permeability by LB mode, KC model and TS model are compared and shown in Figure 7.6. The KC constant in the KC equation is tuned to a value of 44 which gives an average error of 13.4%. The KC constant is an adjustable parameter which highly depends on the material fiber alignment and arrangement. In the work of Gostick *et al*⁸⁶, they estimated the KC constant for different GDL material. In their analysis on the carbon cloth of E-Tek Cloth-A with measured porosity of 78%, a tuned KC constant of 1.45 was obtained which is 30 times lower than the KC constant tuned for the carbon cloth employed in this study. However, by the same author, for another analyzed porous GDL material Ballard P75 which has a measured porosity of 85%, the KC constant is estimated to be 43.5. This result is highly close to the value of 44 tuned for the carbon cloth used in this study. Also, the literature²¹⁸ reported that the KC constant can be higher for materials with porosity larger than 80%, which supports the case on the carbon cloth in this study.

For TS mode, the percolation threshold ε_p and α are tuned to be 0.60 and 1.21, respectively, and this gives an average error of 12.1%. In the work of Tomadakis *et al*^{87, 219} they investigated the TS estimation for randomly overlapped fibres, the percolation threshold range of 0.037 ~ 0.33 was reported, and the α range falls between values of 0.521 to 1.099. In addition, in another work from the same author²²⁰, they suggested that for partially overlapping fiber layout, the threshold percolation value is more close to value of 0.33. Since the carbon cloth has woven structure with regular overlapping fibres, it can be understood that the percolation threshold may increase accordingly.

Besides, the author also suggested that the relationship between percolation threshold and α for fully overlapped fibres structure can be estimated by:

$$\alpha = 2.28\varepsilon_p + 0.35 \quad [7.4]$$

If applying the percolation threshold value of 0.6 to Equation 7.4, it gives the value of α of 1.718. The tuned α value of 1.21 in this study falls within this region which confirms the results.

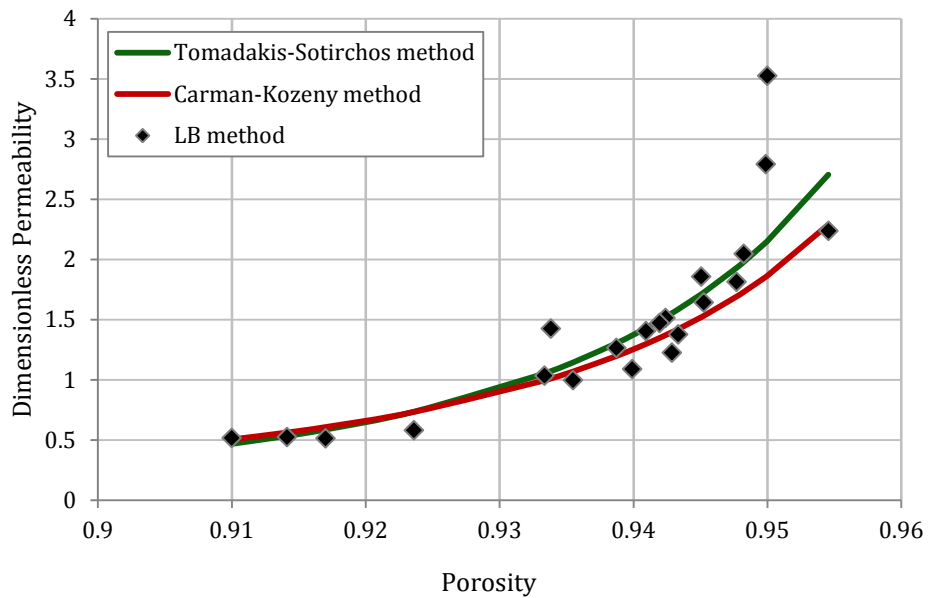


Figure 7.6 Through-plane permeability prediction on porosity by the LB model, the Carman-Kozeny (KC) model, and the Tomadakis-Sotirchos (TS) model.

7.6. Conclusions

In this study the prediction on permeability and degree of anisotropic permeability of a carbon cloth GDL has been simulated by the LB model. The x-ray microtomography imaging technique has been employed to reconstruct the three-dimensional digital image of the carbon cloth. The simulation results conclude that:

<1>. A carbon cloth GDL is studied. The x-ray tomography technique is used to reconstruct the sample into three-dimensional digital image with resolution of $1.74 \mu m$. The image is split into 21 regions with each region having a size of $442 \times 442 \times 223 \mu m^3$.

<2>. The absolute permeabilities for through-plane and in-plane directions of the carbon cloth have been simulated by the SPMC LB model. The results show that the mean through-plane absolute permeability is $2.35 \times 10^{-5} mm^2$ and the absolute permeabilities for in-plane x direction and z direction are $0.53 \times 10^{-5} mm^2$ and $0.65 \times 10^{-5} mm^2$, respectively. The structural inspection explains that the regular overlapping fiber layout with tight arrangement results in lower permeability; while in the area of intersection fiber bundle exists large void space which enables the gas transport easily hence results in higher permeability.

<3>. The degree of anisotropic is obtained by comparing the in-plane permeability to the through-plane permeability. The results show that the degree of anisotropy for in-plane x direction to through-plane y direction is 0.22 and for in-plane z direction to y direction is 0.27. These results agree well with the experimental measured value of 0.19. By inspecting the fiber structure of the material, it has been found that the degree of anisotropy is influenced by the fiber intersection layout as well as the resulted void space.

<4>. The Carman-Kozeny (KC) equation and the Tomadakis-Sotirchos (TS) equation are employed which have successful described the dependence of through-plane permeability to the porosity predicted by the LB mode. Within the porosity range of 91% to 95.5%, tuning the KC constant to a value of 44 gives an average error of 13.4 for the KC model; while the TS model reported an average error of 12.1% by tuning the percolation threshold ε_p and α values to 0.6 and 1.21, respectively.

CHAPTER 8. Numerical Studies on Compressed Carbon Cloth Gas Diffusion Layer

8.1. Introduction

The GDL of a PEMFC is a critical component as it ensures the connection between the gas channel and the catalyst layer. In a fuel cell system, all the components are bonded together under compression load to reduce the leakage problem; however, over-compression will result in heavy deformation of the GDL structure. The literatures have contributed many works on compression issue in fuel cell. On experimental side, Lee *et al*²²¹ studied the compression effects on PEM fuel cell performance for three different GDL materials of carbon cloth and carbon paper. The internal pressure was measured at various bolt torques. The results showed that the internal pressure increases with GDL thickness at a given torque. In addition, the internal pressure can also be affected by thickness between the gasket and the GDL. Ge *et al*²²² also investigated the compression effects on PEM fuel cell performance for both carbon cloth and carbon paper. The experimental results revealed that for both carbon cloth and carbon paper, the compressions has a significant influence on PEM fuel cell performance. They observed that the compression effect is greater at high current density range. They suggested that an appropriate level of compression needs to be controlled in order to reach the optimum PEM fuel cell performance without over-compressing which otherwise decreases the cell performance. Similar experimental results were reported by Lin *et al*²²³. Nitta *et al*²²⁴ presented an experimental work which considered the inhomogeneous compressions effect on the physical properties of the carbon paper GDL. They found that the GDL thickness changes dramatically under the ribs due to loss of porosity; however the GDL under the channel almost remains the original thickness and

is only slightly compressed at high compression pressure. The experimental results reported that the in-plane permeability decreases with decreasing of compressed GDL thickness. Also they reported the linear dependency of bulk conductivity of both through-plane and in-plane to the compressed thickness. On numerical side, Hottinen *et al*²²⁵ carried out the numerical study on modeling the inhomogeneous compression effects on the PEM fuel cell performance. They also reported the significant current distribution variation on the GDL and electrode interface due to the inhomogeneous compression. A noticeable portion of current transport through the GDL in the in-plane direction under the rib was observed where lower contact resistance exists. Similarly, Su *et al*²²⁶ simulated the compression effect on gas transport phenomena through the rib and under channel area with supplying the physical properties of the GDL from the experiments. Their results concluded that the compression needs to be controlled precisely since a significant current density variation exists near the corner of the rib where hot spot might occur. Other works were reported by Shi *et al*²²⁷ on compression effects on water management in PEM fuel cell and by Hottinen and Himanen²²⁸ on temperature distribution due to inhomogeneous compression in PEM fuel cell.

The literature reports on compression on GDLs are not exhaustive. These literatures results provide valuable insights into the effect of compression on the cell performance through experimental visualization or macroscopic numerical simulation. However the relationship between the compressed structure of the GDL, its transport property and the flow transport characteristics within the structure are less reported due to the complex porous structure involved, since it is difficult to carry on direct measurement and three-dimensional numerical simulation from micron-scale point of view.

Previous studies on the GDL carbon paper and carbon cloth have demonstrated the capability of using the three-dimensional single phase LB model to simulate the single component and multicomponent transport within the reconstructed 3D digital GDL structure which is generated by the x-ray tomography technique. In this chapter, the compression effect on structural deformation, physical parameters of the carbon cloth GDL and the multicomponent flow transportation characteristics are studied using the same combined technique. The carbon cloth GDL samples are compressed at different levels up to 100 MPa. The x-ray tomography technique is used to reconstruct the three-dimensional digital structures of the samples. The pore size distribution and the porosity of the compressed samples are acquired using the standard computational

techniques²²⁹. The through-plane permeability, degree of anisotropy and the through-plane tortuosity are calculated by the LB model.

8.2. Methodology

8.2.1. Sample preparation

The carbon cloth or carbon paper GDLs can be reconstructed by x-ray tomography without special treatment. In this study, in order to present the compressed carbon cloth structure, it is necessary to pre-treat the material before starting the imaging process. Firstly, the carbon cloth GDL is immersed and saturated with polydimethylsiloxane (PDMS). PDMS is a silicon-based organic polymer which is transparent clear. Depending on the time and temperature, it can cure to form an elastomer which is chemically and mechanically flexible and stable²³⁰. Then the GDL saturated with PDMS is compressed at a given load in an oven at 333K for 30 mins. Thin aluminum sheets are used to cover both sides of the sample before they are compressed to enable the whole sample can be removed easily after curing. The pre-selected load is applied to ensure the uniform compression pressure on the GDL. Seven carbon cloth GDLs are compressed with compression pressure of 0.1MPa, 0.3MPa, 1.0MPa, 3.3MPa, 10.0MPa, 20.0 MPa and 100MPa, and are reconstructed into three-dimensional digital images. Figure 8.1 shows a PMDS cured sample after compression. The sample is in size of $1 \times 1 \text{ cm}^2$.

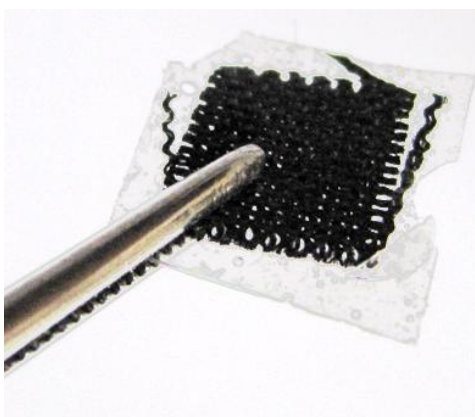


Figure 8.1 A compressed $1 \times 1 \text{ cm}^2$ carbon cloth GDL encapsulated in PDMS

8.2.2. Three-dimensional reconstruction

The 3D digital model of the carbon cloth can be imaged by the x-ray microtomography as reported in previous studies. It follows the procedure of (1) 2D shadow image acquisition; (2) thresholding process and (3) three-dimensional digital reconstruction. In this study, the z-direction is set as the through-plane direction, and x- and y-directions are the two in-plane direction. The resolution of the images is $1.73 \mu\text{m}$. Since the samples were cured by PDMS, after reconstructing the compressed samples it is necessary to remove a number of layers on the x-y plane to ensure that there is no excess PDMS and residual protective materials left on the samples. Due to this reason, the thickness of each sample, which is the size in z-direction, can be various from sample to sample. Therefore the size in z-direction of each sample may not represent the actual thickness after the compression. Table 8.1 lists the actual image sizes of the samples upon the compression pressures as well as the porosity of each sample.

Image size, μm	Compression Pressure, MPa							
	0.0	0.1	0.3	1.0	3.3	10.0	20.0	100.0
z direction	372.6	174.0	242.6	173.3	272.1	173.3	138.6	150.7
x direction	693.2	696.0	693.2	658.5	693.2	693.2	693.2	693.2
y direction	519.9	522.0	519.9	519.9	519.9	519.9	519.9	519.9
Porosity	78%	66%	64%	53%	62%	40%	48%	45%

Table 8.1 Image sizes of 3D reconstructed carbon cloth GDL from x-ray microtomography

8.2.3. Key Equations

The single phase LB model has been employed in previous studies on characteristics of carbon paper and carbon cloth GDLs and shows the capability on single- and multi-component simulation. Basically the LB method is implemented by collision step and streaming step through which the particles collide with each other and redistribute to neighboring nodes. The D3Q19 scheme is used which allows the particles distribute in 19 velocities. The bounce-back method is employed to solve the void-solid interface. The Key equations in LB simulation were explained in Chapter 3. The permeability of the carbon cloth can be obtained through the detailed gas velocity distribution in the porous

structure calculation by LB model. From macroscopic point of view, the absolute permeability can be calculated by Darcy's law. By applying a pressure gradient along the thickness direction of the sample, the permeability tensors in through-plan and in-plane directions can be calculated. The anisotropic permeability is defined as the ratio of in-plane permeability over the through plane permeability.

In order to investigate the compression effects on the carbon cloth structure, the tortuosity is defined as the ratio of the free diffusion coefficient of a gas in free space, D_0 , to its effective diffusion coefficient in the porous structure D_e :

$$\sigma = \frac{D_0}{D_e} \quad [8.1]$$

D_0 is related to the relaxation parameter τ_D by:

$$D_0 = \frac{2\delta x^2(\tau_D - 0.5)}{7\delta t} \quad [8.2]$$

where is δx the characteristics length of a voxel in the three-dimensional digital model; τ_D is the relaxation parameter which indicates the rate of the particle distribution function reaching the equilibrium state and δt is the computational time step.

D_e is calculated by:

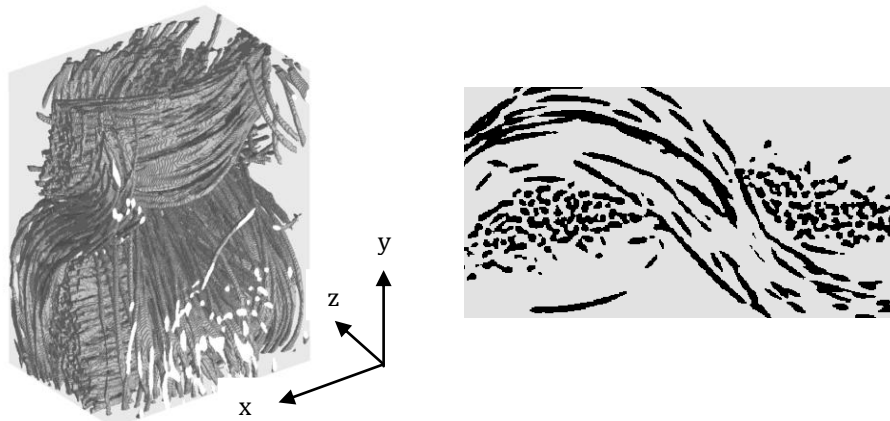
$$D_e = \frac{L}{N\Delta c} \sum_{i=1}^N q_{x,i} \quad [8.3]$$

where N is the total number of pore voxels in the structure; Δc is the concentration gradient applied across the thickness of the structure; L is the length along thickness direction where the concentration gradient is imposed. $q_{x,i}$ is the species flow towards x direction at node i in the 3D lattice and was given in Equation 6.14.

8.3. Simulation Results

8.3.1. Compressions Effects on Structure and Pore Size Distribution

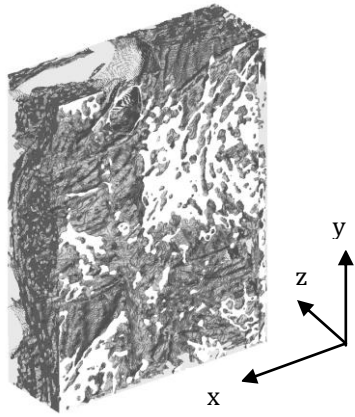
Figure 8.2 illustrates the reconstructed structures of GDL samples with different levels of compression and their corresponding 2D cross section images. The size of each 3D image is shown in Table 8.1. It can be seen that the sample structural change by the exerted compressions is regular upon the compression. At low compression pressure up to 0.3 MPa, the overall structure becomes more compact. This initial structure change can be distinguished in Figure 8.2 by comparing the uncompressed structure (a-2) with structures shown in (b-2) and (c-2) which are compressed up to 0.1 MPa and 0.3 MPa, respectively. It can be observed that this causes eliminating of large and loose void space in the structure. When increasing the compression pressure towards the thickness direction up to 3.3 MPa, the fibers bundles are forced bounded tighter and spread towards x- and y- direction. This structural change can be observed from structures illustrated in Figure (d-1) and (e-1). It also can be found that the pore space keeps reducing as can be seen from the structures shown in Figure (d-2) and (e-2). For the structures with compression pressure of 10.0 MPa and 20.0 MPa, the weave pattern of the fiber bundles has been straightened along their length and invade into void space where intersecting bundles lies. This results in decreasing of the pore volumes in and around these areas as can be seen from figure (f-2) and (g-2). By applying high compression pressure of 100.0 MPa onto the structure, the void space among the intersecting bundles significantly decrease and the intersecting bundles can hardly be identified since void space within the intersecting bundles is forced filled by individual and the fiber bundle structures are deformed heavily. This is shown in (h-2).



(a-1)

(a) 0.0 MPa

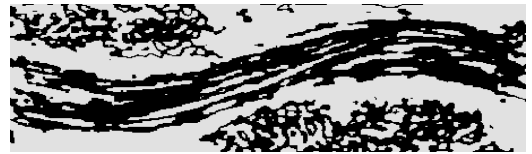
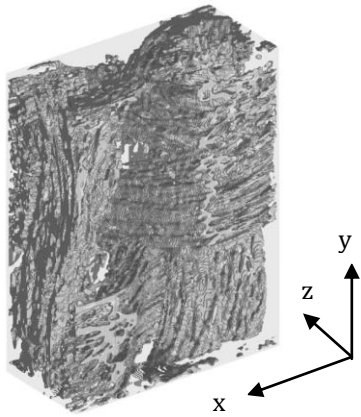
(a-2)



(b-1)

(b) 0.1 MPa

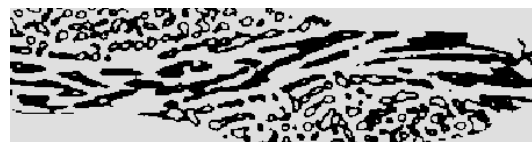
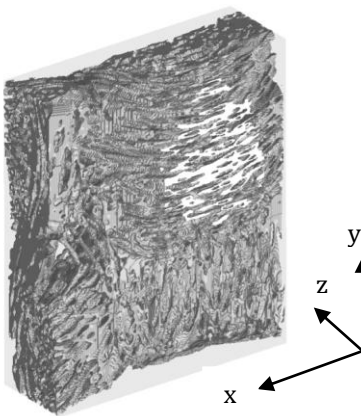
(b-2)



(c-1)

(c) 0.3 MPa

(c-2)

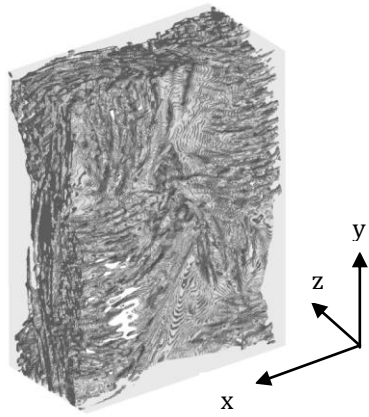


(d-1)

(d) 1.0 MPa

(d-2)



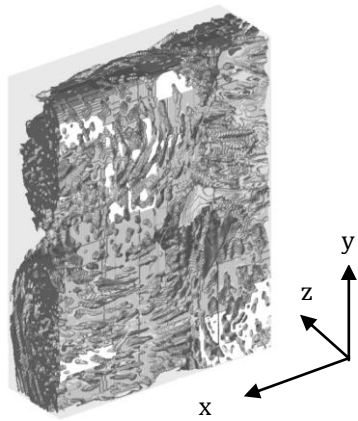


(e-1)



(e-2)

(e) 3.3 MPa

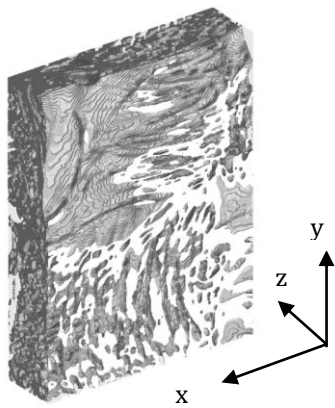


(f-1)



(f-2)

(f) 10.0 MPa



(g-1)



(g-2)

(g) 20.0 MPa

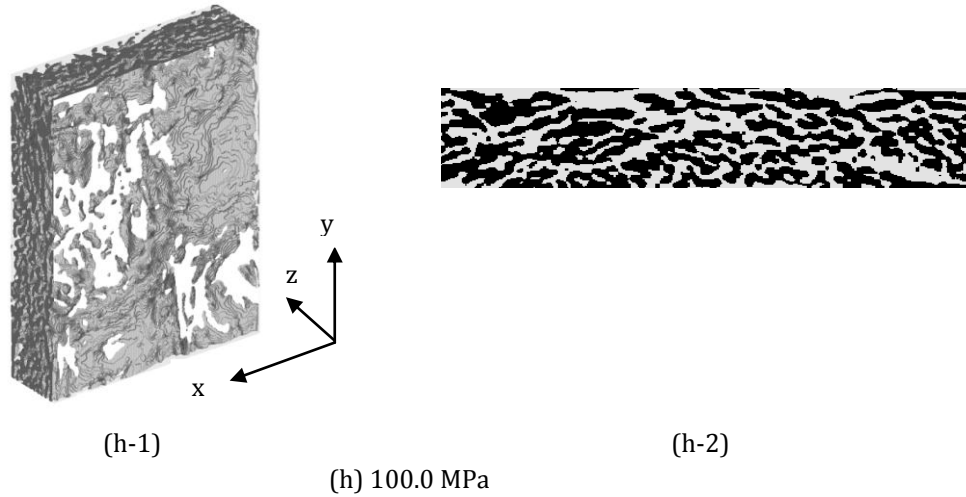
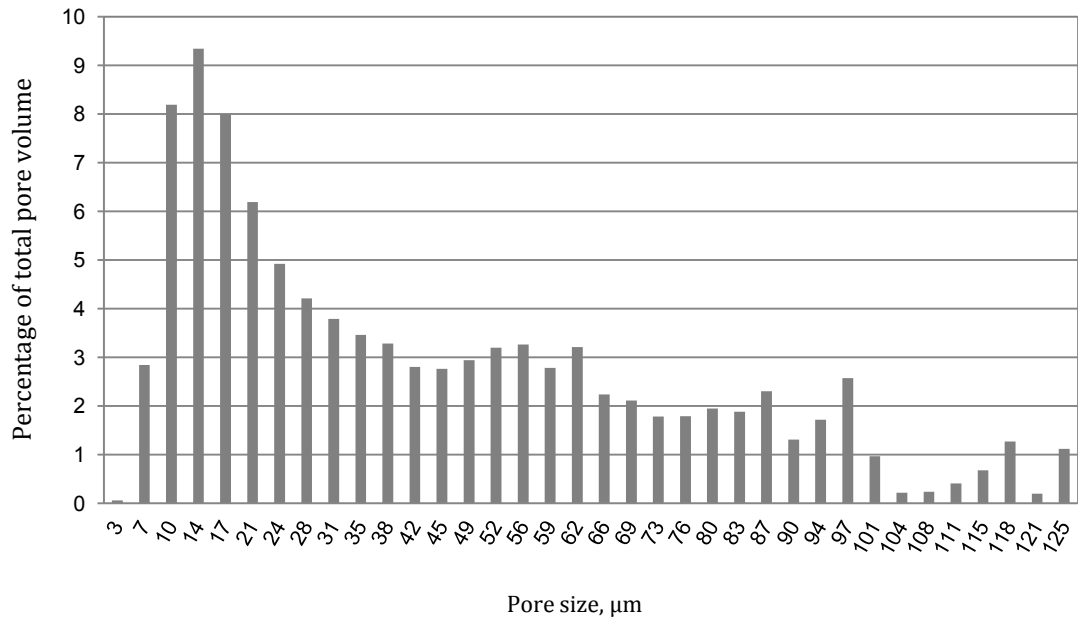
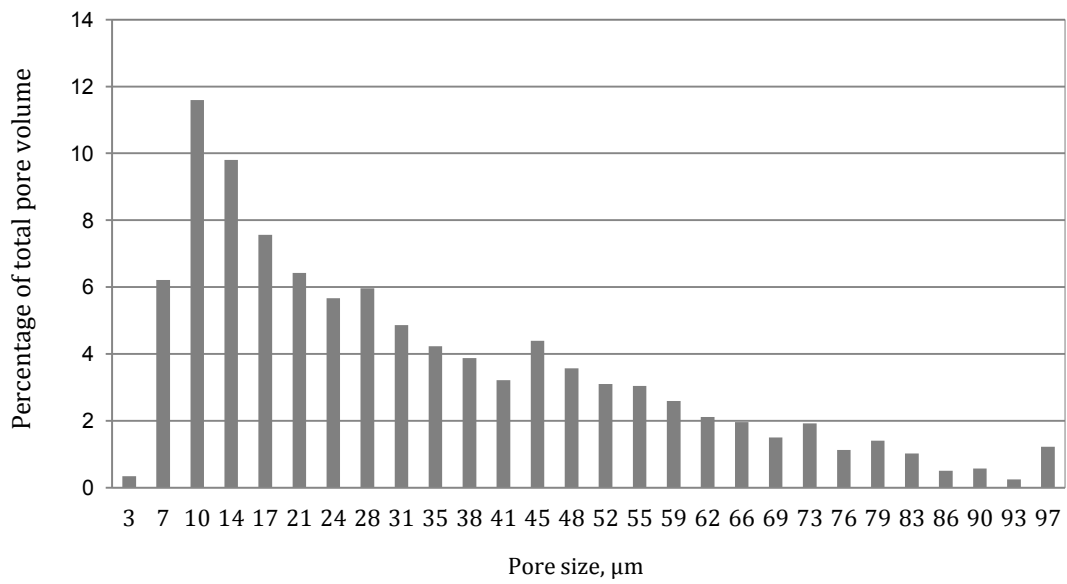


Figure 8.2 Reconstructed structures (grey) and corresponding binary cross section image (black) of the compressed carbon cloth GDL under compression pressure of (a) 0.0 MPa; (b) 0.1 MPa; (c) 0.3 MPa; (d) 1.0 MPa; (e) 3.3 MPa; (f) 10.0 MPa; (g) 20.0 MPa; (h) 100.0 MPa. The compression load is applied in the through-plane z-direction.

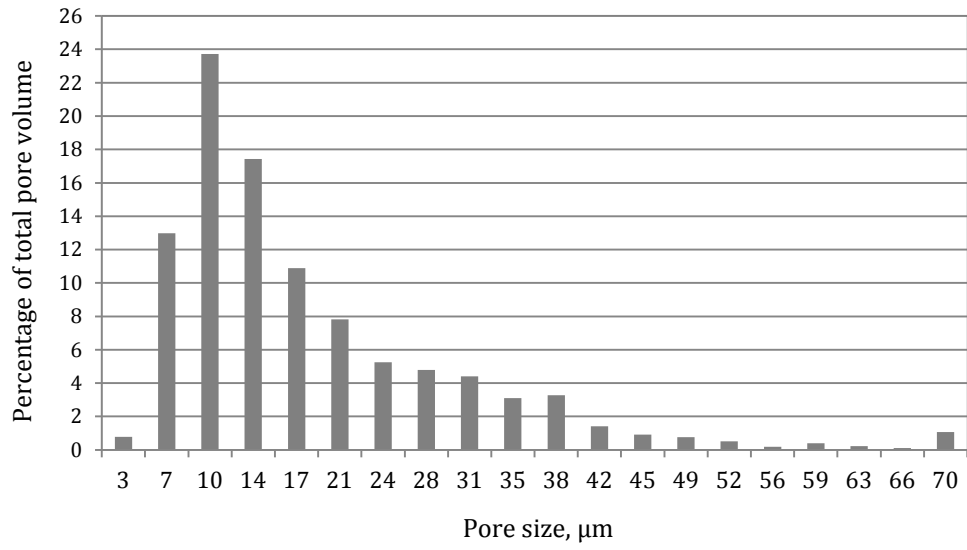
Figure 8.3 (a)~(f) show the pore size distribution (PSD) data for uncompressed carbon cloth sample as well as the compressed samples at 0.1 MPa, 1.0 MPa, 10.0 MPa, 20 MPa and 100.0 MPa compression pressure. It is worth to note that in order to guarantee the accurate results can be obtained when deciding the PSD data, all void spaces that are part of the binary image however outside the GDL structure are not considered since these void spaces are not part of the porous network, therefore their existence would give inaccurate results. It can be seen from Figure 8.3 that for uncompressed carbon cloth GDL structure, the pore size covers a wide range of 3~125 μm . For the GDL samples with 0.1 MPa and 1.0 MPa compression pressure, the range of the pore size becomes 3~97 μm and 3~70 μm , respectively. For the compression pressure higher than 10.0 MPa, the range of the pore size has been largely narrowed down to 3~31 μm at 100.0 MPa compression pressure case. Besides, it also can be observed that for all the PSD data shown in Figure 8.3, the pore sizes within the range of 10~14 μm has the largest population in the overall pore volume for both uncompressed GDL and compressed ones.



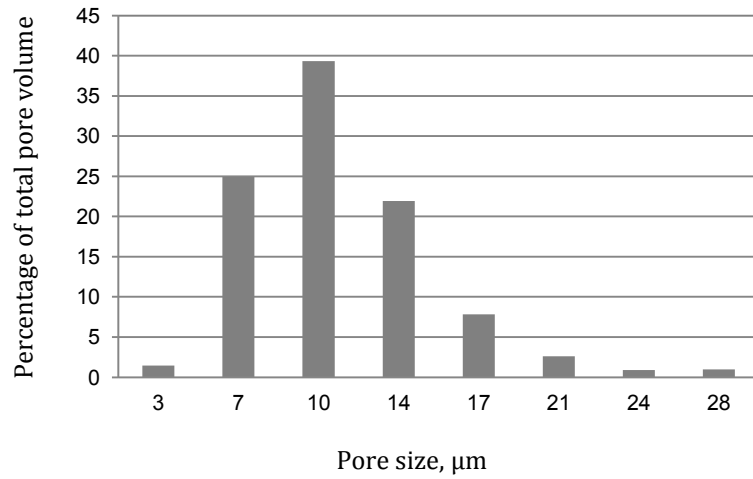
(a) 0.0 MPa



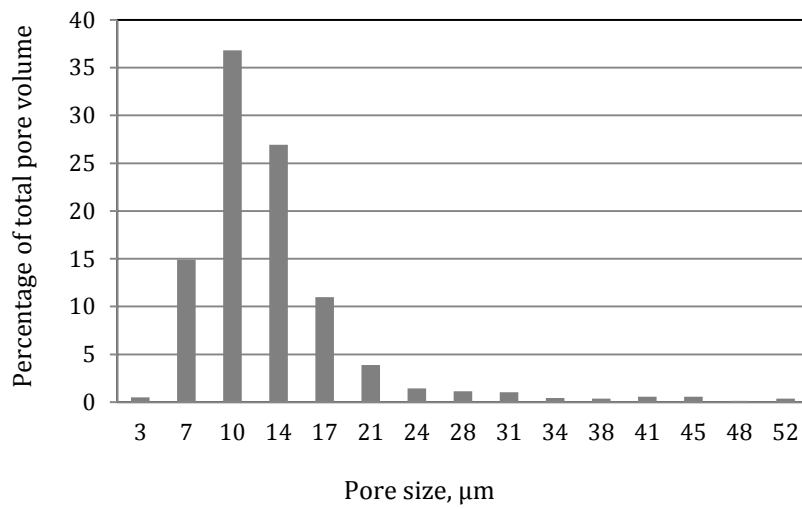
(b) 0.1 MPa



(c) 1.0 MPa



(d) 10.0 MPa



(e) 20.0 MPa

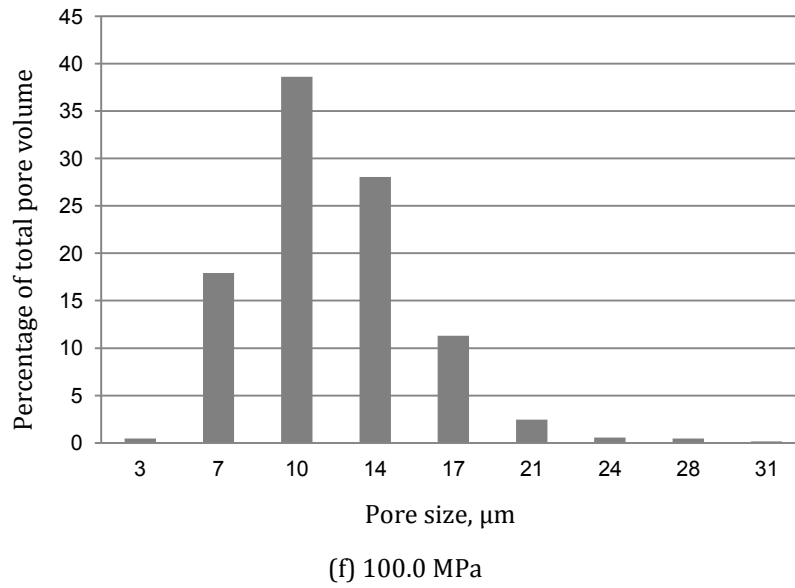


Figure 8.3. Pore size distribution data of the carbon cloth GDL with compression pressure of: (a) 0.0 MPa; (b) 0.1 MPa; (c) 1.0 MPa; (d) 10.0 MPa; and (e) 20.0 MPa and (f) 100.0 MPa.

Figure 8.4 summarizes the mean pore size and the maximum pore size as functions of the GDL compression pressure and Figure 8.5 describes the contribution of the main pore size range of 10~14 μm to the overall pore volume as a function of the GDL compression pressure. The x-axis is the compression pressure on a logarithmic scale. The results shown in both of the two figures are based on the PSD data illustrated in Figure 8.3(b)~(f). Figure 8.4 shows that the mean pore size decreases from 33 μm at 0.1 MPa compression pressure to 12 μm at 100.0 MPa compression pressure. Comparing with the average fiber diameter of 8 μm of the carbon cloth GDL in this study, it indicates that at highest compression pressure of 100 MPa, the carbon cloth GDL remains an average pore space around 1.5 times of a single fiber diameter. The maximum pore size decreases dramatically from 97 μm to 31 μm . Figure 8.3 reports that the pore size within range of 10~14 μm contributes to the largest portion in the overall pore volume and this occurs in both uncompressed and compressed the structures. Figure 8.5 shows that this range of pore size constitutes 21% of the total pore volume at 0.1 MPa compression and increases to 61% at 10.0 MPa compression pressure. At 100.0 MPa, this range of pore size reaches 67%.

According to previous discussion reported on structural change upon compression pressure, it can be seen that results shown in Figure 8.4 and Figure 8.5 agree with the

structural deformation process with compression. As the GDL structure is compressed, the porous structure body is firstly compacted and this narrows large pore size. Therefore the maximum pore size decreases to 70 μm at 1.0 MPa and this simultaneously decreases the mean pore size down to 18 μm . Reversely, the portion of 10~14 μm pore size band in the structure increases to 41%, since large pores are narrowed down to relative small pores. By increasing the compression pressure to 10.0 MPa, the fiber bundles are compacted even tighter and stretched in the x and y direction. Figure 8.4 and 8.5 again confirm that upon this compression level the maximum pore size becomes 28 μm and 61% of the pore size falls within the range of 10~14 μm . At 100.0 MPa compression pressure, there are 67% of the pore size within 10~14 μm and the maximum pore size and mean pore size are limited to 31 μm and 12 μm , respectively. The results again show that at 100.0 MPa the pore space in between the intersection fiber bundles has been invaded by individual fibers and the fiber bundles are deformed dramatically. At 20.0 MPa compress case, the largest pore size of 52 μm is observed which is out of the trend shown in Figure 8.4, but its main pore size is still within the range of 10 -14 μm . Therefore it is not surprising to know that a special pore volume characteristic exists in the actual porous

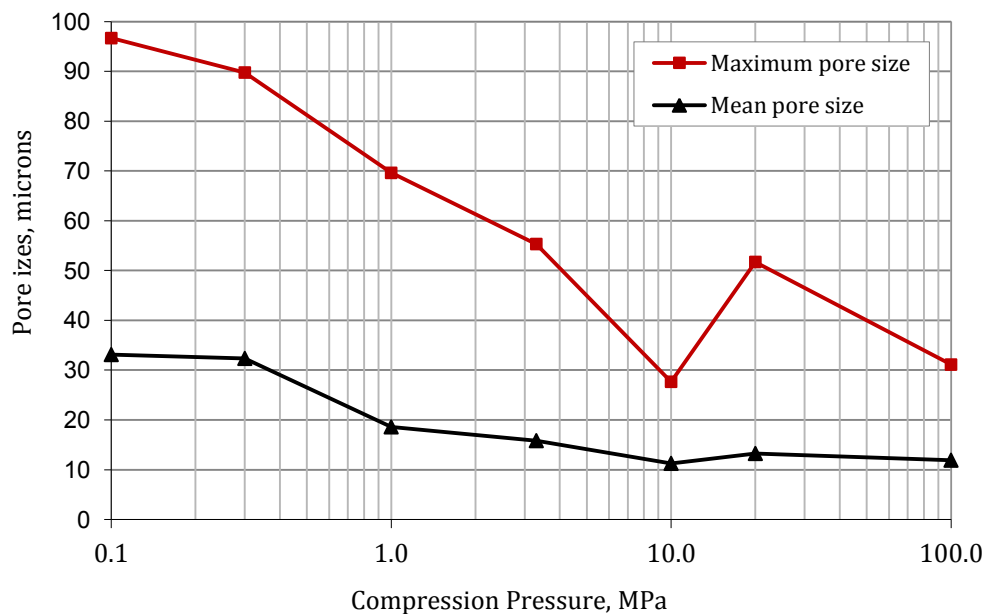


Figure 8.4 Maximum pore size and mean pore size against compression pressure, as summarized from PSD data in Figure 8.3

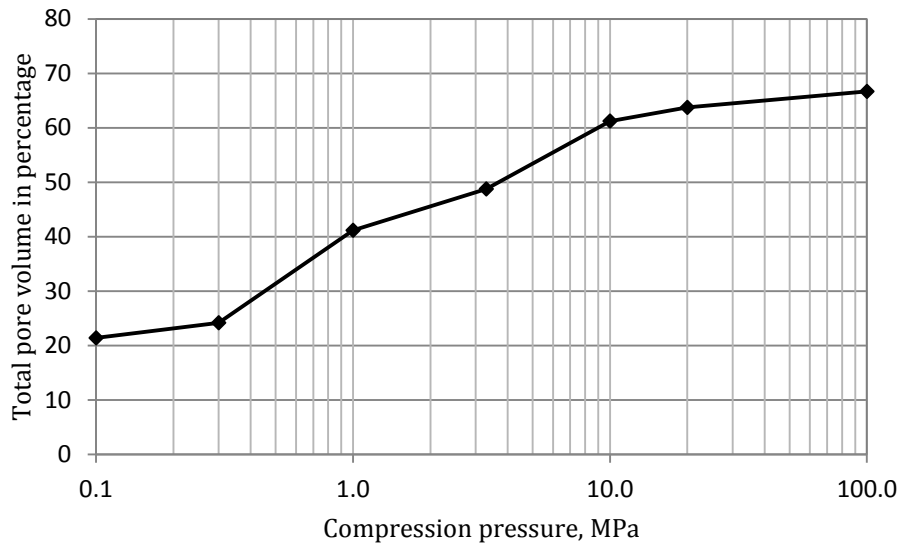


Figure 8.5 Population of main pore size range of 10 -14 μm in overall pore volume in percentage against compression pressure.

8.3.2. Compression Effects on Anisotropic Permeability

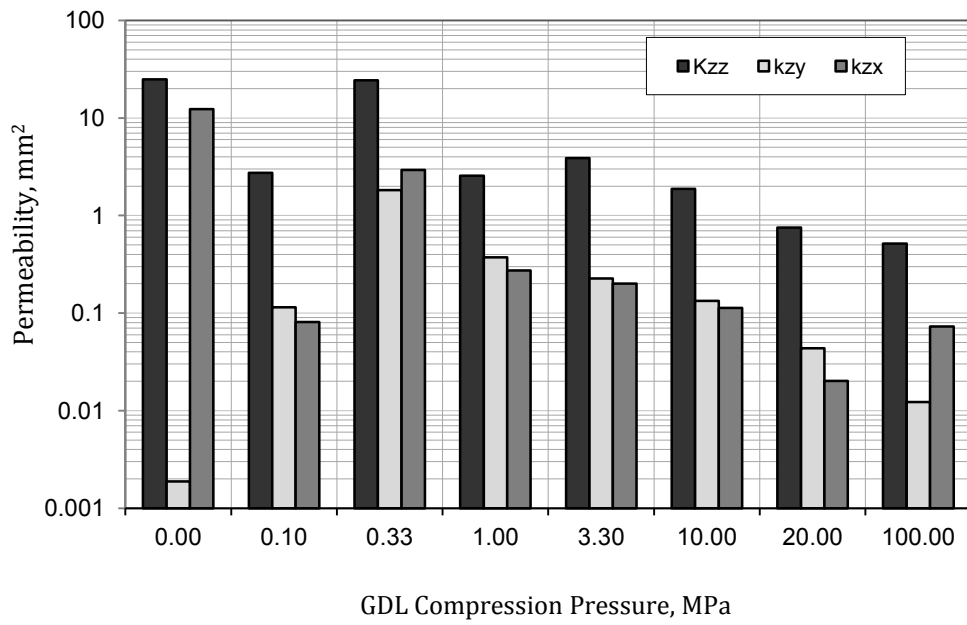
Figure 8.6(a) shows the through-plane permeability and the two in-plane permeability tensors. The corresponding degree of anisotropy is calculated by Equation [7.1] and is shown in Figure 8.6(b). The pressure gradient is applied in through-plane z-direction. Figure 8.6(a) shows that the in-plane permeability values are at least one order of magnitude smaller than that of the through-plane permeability at all compression cases. However, for the uncompressed GDL sample, the exception is found that the in-plane permeability for y direction (k_{xz}) is higher up to the same order of magnitude as its through-plane permeability; and the in-plane permeability of x direction (k_{zy}) is at least one order of magnitude smaller than that of the compressed cases as shown. This may be due to the existence of certain local weave features in the selected uncompressed GDL structure that makes the LB model gives this different result, since the LB model deals with collision and streaming in the pore-scale of the structure. Therefore this accordingly gives high degree of anisotropy value of k_{zx}/k_{zz} for the uncompressed GDL of 0.49 in in-plane y-direction as shown in Figure 8.6(b)

It can be observed from Figure 8.6(a) that both the through-pane permeability and the two in-plane permeability values initially peak at 0.3 MPa and then decrease with compression. Figure 8.6(b) also shows that the degree of anisotropy of both in-plane x-and y-directions increase and peak at compression of 0.3 MPa to 1.0 MPa and there is

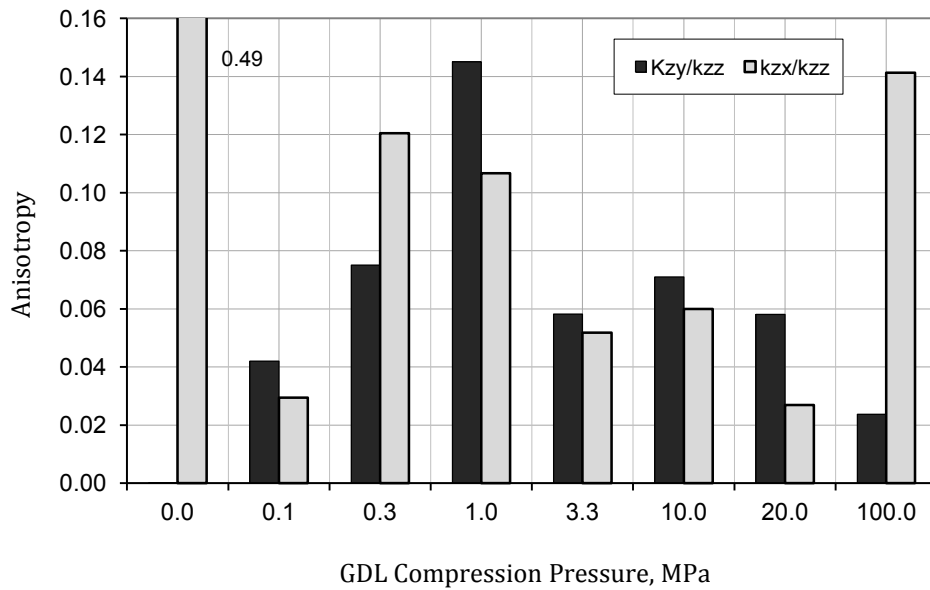
a second increase at 10.0 MPa. But general trend of the degree of anisotropy for the two in-plane directions gradually decreases with the compression pressure. Again the exceptional case occurs on the GDL sample with 100.0 MPa compression pressure. It can be seen that the degree of anisotropy k_{zx}/k_{zz} in in-plane y-direction of the 100.0 MPa GDL is 0.14 which is about one order of magnitude higher than what might be expected according to the general correlations as captured in Figure 8.6(b). However for this 100.0 MPa compression pressure pressed GDL sample, the values of degree of anisotropy k_{zy}/k_{zz} in in-plane x-direction, through-plane permeability k_{zz} and in-plane permeability k_{zy} in x-direction have the order of magnitude within the expected reasonable correlation as can be observed in Figure 8.6 (b) and (a). Therefore this exceptional case may be also due to the special local features of the selected sample that results in the exceptional results by the LB calculation.

By the structural inspection, the results showed in Figure 8.6 also can be explained by previous presented structural images in Figure 8.2. The initial compression will firstly tighten the structural and with increasing the compression pressure the fiber bundles are stretched and spread along their length directions as shown in Figure 8.2(b)~(d) for compression of 0.1~1.0 MPa. This results in initial increasing of higher values in-plane permeability relative to the through-plane permeability as shown in Figure 8.6 at 0.1~1.0 MPa. For compression pressure from 1.0 MPa to 10.0 MPa, the parallel individual fibers in the fiber bundles are tightened along their length directions and this however restricts the in-plane permeability. This can be observed in Figure 8.6(a) on the gradually decreasing of the in-plane permeability value within compression pressure range of 1.0 ~ 100.0 MPa.

The results calculated by the LB model show that in compression pressure range of 0.3~10.0 MPa the in-plane permeability is relative higher to the through-plane permeability, which suggests that it is possible to improve the species transport in-plane direction over the through-plane direction by applying the compression pressure within the optimal range of 0.3~10.0 MPa. This could be an important reference for fuel cells which employ interdigitated flow fields where the supplied through-plane gases and the reaction products need to move along in-plane path under the shoulder area of the channel to the outlets.



(a)



(b)

Figure 8.6 (a) Calculated through-plane and in-plane permeability tensors, and (b) Calculated degree of anisotropy on the compression pressure. k_{zz} for through-plane z-direction, k_{zy} and k_{zx} for in-plane x-direction and y-direction, respectively

8.3.3. Compression Effects on Porosity

In order to exam the effects of compression pressure applied on the fuel cell in practical environment, the following few sections will focus on the compression pressure range of 0.1~20.0 MPa.

The relationship between the compression pressure and the porosity of the samples is shown in Figure 8.7. The fit line of logarithm expression of the compression pressure range of 0.1~20.0 MPa draws the relationship below:

$$\varepsilon = -3.4\ln(P_{comp}) + 57.6 \quad [8.4]$$

This result simply presents how the porosity of the carbon cloth GDL changes with the applied compression pressure. Within the compression pressure range of 0.1~20.0 MPa, the porosity of the sample decreases exponentially with increasing the compression pressure. It can be seen from Figure 8.7 that when the compression pressure increases two orders of magnitude from 0.1MPa to 20.0 MPa, the porosity are reduced about 20% from 67% down to 48%. This is because that the applied compression pressure compacts the porous fiber structure and tighten the individual fibers which result in diminishing of the pore volume of the GDL structure as discussed previously.

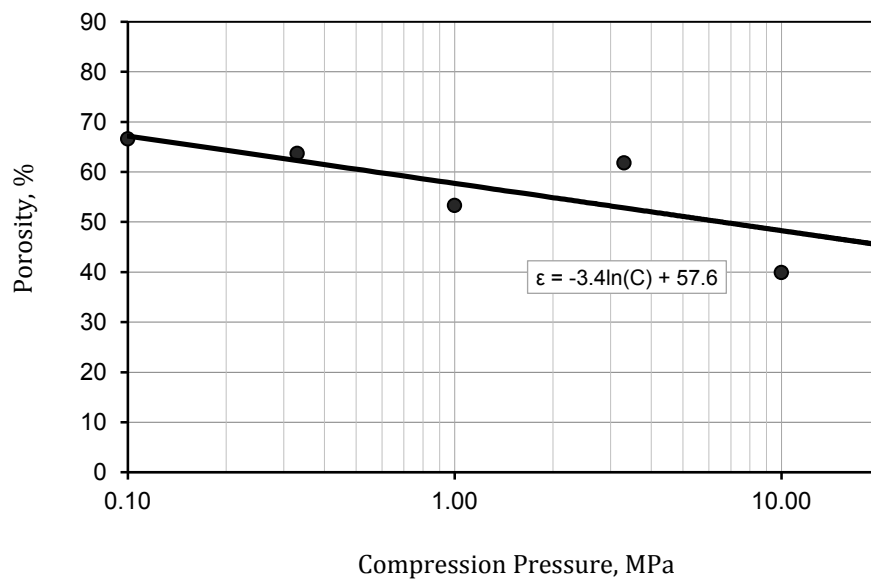


Figure 8.7. Porosity variation on compression pressure for compressed samples with compression pressure of 0.1~20.0 MPa

In order to have a deeper understanding on the compression effect on the micro-structural of the carbon cloth material, it is necessary to find out the relationship between the through-plane permeability and the compression pressure. Firstly, Figure 8.8 presents the relationship between non-dimensional permeability and the porosity for compression range of 0.1 MPa to 20.0 MPa. The permeability values are non-dimensionalised by dividing the values against the square of the fiber radius which is determined from the GDL sample in Figure 8.2(a) and is obtained as $4 \mu\text{m}$. As can be seen from Figure 8.7, the LB model prediction shows that the decrease in porosity can result in a decreasing of the through-plane permeability. This agrees well with the predicted relationship by the Kozeny-Carmen (KC) equation $\frac{k}{r^2} = \frac{\varepsilon^3}{4K_{KC}(1-\varepsilon)^2}$ previously introduced in Equation [7.2]. The KC constant K_{KC} is tuned to a value of 1.3 which is close to the KC constant value of 1.4 for E-Tek cloth 'A' in the work by Gostick *et al*⁸⁶ who reported the experimental measurement on permeability.

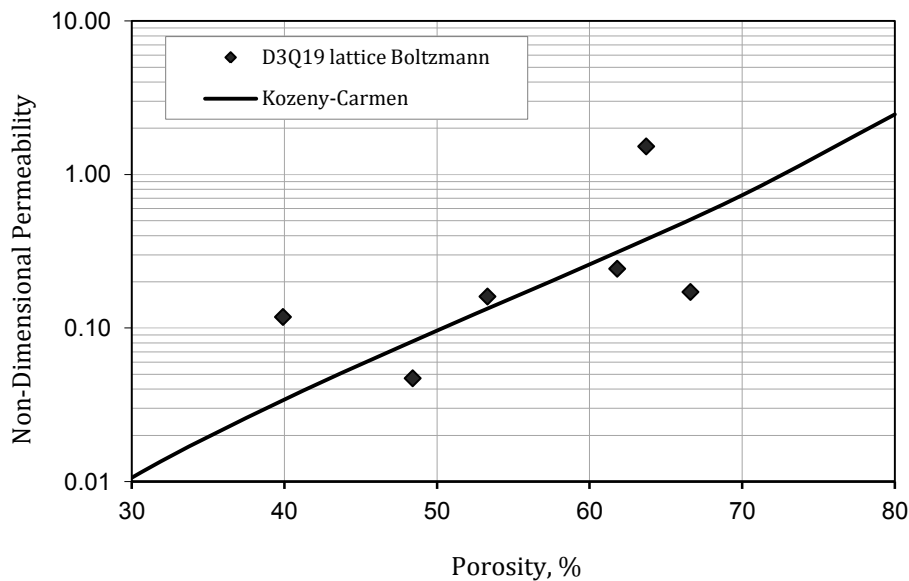


Figure 8.8. Non-dimensional through-plane permeability against the corresponding porosity

The non-dimensional permeability relationship with compression pressure is illustrated in Figure 8.9. The predicted results show good agreement between the data from LB model and the calculated from the Equation [8.4] and Equation [7.2]. The results indicate that as increasing the compression pressure by two orders of magnitude from

0.1 MPa to 20.0 MPa, the through-plane permeability can be reduced at least one order of magnitude. Figure 8.7 presents the porosity as a function of compression pressure and Figure 8.8 shows the permeability and porosity relationship. This therefore establishes the relationship between the through-plane permeability and the compression pressure.

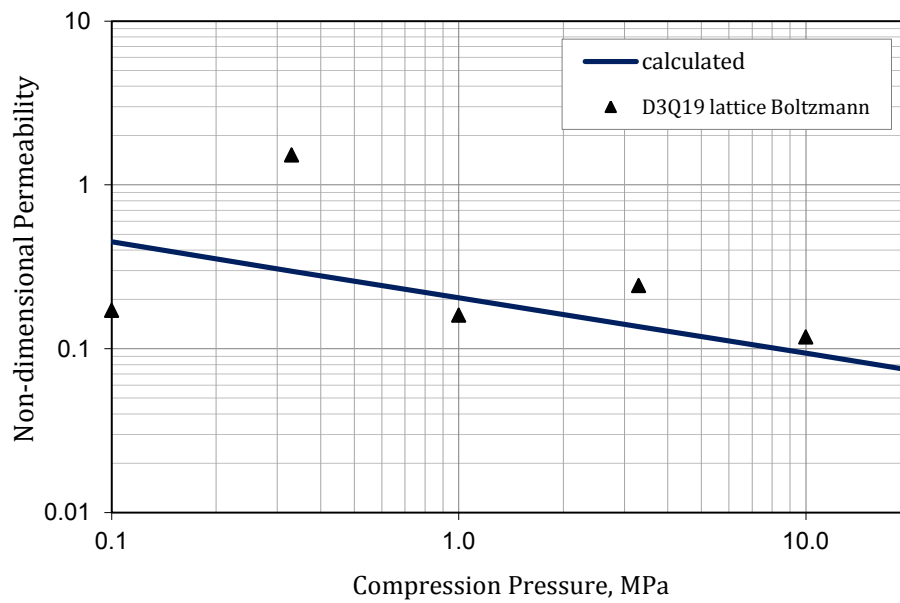


Figure 8.9. non-dimensional through-plane permeability as a function of carbon cloth GDL compression pressure

8.3.4. Compression Effects on Tortuosity

The tortuosity is defined as the ratio of the actual path of the fluid flow through the porous media to the thickness of the porous media in the flow direction. Figure 8.10 shows the effect of the compression pressure on the tortuosity σ in the through-plane direction of the compressed carbon cloth GDL. The predicted data are fitted by the generalized equations²³¹:

$$\sigma = (\varepsilon - \varepsilon_0)^q \quad [8.5]$$

where ε_0 is the percolation threshold which is a tunable parameter to control the fluid flow transport through the porous media. q is an exponent and equals to -1.5. The value of the percolation threshold ε_0 is rarely reported in the literature. Therefore it is difficult to estimate the value for a specific range for the carbon cloth since it depends on the fiber arrangement. In the previous study of uncompressed regular woven carbon cloth GDL in Chapter 7, the percolation threshold ε_0 is tuned to a value of 0.6 for the best results. For the compressed carbon cloth employed in this study, the percolation threshold ε_0 is set to 0.09 which falls within the range of 0.037 ~ 0.33 as reported by Gostick *et al*⁸⁶ for porous medium with randomly overlapping fiber structures.

Basically, the results show that the decrease in porosity will result in an increasing of the tortuosity. For uncompressed sample with porosity around 80% the through-plane tortuosity has a value around 2. With decreasing the porosity down to 40% due to the exerted compression pressure, the tortuosity reaches a value of 5 which demonstrates that 40% decrease in porosity can result in about 150% increasing in tortuosity for the carbon cloth GDL studied. This indicates that the compaction of the fiber bundles of the GDL structure with increasing compression pressure changes the pore distribution and connection within the GDL therefore extends the actual pathways which become more tortuous for gas transport through.

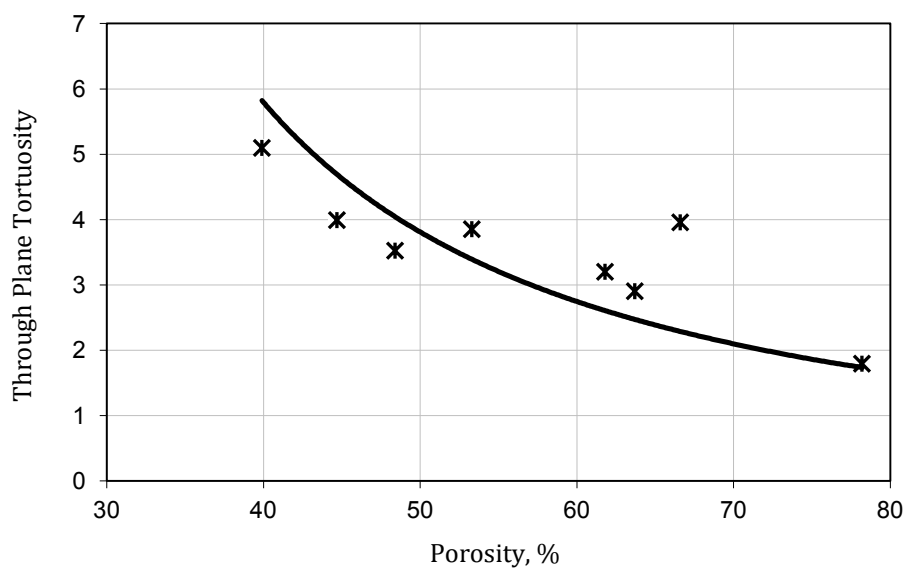


Figure 8.10. Through-plane tortuosity as a function of porosity for all uncompressed and compressed carbon cloth GDL samples.

8.3.5. Compression Effect on 1D Partial Pressure

The compression effects on the GDL structure and the transport properties have been reported in previous section. Therefore in this section one dimensional partial pressure of water and oxygen across uncompressed and compressed GDLs in through-plane direction are simulated using LB model for the purpose of understanding the compression effects on the flow transportation within the GDL. The simulations are carried out at current density range of 0.2 ~1.2 A/cm². The cell operating conditions for the simulation are shown in Table 8.2.

Properties	Values
Cell temperature, °C	70.0
Cell area, cm ²	5.0
PEM thickness, μm	25.4
PEM equivalent weight, g/cm ³	1100.0
Cathode pressure, bar	1.0
Cathode RH	50%
Anode pressure, bar	1.5
Anode RH	0%

Table 8.2. Thermodynamic operating conditions for calculating the boundary conditions for LB model by the 1D GTE fuel cell model.

In the SPMC LB model, the channel/GDL interface and GDL/catalyst layer interface are the two boundaries where the partial pressure and flow rates of each species are specified, respectively. However, due to the compression effect, the parameters of the compressed GDL such as thickness, porosity, permeability and tortuosity are changed. The boundary conditions for all compressed GDLs therefore are different and need to be calculated according to the GDL structural parameters. In previous section the results of porosity, permeability and tortuosity of the compressed GDLs are presented and validated. These parameters were supplied to the 1D GTE model to calculate the boundary conditions of partial pressure and flow rate for the GDL samples. The details were explained previously in section 6.3 of Chapter 6.

Water Partial Pressure

Figure 8.11~8.13 illustrate the one dimensional water partial pressure distribution of the compressed GDL samples in the through-plane flow direction which is perpendicular to the x-y plane. The compressed GDL samples employed are of 0.1 MPa, 1.0 MPa, 10.0 MPa and 20.0 MPa compression pressure. The simulations are carried out at three operating current densities of 0.2 A/cm², 0.6 A/cm² and 1.2 A/cm². The x-axis represents the non-dimensional thickness of the GDL where the 0.0 position represents the channel side of the GDL and the 1.0 position represents the catalyst layer side of the GDL.

Similar to the previous work done in Chapter 6, the water and oxygen flow rate at the GDL/catalyst layer boundary is presented in Figure 8.14 to clarify the flow direction. Since the pressure profile in all the samples shows the same gradient, water and oxygen flow rate data for the 1.0 MPa sample is used and generated at 0.2 A/cm², 0.6 A/cm² and 1.2 A/cm² current density. The positive value of the flow rate shows that the flow transports from channel side of the GDL to the catalyst layer side. This is because the molecular diffusion overcomes the electro-osmotic dragged flow which results in the flow transport towards the catalyst side. As for the negative value, it indicates that the flow transports in from catalyst layer side of the GDL to the channel side due to the strong electro-osmotic drag.

At low current density of 0.2 A/cm² as shown in Figure 8.11, water moves from channel side of the GDL towards the catalyst layer side of the GDL which causes the water pressure decreases from channel side of the GDL towards catalyst side. This is because the stronger diffusion of water overcomes the electro-osmotic drag which drives water flows through the GDL towards catalyst layer side as can be seen in Figure 8.14. For the uncompressed GDL, the pressure difference across the GDL is 36.3 Pa. By increasing the compression pressure from 0.1 MPa to 20.0 MPa, the pressure difference across the GDL increases 64.4% from 37.4 Pa to 105.2 Pa. It has been reported previously that the compaction of the GDL fiber bundle structures due to the compression causes reduction of porosity and through-plane permeability and increase in tortuosity. This therefore restricts the gas transport through the GDL.

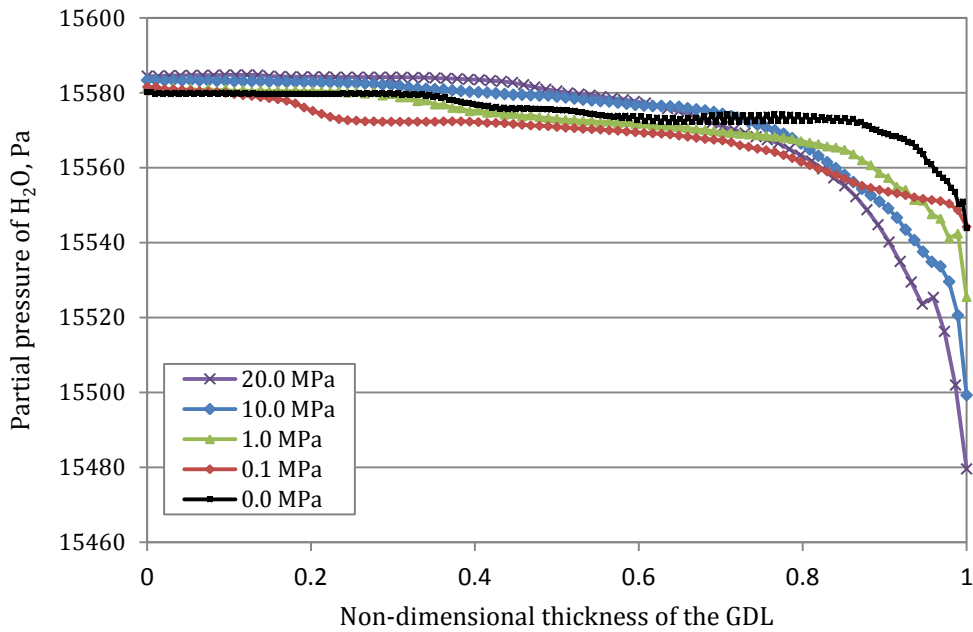


Figure 8.11. Compression effect on partial pressure of water at 0.2 A/cm² current density

At medium current density of 0.6 A/cm² as shown in Figure 8.12, the water pressure decreases towards channel side of the GDL. This pressure gradient can be explained by the water flow rate presented in Figure 8.14. The water flow rate at medium and high current density conditions gives negative values which means that the water flow transports from GDL/catalyst layer side towards channel side. This is because at the GDL/ catalyst layer interface the electro-osmotic drag overcomes the water diffusion. Therefore it can be understood that the water pressure decreases from catalyst side of the GDL to the channel side of the GDL. The results show that for uncompressed GDL the pressure at channel side of GDL is 153 Pa lower than that at the catalyst side. By increasing the compression pressure from 0.1 MPa to 20.0 MPa, the LB model suggests that the pressure difference from catalyst side to the channel side of the GDL increases 66.2% from 158 Pa to 467 Pa. This is again due to the decrease in porosity and through-plane permeability of the computation of the GDL structures with compression pressure. Besides, the increase in tortuosity with compression pressure also brings the difficulties to the flow to transport through the GDL.

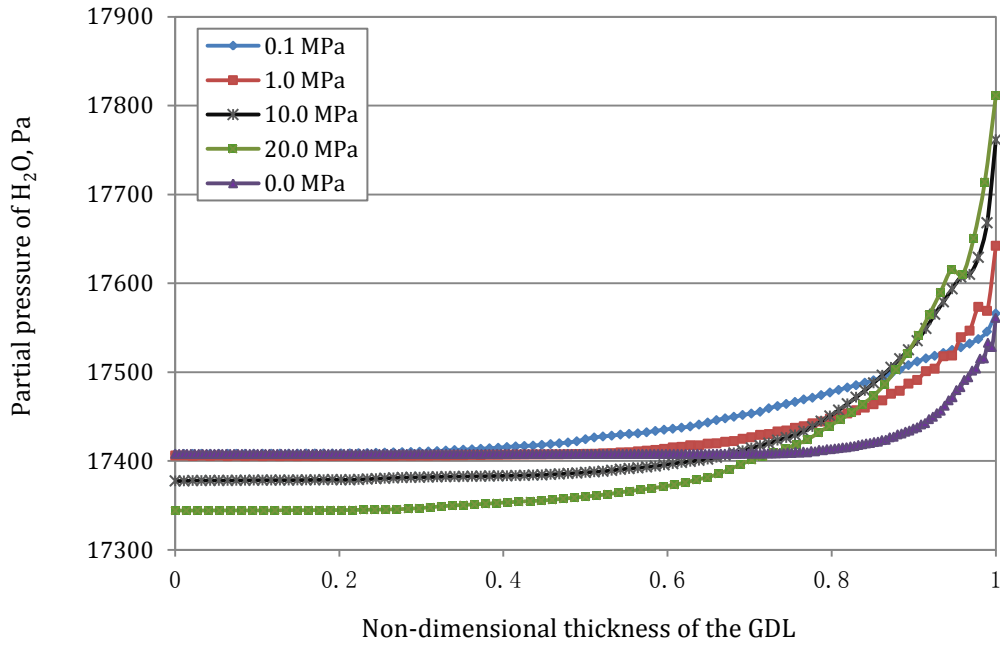


Figure 8.12. Compression effect on partial pressure of water at 0.6 A/cm² current density

In Figure 8.13 at high current density of 1.2 A/cm², the water flow leaves the GDL towards the channel, therefore the water pressure decreases from catalyst side of the GDL towards channel side. For the GDL with 0.1 MPa compression load, the pressure at catalyst side of GDL is 438 Pa higher than that at the channel side of the GDL. However for the 20.0 MPa compression case, the pressure difference from catalyst side to channel side of the GDL reaches 5008 Pa which is 91.2% higher than that of 0.1 MPa compression pressure. The results again indicate that the water partial pressure can be influenced by the compression pressure since the porosity and through-plane permeability of the GDL are reduced.

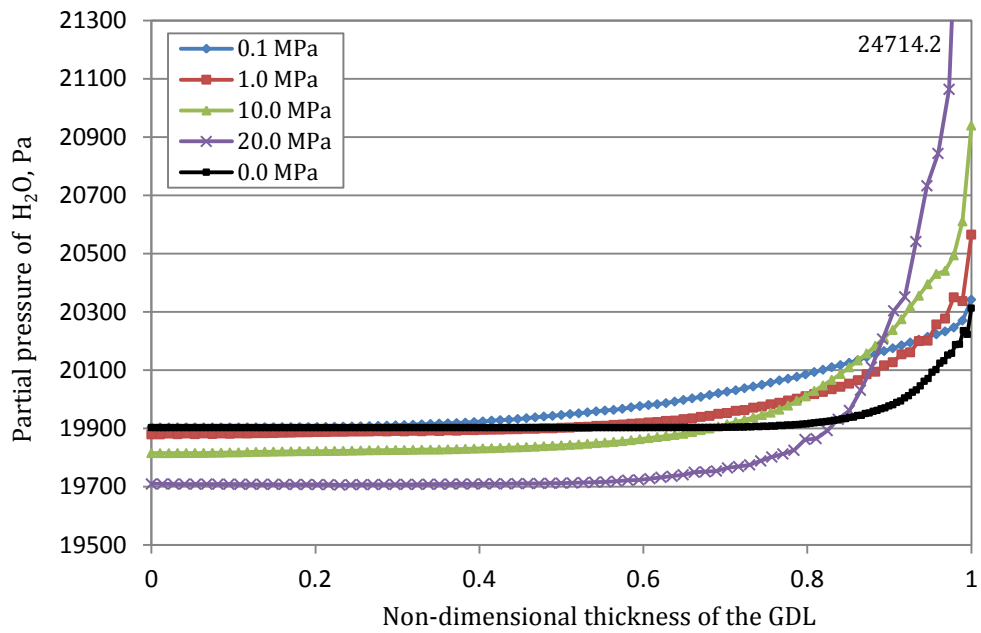


Figure 8.13. Compression effect on partial pressure of water at 1.2 A/cm² current density

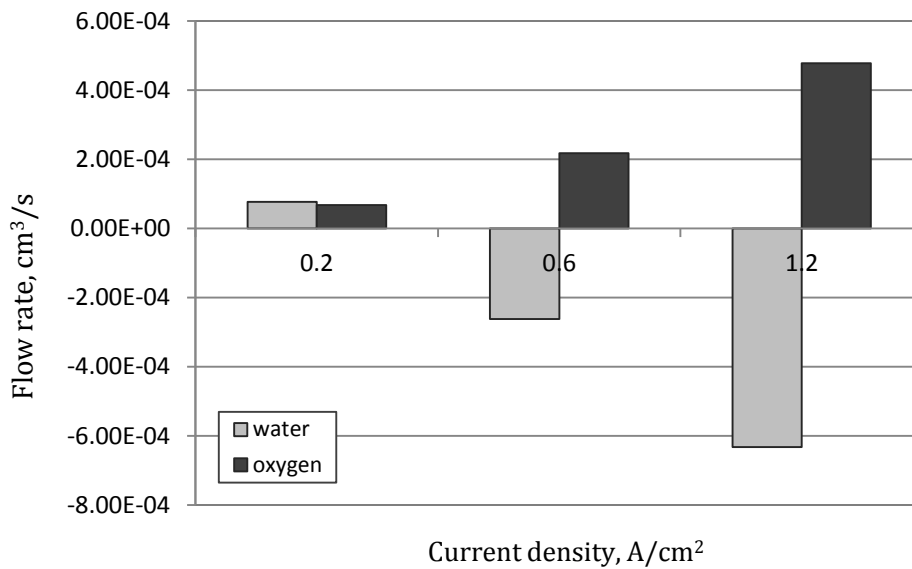


Figure 8.14 Simulated water flow rate at GDL/catalyst layer interface for the GDL with 1.0 MPa compression pressure at 0.2 A/cm², 0.6 A/cm² and 1.2 A/cm² current density condition.

Oxygen Partial Pressure

Figure 8.15~8.17 show the one dimensional oxygen partial pressure distribution across the GDLs compressed at 0.1 MPa, 1.0 MPa, 10.0 MPa and 20.0 MPa compression

pressure and uncompressed GDL at 0.2 A/cm², 0.6 A/cm² and 1.2 A/cm² current densities. The x-axis representation of the GDL is the same as in Figure 8.11~8.13. Since the oxygen is supplied to the channel and consumed at GDL side of catalyst layer, the oxygen pressure decreases along the through-plane flow direction towards catalyst layer side of the GDL. Overall it can be seen from Figure 8.15~8.17 that the oxygen pressure difference across the GDL increases with increasing the compression pressure. At low current density of 0.2 A/cm² in Figure 8.15, the values pressure drop from the channel side to the catalyst side for all cases are within 0.9%. In Figure 8.16, at 0.6 A/cm², for the GDL with 0.1 MPa compression pressure, the pressure at catalyst side of the GDL is 1.1% lower than that at channel side. This pressure drop increases to 3.3% for the GDL compressed to 20.0 MPa compression pressure. At high current density of 1.2 A/cm² as can be observed in Figure 8.17, for 20.0 MPa compression case, the pressure at the catalyst side of the GDL is 94.6% lower than that at the channel side of the GDL. The reasons of these results again are that the porosity and the through-plane permeability are reduced by the applied compression pressure; also the tortuosity of the GDL increases due to the compression effect.

Incidentally, the oxygen partial pressure for the 20.0 MPa sample in Figure 8.15 shows relatively higher than others; however it exhibits the same pressure gradient compared to others. By comparing the pressure drop for the 20.0 MPa sample to that of the other samples, as illustrated in Figure 8.19, it can be observed that the pressure drop across the GDL sample increases with increasing the compression pressure; and the higher pressure drop happens on 20.0 MPa sample. This would suggest that the reasonable result of pressure drop obtained for the 20.0 MPa sample is possible to prove the correct prediction on the pressure profile. As for the visible pressure appearance of the 20.0 MPa sample shown in this figure, it might be due to the small scale of the pressure drop at low current density which enlarges the difference of the pressure profile between different samples.

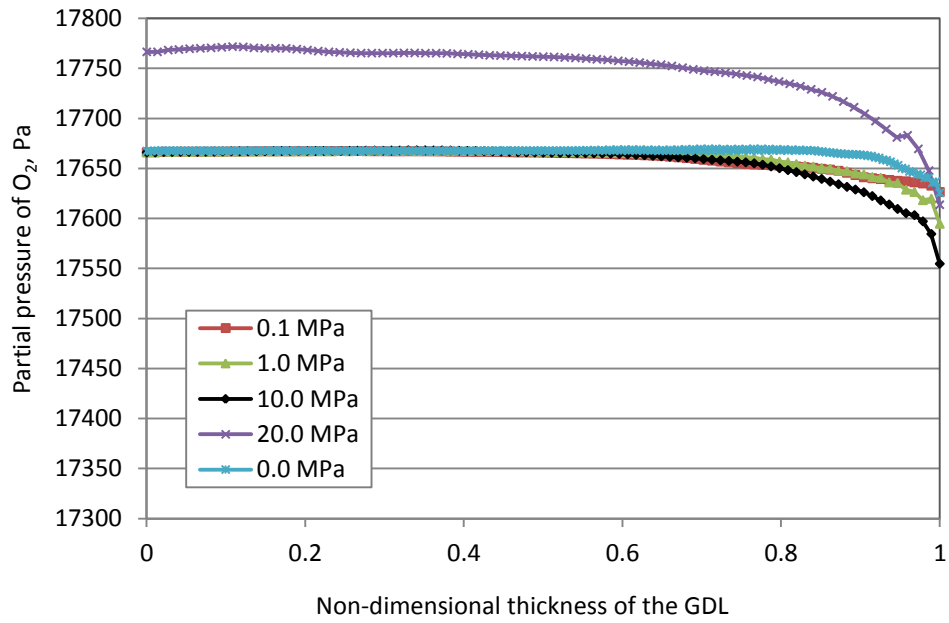


Figure 8.15 Compression effect on partial pressure of oxygen at 0.2 A/cm² current density

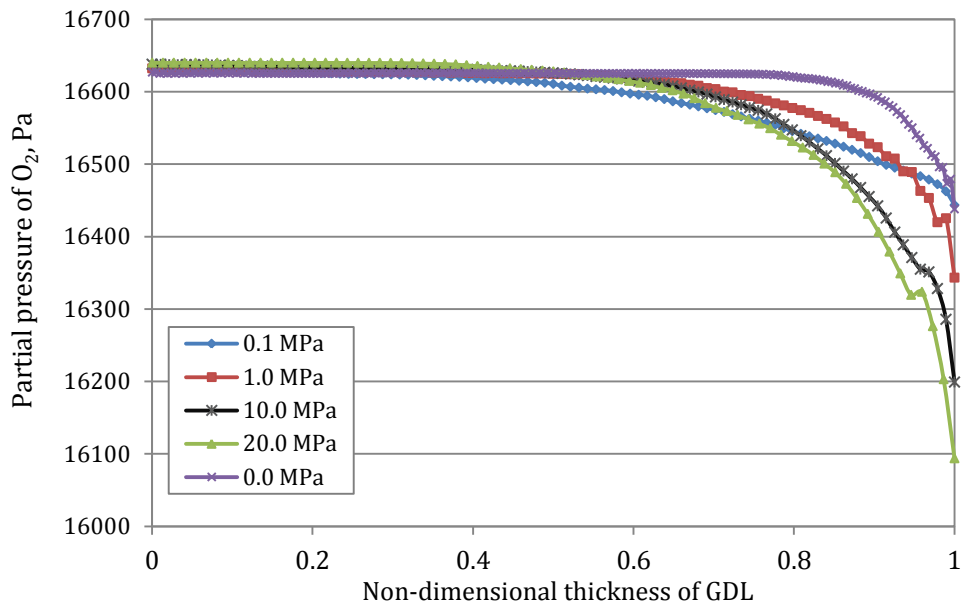


Figure 8.16. Compression effect on partial pressure of oxygen at 0.6 A/cm² current density.

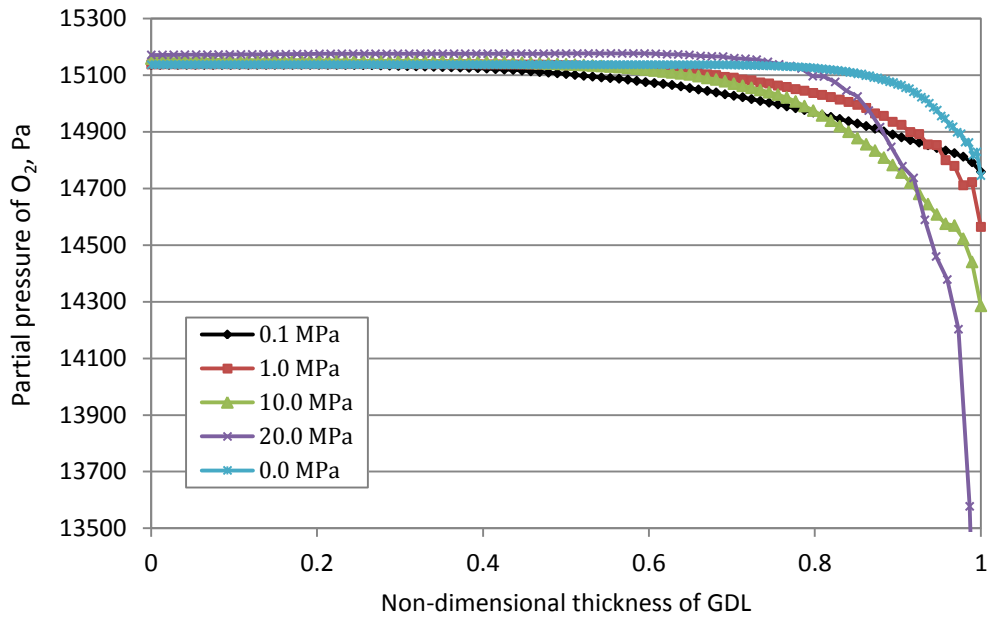


Figure 8.17. Compression effect on partial pressure of oxygen at 1.2 A/cm² current density.

The pressure difference across the GDL of water and oxygen has been summarized in Figure 8.18 and Figure 8.19, respectively. The y-axis represents the pressure difference across the GDL from the channel side to the catalyst side. Therefore the negative values of the pressure difference shown in Figure 8.17 means that the pressure decreases across the GDL from catalyst side to the channel side. It can be observed from both Figure 8.18 and Figure 8.19 that the pressure difference across the GDL increases with increasing the current density for all GDL cases. It also can be seen that the uncompressed GDL has the smallest pressure difference at all three current densities and the pressure difference increases with compression. Therefore it confirms that the water and oxygen transport across the GDL thickness can be influence by the compression exerted onto the GDL, since the porosity and through-plane permeability are reduced with compression which also reversely increases the tortuosity of the GDL due to the structural change explained previously.

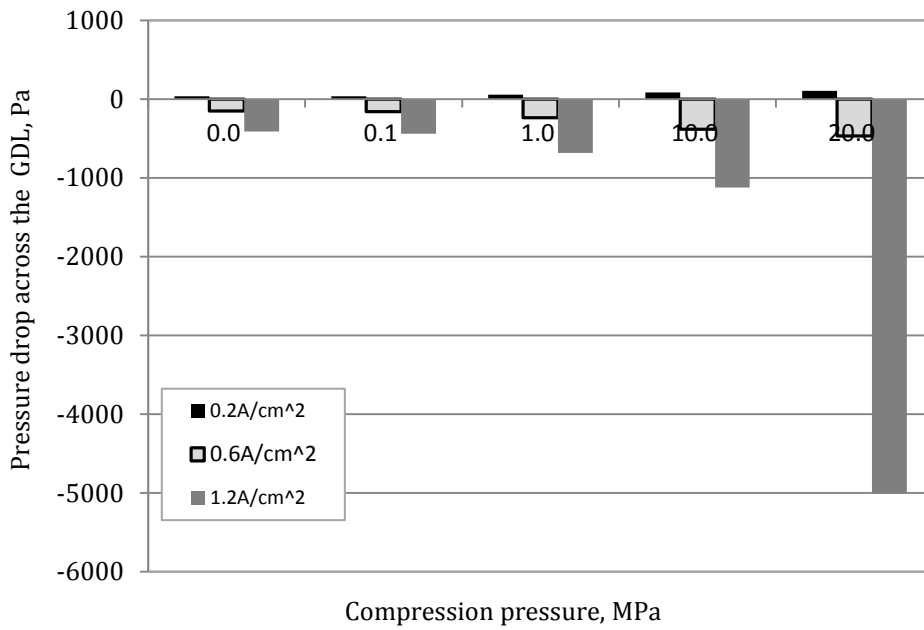


Figure 8.18 The pressure drop of water vapour across the GDL against the compression pressure of 0.0~20.0 MPa at current density of 0.2 A/cm², 0.6 A/cm² and 1.2 A/cm².

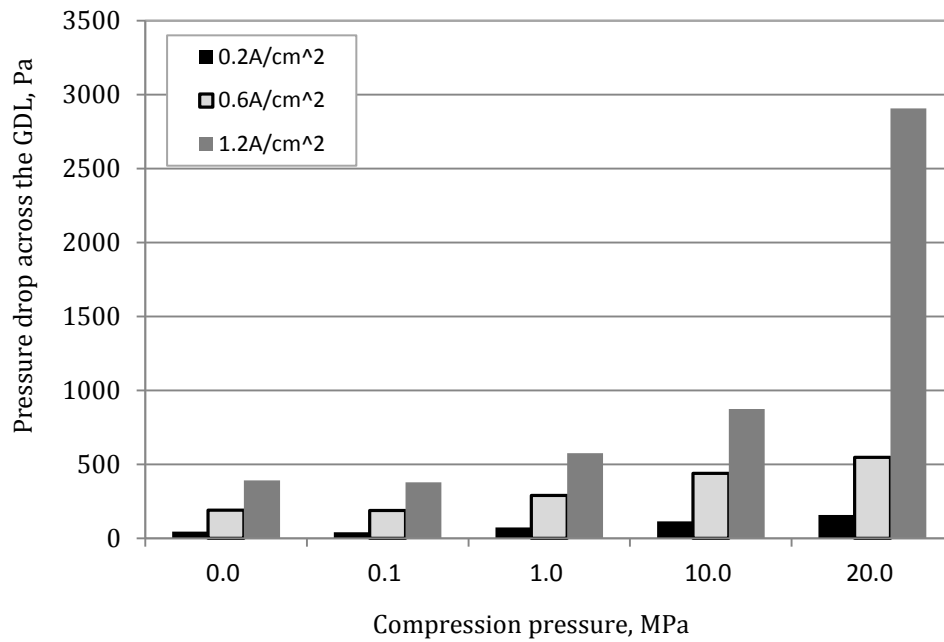


Figure 8.19 The pressure drop of oxygen across the GDL against the compression pressure of 0.0~20.0MPa at current density of 0.2 A/cm², 0.6 A/cm² and 1.2 A/cm².

8.4. Conclusions

During fuel cell assembly the assembly compression pressure applied to the fuel cell is necessary since proper compression pressure can prevent from leakage problem, but this compression pressure also has effects on the porous GDLs which provide pathways for reactant and product water transport through. However due to the complex geometry and micro-scale of the GDL interior structure, it is difficult to carry out detailed study on physical properties of GDLs and the flow characteristics within the GDLs. Therefore in order to have a deeper understanding of the compression effects on the porous GDL structure and the transport properties and the flow transport within the GDL, in this study it reports the Lattice Boltzmann simulation on the reconstructed 3D digital images of the actual compression GDL structure which are generated using the x-ray tomography technique. The following conclusions are drawn from this study:

<1>. All the samples are from the same batch of carbon cloth GDL and are compressed individually at different compression levels in the range of 0 ~ 100 MPa. The compression process is carried out by saturating the carbon cloth GDL with PDMS and then hot-pressed to form flexible elastomer. The x-ray tomography then is used to carry out the imaging process of the PDMS treated samples. The compressed GDL samples are reconstructed to 3D digital binary images.

<2>. The structural inspection of the three-dimensional reconstructed of the compressed GDLs have shown that the general compaction of the fiber bundles can be found at initial compression up to 0.3 MPa compression. With increasing the compression pressure to 3.3 MPa, the fiber bundles are extended towards their length directions which reduce large pore space in areas of intersection fiber bundles. As the compression increases up to 100.0 MPa the deformation of individual fibers occurs.

<3>. The pore size distribution (PSD) data of the compressed carbon cloth samples are generated. The results explain that the increasing in compression pressure on the carbon cloth structure will reduce the pore size. The maximum pore size of the samples drops from 125 μm of uncompressed sample to 31 μm by 100 MPa compression pressure. The average pore size reduces from 33 μm to 12 μm , however, the pore sizes in the range of 10 ~14 microns has the largest population within the GDL for both compressed and uncompressed GDL samples.

<4>. The compression effects on permeability, porosity and tortuosity are studied. The results of the degree of anisotropy of GDLs with compression of 0.1 MPa to 20.0 MPa compressions show that the compression range of 0.3 to 10.0 MPa will give optimum in-plane permeability to through-plane permeability. The porosity is presented as a function of compression pressure and fit by a logarithmic expression. The result shows the decreasing of porosity with increasing of compression loads. The relationship of non-dimensional permeability as a function of porosity agrees well with Kozeny-Carmen equation with KC constant set to 1.3. The through-plane permeability is correlated to compression pressure. The result shows the decreasing in through-plane permeability with increasing the compression pressure. The through-plane tortuosity as a function of porosity is presented with the threshold percolation ε_0 set to 0.09. The results indicate that decreasing of porosity reversely increases the tortuosity under compression pressure.

<5> One-dimensional partial pressure of water and oxygen across the GDL in the through-plane direction is presented at three operating conditions: 0.2 A/cm², 0.6 A/cm² and 1.2 A/cm². The GDLs selected are with compression pressure of 0.0~20.0 MPa. The results show that compression pressure applied across the GDL can influence the 1D partial pressure of water and oxygen. By increasing the compression pressure from 0.1 MPa to 20.0 MPa, the values of pressure difference of water increase by 64.6%, 66.2% and 91.2% at 0.2 A/cm², 0.6 A/cm² and 1.2 A/cm² current density, respectively. The results of oxygen partial pressure also show an increasing in the pressure difference across the GDL with compression pressure. These results demonstrate that the flow transport within the GDL can be affected due to the decrease in porosity and through-plane permeability and increase in tortuosity with compression.

CHAPTER 9. **Conclusions**

9.1. Conclusions

This research work is specialized in the study of carbon based GDL material and the simulation of flow characteristics within the GDL. The main contribution of the work is primarily made to establish the integrated simulation methodology of LB model and x-ray tomography imaging technique. The developed x-ray tomography based LB model aims at providing a better understanding on the microstructure of the porous media and the flow transport phenomena within it.

The GDLs play important roles in a PEM fuel cell of transporting reactant to the catalyst layers, removing excess water out of the catalyst layer and conducting electrons. Due to the high porosity and electrical conductivity, carbon based materials are usually chosen to make the GDLs. The common two GDL materials are carbon paper and carbon cloth. The carbon paper GDL is produced by randomly arrangement of carbon fiber and the carbon cloth GDL consists of regular woven bundles in weave pattern. Due to the difference in fiber arrangement, the structural influence of carbon paper and carbon cloth on GDL characteristics and flow transport phenomena within are different. However both the types of GDL structures exhibit porous and heterogeneous nature. Literatures have reported many works on the GDL study at various aspects. Most of the models are based on macroscopic approach to describe the transport phenomena of the GDLs; a few groups have studied the GDLs at pore-level using pore-network model; CFD method also have been used as a numerical tool to investigate the fluid flow within the GDL. These models simulate the fluid flow transportation phenomena by either volume averaged frame or by solving complex partial differential equations. Besides, due to the

complex micron-scale structure involved, almost all of the existing works employ stochastic techniques to reconstruct digital three-dimensional models of the carbon based GDLs. In order to gain in-depth understanding of the transport properties and flow characteristics in the GDL at micro-scale, new image reconstruction techniques are required to reveal the actual structural characteristics of the GDL.

More recently, advanced imaging techniques have been employed as a tool to capture detailed microstructural characteristics and flow transportation within the GDL such as scanning electron microscopy (SEM), nuclear magnetic resonance (NMR) microscopy, neutron imaging, micro/nano tomography and fluorescence microscopy. Among them, the x-ray tomography imaging technique has been proved as a noninvasive technique to reconstruct the three-dimensional images based on the actual structures of the carbon paper/cloth GDLs with resolution up to micron scale. The usage of the x-ray tomography ensures the reconstructed GDL structures employed for the simulation close to reality to the maximum. The x-ray tomography system consists of x-ray sources and x-ray detectors. The process of reconstructing a three-dimensional porous GDL structures by x-ray tomography includes mainly three steps: (1) two-dimensional image acquisition. This first step will generate two-dimensional shadow images which are all in grey scale; (2) the obtained two-dimensional shadow images have to be processed and threshold-tuned before the images can be reconstructed into three-dimensional structures and (3) reconstruction of the three-dimensional binary images using CTAn software. The 3D reconstructed digital binary images generated by the x-ray tomography can be directly read by the LB model for simulation.

Simulation on fluid transport within the GDL has been reported in literatures. Most of the works use the traditional simulation methodologies such as CFD which solves the complex partial differential equation. However, the LB method, originally from the LGCA, has the capacity of simulating the fluid flow in complex porous geometry by tracking collision and streaming of the particles in the porous GDL. The LB method constructs micro/mesoscopic behavior of particles to investigate the macroscopic phenomena but also independently focus on micro-world without being restrained by the macroscopic phenomena of the system. The basic unit in the LB method is a regular lattice. The D3Q19 lattice scheme used for this research states that for particles on a three-dimensional lattice cube, there are 19 velocity directions available for moving. The bounce-back method is employed for the treatment of void-solid boundary in the LB

simulation due to its simplicity. The adoption of the single relaxation term of BGK in the LB method helps the velocity distribution function gets close to equilibrium state.

The work presented in this research employs a modified single phase LB model which was previously developed for application on soil structure to simulate the fluid flow transportation within the GDL. The three-dimensional microstructures of the carbon paper and carbon cloth GDLs are generated by the x-ray tomography imaging technique. The boundary conditions of flow rate and partial pressures of the reactants at the two side of the GDL are supplied. The single component LB model is used to calculate the transport properties of the GDL such as porosity, permeability and tortuosity; and the multi-component LB model is capable of simulating the flow transport within the GDL. Simulation studies are carried out in two groups. One group of study is on the carbon paper GDL and the other group is on the carbon cloth GDL. Due to the limitation of the x-ray detector area as well as the computational resource, it is difficult to image and carry out simulation on large size of gas diffusion layer samples. Therefore for large carbon paper or carbon cloth samples, they are divided into small-sized regions for imaging and simulation.

The study of carbon paper GDLs can be summarized as:

<1>. Based upon the three-dimensional reconstructed structures acquired by the x-ray tomography from the actual carbon paper GDL structures, the 3D single phase LB simulation show that for the carbon paper employed in this research the mean absolute through-plane permeability is around two orders higher than that of the in-plane. The results have been validated with the experimental values and show good agreement.

<2>. When the pressure is applied in the through-plane direction, the flow will travel not only in through-plane direction but also in the in-plane direction. The structural inspection of the carbon paper GDL show that the existence of large pore volume in the structures ensure higher through-plane permeability while lower through-plane permeability is due to the tight structure and lacking of large pore space.

<3>. The one-dimensional partial pressure of water, oxygen and nitrogen are obtained under four different operating conditions. The non-linearity of the pressure profiles of all the gases predicted by the LB model indicates the heterogeneity of the porous GDL structure, since the LB simulation is performed by tracking the collisions between particles and with the walls.

Different from carbon paper, the carbon cloth material is structured by regular woven bundle and can be compressed by 30%~50%. So for the carbon cloths GDLs there are two sets of studies: uncompressed GDL and compressed GDL. All the GDL structures are reconstructed using the x-ray tomography technique so that the reconstructed three-dimensional binary images contain the actual information of the GDL. For the carbon cloth GDL without compression, the results show that:

<1>. The value of mean through-plane permeability of the carbon cloth is one order of magnitude higher than that of the in-plane permeability. The structural inspection explains that the lower permeability of the structures can be due to the tight arrangement of the regular weave pattern fiber bundle layout. The existence of large void space especially at areas where two fiber bundles intersect allows the gas transport easily hence higher permeability.

<2>. The results of degree of anisotropy of different regions of one cloth have been obtained and agree well with the experimental values. By examining the fiber alignment of the samples it has been found out that the degree of anisotropy can be influenced by the fiber bundle layout and individual fiber arrangement. Higher anisotropic permeability exists in areas where contains void space between or around the four intersecting fiber bundles.

<3>. The dependency of the dimensionless permeability to the porosity of the carbon cloth GDL has been obtained and agrees well with the Carman-Kozeny (KC) equation and Tomadakis-Sotirchos (TS) equation. The KC constant value of has been tuned to 44 for the porosity range of 91% ~ 95.5%; and in the TS model the percolation threshold ε_p is tuned to 0.61. These two methods give the average errors of 13.4% and 12.1%, respectively.

Since the assembly pressure is applied to the operating fuel cell, the GDLs are also compressed due to these pressures however the GDLs have to provide pathways for the reactant and product water transport. So the compression effects on the carbon cloth GDL structure and transport properties and flow transport within the GDL are studied. The results are summarized below:

<1>. The samples that are from the same batch of carbon cloth GDL are compressed at different compression levels of 0.1 MPa, 0.33 MPa, 1.0 MPa, 3.3 MPa, 10.0 MPa, 20.0 MPa

and 100.0 MPa. The structural inspection of the three-dimensional reconstructed of the compressed GDLs have shown that the general compaction of the fiber bundles can be found at initial compression up to 0.3 MPa compression. With increasing the compression pressure to 3.3 MPa, the fiber bundles are extended towards their length directions which reduce large pore space in areas of intersection fiber bundles. As the compression increases up to 100.0 MPa the deformation of individual fibers occurs.

<2>. The pore size distribution (PSD) data of the compressed carbon cloth samples are generated. The results reveal the pore size distribution with the compression loads. It has been found out that the maximum pore size drops from 125 μm of uncompressed sample to 31 μm of 100 MPa sample. The average pore size also decreases from 33 μm to 12 μm . However, the main pore sizes are in the range of 10 ~14 microns. This band of pore size contributes to the largest population within the GDL for both uncompressed and compressed GDLs.

<3>. The compression effects on through-plane permeability, porosity and through-plane tortuosity are studied. The porosity is presented as a function of compression pressure and fit by a logarithmic expression. The results show decrease in porosity with increasing the compression pressure. The relationship of non-dimensional permeability as a function of porosity agrees well with Kozeny-Carmen equation with KC constant set to 1.3. The results of through-plane permeability against compression pressures show decreasing of through-plane permeability with increasing the compression pressure. The through-plane tortuosity as a function of tortuosity indicates that decreasing in porosity reversely increases in tortuosity.

<4>. One-dimensional partial pressure of water and oxygen across GDL thickness is presented at three operating conditions: 0.2 A/cm², 0.6 A/cm² and 1.2 A/cm². The GDLs selected are with compression loads between 0.0 MPa to 20.0 MPa. The results show that the compression pressure applied across the GDL can influence the 1D partial pressure of water and oxygen. This is mainly due to the decrease in porosity and through-plane permeability and the increase in tortuosity with compression.

Overall this research has demonstrated the capability of using three-dimensional single phase LB model and x-ray tomography imaging technique to investigate the microstructure and transport properties of the porous media of GDLs and to predict flow characteristics in gas diffusion layer. The good agreement between the results

generated by the LB model and the published literature data proves the reliability of this combined methodology in produce accurate results. In summary, this x-ray tomography based LB method distinguished itself from others methodologies in that:

<1> The LB method simulates the fluid dynamics by tracking the streaming and collision of a number of fictitious particles in a lattice, rather than directly solve the partial differential equations.

<2> The x-ray tomography imaging technique as a noninvasive technique is able to reconstruct three-dimensional digital images based on actual microstructures of the porous carbon based GDLs that does not need sample preparation.

<3> The 3D digital images of the carbon GDLs samples can be directly uploaded to the LB model for flow simulation based on the actual GDL geometry. The single phase LB model can calculate the transport properties such porosity, permeability and tortuosity; and the multicomponent LB model can predict the flow transport within the GDL.

9.2. Recommendation for Future Work

The work presented in this thesis proves the capacity of the x-ray tomography based LB model in predicting flow characteristics and transport phenomena in porous media. However it is still at an early stage of its evolution to be developed to a comprehensive LB tool in aspects of integration and efficiency. Based on the experience gained through this research work, the following recommendations for the future work on aspects of porous media modelling in fuel cell context and LB simulation are provided:

For the porous media simulation in PEM fuel cell, future work on the following areas may be carried out to extend the research to gain better understanding on the porous media and the PEM fuel cell performance:

<1> The water management issue is one of the most important part in the PEM fuel cell since the accumulation of liquid water can block pores of the porous GDL and cathode catalyst layer causing water flooding. In the current study, the simulation was carried out only on gas phase and liquid water existence is not considered. The liquid water treatment could be included by extending the single phase LB model to two phase LB model.

<2> The MPL is a microporous layer containing hydrophobic agent. This layer can provide proper surface pore size and hydrophobicity to avoid flooding problem and to provide intimate electronic contact with the catalyst layer. The GDL samples employed in this research contain no MPL. The MPL model could be added to the current model in future work so that full GDL function within the PEM fuel cell can be simulated and better understood.

<3> The electrical and thermal conductivity of the GDL can be affected by the inhomogeneous compression exerted by the flow field plate when the fuel cell is assembled together by the applied compression pressure. Increasing the compression pressure improves the electrical and thermal conductivity however hinders reactant transport and water removal. Therefore it could be important to target the appropriate compression pressure range to maintain the optimal cell performance.

<4> The limiting current is a representative parameter of oxygen transport limitations through layers where no electrochemical reaction taking place, such as the GDL. In literature, however, few works has been done to correlate the GDL characteristics to the limiting current or the systematic performance effects. This research area might worth to be carried out for updating the understanding of the GDL properties on the PEM fuel cell performance.

For the improvement on the LB model for future applications, the following aspects could be considered to meet wide demands on LB simulation:

<1> The LB simulation requires large computational resource and processing time which in reality limits the image size which can be handled by the LB model. Parallel computing could be an advantage for LB simulation to meet its large computational demands so that large image mesh that may contain more representative features of the interested structure could be processed.

<2> In the LB simulation, the spatial resolution of the LB model has to match the resolution of the 3D binary image according to the image size, the complexity of the 3D structure and the computational resources available. The relationship between the optimum spatial resolution of the LB model and the resolution of the 3D image could be an area to be explored as the sensitivity study by examining the influence of varying the spatial resolution of the LB model on the accuracy of the results which is not included in the current research.

<3> The LB model developed in this research is still at its early stage, the LB simulation procedure could be difficult to operate directly by users. Therefore future development on the LB model could be carried out to normalize the LB simulation frame to a user-friendly platform to save manpower and be developed into a LB simulation software package for more comprehensive applications.

REFERENCE

- ¹ http://en.wikipedia.org/wiki/Fuel_cell
- ² <http://americanhistory.si.edu/fuelcells/pem/pemmain.htm>
- ³ Djilali, N., “*Computational Modeling of Polymer Electrolyte Membrane (PEM) Fuel Cells: Challenges and Opportunities*”, *Energy*, 2007, 32, 269–280
- ⁴ O’Hayre, R., Cha, U. W., Colella, W., Prinz, F. B., “*Fuel Cell Fundamentals*”, John Wiley & Sons Inc., 2009. pp. 262.
- ⁵ James Larminie, Andrew Dicks, “*Fuel Cell Systems Explained*”, 2nd ed., Wiley, 2003.
- ⁶ Electrochemistry Encyclopedia, *Proton Exchange Membrane or Polymer Electrolyte Membrane (PEM) Fuel Cells*, “ <http://electrochem.cwru.edu/encycl/>”, Ryan Baker and Jiujun Zhang, April, 2011
- ⁷ Amphlett, J. C., Baumert, R. M., Mann, R. F., Peppley, B. A., Roberge, P. R., and Harris, T. J. “*Performance Modelling of the Ballard Mark IV Solid Polymer Electrolyte Fuel Cell*”, *J. Electrochem. Soc.* 1995, 142, 1–8.
- ⁸ Kim, J. S.-M. Lee, S. Srinivasan, and C. E. Chamberlain, “*Modelling of Proton Exchange Fuel Cell Performance with An Empirical Equation*”, *J. Electrochem. Soc.*, 1999, 2, 197-200
- ⁹ Mishra, V., Fang, Y., Pitchunani, R., “*Analysis and Design of PEM Fuel Cells*”, *J. Power Sources*, 2005, 141, 47-64
- ¹⁰ Stambouli, A., Traversa, E., “*Fuel Cells, An Alternative to Standard Sources of Energy*”, *Renew. Sust. Energy Rev.* 2002, 6, 295–304.
- ¹¹ Arvind Parthasarathy, Supramaniam Srinivasan, A. John Appleby, and Charles R. Martin, “*Temperature Dependence of the Electrode Kinetics of Oxygen Reduction at the Platinum/Nafion® Interface—A Microelectrode Investigation*”, *J. Electrochem. Soc.* 1992, 139, 2530.
- ¹² Arvind Parthasarathy, Supramaniam Srinivasan, A. John Appleby, and Charles R. Martin, “*Pressure Dependence of the Oxygen Reduction Reaction at the Platinum*

Microelectrode/Nafion Interface: Electrode Kinetics and Mass Transport, J. Electrochem. Soc. 1992, 139, 2856.

¹³ Ticianelli, E. A., Derouin, C. R., Redondo, A., and Srinivasan S., “*Methods to Advance Technology of Proton Exchange Membrane Fuel Cells*”, J. Electrochem. Soc. 1988, 135, 2209.

¹⁴ Junbom Kim, Seong-Min Lee, Supramaniam Srinivasan, and Charles E. Chamberlin, “*Modelling of Proton Exchange Membrane Fuel Cell Performance with an Empirical Equation*”, J. Electrochem. Soc. 1995, 142, 2670.

¹⁵ Chu, H.-S.; Yeh, C.; Chen, F., “*Effects of Porosity Change of Gas Diffuser on Performance of Proton Exchange Membrane Fuel Cell*”, J. Power Sources, 2003, 123, 1.

¹⁶ Berning, T., Djilali, N., “*A 3D, Multiphase, Multicomponent Model of the Cathode and Anode of a PEM Fuel Cell*”, J. Electrochem. Soc. 2003, 150, A1598.

¹⁷ Rowe, A.; Li, X. G., “*Mathematical Modelling of Proton Exchange Membrane Fuel Cells*, J. Power Sources, 2001, 102, 82.

¹⁸ Cheddie, D., Munroe, N., “*Review and Comparison of Approaches to Proton Exchange Membrane Fuel Cell Modeling*”, J., Power Sources, 2005, 147, 72–84

¹⁹ Biyikoglu, A., “*Review of Proton Exchange Membrane Fuel Cell Models*”, Intl. J. Hydrogen Energy, 2005, 30, 1181 – 1212.

²⁰ Bernardi, D. M. and Verbrugge, M. W., “*Mathematical Model of A Gas-Diffusion Electrode Bonded to A Polymer Electrolyte*”. Am. Inst. Chem. Eng., 1991, 37, 1151.

²¹ Bernardi, D. M. and Verbrugge, M. W., “*A Mathematical Model of the Solid-Polymer-Electrolyte Fuel Cell*”. J. Electrochem. Soc., 1992, 139, 2477–2491.

²² Springer, T. E., Zawodzinski, T. A., and Gottesfeld, S., “*Polymer Electrolyte Fuel Cell Model*”. J. Electrochem. Soc., 1991, 138, 2334.

²³ Verbrugge, M. W., Hill, R. F., “*Analysis of Promosing Perfluorosulfonic Acid Membranes for Fuel-Cell Electrolytes*”, J Electrochem Soc 1990; 137(12): 3770–7.

-
- ²⁴ Hill, R. F., Verbrugge, M. W., "Ion and Solvent Transport in Ionexchange Membranes II. A Radiotracer Study of the Sulfuricacid, Nafion 117 system", J Electrochem Soc 1991; 137: 893-9.
- ²⁵ Zawodzinski, T. A., Derouin, C., Radzinski, S., Sherman, R. J., Smith, V. T., Springer, T. E., and Gottfeld, S., "Water Uptake by and Transport Through Nation 117 Membranes", J. Electrochem. Soc., 993, 140, 4, 1041-1047.
- ²⁶ Fuller, T. F. and Newman, J., "Water and Thermal Management in Solid-Polymer-Electrolyte Fuel Cells". J. Electrochem. Soc., 1993, 140, 1218-1225.
- ²⁷ Nguyen, T. V. and White, R. E. "A Water and Heat Management Model for Proton-Exchange-Membrane Fuel Cells". J. Electrochem. Soc., 1993, 140, 2178-2186.
- ²⁸ Singh, D., Lu, D., Djilali, N., "A Two-Dimensional Analysis of Mass Transport in Proton Exchange Membrane Fuel Cells", Int. J. Eng. Sci., 1999, 37, 431-452.
- ²⁹ Gurau, V., Liu, H., Kakac, S., "A Two Dimensional Model for Proton Exchange Fuel Fells", AIChE J. 1998, 44, 2410-2422.
- ³⁰ Amphlett, J. C., Baumert, R. M., Mann, R. F., Peppley, B. A., and Roberge, P. R., "Performance Modeling of the Ballard Mark IV Solid Polymer Electrolyte Fuel Cell I. Mechanistic Model Development", J. Electrochem. Soc. 1995,142, 1.
- ³¹ Amphlett, J. C., Baumert, R. M., Mann, R. F., Peppley, B. A., and Roberge, P. R., "Performance Modeling of the Ballard Mark IV Solid Polymer Electrolyte Fuel Cell II. Emperical Model Development", J. Electrochem. Soc. 1995,142, 9.
- ³² Mennola, T., Noponen, M., Aronniemi, M., Hottinen, T., Mikkola, M., Himanen, O., Lund, P., "Mass Transport in the Cathode of a Freebreathing Polymer Electrolyte Membrane Fuel Cell", J. Appl. Electrochem., 2003, 33., 979-987.
- ³³ Springer, T. E., Wilson, M. S., Zawodzinski, T. A., "Modeling and Experimental Diagnostics in Polymer Electrolyte Fuel Cells". J Electrochem Soc., 1993;140:3513-26.
- ³⁴ Khakpour, M., Vafai, K., "Analysis of Transport Phenomena within PEM Fuel Cells – An Analytical Solution", Intl. J. Heat and Mass Transfer, 2008, 51, 3712-3723.

-
- ³⁵ Mazumder, S., Cole, J., "Rigorous 3-D Mathematical Modeling of PEM Fuel Cells, Part II. Model Predictions with Liquid Water Transport", J. Electrochem. Soc. 2003, 150, A1510–A1517.
- ³⁶ Nam, J., Kaviany, M., "Effective Diffusivity and Water-Saturation Distribution in Single- and Two-layer PEMFC Diffusion Medium", Int. J. Heat Mass Transfer, 2003, 46, 4595–4611.
- ³⁷ Natarajan, D., Nguyen, T. V., "Three-Dimensional Effects of Liquid Water Flooding in the Cathode of a PEM Fuel Cell", J. Power Sources, 2003, 115, 1, 66-80.
- ³⁸ Kulikovskiy, A. A. "Quasi-3D Modeling of Water Transport in Polymer Electrolyte Fuel Cells", J. Electrochem. Soc. 2003, 150, A1432
- ³⁹ Weber, A., Newman, J., "Transport in Polymer Electrolyte Membranes I. Physical Model", J. Electrochem. Soc. 2003, 150(7), A1008-A1015.
- ⁴⁰ Weber, A., Newman, J., "Transport in Polymer Electrolyte Membranes II. Mathematical Model", J. Electrochem. Soc. 2004, 151(2), A311-A325.
- ⁴¹ Weber, A., Newman, J., "Transport in Polymer Electrolyte Membranes III. Model Validation in a Simple Fuel Cell Model", J. Electrochem. Soc. 2004, 151(2), A326–A339.
- ⁴² Kazim, A., Liu, H., Forges, P., "Modelling of Performance of PEM Fuel Cells with Conventional and Interdigitated Flow Fields", J. Appl. Electrochem. 1999, 29, 1409–1416.
- ⁴³ He, W., Yi, J., Nguyen, T., "Two-phase Flow Model of the Cathode of PEM Fuel Cells using Interdigitated Flow Fields", AIChE J. 2000, 46, 2053–2064.
- ⁴⁴ Yi, J. S., and Nguyen, T. V., "Multicomponent Transport in Porous Electrodes of Proton Exchange Membrane Fuel Cells Using the Interdigitated Gas Distributors", J. Electrochemical Soc., 1999, 146 (1), 38-45.
- ⁴⁵ Wang, Y., Basu, S., Wang, C. Y., "Modeling Two-Phase Flow in PEM fuel Cell Channels", J. Power Sources, 2008, 179, 603–617.

-
- ⁴⁶ Li, P., Schaefer, L., Wang, Q., Zhang, T., Chyu, M., "Multi-gas Transportation and Electrochemical Performance of a Polymer Electrolyte Fuel Cell with Complex Flow Channels", *J. Power Sources*, 2003, 115, 90–100.
- ⁴⁷ Um, S., Wang, C., "Three-Dimensional Analysis of Transport and Electrochemical Reactions in Polymer Electrolyte Fuel Cells", *J. Power Sources*, 2004, 125, 40–51.
- ⁴⁸ Eikerling, M., Kornyshev, A. A., "Modeling the Performance of the Cathode Catalyst Layer of Polymer Electrolyte Fuel Cells", *J Electroanal Chem.*, 1998, 453:89.
- ⁴⁹ You, L., Liu, H. T., "A Pseudo-Homogeneous Model for Cathode Catalyst Layer in PEMFCs", *ASME HTD*, 2000, vol. 366-1.
- ⁵⁰ Siegel, N. P., Ellis, M. W., Nelson, D. J., M. R. von Spakovsky, "Single Domain PEMFC Model Based on Agglomerate Catalyst Geometry", *J. Power Sources*, 2003, 115, 81.
- ⁵¹ Pisani, L.; Valentini, M.; Murgia, G., "Analytical Pore Scale Modelling of the Reactive Regions of Polymer Electrolyte Fuel Cells", *J. Electrochem. Soc.* 2003, 150, A1558.
- ⁵² Choi, P.; Datta, R., "Sorption in Proton-Exchange Membranes", *J. Electrochem. Soc.* 2003, 150, E601.
- ⁵³ Jaouen, F.; Lindbergh, G.; Sundholm, G. "Investigation of Mass-Transport Limitations in the Solid Polymer Fuel Cell Cathode", *J. Electrochem. Soc.* 2002, 149, A437.
- ⁵⁴ Ahmed, S., Kopasz, J., Kumar, R., Krumpelt, M., "Water Balance in A Polymer Electrolyte Fuel Cell System", *J. Power Sources* 2002, 112, 519.
- ⁵⁵ Mathias, M., Roth, J., Fleming, J., Lehnert, W., in: Vielstich, W., Lamm, A., Gasteiger, H. A. (Eds.), "Handbook of Fuel Cells: Fundamentals, Technology, Applications", Wiley, 2003, pp. 46.1–46.21.
- ⁵⁶ Hoogers, G. in: Hoogers G. (Ed.), "Fuel Cell Technology Handbook", CRC Press LLC, 2003, pp. 4.1–4.27.
- ⁵⁷ Moreira, J., Ocampo, A. L., Sebastian, P. J., Smit, M. A., Salazar, M. D., P. del Angel, Montoya, J. A., Peirez, R., Martiinez, L., "Influence of the Hydrophobic Material Content in the Gas Diffusion Electrodes on the Performance of a PEM Fuel Cell", *J. Int. Hydrogen*

Energy, 2003, 28, 625–627.

⁵⁸ Park, S., Lee, J. W., Popov, B. N., “*Effect of Carbon Loading in Microporous Layer on PEM Fuel Cell Performance*”, J. Power Sources, 2006, 163, 357–363.

⁵⁹ Giogi, L., Antolini, E., Pozio, A., and Passalacqua, E., “*Influence of PTFE Content in the Diffusion Layer of Low-Pt Loading Electrodes for Polymer Electrolyte Fuel Cells*”, Electrochim. Acta, **43**, 3675, 1998.

⁶⁰ Lufrano, F., Passalacqua, E., Squadrito, G., Patti, A., and Giorgi, L., “*Improvement in the diffusion characteristics of low Pt-loaded electrodes for PEFCs*”, J. Appl. Electrochem., 1999, 29, 445.

⁶¹ Paganin, V. A., Ticianelli, E. A., and Gonzalez, E. R., “*Development and Electrochemical Studies Gas Diffusion Electrodes for Polymer Electrolyte Fuel Cells*”, J. Appl. Electrochem., 1996, 26(3), 297-304.

⁶² Lim, C., Wang, C. Y., “*Effects of Hydrophobic Polymer Content in GDL on Power Performance of a PEM Fuel Cell*”, Electrochim. Acta., 2004, 49, 4149–4156.

⁶³ Lin, G. Y., Nguyen, T. V. “*Effect of Thickness and Hydrophobic Polymer Content of the Gas Diffusion Layer on Electrode Flooding Level in a PEMFC*”, J. Electrochem. Soc. 2005, 152, A1942–A1948.

⁶⁴ Gostick, J. T., Fowler, M. W., Ioannidis, M. A., Pritzker, M. D., Volkovich, Y. M., Sakars, A., “*Capillary Pressure and Hydrophilic Porosity in Gas Diffusion Layers for Polymer Electrolyte Fuel Cells*”, J. Power Sources, 2006, 156, 2, 375-387.

⁶⁵ Liu, C. H., Ko, T. H., Shen, J. W., Chang, S. I., Chang, S. I., Liao, Y. -K., “*Effect of Hydrophobic Gas Diffusion Layers on the Performance of the Polymer Exchange Membrane Fuel Cell*”, J. Power Sources, 2009, 191, 489–494.

⁶⁶ Prasanna, M., Ha, H., Y., Cho, E. A., Hong, S. A., Oh, I. H., “*Influence of Cathode Gas Diffusion Media on the Performance of the PEMFCs*”, J. Power Sources, 2004, 131, 147–154.

⁶⁷ Jordan, L. R., Shukla, A. K., Behrsing, T., Avery, N. R., Muddle, B. C., Forsyth, M.,

"Diffusion Layer Parameters Influencing Optimal Fuel Cell Performance", J. Power Sources, 2000, 86, 250–254.

⁶⁸ Park, S., Lee, J. W., Popov, B. N., *"Effect of PTFE Content in Microporous Layer on Water Management in PEM Fuel Cells"*, J. Power Sources, 2008, 177, 457–463.

⁶⁹ Nakajima H., Konomi, T., Kitahara, T., *"Direct Water Balance Analysis on a polymer Electrolyte Fuel Cell (PEFC): Effects of Hydrophobic Treatment and Micro-Porous Layer Addition to the Gas Diffusion Layer of a PEFC on Its Performance During a Simulated Start-Up Operation"*, J. Power Sources, 2007, 171, 457–463.

⁷⁰ Weber, A. Z., Newman, J., *"Effects of Microporous Layers in Polymer Electrolyte Fuel Cells, J. Electrochem"*, Soc., 2005, 152, A677–A688.

⁷¹ Weber, A. Z. and Newman, J., *"Modeling Transport in Polymer-Electrolyte Fuel Cells"*, Chem. Rev. 2004, 104, 4679-4726

⁷² Cindrella, L., Kannan, A. M., Lin, J. F., Saminathan, K., Ho, Y., Lin, C. W., Wertz, J., *"Gas Diffusion Layer for Proton Exchange Membrane Fuel Cells—A Review"*, J. Power Sources, 2009, 194, 146–160.

⁷³ Williams, M. V., Begg, E., Bonville, L., Kunz, H. R., Fenton, J. M., *"Characterization of Gas Diffusion Layers for PEMFC"*, J. Electrochem. Soc. 2004, 151, A1173–A1180.

⁷⁴ Yan, W. M., Soong, C. Y., Chen, F. L., Chu, H. S., *"Effects of Flow Distributor Geometry and Diffusion Layer Porosity on Reactant Gas Transport and Performance of Proton Exchange Membrane Fuel Cells"*, J. Power Sources, 2004, 125, 27–39.

⁷⁵ Zhan, Z. G., Xiao, J. S., Li, D. Y., Pan, M., Yuan, R. Z., *"Effects of Porosity Distribution Variation on the Liquid Water Flux Through Gas Diffusion Layers of PEM Fuel Cells"* J. Power Sources, 2006, 160, 1041–1048.

⁷⁶ Wang, X. L., Zhang, H. M., Zhang, J. L., Xu, H. F., Tian, Z. Q., Chen, J., Zhong, H. X., Liang, Y. M., Yi, B. L., *"Micro-Porous Layer with Composite Carbon Black for PEM Fuel Cells"*, Electrochim. Acta., 2006, 51, 4909–4915.

⁷⁷ Gostick, J. I., Ioannidis, M. A., Fowler, M. W., Pritzker, M. D., *"Pore Network Modelling of*

Fibrous Gas Diffusion Layers for Polymer Electrolyte Membrane Fuel Cells", J. Power Sources, 2007, 173, 277–290.

⁷⁸ Roshandel, R., Farhanieh, B., Saievar-Iranizad, E., "The Effects of Porosity Distribution Variation on PEM Fuel Cell Performance", Renew. Energy, 2005, 30, 1557–1572.

⁷⁹ Tang, H. L., Wang, S. L., Pan, M., Yuan, R. Z., "Porosity-Graded Micro-Porous layers for Polymer Electrolyte Membrane Fuel Cells", J. Power Sources 166 (2007) 41–46.

⁸⁰ Chen, F. L., Chang, M. H., Hsieh, P. T., "Two-Phase Transport in the Cathode Gas Diffusion Layer of PEM Fuel Cell with a Gradient in Porosity", Int. J. Hydrogen Energy, 2008, 33, 2525–2529.

⁸¹ Zhan, Z. G., Xiao, J. S., Zhang, Y. S., Pan, M., Yuan, R. Z., "Gas Diffusion Through Differently Structured Gas Diffusion Layers of PEM Fuel Cells", Int. J. Hydrogen Energy, 2007, 32, 4443–4451.

⁸² Atiyeh, H. K., Karan, K., Peppley, B., Phoenix, A., Halliop, E., Pharoah, J., "Experimental Investigation of the Role of a Microporous Layer on the Water Transport and Performance of a PEM Fuel Cell", J. Power Sources, 2007, 170, 111–121.

⁸³ Han, M. J., Xu, H., Chan, S. H., Jiang, S. P., "Characterization of Gas Diffusion Layers for PEMFC", Electrochim. Acta, 2008, 53, 5361–5367.

⁸⁴ Kannan, A. M., Cindrella, L., Munukutla, L., "Functionally Graded Nano-Porous Gas Diffusion Layer for Proton Exchange Membrane Fuel Cells under Low Relative Humidity Conditions", Electrochim. Acta., 2008, 53, 2416–2422.

⁸⁵ Pharoah, J. G., "On the Permeability of Gas Diffusion Media Used in PEM Fuel Cells", J. Power Sources, 2005, 144, 77–82.

⁸⁶ Gostick, T., Fowler, M. W., Pritzker, M. D., Ioannidis, M. A., Behra, L. M., "In-Plane and Through-Plane Gas Permeability of Carbon Fiber Electrode Backing Layers", J. Power Sources, 2006, 162, 228–238.

⁸⁷ Tomadakis, M. M., Robertson, T. J., "Viscous Permeability of Random Fiber Structures: Comparison of Electrical and Diffusional Estimates with Experimental and Analytical

Results”, J. Compos. Mater., 2005, 39, 163–188.

⁸⁸ Feser, J. P., Prasad, A. K., Advani, S. G., “*Experimental Characterization of In-Plane Permeability of Gas Diffusion Layers*”, J. Power Sources, 2006, 162, 1226–1231.

⁸⁹ Lum, K. W., McGuirk, J. J., “*Three-Dimensional Model of a Complete Polymer Electrolyte Membrane Fuel Cell—Model Formulation, Validation and Parametric Studies*”, J Power Sources, 2005, 143, 103–124.

⁹⁰ Gurau, V., Bluemle, M. J., S. De Castro, E., Tsou, Y. M., Zawodzinski Jr., T. A., “*Characterization of Transport Properties in Gas Diffusion Layers for Proton Exchange Membrane Fuel Cells: 2. Absolute Permeability*”, J. Adin Mann Jr., J. Power Sources, 2007, 165, 793–802.

⁹¹ He, G. L., Zhao, Z. C., Ming, P. W., Abuliti, A., Yin, C. Y., “*A Fractal Model for Predicting Permeability and Liquid Water Relative Permeability in the Gas Diffusion Layer (GDL) of PEMFCs*”, J. Power Sources, 2007, 163, 846–852.

⁹² Ahmed, D. H., Sung, H. J., Bae, J., “*Effect of GDL Permeability on Water and Thermal Management in PEMFCs—I. Isotropic and Anisotropic Permeability*”, Intl. J. Hydrogen Energy, 2008, 33, 3767 – 3785.

⁹³ Hussaini, I. S., Wang, C. Y., “*Measurement of Relative Permeability of Fuel Cell Diffusion Media*”, J. Power Sources, 2010, 195, 3830–3840.

⁹⁴ Tamayol, A., Bahrami, M., “*In-Plane Gas Permeability of Proton Exchange Membrane Fuel Cell Gas Diffusion Layers*”, J. Power Sources, 2011, 196, 3559–3564.

⁹⁵ Meng, H., Wang, C. Y., “*Electron Transport in PEFCs*”, J. Electrochem. Soc., 2004, 151, A358–A367.

⁹⁶ Natarajan, T. D., Nguyen, V., “*Effect of Electrode Configuration and Electronic Conductivity on Current Density Distribution Measurements in PEM Fuel Cells*”, J. Power Sources, 2004, 135, 95–109.

⁹⁷ Sui, P. C., Djilali, N., “*Analysis of Coupled Electron and Mass Transport in the Gas Diffusion Layer of a PEM Fuel Cell*”, J. Power Sources, 2006, 161, 294–300.

-
- ⁹⁸ Zhang, L. H., Liu, Y., Song, H. M., Wang, S. X., Zhou, Y. Y., Hu, S. J., “*Estimation of Contact Resistance in Proton exchange Membrane Fuel Cells*”, J. Power Sources, 2006, 162, 165–1171.
- ⁹⁹ Sun, H., Zhang, G. S., Guo, L. J., Liu, H. T., “*A Novel Technique for Measuring Current Distributions in PEM Fuel Cells*”, J. Power Sources, 2006, 158, 326–332.
- ¹⁰⁰ Zhou, Y., Lin, G., Shih, A. J., Hu, S. J., “*A Micro-Scale Model for Predicting Contact Resistance Between Bipolar Plate and Gas Diffusion Layer in PEM Fuel Cells*”, J. Power Sources, 2007, 163, 777–783.
- ¹⁰¹ Wu, Z. L., Zhou, Y. Y., Lin, G. S., Wang, S. X., Hu, S. J., “*An Improved Model for Predicting Electrical Contact Resistance Between Bipolar Plate and Gas Diffusion Layer in Proton Exchange Membrane Fuel Cells*”, J. Power Sources, 2008, 182, 265–269.
- ¹⁰² Freunberger, S. A., Reum, M., Evertz, J., Wokaun, A., Buchi, F. N., “*Measuring the Current Distribution in PEFCs with Sub-Millimeter Resolution*”, J. Electrochem. Soc., 2006, 153, A2158–A2165.
- ¹⁰³ Wang, L., Liu, H. T., “*Separate Measurement of Current Density under the Channel and the Shoulder in PEM Fuel Cells*”, J. Power Sources, 2008, 180, 365–372.
- ¹⁰⁴ Barber, M., Sun, T. S., Petrach, E., Wang, X., Zou, Q., “*Contact Mechanics Approach to Determine Contact Surface area Between Bipolar Plates and Current Collector in Proton Exchange Membrane Fuel Cells*”, J. Power Sources, 2008, 185, 1252–1256.
- ¹⁰⁵ Bapat, C. J., Thynell, S. T., “*Effect of Anisotropic Electrical Resistivity of Gas Diffusion Layers (GDLs) on Current Density and Temperature Distribution in a Polymer Electrolyte Membrane (PEM) Fuel Cell*”, J. Power Sources, 2008, 185, 428–432.
- ¹⁰⁶ Lai, X. M., Liu, D. A., Peng, L. F., Ni, J., “*A Mechanical–Electrical Finite Element Method Model for Predicting Contact Resistance Between Bipolar Plate and Gas Diffusion Layer in PEM Fuel Cells*”, J. Power Sources, 2008, 182, 153–159.
- ¹⁰⁷ Li, I., Wang, C. Y., Su, A., “*Prediction and Experimental Validation of In-Plane Current Distribution between Channel and Land in a PEFC*”. J. Electrochem. Soc., 2008, 155, B64–B69.

-
- ¹⁰⁸ Mathias, M. F., Roth, J., Fleming, J., Lehnert, W., "*Handbook of Fuel Cells-Fundamentals, Technology and Applications*", Vol 2, John Wiley and Sons, 2003, pp.517.
- ¹⁰⁹ Wang, Y., Wang, C. Y., Chen, K. S., "*Elucidating Differences Between Carbon Paper and Carbon Cloth in Polymer Electrolyte Fuel Cells*", *Electroch. Acta*, 2007, 52, 3965–3975.
- ¹¹⁰ Radhakrishnan, V., Haridoss, P., "*Differences in Structure and Property of Carbon Paper and Carbon Cloth Diffusion Media and Their Impact on Proton Exchange Membrane Fuel Cell Flow Field Design*", *Materials and Design*, 2011, 32, 861–868.
- ¹¹¹ Park, S., Popov, B. N., "*Effect of a GDL Based on Carbon Paper or Carbon Cloth on PEM Fuel Cell Performance*", *Fuel*, 2011, 90, 436-440.
- ¹¹² Lin, J. F., Wertz, J., Ahmad, R., Thommes, M., Kannan, A. M., "*Effect of Carbon Paper Substrate of the Gas Diffusion Layer on the Performance of Proton Exchange Membrane Fuel Cell*", *Electroch. Acta*, 2010, 55, 2746–2751.
- ¹¹³ Zamel, N., Li, X. G., Shen, J., Becker, J., Wiegmann, A., "*Estimating Effective Thermal Conductivity in Carbon Paper Diffusion Media*", *Chem. Eng. Sci.*, 2010, 65, 3994–4006.
- ¹¹⁴ Liu, C. H., Ko, T. H., Kuo, W. S., Chou, H. K., Chang, H. -W., Liao, Y. K., "*Effect of Carbon Fiber Cloth with Different Structure on the Performance of Low Temperature Proton Exchange Membrane Fuel Cells*", *J. Power Sources*, 2009, 186, 450–454.
- ¹¹⁵ Sun, W., Peppley, B. A., Karan, K., "*Modeling the Influence of GDL and Flow-Field Plate Parameters on the Reaction Distribution in the PEMFC Cathode Catalyst Layer*", *J. Power Sources*, 2005, 144, 42–53.
- ¹¹⁶ Shi, Z. Y., Wang, X., "*A Numerical Study of Flow Crossover between Adjacent flow Channels in a Proton Exchange Membrane Fuel Cell with Serpentine Flow Field*", *J. Power Sources*, 2008, 185, 985–992.
- ¹¹⁷ Jang, J. H., Yan, W. M., Shih, C. C., "*Numerical Study of Reactant Gas Transport phenomena and Cell Performance of Proton Exchange Membrane Fuel Cells*", *J. Power Sources*, 2006, 156, 244–252.
- ¹¹⁸ Feser, J. P., Prasad, A. K., Advani, S. G., "*On the Relative Influence of Convection in*

Serpentine Flow Fields of PEM Fuel Cells", J. Power Sources, 2006, 161, 404–412.

¹¹⁹ Jeng, K. T., Lee, S. F., Tsai, G. F., Wang, C. H., "Oxygen Mass Transfer in PEM Fuel Cell Gas Diffusion Layers", J. Power Sources, 2004, 138, 41–50.

¹²⁰ Pharoah, J. G., Karan, K., Sun, W., "On Effective Transport Coefficients in PEM Fuel Cell Electrodes: Anisotropy of the Porous Transport Layers", J. Power Sources, 2006, 161, 214–224.

¹²¹ Park, J., Li, X. G., "An Experimental and Numerical Investigation on the Cross Flow through Gas Diffusion Layer in a PEM Fuel Cell with a Serpentine Flow Channel", J. Power Sources, 2007, 163, 853–863.

¹²² Markicevic, B., Bazylak, A., Djilali, N., "Determination of Transport Parameters for Multiphase Flow in Porous Gas Diffusion Electrodes using a Capillary Network Model", J. Power Sources, 2007, 171, 706–717.

¹²³ Berning, T., Djilali, N., "A 3D Multiphase Multicomponent Model of the Cathode and Anode of a PEM Fuel Cell", J. Electrochem. Soc., 2003, 150, A1589–A1598.

¹²⁴ Vogel, H. J., Tolke, J., Schulz, V. P., Krafczyk, M. and Roth, K., "Comparison of a Lattice-Boltzmann Model, a Full-Morphology Model, and a Pore Network Model for Determining Capillary Pressure–Saturation Relationships", Vadose Zone Journal, 2005, Volume: 4, Issue: 2, 380–388

¹²⁵ Sinha, P. K., Wang, C. Y., "Pore-Network Modeling of Liquid Water Transport in Gas Diffusion Layer of a Polymer Electrolyte Fuel Cell", Electrochim. Acta, 2007, 52, 7936–7945.

¹²⁶ Chapuis, O., Prat, M., Quintard, M., Chane-Kane, E., Guillot, O., Mayer, N., "Two-Phase Flow and Evaporation in Model Gibrus Media Application to the Gas Diffusion Layer of PEM Fuel Cells", J. Power Sources, 2008, 178, 258–268.

¹²⁷ Lee, K. J., Nam, J. H., Kim, C. J., "Pore-Network Analysis of Two-Phase Water Transport in Gas Diffusion Layers of Polymer Electrolyte Membrane Fuel Cells", Electrochim. Acta, 2009, 54, 1166–1176.

-
- ¹²⁸ Shimpalee, S., Beuscher, U., Van Zee, J. W., "*Investigation of Gas Diffusion Media Inside PEMFC using CFD Modeling*", *J. Power Sources*, 2006, 163, 480–489.
- ¹²⁹ Martinez, C. B., Travis, R., Bang, M., "*Three-Dimensional, Single-Phase, Non-Isothermal CFD Model of a PEM Fuel Cell*", *J. Power Sources*, 2008, 178, 269–281.
- ¹³⁰ Dawes, J. E., Hanspal, N. S., Family, O. A., Turan, A., "*Three-Dimensional CFD Modelling of PEM Fuel Cells: An Investigation into the Effects of Water Flooding*", *Chemical Engineering Science*, 2009, 64, 2781 – 2794.
- ¹³¹ Siegel, C., "*Review of Computational Heat and Mass Transfer Modeling in Polymer-Electrolyte-Membrane (PEM) Fuel Cells*", *Energy*, 2008, 33, 1331– 1352.
- ¹³² Um, S., Wang, C. Y., and Chen, K. S., "*Computational Fluid Dynamics Modeling of Proton Exchange Membrane Fuel Cells*", *J. Electrochemical Soc.*, 2000, 147 (12) 4485-4493.
- ¹³³ Sivertsen, B. R., Djilali, N., "*CFD-Based Modelling of Proton Exchange Membrane Fuel Cells*", *J. Power Sources*, 2005, 141, 65–78.
- ¹³⁴ Djilali, N., "*Computational Modelling of Polymer Electrolyte Membrane (PEM) Fuel Cells: Challenges and Opportunities*", *Energy*, 2007, 32, 269–280.
- ¹³⁵ Berning, T., Lu, D. M., Dajilali, N., "*Three-dimensional Computational Analysis of Transport Phenomena of a PEM Fuel Cell*", *J. Power Sources*, 2002, 106, 284-294.
- ¹³⁶ Siegel, N., Ellis, M., Nelson, D., M. von Spakovsky, "*A Two-Dimensional Computational Model of a PEMFC with Liquid Water Transport*", *J. Power Sources*, 2004, 128, 173–184.
- ¹³⁷ Dutta, S., Shimpalee, S., Zee, J. W. V., "*Three-Dimensional Numerical Simulation of Straight Channel PEM fuel Cells*", *J. Appl. Electrochem*, 2000, 30, 135–146.
- ¹³⁸ Dutta, S., S. Shimpalee, Zee, J. W. V., "*Numerical Prediction of Mass Exchange Between Cathode and Anode Channels in a PEM Fuel Cell*", *Int. J. Heat Mass Transfer*, 2001, 44, 2029–2042.
- ¹³⁹ Dawes, J. E., Hanspal, N. S., Family, O. A., and Turan, A., "*Three-Dimensional CFD Modelling of PEM Fuel Cells: An Investigation into the Effects of Water Flooding*", *Chem. Engineering Science*, 2009, Vol. 64, 12, 2781-2794.

-
- ¹⁴⁰ Park, J., Li, X., “*Multi-phase Micro-scale Flow Simulation in the Electrodes of a PEM Fuel Cell by Lattice Boltzmann Method*”, J. Power Sources, 2008, 178, 248 - 257
- ¹⁴¹ Ju, H., “*Investigation of the Effects of the Anisotropy of Gas-diffusion Layers on Heat and Water Transport in Polymer Electrolyte Fuel Cells*”, J. of Power Sources, 2009, 191, 259–268
- ¹⁴² Munekata, T., Inamuro, T., and Hyodo, S. A., “*Gas Transport Properties in Gas Diffusion Layers: A Lattice Boltzmann Study*”, Commun. Comput. Phys., 2011, 9, pp. 1335-1346.
- ¹⁴³ Wang, L., P., Afsharpoya, B., “*Modeling Fluid Flow in Fuel Cells Using the Lattice Boltzmann Approach*”, Mathematics and Computers in Simulation, 72, 2006, 242–248
- ¹⁴⁴ Hao L., Cheng, P., “*Pore-scale Simulations on Relative Permeabilities of Porous Media by Lattice Boltzmann Method*”, Intl. J. of Heat and Mass Transfer, 2010, 53, 1908–1913
- ¹⁴⁵ Niu X. D., Munekata, T., Hyodo, S. A., and Suga, K., “*An Investigation of Water-Gas Transport Processes in the Gas Diffusion Layer of a PEM Fuel Cell by a Multiphase Multiple-relaxation-time Lattice Boltzmann Model*”, J. Power Sources, 2007, 172, 542–552.
- ¹⁴⁶ Hao, L., Cheng, P., “*Lattice Boltzmann Simulations of Anisotropic Permeabilities in Carbon Paper Gas Diffusion Layers*”, J. Power Sources, 2009, 186, 104–114.
- ¹⁴⁷ Bazylak, A., Sinton, D., Liu, Z. S., Djilali, N., “*Effect of Compression on Liquid Water Transport and Microstructure of PEMFC Gas Diffusion Layers*”, J. Power Sources, 2007 163, 784–792.
- ¹⁴⁸ Lim, C., Wang, C., “*Effects of Hydrophobic Polymer Content in GDL on Power Performance of a PEM Fuel Cell*”, Electrochim. Acta, 2004, 49, 4149 - 4156.
- ¹⁴⁹ Kramer, D., Zhang, J., Shimo, R., Lehmann, E., Wokaun, A., Shinohara, K., Scherer, G., “*In Situ Diagnostic of Two-Phase Flow Phenomena in Polymer Electrolyte Fuel Cells by Neutron Imaging Part A. Experimental, Data Treatment, and Quantification*”, Electrochim. Acta, 2005, 50, 2603–2614.

-
- ¹⁵⁰ Lee, S. J., Lim, N. Y., Kim, S., Park, G. G., and Kim, C. S., “*X-ray Imaging of Water Distribution in a Polymer Electrolyte Fuel Cell*”, *J. Power Sources*, 2008, 185, 2, 867-870.
- ¹⁵¹ Litster, S., Sinton, D., Djilali, N., “*Ex Situ Visualization of Liquid Water Transport in PEM Fuel Cell Gas Diffusion Layers*”, *J. Power Sources*, 2006, 154, 95–105.
- ¹⁵² Chen, S., Doolen, G.D., “*Lattice Boltzmann Method for Fluid Flows*”. *Annu. Rev. Fluid Mech.* 1998, 30, 329–364.
- ¹⁵³ Toffoli, T., Farmer D., and Wolfram S., “*Cellular Automata, Proceedings of an Interdisciplinary Workshop*”, Los Alamos, Volume 10, Physica D., Borth Holland, 1984.
- ¹⁵⁴ Sukop, M., C. Thorne, D., T. Jr. “*Lattice Boltzmann Modeling: An Introduction for Geoscientists and Engineers*”, Springer, 2005
- ¹⁵⁵ Chopard, B., Luthi, P., Masselot, A., “*Cellular Automata and Lattice Boltzmann Techniques : An Approach To Model And Simulation Complex Systems*”, *J. Adv. in Complex Systems*, 2002 (2), 05, 103-246
- ¹⁵⁶ Boon J., P., “*Advanced Research Workshop on Lattice Gas Automata Theory: Implementations, and Simulations*”, *J. Statistical Physics.* 1992, 68.
- ¹⁵⁷ Pires, A., Landau, D., P., and Herrmann, H., “*Computational Physics and Cellular Automata*”, World Scientific, 1990.
- ¹⁵⁸ Chopard, B., and Droz, M., “*Cellular Automat Modeling of Physical Systems*”, Cambridge University Press, 1998.
- ¹⁵⁹ Livi, R., Ruffo, S., Ciliberto, S., and Buiatti, M., “*Chaos and Complexity*”, World Scientific, 1988.
- ¹⁶⁰ Dollen, G., “*Lattice Gas Method for Partial Differential Equations*”, Addison Wesley, 1990.
- ¹⁶¹ Perdang, J., M., and Lejeune, A., “*Cellular Automata: Prospect in Astrophysical Applications*”, World Scientific, 1993.

-
- ¹⁶² Toffoli, T., and Margolus, N., "*Cellular Automata Mechines: a New Environment for Modeling*", The MIT Press, 1987.
- ¹⁶³ Rothman D., and Zaleski, S., "*Lattice-Gas Cellular AutomataL Simple Models of Complex Hydrodynamics*", Collection Alea, Cambridge University Press, 1997.
- ¹⁶⁴ Wolfram, S., "*Cellulat Automata and Complexity*", Addison Wesley, Reading MA, 1994.
- ¹⁶⁵ Frisch, U., Hasslacher, B., Pomeau, Y., "*Lattice-Gas Automata for the Navier- Stokes Equation*", Phys. Rev. Lett., 1986, Volume 56, Number 14.
- ¹⁶⁶ Broadwell, J., E., "*Study of Rarefied Shear Flow by the Discrete Velocity Method*", J. Fluid Mech. 1964. 19:401-14.
- ¹⁶⁷ Kadanoff, L., "*On two levels*", Phys. Today, 1986. 39:7-9
- ¹⁶⁸ Chopard, B., Masselot, A., "*Cellular Automata and Lattice Boltzmann Methods: A New Approach to Computational Fluid Dynamics and Particle Transport*", Future Generation Computer Systems, 1999, Volume 16, Issues 2-3, 249-257
- ¹⁶⁹ McNamara, G., R., Zanetti, G., "*Use of the Boltzmann Equation to Simulate Lattice-Gas Automata*", Phys. Rev. Lett. 1988.61:2332-35
- ¹⁷⁰ Higuera, F., J., Jimenez, J., "*Boltzmann Approach to Lattice Gas Simulations*", Europhys, Lett, 1989, 9:663-68
- ¹⁷¹ Higuera, F., J., Succi, S., "*Simulating the Flow Around A Circular Cylinder With A Lattice Boltzmann Equation*", Europhys. Lett. 1989, 8:517-21
- ¹⁷² Qian, Y. H., d'Humi`eres, D., Lallemand, "*Lattice BGK Models for Navier-Stokes Equation*". Europhys. Lett. P. 1992. 17:479-84
- ¹⁷³ Chen. S., Chen, H. D., Martinez, D., and Matthaeus, W., "*Lattice Boltzmann Model for Simulation of Magnetohydrodynamics*". Phys Rev. Lett. 1991, 67:3776-79
- ¹⁷⁴ Succi S. "*The Lattice Boltzmann Equation for Fluid Dynamics and Beyond*", Oxford University Press: Oxford, 2001.

-
- ¹⁷⁵ He X, Luo L. “*Lattice Boltzmann Model for the Incompressible Navier–Stokes Equation*”. *J. Statistical Physics*, 1997; 88: 927-948
- ¹⁷⁶ Chen, H. D., Chen, S. Y., Matthaeus, W.H., “*Recovery of the Navier-Stokes Equations Using a Lattice-Gas Boltzmann Method*”, *Phys. Rev., A*, 1992, 45, 8.
- ¹⁷⁷ Wolfram, S., “*Cellular Automaton Fluids 1: Basic Theory*”, *J. Stat. Phys.* 1986 45:471–526
- ¹⁷⁸ Lavallée, P., Boon, J., P., Noullez, A., “*Boundaries in Lattice Gas Flows*”, *Physica*, 1991. D 47:233–40
- ¹⁷⁹ Verberg, R., Ladd, A.J.C., “*Lattice-Boltzmann Model with Sub-grid-scale Boundary Conditions*”. *Phys Rev Lett.* , 2000, 84:2148-2151
- ¹⁸⁰ Noble, D. R., Chen, S., Georgiadis, J.G., and Buckius, R.O., “*A Consistent Hydrodynamic Boundary Condition for the Lattice Boltzmann Method*”. *Phys Fluids*, 1995, 7:203-209
- ¹⁸¹ Inamuro, T., Yoshino, M., and Ogino, F., “*A Non-slip Boundary Condition for Lattice Boltzmann Simulations*”. *Phys Fluids*, 1995, 7:2928-2930
- ¹⁸² Ginzbourg I, d’Humières D “*Multireflection Boundary Conditions for Lattice Boltzmann Models*”. 2003, *Phys Rev., E* 68: 066614
- ¹⁸³ Ketcham, R. A., Carlson, W., D., “*Acquisition, Optimization and Interpretation of X-ray Computed Tomographic Imagery: Applications to the Geosciences*”, *Computers & Geosciences*, 2001, 27, 381–400
- ¹⁸⁴ Coker, D.A., Torquato, S., Dunsmuir, J.H., “*Morphology and Physical Properties of Fontainebleau Sandstone Via a Tomographic Analysis*”, *J. of Geophysical Research*, 1996, 101 (B8), 17,497–17,506.
- ¹⁸⁵ Flannery, B.P., Deckman, H.W., Roberge, W.G., D’Amico, K.L., “*Three-Dimensional X-ray Microtomography*”, *Science* 1987, 237, 1439–1444.
- ¹⁸⁶ Kinney, J.H., Breuning, T.M., Starr, T.L., Haupt, D., Nichols, M.C., Stock, S.R., Butts, M.D., Saroyan, R.A., “*X-ray Tomographic Study of Chemical Vapor Infiltration Processing of Ceramic Deposits*”, *Science*, 1993, 260, 782–789.

-
- ¹⁸⁷ McNulty, I.; Haddad, W.S.; Trebes, J.E.; and Anderson, E.H. "Soft X-ray Scanning, Microtomography with Submicron Resolution", *Rev. Sci. Instrum.* 1995, 66 (2), 1431-1435.
- ¹⁸⁸ Sasov, A. "X-ray nanotomography, developments in X-ray tomography IV". Proceedings of the SPIE, 2004, 5535, 201-211
- ¹⁸⁹ Skyscan Microtomography, "CT-Analyser Users Guide," Version 1.6.1, pp. 16-29 and 61-63.
- ¹⁹⁰ Ding, M., Odgaard A., Hvid, I., "Accuracy of Cancellous Bone Volume Fraction Measured By Micro-CT Scanning", *J. Biomech.*, 1999, 32, 323-326
- ¹⁹¹ Hara, T., Tanck, E., Homminga, J., Huiskes, R., "The Influence of Microcomputer Tomography Threshold Variation on the Assessment of Structural and Mechanical Trabecular Bone Properties", *Health Sci. J., Bone*, 2002, 23, (2), 163-169
- ¹⁹² Ostadi, H., Jiang, K., Prewett, P.D., "Micro/nano X-ray Tomography Reconstruction Fine Tuning Using Scanning Electron Microscope Images", *Micro Nano Lett.*, 2008, 3(4), 106-109.
- ¹⁹³ Ostadi, H., Rama, P., Liu, Y., Chen, R., Zhang, X. X., Jiang, K., "Threshold Fine-Tuning and 3D Characterisation of Porous Media Using X-ray Nanotomography", *Current Nanoscience*, 2010, 6(2), 226-231.
- ¹⁹⁴ Ostadi, H., Jiang, K., Prewett, P. D., "Micro/Nano X-Ray Tomography Reconstruction Fine-Tuning Using Scanning Electron Microscope Images", *Micro & Nano Letters*, V3, 2008, 4, pp.106-109,
- ¹⁹⁵ "Manual for SkyScan CT-Analyser", v. 1.10, SkyScan, 2010.
- ¹⁹⁶ Benziger, J., Nehlsen, J., Blackwell, D., Brennan, T., and Itescu, J., "Water Flow in the Gas Diffusion Layer of PEM Fuel Cells," *J. Membr. Sci.*, 2005, 261, 98-106.
- ¹⁹⁷ M. A. Van Doormaal, and Pharoah, J. G., "Determination of Permeability in Fibrous Porous Media Using the Lattice Boltzmann Method With Application to Fuel Cells," *Int. J. Numer. Methods Fluids*, 2009, 59, 75-89
- ¹⁹⁸ Sinha, P. K., Mukherejee, P. P., and Wang, C. Y., "Impact of GDL Structure and

Wettability on Water Management in Polymer Electrolyte Fuel Cells, J. Mater. Chem., 2007, 17(30), 3089–3103

¹⁹⁹ Koido, T., Furusawa, T., and Moriyama, K., “*An Approach to Modelling Two-Phase Transport in the Gas Diffusion Layer of a Proton Exchange Membrane Fuel Cell,*” J. Power Sources, 2008, 175, 127–136.

²⁰⁰ Sinha, P. K., Wang, C. Y., “*Pore-Network Modeling of Liquid Water Transport in Gas Diffusion Layer of Polymer Electrolyte Fuel Cell,*” Electrochim. Acta, 2007, 52(28), 7936–7945.

²⁰¹ Schulz, V. K., Becker, J., Wiegmann, A., Mukherjee, P. P., Wang, C. Y., “*Modeling of Two-Phase Behavior in the Gas Diffusion Medium of PEFCs Via Full Morphology Approach,*” J. Electrochem. Soc., 2007, 154(4), B419–B426.

²⁰² Joshi, A. S., Peracchio, A. A., Grew, K. N., and Chiu, W. K. S., “*Lattice Boltzmann Method for Continuum, Multi-Component Mass Diffusion in Complex 2D Geometries,*” J. Phys. D: Appl. Phys., 2007, 40, 961–2971.

²⁰³ Zhang, X. X., and Ren, L., “*Lattice Boltzmann Model for Agrochemical Transport in Soils,*” J. Contam. Hydrol., 2003, 67, 27–42.

²⁰⁴ Zhang, X., Crawford, J. W., Bengough, A. G., and Young, I. M., “*On Boundary Conditions in the Lattice Boltzmann Model for Advection and Anisotropic Dispersion Equation,*” Adv. Water Resour., 2002, 25, 601–609.

²⁰⁵ Bevers, D., Rogers, R., and von Bradke, M., “*Examination of the Influence of PTFE Coating on the Properties of Carbon Paper in Polymer Electrolyte Fuel Cells,*” J. Power Sources, 1996, 63, 193–201

²⁰⁶ Nie, X. B., Doolen, G. D., and Chen S. Y., “*Lattice Boltzmann Simulation of Fluid Flows in MEMS,*” J. Stat. Phys. 2002, 107, 279.

²⁰⁷ Rama, P., Chen, R., and Thring, R., “*Polymer Electrolyte Fuel Cell Transport mechanisms: A Universal Modelling Framework From Fundamental Theory,*” Proc. IMechE Part A: J. Power and Energy, 2006, 20, 535 - 550

-
- ²⁰⁸ Arcidiacono, S., Karlin, I. V., Mantzaras, J., and Frouzakis, C. E., “*Lattice Boltzmann Model for the Simulation of Multicomponent mixtures*”, *Physical Review E*, 2007, 76(046703), 1-11
- ²⁰⁹ Joshi, A. S., Grew, K. N., Peracchio, A. A., Chiu, and W. K. S. “*Lattice Boltzmann Modeling of 2D Gas Transport in a Solid Oxide Fuel Cell Anode*”, *J. Power Sources*, 2007, 164(2), 631-638
- ²¹⁰ Chiu, W. K. S., Joshi, A. S., and Grew, K. N., “*Lattice Boltzmann Model for Multi-component Mass Transfer in a Solid Oxide Fuel Cell Anode with Heterogeneous Internal Formation and Electrochemistry*”, *Eur. Phys. J. Special Topics*, 2009, 171, 159-165
- ²¹¹ Luo, L. S., Girimaji, S. S., “*Theory of the Lattice Boltzmann method: Two-Fluid Model for Binary Mixtures*”, *Physical Review E*, 2003, 67(3), 036302
- ²¹² Luo, L. S., and Girimaji, S. S., “*Lattice Boltzmann model for binary mixtures*”, *Physical Review*, 2002, E 66, 035301(R)
- ²¹³ Wang, M., He, J. H., Yu, J. Y., Pan, N., “*Lattice Boltzmann modeling of the effective thermal conductivity for fibrous materials*”, *Intl. J. Therm. Sci.* 2007, 46, 848–855
- ²¹⁴ Hao, L., Cheng, P., “*Lattice Boltzmann simulations of water transport in gas diffusion layer of a polymer electrolyte membrane fuel cell*”, *J. Power Sources*, 2010, 1953870–3881
- ²¹⁵ Ziegler, C., Gerteisen, D., “*Validity of two-phase polymer electrolyte membrane fuel cell models with respect to the gas diffusion layer*”, *J. Power Sources*, 2009, 188, 184–191
- ²¹⁶ Park, J., Matsubara, M., Li, X., “*Application of Lattice Boltzmann Method To A Micro-Scale Flow Simulation In The Porous Electrode Of A PEM Fuel Cell*”, *J. Power Sources* 2007, 173, 404–414
- ²¹⁷ Tomadakis, M. M., Sotirchos, S. V., “*Ordinary and Transition Regime Diffusion in Random Fiber Structures*”, *J. AICHE*, 1993, 39, 397–412.

-
- ²¹⁸ Matteson, M. J., Orr, C., *"Filtration: Principles and Practices"*, pp 180 Marcel Dekker, INC., New York, 1987
- ²¹⁹ Tomadakis, M. M., Sotirchos, S. V., *"Effective Knudsen Diffusivities in Structures of Randomly Overlapping Fibers"*, J. AIChE, 1991, 37(1):74-85
- ²²⁰ Tomadakis, M. M., Sotirchos, S. V., *"Knudsen Diffusivities and Properties of Structures of Unidirectional Fibers"*, J. AIChE, 1991, 37(8):1175-1186
- ²²¹ Lee, W. K., Ho, C. H., Van Zee, J. W., Murthy, M., *"The Effects of Compression and Gas Diffusion Layers On the Performance of A PEM Fuel Cell"*, J. Power Sources, 1999, 84, 45-51
- ²²² Ge, J. B., Higier, A., Liu, H. T., *"Effect of Gas Diffusion Layer Compression on PEM Fuel Cell Performance"*, J. Power Sources, 2006, 159, 922-927
- ²²³ Lin, J. H., Chen, W. H., Su, Y. J., Ko, T. H., *"Effect of Gas Diffusion Layer Compression on the Performance in a Proton Exchange Membrane Fuel Cell"*, Fuel, 2008, 87, 2420-2424
- ²²⁴ Nitta, I., Hottinen, T., Himanena, O., Mikkola, M., *"Inhomogeneous Compression of PEMFC Gas Diffusion Layer Part I. Experimental"*, J. Power Sources, 2007, 171, 26-36
- ²²⁵ Hottinen, T., Himanen, O., Karvonen, S., Nitta, I., *"Inhomogeneous Compression of PEMFC Gas Diffusion Layer Part II. Modeling the Effect"*, J. Power Sources, 2007, 171, 113-121
- ²²⁶ Su, Z. Y., Liu, C. T., Chang, H. P., Li, C. H., Huang, K. J., Sui, P. C., *"A Numerical Investigation of the Effects of Compression Force on PEM Fuel Cell Performance"*, J. Power Sources, 2008, 183, 182-192
- ²²⁷ Shi, Z. Y., Wang, X., Guessous, L., *"Effect of Compression on the Water Management of a Proton Exchange Membrane Fuel Cell With Different Gas Diffusion Layers"*, ASME Journal of Fuel Cell Science and Technology 2010, [DOI: 10.1115/1.3177451], 2010, APRIL, Vol. 7 / 021012-1
- ²²⁸ Hottinen, T., Himanen, O., *"PEMFC Temperature Distribution Caused by Inhomogeneous Compression of GDL"*, Electrochemistry Communications, 2007, 9,

²²⁹ Hildebrand, T. and Ruegsegger, P., '*A New Method for the Model Independent Assessment of Thickness in Three Dimensional Images*', J. Microscopy, 1997, 185: 67-75

²³⁰ Lotters, J. C., Olthuisy, W., Veltink, P. H., Bergveld, P., "*Polydimethylsiloxane as An Elastic Material Applied in a Capacitive Accelerometer*", J. Micromech. Microeng, 1996, 6, 52–54.

²³¹ Paddison, S. J., Promislow, K. S.(Eds.), '*Device and Materials Modelling in PEM fuel cells*', Springer Science, New York, 2009.